THE UNIVERSITY
of EDINBURGH

NON-ASSOCIATIVE PLASTICITY FOR STRUCTURAL INSTABILITY OF CYLINDRICAL SHELLS IN THE INELASTIC RANGE

THE UNIVERSITY *of* EDINBURGH
Institute for Infrastructure and Environment

Apostolos Nasikas

This dissertation is submitted for the degree of

Doctor of Philosophy

July 2022

To Barney

DECLARATION

I hereby declare that except where specific reference is made to the work of others, the contents of this dissertation are original and have not been submitted in whole or in part for consideration for any other degree or qualification in this, or any other university. This dissertation is my own work and contains nothing which is the outcome of work done in collaboration with others, except as specified. Some of the work has been presented in the following publications:

A. Nasikas, S.A. Karamanos and S.A. Papanicolopulos (2019) Non-Associative Plasticity Models for Structural Instability Calculations in Thick-Walled Metal Shells Invited lecturer in COMPLAS 2019, International Conference on Computational Plasticity.

A. Nasikas, S.A. Karamanos and S.A. Papanicolopulos (2022) A framework for formulating and implementing non-associative plasticity models for shell buckling computations, International Journal of Solids and Structures https://doi.org/10.1016/j.ijsolstr.2022.111508

Apostolos Nasikas

ABSTRACT

Thick-walled cylindrical metal shells, commonly used in tubular structures and pipelines, during their lifetime may be subjected to considerable compressive loads, which can lead to local buckling. In modelling their structural behaviour, the use of standard J_2 flow plasticity is known to produce unrealistically high buckling load estimates. Alternative constitutive models, which consider the formation of yield surface 'corners', can provide more accurate predictions, but they have been used scarcely, due to the limitations and complexities they introduce.

The present work develops an efficient and versatile plasticity model to simulate the structural response of metal shells under compressive loads. It combines the simplicity of a Von Mises yield surface, with a non-associative flow rule, mimicking the effect of a yield surface corner. The model allows for tracing the equilibrium path of the shells and identifying structural instability in a consistent manner. A robust backward-Euler integration scheme is developed, suitable for three-dimensional (solid) and shell finite elements. The corresponding algorithmic moduli are obtained for nonlinear isotropic hardening materials. The nonlinear dependence of plastic strain increments on the direction of total strain increments is accounted for rigorously.

The constitutive model is implemented in Abaqus as a user material subroutine (UMAT). Simulations of thick-walled metal cylinders under uniform compression show good agreement with experimental data in predicting the buckling and post-buckling performance of shells. The influence of geometric imperfection is considered, and comparisons are made with models employing the J_2 flow plasticity. The reliability of the developed approach is further demonstrated by investigating more demanding problems of bending and pressure in inelastic cylinders, taking into account ovalization, bifurcation instabilities, imperfection. These problems involve non-trivial prebuckling equilibrium paths, non-uniform loading and significant non-proportionality, before instability onsets, which activate the model's particular features, and illustrate their role in the evolution of buckling. Analyses showcase the model's capabilities, producing accurate instability estimates, ultimate load and deformation predictions in line with experiments and clarify aspects of the buckling of inelastic shells. Extending a traditional practice, a simple method is presented for estimating the instability of inelastic cylinders under bending and pressure loads, drawing on similarities in their buckling with that of cylinders under compression.

LAY SUMMARY

Long thick-walled metal cylinders are widely used in tubular structures and pipeline applications. During their installation, operation and in extreme events, they may be subjected to significant compressive loads, which can lead to structural instability in the form of local buckling (wave-like deformations developing in parts of the cylinder). In thin-walled cylinders, local buckling is considered as failure, as it is followed by an abrupt loss of strength and collapse of the tube section. For thicker cylinders, with diameter-over-thickness ratios (D/t) less than 60, the post-buckling behaviour can be smoother, and a series of events can precede collapse. To take advantage of this additional strength in the design of tubes, simulation tools are needed to accurately estimate the onset of buckling, the structural behaviour until failure, and the factors that influence them.

Since the 50s, the structural performance of thick-walled cylinders has been attracting research attention. These shells experience instability while loaded in the inelastic (plastic) range of the material, and the key subject of buckling estimation is known to be sensitive to the plasticity model used. The standard model has been found to produce overly high buckling load estimates, which may be attributed to sudden changes in the material loading that occur at buckling. More advanced material models, that account for lower material strength under such conditions, produce more realistic buckling estimates, in agreement with experimental data. However, these models have been employed scarcely in structural calculations due to limitations and complexities they introduce.

The present research reviews the influence of material modelling in structural stability calculations of tubulars under compressive loads. An efficient and versatile material model is developed that accounts for properties of advanced material models in a simplified and effective manner. It is programmed and introduced in modern structural engineering tools, to reliably simulate the behaviour of thick-walled cylinders. Numerical analyses are performed to investigate the structural performance of tubulars under uniform compression, bending and pressure loads, which represent a wide range of load cases of practical interest. Simulated behaviours are in agreements with experimental data and aspects of instability in tubulars are clarified. The developed work frame may be used towards the accurate assessment of buckling and the post-buckling behaviours of tubulars, necessary for safe and economic design.

ACKNOWLEDGEMENTS

I want to express my sincere gratitude to my supervisor Prof. Spyros A. Karamanos, who followed and supported me during my Ph.D. His experience, guidance and rigorous scrutiny were paramount for the research that was conducted. I am indebted to him for the personal interest, patience and understanding he showed; for always encouraging me during this intense research period, for investing considerable time and effort in my work and for the research opportunities he created.

I am grateful to my assistant supervisor Dr Stefanos Aldo Papanicolopulos for his valuable suggestions; for his direct support and effective solutions, when unexpected difficulties arose, and for offering an objective perspective throughout this time.

I warmly acknowledge my fellow Ph.D. researchers Ilias, Kostis, Rania, George, Zeynep for their valuable input and comradeship throughout this endeavour. I profoundly thank Daniela and James for their friendship, support, and for encouraging me to develop beyond academia, actively intervening to motivate me.

I am grateful to my family for supporting me when circumstances called for my return to Volos, and in particular, to my sister Stella who worked besides me during this trying period.

I thank Ioanna Charalambous-Moisidou for referring me for this Ph.D., and the School of Engineering, The University of Edinburgh for funding my research. I thank my examiners Dr Yuner Huang and Dr Mohammed Hjiaj for their interesting questions during my viva and for their valuable suggestions. I thank Christos and Aris for helping review my writing.

Apostolos Nasikas

CONTENTS

LIST OF TABLES

LIST OF FIGURES

LIST OF SYMBOLS AND ACRONYMS

D	Diameter of the cylinder
D_o	Mean diameter of the cylinder ($D_o = D - t$)
$\mathbf{D}$	Elastic rigidity (fourth order elastic stiffness tensor)
$\mathbf{D}_{ep}$	Instantaneous elastoplastic rigidity tensor (continuum tangent moduli)
$\mathbf{D}_{ep}^{c}$	Consistent (algorithmic) elastoplastic rigidity tensor
$\mathbf{D}_{ep}^{cc}$	Condensed consistent (algorithmic) elastoplastic rigidity tensor for shell elements
E	Young's Modulus
E_S	Secant Modulus
E_T	Tangent Modulus
$\mathbf{e}$	Deviatoric part of total strain tensor $\boldsymbol{\varepsilon}$
$\dot{\mathbf{e}}$	Deviatoric part of total strain rate tensor $\dot{\boldsymbol{\varepsilon}}$
G	Shear Modulus
H	Hardening Modulus $H = dk/d\varepsilon_q = [E_T^{-1} - E^{-1}]^{-1}$
h	$h = k/\varepsilon_q = [E_S^{-1} - E^{-1}]^{-1}$
$\bar{h}$	Non- associative hardening modulus
h_1	$h_1^{-1} = H^{-1} - h^{-1}$
$\mathbf{I}$	Second order identity tensor $I_{ij} = \delta_{ij}$
$\mathbf{I}^{sym}$	Symmetric fourth order identity tensor $I_{ijkl}^{sym} = 1/2\ [\delta_{ik}\delta_{jl} + \delta_{il}\delta_{jk}]$
$\mathbf{I}^{vol}$	Volumetric fourth order identity tensor $I_{ijkl}^{vol} = 1/3\ \delta_{ij}\delta_{kl}$
$\mathbf{I}^{dev}$	Deviatoric fourth order identity tensor $\mathbf{I}^{dev} = \mathbf{I}^{sym} - \mathbf{I}^{vol}$
J2CT	J_2 corner theory
J2DT	J_2 deformation theory
J2FT	J_2 flow theory
J2NA	J_2 non-associative model
K	Bulk modulus
k	Material yield stress in uniaxial tension $k(\varepsilon_q)$
L	Length of tube segment
LBH	Local Buckling Hypothesis
M_0	Full plastic moment of cylindrical shell $M_0 = \sigma_o D_o^2 t$

$\mathbf{m}$	Unit tensor perpendicular to the deviatoric stress **s**, in the direction of the strain rate $\dot{\mathbf{e}}$
$\mathbf{n}$	Unit tensor in the direction of the deviatoric stress **s**
p	Hydrostatic part of the stress tensor $p = -1/3\ \mathbf{I} \cdot \boldsymbol{\sigma}$
p_o	Yield pressure of cylindrical shells $p_o = \sigma_o t/D_0$
p_c	Critical external pressure of cylindrical shells
q	Von Mises equivalent stress
R	Radius (mean) of the cylinder
R_{eq}	Local hoop radius at the intrados of the cylinder under bending
$\dot{q}$	Rate of the Von Mises equivalent stress
$\mathbf{s}$	Deviatoric stress tensor $\mathbf{s} = \mathbf{I}^{dev} \cdot \boldsymbol{\sigma}$
$\dot{\mathbf{s}}$	Rate of the deviatoric stress tensor
t	Cylinder thickness
w^*	(Normalized) Plastic production ratio
Δ	Cylinder ovalization $\Delta = (D_{max} - D_{min})/(D_{max} + D_{min})$
$\Delta\boldsymbol{\varepsilon}$	Total strain increment
$\Delta\boldsymbol{\varepsilon}^e$	Elastic strain increment
$\Delta\mathbf{e}^p$	Plastic strain increment
$\Delta\bar{\boldsymbol{\varepsilon}}$	Know part of total strain increment - no component $\Delta\varepsilon_{33}$ (shell element)
$\Delta\varepsilon_q$	Equivalent (accumulated) plastic strain increment
$\boldsymbol{\varepsilon}$	Total strain
$\boldsymbol{\varepsilon}^e$	Elastic strain
$\mathbf{e}^p$	Plastic strain
$\dot{\boldsymbol{\varepsilon}}$	Rate of total strain
$\dot{\boldsymbol{\varepsilon}}^e$	Rate of elastic strain
$\dot{\mathbf{e}}^p$	Rate of plastic strain
ε_q	Equivalent (accumulated) plastic strain
$\dot{\varepsilon}_q$	Rate of equivalent plastic strain
ζ	Angle by which the deviatoric stress rotates between t_n and t_{n+1} $\cos\zeta = (\mathbf{s}_n \cdot \mathbf{s}_{n+1})/(\lVert\mathbf{s}_n\rVert\ \lVert\mathbf{s}_{n+1}\rVert)$
ζ^*	Angle between the deviatoric stress at t_{n+1} and the elastic predictor $\cos\zeta^* = (\mathbf{s}^e \cdot \mathbf{s}_{n+1})/(\lVert\mathbf{s}^e\rVert\ \lVert\mathbf{s}_{n+1}\rVert)$

ζ^e	Angle between the deviatoric stress at t_n and the elastic predictor $\cos\zeta^e = (\mathbf{s}_n \cdot \mathbf{s}^e)/(\|\mathbf{s}_n\| \, \|\mathbf{s}^e\|), \;\; \zeta^e = \zeta + \zeta^*$
θ_n	Angle formed by strain increment and the deviatoric stress at time t_n $\cos\theta_n = (\mathbf{s}_n \cdot \Delta\mathbf{e})/(\|\mathbf{s}_n\| \, \|\Delta\mathbf{e}\|)$
θ_{n+1}	Angle formed by strain increment and the deviatoric stress at time t_{n+1} $\cos\theta_{n+1} = (\mathbf{s}_{n+1} \cdot \Delta\mathbf{e})/(\|\mathbf{s}_{n+1}\| \, \|\Delta\mathbf{e}\|)$
θ_c	Yield surface vertex semi-angle; material property
θ^e	Angle formed by strain increment and the elastic predictor $\cos\theta^e = (\mathbf{s}^e \cdot \Delta\mathbf{e})/(\|\mathbf{s}^e\| \, \|\Delta\mathbf{e}\|)$
θ_p	Angle formed by plastic strain increment and the deviatoric stress at time t_{n+1} $\cos\theta_p = (\mathbf{s}^e \cdot \Delta\mathbf{e})/(\|\mathbf{s}^e\| \, \|\Delta\mathbf{e}\|)$
κ_1	Curvature normalization parameter $\kappa_1 = t/D_o^2$
λ_c	Wrinkling halfwave of cylinder under compression
λ_{HW}	Wrinkling halfwave of cylinder under bending
$\boldsymbol{\sigma}$	Stress tensor
$\dot{\boldsymbol{\sigma}}$	Rate of the stress tensor
$\boldsymbol{\sigma}^e$	Elastic prediction – Purely elastic trial stress
σ_o	0.2% offset yield stress
ω, ω_R	(Normalized) imperfection amplitude $\omega = a/t$, $\omega_R = a/R$

NOTATION

Standard notation is used throughout the thesis. Bold face symbols denote tensors whose order is indicated by the context, while normal letters refer to scalars. Let $\mathbf{a}$, $\mathbf{b}$ be vectors, $\mathbf{A}$, $\mathbf{B}$ be second order tensors and $\mathbf{C}$ a fourth order tensor, with their respective cartesian components a_i, b_i, A_{ij}, B_{ij}, C_{ijkl}.

The inner product operator has the following meaning depending on the types of variables it is applied on:

$$\mathbf{a} \cdot \mathbf{b} = a_i b_i$$

$$\mathbf{A} \cdot \mathbf{B} = A_{ij} B_{ij}$$

The norm operator is defined as

$$\|\mathbf{A}\| = \sqrt{\mathbf{A} \cdot \mathbf{A}} = \sqrt{A_{ij} A_{ij}}$$

and

$$\mathbf{b} = \mathbf{A}\mathbf{a} \rightarrow b_i = A_{ij} a_j$$

$$\mathbf{B} = \mathbf{C}\mathbf{A} \rightarrow B_{ij} = C_{ijkl} A_{kl}$$

The dyad product operator has the following meaning depending on the types of variables it is applied on:

$$\mathbf{A} = \mathbf{a} \otimes \mathbf{b} \rightarrow A_{ij} = a_i b_j$$

$$\mathbf{X} = \mathbf{A} \otimes \mathbf{b} \rightarrow X_{ijk} = A_{ij} b_k$$

$$\mathbf{Y} = \mathbf{A} \otimes \mathbf{B} \rightarrow Y_{ijkl} = A_{ij} B_{kl}$$

Additionally, it is useful to note that any symmetric second order tensor can be split into two components: a volumetric (or spherical) and a deviatoric, as follows

$$\mathbf{A} = \mathbf{I}^{sym}\mathbf{A} = [\mathbf{I}^{vol} + \mathbf{I}^{dev}]\mathbf{A} = \mathbf{A}^{vol} + \mathbf{A}^{dev}$$

Two important identities for operations with symmetric second order tensors $\mathbf{A}$, $\mathbf{B}$ are:

$$\mathbf{A}^{vol} \cdot \mathbf{B}^{dev} = 0$$

$$\mathbf{A} \cdot \mathbf{B}^{dev} = \mathbf{A}^{dev} \cdot \mathbf{B}^{dev} = \|\mathbf{A}^{dev}\| \|\mathbf{B}^{dev}\| \cos\theta$$

where θ represents an angle, formed between the two tensors in the deviatoric hyperspace.

1 INTRODUCTION

Elastic-plastic instability of structures is a broad field of study with a range of applications in civil, mechanical engineering and marine structures. In particular, the structural performance of cylindrical metal shells under compressive loads is a classic problem of mechanics, with numerous applications that include tubular structures, nuclear power plant piping components, offshore and onshore pipelines transporting oil, natural gas, hydrocarbons, water.

Operation and shut-down-for-maintenance conditions of pipelines can lead to considerable axial loads, due to temperature changes, combined with high pressure loads (Limam et al., 2010). The deep-water installation process of offshore pipelines induces high bending loads, into the plastic range of the material, combined with tension and external pressure (Kyriakides & Corona, 2007). Severe loading events, earthquakes, ground movements, landslides, subsidence, faulting, can further cause significant bending and axial loading in tubular sections (Kaya et al., 2017).

The resulting high compressive stresses and strains in the shell wall may lead to cross-sectional distortion, local buckling and failure. For a safe and economic design, it is desirable to estimate reasonably closely the circumstances that lead tubulars to buckle, when subjected to compressive loads. So, continuous research attention is directed towards the cross section capacity of thick-walled shells, e.g. (Fatemi & Kenny, 2017; Takla, 2018; Tabeshpour et al., 2019; Meng et al., 2020)

The behaviour of thick-walled tubulars is governed by the interaction of nonlinearities in the metal material properties and inherent geometric nonlinearities (e.g., cross section

ovalization in bending) which are further exacerbated by the occurrence local buckling. Beam theory approaches that are sufficient for designing most steel members, cannot capture the structural behaviour of tubular members when bifurcation-type instabilities (local buckling) occur, which involve sudden changes in geometry (cross section shape) leading to loss of structural strength. Additionally, for thick-walled cylinders, the bifurcation from the primary equilibrium path (buckling) takes place into the inelastic range of the material, which complicates estimations, as predictions are reportedly sensitive to the elastoplastic constitutive model that is employed.

1.1 State of the art

Inelastic constitutive models based on associative plasticity can accurately simulate metal material behaviour and are suitable for general-purpose analyses of metal components and structures. However, in problems of plastic buckling and strain localization, which occur well into the inelastic range of the material, the use of the J_2 flow theory (J2FT) often results in bifurcation load predictions significantly higher than those observed experimentally. On the other hand, approaches that use the J_2 deformation theory (J2DT) provide estimates more consistent with the experimental data e.g. (Batdorf, 1949; Gerard & Becker, 1957).

In structural instability problems, it is quite difficult to identify accurately the onset of bifurcation, mainly because of its tangential (non-abrupt) character (Kyriakides & Corona, 2007). Furthermore, end support effects and, most importantly, the presence of inevitable small geometric and other imperfections do not allow for clear interpretation of experimental buckling results. In this perspective, the introduction of imperfections in modelling using J2FT may suffice to predict maximum buckling loads observed in buckling experiments e.g. (Shamass et al., 2014). Nonetheless, to obtain good predictions in terms of bucking load and, more markedly, in terms of the corresponding deformation, the necessary imperfection amplitudes can become unrealistically high, particularly in thick-walled shells or materials with considerable hardening (Hutchinson & Budiansky, 1976; Ore & Durban, 1992)

The documented superiority of J2DT in estimating the bifurcation point (Tuğcu, 1991; Blachut et al., 1996; Wang, et al., 2001) can be explained by the material stiffness moduli that J2DT employs, which are less stiff compared to the J2FT. As a result, plastic strain increments may develop in directions tangent to the Von Mises yield surface, not exclusively perpendicular to it. This more compliant material behaviour can be attributed

to the development of corners in the yield surface of real materials (Batdorf & Budiansky, 1949) when abrupt changes in stress direction occur, which was investigated in the 60s (Hecker, 1972) and was observed experimentally more recently (Kuroda & Tvergaard, 1999; Kuwabara et al., 2000).

Budiansky (1959) argued for the applicability of J2DT for a range of problems with load paths which do not involve unloading, as the J2DT does not have such a condition. It has been used to trace the prebuckling and instability of cylinders under compression and bending e.g. (Gellin, 1979; Gellin, 1980; Kyriakides & Shaw, 1982). However, in the post-buckling, parts of the shell may unload, so the use of J2DT may not be an appropriate material model e.g.(Guarracino & Simonelli, 2018). A hybrid approach has been suggested to overcome this issue: using the J2FT for tracing the primary equilibrium path of the structures, and the J2DT material moduli for estimating bifurcation. This method has been suggested in early works (Batdorf, 1949; Bushnell, 1974, 1982) and used successfully in problems of structural instability of tubes under compressive loads (Ju & Kyriakides, 1991, 1992; Bardi et al., 2006; Corona et al., 2006; Peek & Hilberink, 2013). Still, it requires the use of two distinct constitutive laws for the same material within the analysis, while it might not allow for tracing consistently the post-buckling behaviour, as it might not lead to an instantaneous jump to the non-trivial post-buckling branch.

Alternatively, the adoption of more elaborate constitutive models has been suggested for predicting accurately the buckling of thick-walled metal shells loaded into the plastic range. Advanced constitutive models have been proposed by (Christoffersen & Hutchinson, 1979; Gotoh, 1985; Goya & Ito, 1991) incorporating a yield surface with a vertex; a detailed overview is given in Schurig (2006). These models can account for less stiff behaviour for non-proportional loading [1] and higher plastic deformations, when compared to J2FT. In particular, the J_2 corner theory, developed by Christoffersen & Hutchinson (1979), employs the rate form of the J2DT for a range of strain rate directions, elastic unloading within a conical yield surface, and partial loading in between. It has been employed successfully in problems of shear band formation (Christoffersen & Hutchinson, 1979; Needleman & Tvergaard, 1984) and in structural instability investigations of compressed cylinders and cylindrical panels (Tvergaard, 1983a, 1983b; Giezen, 1988; Tvergaard & Needleman, 2000). However, the calibration and

[1] Proportional are loading paths during which the stress components increase in constant ratio to each other, e.g. uniaxial loading

implementation of such models in an implicit finite element environment may become quite cumbersome, making their use unattractive for structural computations.

To circumvent the complexity and the computational cost of corner theories, simpler plasticity models were suggested which employ flow rules that mimic the increased plastic flow caused by yield surface corners, while maintaining the smooth shape of a Von Mises yield surface. Hughes & Shakib (1986) developed an associative flow rule with increased plastic flow, based on a hardening modulus dependent on the direction of the strain increment. Yet, it demands significant hardening and no application in structural stability problems has been identified by the author. Simo (1987) presented a non-associative flow rule which mimics the effect of a yield surface corner, applicable independently of the level of hardening. However, the corresponding instantaneous and linearized stiffness moduli were not presented, neither was the model implementation for nonlinear hardening materials. This model was used by Rønning et al. (2010) for modelling the torsional buckling of cruciform columns, and it was the basis for the non-associative models by (Kuroda & Tvergaard, 2001; Kuroda, 2004, 2015; Yoshida, 2017).

To inherit the effectiveness of J2DT in buckling predictions, some models were developed that employ its rate form, along with a smooth Von Mises yield surface. However, in this approach, accounting for elastic unloading creates a discontinuity in the production of plastic flow in directions tangent to the yield surface. To eliminate this discrepancy, Peek (2000) relaxed the demand for elastic unloading, allowing for some plastic deformation to take place for stress paths directed inward the yield surface. Pappa & Karamanos (2016) employed a different tactic: they maintained elastic unloading but modified the J2DT flow for a range of strain directions close to the yield-surface tangent, so that plastic production is smoothly zeroed for tangent directions. Yet, the ensuing strain-direction dependency was not fully incorporated in the presented formulation. These models were used to investigate the buckling response of metal tubes under compression.

1.1.1 Research needs

The above constitutive models were incrementally developed to approach problems of inelastic instability in an effective and progressively simpler manner. Each exhibits advantages and drawbacks mainly related to the implementation and application aspect of the model. Their adoption within modern implicit finite element algorithms is not trivial and has not been discussed thoroughly, while their particular, non-standard

properties demand special consideration. Additionally, rather limited reported application in practical investigations has been identified for several of these models, so their effectiveness in inelastic instability calculations and convergence performance in simulations may demand further examination. These observations are a starting point to the present research directed to studying structural instability of metal shells in the inelastic range, by accounting for 'corner effects' in the constitutive law.

1.2 Aims and objectives

This research aims to develop and implement efficient numerical (finite element) tools to reliably simulate the structural behaviour of thick-walled metal shells loaded in the inelastic range. Accounting for non-standard material behaviours, the present investigation aspires to further the understanding on instabilities and other factors that influence the structural performance of inelastic shells under compressive loads.

Considering the disparity between buckling estimates employing the J2FT and experimental data, an examination is undertaken of alternative, advanced constitutive laws that may offer the capability to both (a) trace accurately the equilibrium path of inelastic metal shells and (b) to estimate instability in a consistent manner, using established computational tools. The variety and complexities of these material models motivates the development of a framework for systematically studying and implementing non-associative, 'pseudo-corner' models in implicit algorithms. Focusing on simplicity and direct applicability in FE simulations, a new special-purpose constitutive law is synthesised. It is introduced as an efficient extension of modern structural analysis software, to investigate the structural response of inelastic metal shells, accurately tracing their equilibrium paths and consistently assessing stability.

Motivated by offshore and pipeline engineering, several aspects of the instability of thick-walled cylindrical metal shells are examined, under a range of demanding loading conditions of practical interest. Verification of the performance and the extend of applicability of the constitutive model within large scale finite element calculations is pursued and validation of its capacity to accurately simulate structural performance of shells, well into the post buckling.

Key objectives of the research are:

- Investigating the methods used in modelling the behaviour of thick-walled shells under compressive loads.

- Reviewing the literature to pinpoint the role of material constitutive laws in modelling the instability in the inelastic range.
- Selecting an appropriate constitutive model to reliably simulate the structural behaviour and instabilities of inelastic shells under compressive loads and implementing it within available computational finite element tools in an efficient manner
- Collecting appropriate experimental data from the literature and performing numerical simulations to validate and calibrate the model
- Verifying the extend of applicability of the constitutive model, considering various load scenarios that lead to inelastic buckling and validating its capability to accurately simulate structural performance of shells well into the post-buckling range
- Testing the model performance in big scale finite element analyses, to thoroughly investigate its convergence in demanding structural calculations characterized by structural instabilities and load path changes
- Assessing the influence of constitutive modelling in shell instability (primary equilibrium, bifurcation post-buckling paths) and the imperfection sensitivity in the inelastic range, in comparison with J2FT
- Elucidating aspects of inelastic instability of shells, the sequence of events from buckling to failure of sections, accounting for geometry, material and various loadings

1.3 Methodology

Advanced material models-candidates for inelastic buckling calculations are identified and used as a starting point for developing a new simplified constitutive model that can be efficiently implemented in available computational tools. This model maintains the basic features of the J2FT plasticity and introduces key enhancements to effectively account for non-standard material behaviours. A smooth Von Mises yield surface is adopted, along with a two-branch non-associative flow rule, that employs material stiffness lower than J2FT, mimicking the influence of a vertex forming in the yield surface. Followingly, this model is referred to as J_2 Non-Associative (J2NA).

Based on considerations of previous ‘corner’ and ‘pseudo-corner’ models, the first branch of J2NA is activated for moderate deviations from proportional loading, and it employs the rate form of the J2DT, to inherit its effectiveness in structural instability predictions

in the plastic range. The second branch is activated for larger deviations from proportional loading, and it is used for strain increment directions approaching the yield-surface-tangent. It is an extension of the approach by Simo (1987), mimicking the effect of a yield surface corner of semi-angle denoted as θ_c, and it is adopted for its robustness and natural geometric interpretation. Fully elastic unloading is employed for strain-increment directions tangent and inward to the yield surface, as suggested in the model by Pappa & Karamanos (2016). The model's behaviour can vary between the stiffer J2FT and the more compliant J2DT, based on the model's material parameter (θ_c) and the direction of the strain rate.

Nonlinear isotropic hardening is considered to address monotonic loading problems in inelastic cylindrical shells. A small-strain formulation is presented, and a detailed backward-Euler numerical integration scheme is developed for three-dimensional elements. An enhanced version is presented for shell elements analyses, accounting for zero stress across the shell thickness. Care is taken to rigorously account for the strain-increment-direction dependence in the numerical integration and consistent linearization of J2NA, an issue commonly overlooked in previous approaches. The developed integration scheme is general enough to allow for implementing behaviours from various other models in the literature, and it may be used as a work frame for implementing non-associative and 'pseudo-corner' constitutive laws within implicit algorithms. The model is tested extensively in large-scale cylinder instability analyses and several non-trivial loading scenarios, involving non-proportional loading, to examine its effectiveness and range of application.

Motivated by the offshore pipeline installation processes and the structural behaviour of offshore tubular members, the present research investigates the local buckling and post-buckling resistance of long thick-walled cylindrical metal shells under various compressive loads and the ensuing types of instabilities.

Numerical simulations are conducted using the commercial general-purpose finite element code Abaqus. Carefully constructed three dimensional (3D) models are used to study the structural behaviour of cylinders subjected to uniform compression, bending and the pressure loads, which represent a range of important load cases. Shell finite elements are employed in analyses considering non-linear geometry, inelastic material properties and initial geometric imperfections. The developed non-associative plasticity model is coded in Fortran and implemented as a material user subroutine (UMAT) in Abaqus/Standard.

J2NA is employed in numerical analyses to investigate the structural behaviour of elastic-plastic cylinders under compressive loads. Using a single constitutive model, it is possible to trace the prebuckling and the post-buckling equilibrium path of the cylinders and consistently estimate instability, utilizing the capabilities of the finite element software. A generalized version of Hill's 'comparison solid' concept is used to identify the onset of instability, and a semi-analytical method is considered for simplified buckling calculations. The influence of the model's features and of initial geometric imperfections on the simulated behaviour of thick-walled tubes is demonstrated, and comparisons are made with respect to J2FT. Imperfection is introduced in the form of the shell's buckling modes. Structural behaviours and bifurcation estimates obtained employing J2NA compared well with predictions and with experimental works from the literature.

1.4 Practical applications

The present research focuses on the structural performance and instabilities of thick-walled cylinders under compressive loads, which experience local instability and ultimately fail while loaded into the inelastic range of the material. These shells have important applications in onshore and offshore structures where high compressive loads need to be carried, but also in piping components and pipelines that are subjected to severe compressive loads during installation, operation, maintenance and in severe loading events. Accurately estimating their instability, post-buckling capacity and performance allow for optimal use of the structural properties of the thick-walled sections, where bifurcation does not immediately imply failure, leading to a more economic design. This can be of importance particularly in applications of pipelines, where their large scale implies that material economy can have a significant impact. Other, structural applications include e.g. offshore platforms (indeterminate systems) where ultimate limit state design can be more economic by accounting for the post-buckling capacity of isolated structural members, as local instability might not be detrimental for the global stability of the structure. Simulating reasonably closely the buckling and post-buckling behaviour of inelastic shells can allow for more efficient use of the material strength and the structural capabilities of the members, which can be of particular interest for members of high strength steel.

Despite focusing this investigation on stability calculations of cylindrical shells with application in offshore and pipeline engineering, this research addresses the critical subject of inelastic buckling of shells. Thus, the developed tools and methodologies may

be extended and applied to investigate the structural behaviour and buckling of inelastic shells of various cross sections and different geometries and further compressive loadings, with applications including e.g., compressed plates and spherical shells subjected to external pressure in vessel components. Besides inelastic shell buckling, metal forming process simulations comprise a domain where the non-associative models are being investigated, offering an extensive range of industrial applications, but also problems of strain localization, metal sheet necking. From a research perspective, this work treats ‘pseudo-corner’ and non-associative models in a unified manner and outlines their implementation process in finite element codes, so, it can be used as a guide to develop several flow rules that exhibit similar effects, which may be used to investigate various aspects of the aforementioned problems.

1.5 Outline of the thesis

This thesis is divided in 10 chapters, including the present introduction. A short description of the following chapters is given below.

Chapter 2: A brief introduction in plasticity theory is offered, with special reference to non-standard constitutive laws - candidates for modelling instability in the inelastic range. Motivated by complexities and limitations of these models, a special purpose J_2 non-associative (J2NA) constitutive law is developed for structural stability calculations of thick-walled shells. The model’s formulation is meticulously described and its relation to previous ‘corner’ and ‘pseudo-corner’ constitutive models is explained.

Chapter 3: A numerical integration scheme is presented in detail, towards the implementation of the model in implicit finite element tools. An enhanced version is developed to account for plane stress conditions, applicable in shell elements analyses. Special attention is paid in addressing thoroughly the intricacies of the model, which stem from the reduced material stiffness when changes in the strain path occur. The material behaviour under non-proportional strain paths is demonstrated. The numerical accuracy of the developed integration scheme is discussed.

Chapter 4: The buckling of thick-walled metal cylindrical shells under uniform compression is considered as a classic problem of instability in the inelastic range. It showcases the effectiveness of shell element models employing J2NA in addressing structural instability problems. Finite element analyses are performed, producing behaviours in agreement with the experimental work by Bardi et al. (2006). Aspects of buckling and the relevant modes are considered, with focus in uniform wrinkling and its

localization leading to loss of structural rigidity. The role of geometric imperfection in the structural response of the shells is examined.

Chapter 5: Investigation is extended to problems of pure bending, which entail non-trivial prebuckling equilibrium paths. The structural response of various thick-walled metal cylinders is investigated with respect to their diameter-to-thickness ratios (D/t). The limit states due to ovalization and bifurcation instabilities are examined, along with their interactions and prevalence of either, depending on the shell's geometry, imperfection and boundary conditions. Structural behaviours from numerical simulation are in line with experiments and remarks by Kyriakides & Ju (1992), illustrating the range of application of J2NA.

Chapters 6-7: The capabilities of the model are further evaluated in problems of bending under pressure loads, which are characterized by inherently non-proportional loading conditions. The key features of buckling in pressurized cylinders are addressed using the J2NA in finite element analyses. Simulations accurately describe the experimental behaviours reported by Limam et al. (2010) and Ju & Kyriakides (1991). A simplified buckling estimation method is developed for pressurized cylinders under bending, by considering similarities with buckling behaviours of cylinders under compression.

Chapter 8: A general closure is offered, and the main conclusions of the present research are summarized. Key findings are highlighted, and future directions of the research are indicated.

Chapters 9-10: References are provided, and three appendices are enclosed. Appendices 1, 2 provide additional information and details on the implementation of J2NA and relevant constitutive laws from the literature. In Appendix 3, the formulas for cylinder buckling under axial load and pressure are derived analytically and discussed.

2 CONSTITUTIVE MODELLING

In this chapter, a brief introduction is made to the fundamentals of metal plasticity. An overview is given of plasticity models suggested for addressing problems of instability in the inelastic range, before immersing into the formulation of the non-associative model, developed here, for efficiently simulating the buckling of inelastic shells.

2.1 Uniaxial material behaviour

The primary features of the idealized elastic-plastic behaviour of metals, used in structural analyses, are summarized in the uniaxial stress-strain-curve in Figure 2.1. For small deformations, material behaves elastically, so stress σ and strain ε values are proportional, related through the elasticity (or Young's) modulus $\sigma = E\varepsilon$. Upon removal of the load, the strain is fully recoverable. Material behaves elastically up until the elastic limit is reached (point A) when its yield strength σ_y is exceeded.

Additional deformations have a plastic part which is permanent. Strain beyond the yield point may lead to an increase in the material strength σ (strain or work hardening), as in the cases of high strength steel, stainless steel, aluminium etc., or a plateau may appear, with no increase of strength for a range of deformations before hardening onsets, as in mild streel. The slope E_t of the stress-strain curve after yielding, also called tangent material modulus, is usually significantly lower than the elasticity modulus ($E_t \ll E$).

Upon removal of the axial load (path BC), only the elastic part ε^e of the deformation is recovered. The residual plastic part of the deformation ε^p is permanent and the material does not return to its initial state. Unloading follows path BC, having a slope equal to the elasticity modulus E.

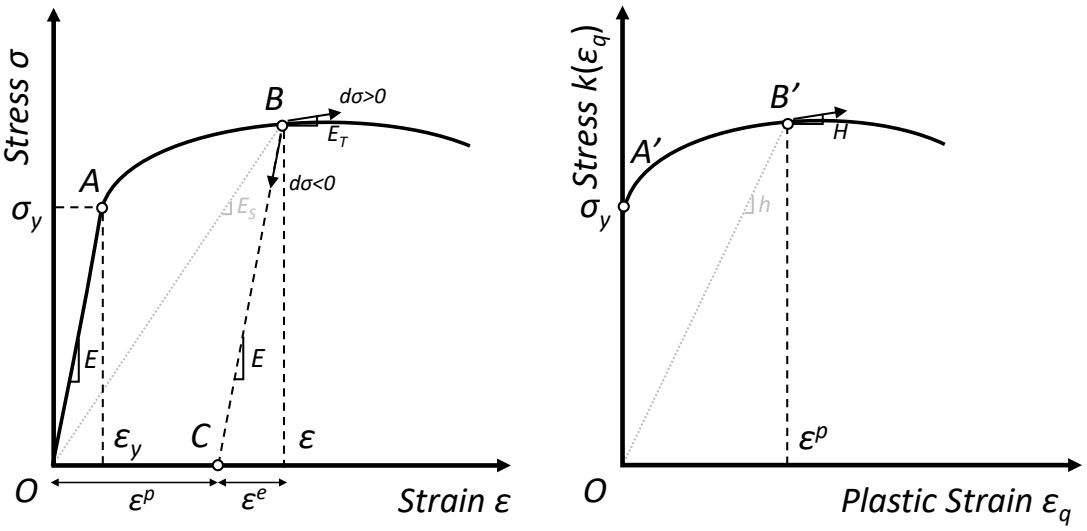

Figure 2.1: Elastic-plastic behaviour under uniaxial loading

2.2 Fundamentals of metal plasticity

Plasticity models replicate this material behaviour under uniaxial loading and appropriately generalize it to multiaxial stress and strain conditions. The following fundamental attributes are shared by plasticity models:

i. the total strain is decomposed into elastic and plastic parts

ii. a yield criterion is adopted in the form of a yield surface in the stress space, that defines the conditions under which inelastic material behaviour initiates

iii. a hardening law defines the evolution of the yield surface with plastic deformation

iv. a flow rule determines the plastic deformation induced by applied stress or strain increments.

These key elements of plasticity are briefly introduced below. For a detailed treatment of plasticity, the reader is referred to the book by de Souza Neto et al. (2008).

2.2.1 Additive decomposition of strain

Under uniaxial loading (Figure 2.1), when the elastic limit is exceeded, the total strain is split into elastic and plastic parts as

$$\varepsilon = \varepsilon^e + \varepsilon^p \tag{2.1}$$

And the stress is calculated as:

$$\sigma = E\varepsilon^e = E(\varepsilon - \varepsilon^p) \tag{2.2}$$

In the framework of incremental small-strain metal plasticity, this principle is extended in multiaxial stress rates and strain rates. The rate of total strain tensor $\dot{\boldsymbol{\varepsilon}}$ is split into elastic ($\dot{\boldsymbol{\varepsilon}}^e$) and plastic ($\dot{\mathbf{e}}^p$) parts as:

$$\dot{\boldsymbol{\varepsilon}} = \dot{\boldsymbol{\varepsilon}}^e + \dot{\mathbf{e}}^p \tag{2.3}$$

and the linear isotropic Hook's law relates the stress rate $\dot{\boldsymbol{\sigma}}$ to the elastic strain rate $\dot{\boldsymbol{\varepsilon}}^e$ as:

$$\dot{\boldsymbol{\sigma}} = \mathbf{D}\dot{\boldsymbol{\varepsilon}}^e = \mathbf{D}(\dot{\boldsymbol{\varepsilon}} - \dot{\mathbf{e}}^p) = \mathbf{D}\dot{\boldsymbol{\varepsilon}} - \mathbf{D}\dot{\mathbf{e}}^p \tag{2.4}$$

The fourth-order elastic stiffness tensor $\mathbf{D}$ is:

$$\mathbf{D} = 3K\,\mathbf{I}^{vol} + 2G\,\mathbf{I}^{dev} \tag{2.5}$$

where G is the shear modulus of the material, K is the bulk modulus and $\mathbf{I}^{vol}$, $\mathbf{I}^{dev}$ are the volumetric and deviatoric fourth-order unit tensors, whose Cartesian components are expressed using the Kronecker delta δ_{ij} as:

$$I^{dev}_{ijkl} = \frac{1}{2}\left(\delta_{ik}\delta_{jl} + \delta_{il}\delta_{jk}\right) - \frac{1}{3}\delta_{ij}\delta_{kl} \tag{2.6}$$

$$I^{vol}_{ijkl} = \frac{1}{3}\delta_{ij}\delta_{kl} \tag{2.7}$$

2.2.2 Yield criterion

The yield criterion is used to identify whether the material behaviour is elastic or inelastic under the current stress state, for any subsequent stress or strain increment. In the uniaxial case, yielding initiates simply when a yield stress is reached ($\sigma - \sigma_y = 0$). In the three-dimensional case, this principle is expressed through the yield function, which, in classical metal plasticity, takes the form:

$$F = F(\boldsymbol{\sigma}, l_k) = 0 \tag{2.8}$$

F is a scalar function of the stress tenson $\boldsymbol{\sigma}$ and a number of material and load history (tensor and scalar) parameters l_k. Eq. (2.8) defines the yield surface, which is a convex hypersurface in the stress space, enclosing all stress states for which the material behaves elastically. During plastic deformation, changes in the geometry of the yield surface may occur that are determined by the evolution of the internal parameters l_k and the hardening

rule.

A fundamental assumption in plasticity is that function F is non-positive ($F \leq 0$): (a) F is negative when the stress state is enclosed by the yield surface, in which case any infinitesimal deformation is elastic, while (b) F is zero when the stress state is on the yield surface and plastic flow is imminent. Assuming the yield surface is smooth, the gradient (outward normal) $\partial F/\partial \sigma_{ij}$ at any point of the yield surface is defined. Considering a stress rate $\dot{\sigma}_{ij}$, all possible loading conditions are summarized as:

- $F = 0$ & $\partial F/\partial \sigma_{ij}\, \dot{\sigma}_{ij} > 0$ → plastic loading
- $F = 0$ & $\partial F/\partial \sigma_{ij}\, \dot{\sigma}_{ij} < 0$ → elastic unloading
- $F = 0$ & $\partial F/\partial \sigma_{ij}\, \dot{\sigma}_{ij} = 0$ → neutral loading (tangent to the yield surface - no plastic deformation)
- $F < 0$ → the material behaves elastically for any stress rate $\dot{\sigma}_{ij}$
- $F > 0$ → is an invalid state. When the material deforms plastically, internal variables l_k update so that $F = 0$ at the new stress state.

2.2.3 Hardening

Strain hardening, or work hardening, is the strengthening of a metal as a result of plastic deformation, instigated by the changes in the material microstructure. The hardening law or hardening rule describes the evolution of material strength under plastic deformation, which is represented through changes in the geometry or translations of the yield surface, expressed by the internal parameters l_k.

Isotropic hardening is the simplest hardening rule. It postulates that plastic deformation leads to expansion of the yield surface uniformly in all directions, when yielding initiates (Figure 2.2). The shape of the yield surface is preserved, without any distortion or translation and its size is directly related to the amount of accumulated plastic strain. For specialized plasticity problems, more elaborate constitutive models may be used, further involving translations and/or distortions of the yield surface with plastic deformation.

2.2.4 Plastic flow rule

The plastic flow rule determines the increment of plastic strain that is caused by an increment of stress during elastoplastic loading. The plastic strain rate $\dot{\mathbf{e}}^p$ is classically obtained by the differentiation of a smooth convex plastic potential Ω:

$$\dot{\mathbf{e}}^p = \dot{\lambda}\frac{\partial \Omega}{\partial \boldsymbol{\sigma}} \tag{2.9}$$

Hence, plastic strain rate is coaxial with the gradient of plastic potential $\partial\Omega/\partial\boldsymbol{\sigma}$, (perpendicular to the hypersurface $\Omega = 0$). Parameter $\dot{\lambda}$ is a non-negative scalar called plastic multiplier, and its value is determined from the consistency condition ($\dot{F} = 0$), accounting for any changes in the yield surface due to the hardening law. Consistency demands that upon yielding the stress point must remain on the yield surface, if no unloading occurs. Plastic strain is accumulated as

$$\mathbf{e}^p = \int \dot{\mathbf{e}}^p \, dt \tag{2.10}$$

Followingly, a few important plasticity models are briefly introduced. Their particular features and properties outline the process towards the development of the J_2 non-associative model for inelastic buckling calculations.

2.3 J_2 flow theory

For a wide range of applications, the J_2 flow theory (J2FT) can accurately model the metal material behaviour and has been used extensively in the literature and in commercial software. For most metals, the pressure does not affect yielding, so the Von Mises yield criterion and an isotropic hardening law suffice to analyse problems of monotonic loading, considered here. The yield function is expressed as:

$$F(\boldsymbol{\sigma}, \varepsilon_q) = \sqrt{3J_2} - k(\varepsilon_q) = \sqrt{3/2}\,\|\mathbf{s}\| - k(\varepsilon_q) = 0 \tag{2.11}$$

where $\mathbf{s} = \mathbf{I}^{dev}\boldsymbol{\sigma}$ is the deviatoric part of the stress tensor and $\|\mathbf{s}\| = \sqrt{\mathbf{s}\cdot\mathbf{s}}$ is the norm of $\mathbf{s}$. Function k expresses the yield strength of the material as a function of the equivalent (accumulated) plastic strain ε_q: a monotonic increasing parameter relating the multi-axial plastic strain history to the behaviour of the material under a uniaxial stress, which is defined as

$$\varepsilon_q = \int \dot{\varepsilon}_q \, dt = \int \sqrt{2/3}\,\sqrt{\dot{\mathbf{e}}^p \cdot \dot{\mathbf{e}}^p}\, dt \tag{2.12}$$

It is noted that under uniaxial load σ, the equivalent Von Mises stress is $q = \sqrt{3/2}\,\|\mathbf{s}\| = \sigma$ and the equivalent plastic strain is equal to the plastic deformation of the material $\varepsilon_q = \varepsilon^p$ (see Figure 2.1).

The Von Mises yield surface is presented for plane stress conditions in Figure 2.2a, when

it takes the form of an ellipse, together with its relation to the material stress-strain curve under uniaxial loading. In the deviatoric stress space and in the principal three-dimensional stress space (π-plane), the Von Mises takes the form of a circle with radius $k(\varepsilon_q)$, which is further shown in Figure 2.2b.

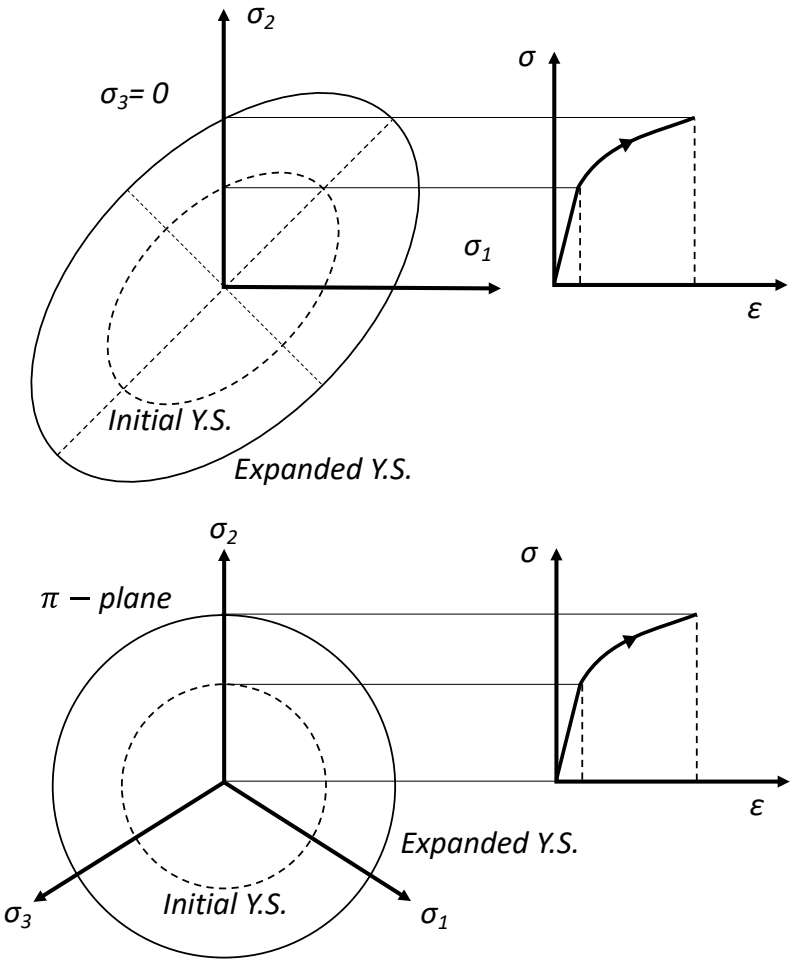

Figure 2.2: Schematic representation of the yield surface evolution considering isotropic hardening and relation to the stress-strain curve of the material.

This flow rule is called associated or associative, because the plastic potential function Ω is chosen to coincide with the yield function F. As $\Omega = F$, the flow relates to the stress tenson only through the invariant $J_2 = \mathbf{s} \cdot \mathbf{s}/2$, after which the model is named. The plastic strain rate is expressed as:

$$\dot{\boldsymbol{\varepsilon}}^p = \dot{\lambda} \frac{\partial F}{\partial \boldsymbol{\sigma}} = \sqrt{3/2}\, \dot{\lambda} \mathbf{n} \tag{2.13}$$

where $\mathbf{n} = \mathbf{s}/\|\mathbf{s}\|$ is the unit tensor in the direction of the deviatoric stress, which is perpendicular to the Von Mises yield surface. This implies that the plastic strain rate tensor is deviatoric ($\dot{\boldsymbol{\varepsilon}}^p = \mathbf{I}^{dev} \dot{\boldsymbol{\varepsilon}}^p$), meaning it has no volumetric component (it is accompanied by no change in material volume). This is consistent with plastic flow being

incompressible for most metallic materials, as it is primarily caused by plastic slip. Eq. (2.13) further implies that $\dot{\lambda} = \sqrt{2/3}\sqrt{\dot{\mathbf{e}}^p \cdot \dot{\mathbf{e}}^p} = \dot{\varepsilon}_q$, and, finally, the consistency equation ($\dot{F} = 0$) allows for expressing $\dot{\lambda}$ as:

$$\dot{\lambda} = \dot{\varepsilon}_q = \frac{1}{1 + H/3G}(\mathbf{n} \cdot \dot{\mathbf{e}}) \tag{2.14}$$

where $H = dk/d\varepsilon_q = (E_T^{-1} - E^{-1})^{-1}$ is the material hardening modulus, directly related to the material tangent and elasticity moduli (Figure 2.1). The plastic strain rate $\dot{\mathbf{e}}^p$ produced by a total strain rate $\dot{\boldsymbol{\varepsilon}}$ is:

$$\dot{\mathbf{e}}^p = \frac{1}{1 + H/3G}\,(\mathbf{n} \otimes \mathbf{n})\dot{\mathbf{e}} \tag{2.15}$$

and the material elastoplastic rigidity tensor ($\mathbf{D}_{ep} = \partial\boldsymbol{\sigma}/\partial\boldsymbol{\varepsilon}$) expressing the changes in stress induced by a strain rate and the flexibility or compliance tensor $\mathbf{C}_{ep} = \mathbf{D}_{ep}^{-1}$, take the from:

$$\mathbf{D}_{ep} = 3K\mathbf{I}^{vol} + 2G[\mathbf{I}^{dev} - \mathbf{n} \otimes \mathbf{n}] + \frac{2G}{1 + 3G/H}(\mathbf{n} \otimes \mathbf{n}) \tag{2.16}$$

$$\mathbf{C}_{ep} = \frac{1}{3K}\mathbf{I}^{vol} + \frac{1}{2G}[\mathbf{I}^{dev} - \mathbf{n} \otimes \mathbf{n}] + \frac{1 + 3G/H}{2G}(\mathbf{n} \otimes \mathbf{n}) \tag{2.17}$$

Despite accurately modelling material behaviour, the J2FT was found to estimate buckling loads that are considerably higher than ones obtained experimentally in problems of buckling of inelastic shells. Oppositely, the simpler J2DT produced buckling estimates in better agreement with experimental values (Batdorf, 1949).

2.4 J_2 Deformation Theory

The J_2 deformation theory (J2DT), or total strain theory (Chakrabarty, 2006), was proposed by (Hencky, 1924) and postulates the existence of a one-to-one a relationship between total strain and total stress. The resulting simplification in calculations was important in the 70s-80s and allowed for numerically investigating plasticity problems including instability e.g. (Gellin, 1979, 1980; Kyriakides & Shaw, 1982), which showed favourable comparisons with experimental results in buckling, but had the side effect of neglecting any load history influence in the post-buckling.

The J2DT adopts the additive decomposition of strain, and Hook's law relates stress and elastic strain. The model postulates that the deviatoric stress $\mathbf{s}$ at any stage of the deformation fully and uniquely defines the direction and size of the total plastic strain $\mathbf{e}^p$,

which is expressed by.

$$\mathbf{e}^p = \lambda\, \mathbf{s} \tag{2.18}$$

The plastic strain $\mathbf{e}^p$ is assumed to be codirectional with the deviatoric stress $\mathbf{s}$ and its size $\|\mathbf{e}^p\|$ is determined by the proportionality scalar λ, which accounts for the plastic properties of the material, obtained from a uniaxial stress-strain curve. Parameter λ is a function of the equivalent Von Mises stress q and the equivalent plastic strain ε_q, which are defined as:

$$q = \sqrt{3J_2} = \sqrt{3/2}\,\|\mathbf{s}\| \tag{2.19}$$

$$\varepsilon_q = \sqrt{2/3}\,\sqrt{\mathbf{e}^p \cdot \mathbf{e}^p} = \sqrt{2/3}\;\|\mathbf{e}^p\| \tag{2.20}$$

This definition of ε_q is similar to the one in J2FT -eq.(2.12)-, except it relates to the total plastic strain tensor $\mathbf{e}^p$, not the history of plastic strain increments $\dot{\mathbf{e}}^p$. Under uniaxial loading, the two definitions are equivalent, and the behaviour of J2DT is identical to that of J2FT.

The Von Mises yield function (2.11) is used to calculate the equivalent plastic strain for a stress state based on the uniaxial material stress-strain curve. The proportionality scalar λ is used to calculate the plastic strain tensor, expressed as:

$$\lambda = \frac{3}{2}\frac{\varepsilon_q}{q} = \frac{3}{2}\frac{1}{h} \tag{2.21}$$

where $h = (E_S^{-1} - E^{-1})^{-1}$ is the secant modulus of material curve $k(\varepsilon_q)$ (Figure 2.1).

As the plastic strain is fully defined by the final stress state, it is independent on the loading history of the material, and J2DT may be unsuitable for describing the plastic behaviour of metals experiencing complicated loading histories. A major issue in J2DT refers to unloading ($\partial F/\partial \sigma_{ij}\,\dot{\sigma}_{ij} < 0$): it is followed by a reduction of the equivalent plastic strain ε_q and a contraction of the yield surface in the stress space so that ($F = 0$). Permanent plastic strain would lead to two stress states (before and after unloading) having the same plastic strain, violating the fundamental postulate of J2DT: a one-to-one relation between stress and strain.

This means that in uniaxial loading the J2DT demands unloading to take place tangentially to the stress-strain curve, following the path BAO in Figure 2.1. Thus, plastic strain is fully recoverable, which is a characteristic of a nonlinear elasticity model. In contrast, incremental plasticity accounts for elastic unloading, following path BC, which

accurately reflects metal material behaviour. In loading scenarios where no unloading takes place, the J2DT may be used as a plasticity model. Such are proportional load paths, in which the components of the deviatoric stress s_{ij} increase monotonically, in constant ratio with respect to each other, e.g. in uniaxial loading. Budianski (1959) argued for the applicability of J2DT in a range of load paths that show deviations from proportional loading but satisfy a number of requirements that ensure plastic strain is irreversible.

The rate equations of the J2DT are of interest in buckling problems, as they are proven to produce accurate instability estimates, while they further form the basis of more elaborate 'corner' models, suggested for instability calculations (Christoffersen & Hutchinson, 1979; Peek, 2000; Pappa & Karamanos, 2016), and the non-associative model developed in the present work.

The rate of plastic strain in J2DT is obtained by differentiating equation (2.18):

$$\begin{aligned} \dot{\boldsymbol{e}}^p &= \frac{3}{2}\frac{\varepsilon_q}{q}\dot{\mathbf{s}} + \frac{3}{2}\left(\frac{\dot{\varepsilon}_q}{q} - \frac{\varepsilon_q \dot{q}}{q^2}\right)\mathbf{s} \\ &= \frac{3}{2}\frac{1}{h}\dot{\mathbf{s}} + \frac{3}{2}\left(\frac{1}{H} - \frac{1}{h}\right)\frac{\dot{q}}{q}\mathbf{s} \end{aligned} \tag{2.22}$$

Accounting for definitions (2.19), (2.20), the codirectional deviatoric stress and plastic strain tensors and for additive strain decomposition -eq.(2.3)-, the following rates are calculated:

$$\dot{\varepsilon}_q = \sqrt{2/3}\,\mathbf{n}\cdot\dot{\mathbf{e}}^p \tag{2.23}$$

$$\dot{q} = \sqrt{3/2}\,\mathbf{n}\cdot\dot{\mathbf{s}} \tag{2.24}$$

$$\dot{\mathbf{s}} = 2G(\dot{\mathbf{e}} - \dot{\mathbf{e}}^p) \tag{2.25}$$

And when inserted in (2.22), the plastic strain rate can be rewritten in the form:

$$\dot{\mathbf{e}}^p = \frac{1}{1 + h/3G}(\mathbf{I}^{dev} - \mathbf{n}\otimes\mathbf{n})\,\dot{\mathbf{e}} + \frac{1}{1 + H/3G}\,(\mathbf{n}\otimes\mathbf{n})\dot{\mathbf{e}} \tag{2.26}$$

This shows the similarity to the plastic strain rate in J2FT in eq.(2.15), but also an additional component, along the component of $\dot{\mathbf{e}}$ which is perpendicular to $\mathbf{n}$, demonstrating that non-proportional loading leads to higher plastic deformations in J2DT. Finally, the tangent material moduli of the J2DT are expressed as:

$$\mathbf{D}_{ep} = 3K\,\mathbf{I}^{vol} + \frac{2G}{1 + 3G/h}[\mathbf{I}^{dev} - \mathbf{n}\otimes\mathbf{n}] + \frac{2G}{1 + 3G/H}\,(\mathbf{n}\otimes\mathbf{n}) \tag{2.27}$$

and the compliance tensor:

$$\mathbf{C}_{ep} = \frac{1}{3K}\mathbf{I}^{vol} + \frac{1+3G/h}{2G}[\mathbf{I}^{dev} - \mathbf{n}\otimes\mathbf{n}] + \frac{1+3G/H}{2G}(\mathbf{n}\otimes\mathbf{n}) \qquad (2.28)$$

The J2DT employs the same moduli with the J2FT for proportional strain rates ($\dot{\mathbf{e}} = k\mathbf{n}$), while for non-proportional paths ($\dot{\mathbf{e}} \neq k\mathbf{n}$), the effective shear modulus $G_S = G/(1+3G/h)$ is lower. This reduced material stiffness governs the material response in abrupt changes in the strain path, which may occur at buckling.

As noted by (Christoffersen & Hutchinson, 1979), the prebuckling and bifurcation of structures can be estimated using J2DT, but the post buckling, and indeed the nonlinear response of imperfect structures near the critical point involve strongly non-proportional loading. Under these conditions, the possibility of unloading should not be excluded which limits the use of J2DT. Addressing bifurcation and consistently investigating the post-bifurcation response of structures, accounting for the influence of imperfection, demands more sophisticated material models.

2.5 Corner theories

Early studies of (Batdorf, 1949) and (Sanders, 1954) suggested this challenge could be addressed with a plastic flow model where the smooth yield surface is discarded, and a sharp corner develops in the yield surface at the loading point. Batdorf & Budiansky (1949) developed a sophisticated slip theory based on observations on metal plasticity mechanisms, which allowed the formation of yield surface corners. Yet, the simplest form of this theory may still be too complicated for local instability calculations. However, it was shown that a flow theory with a sharp corner developed at the loading point in the yield surface could lead to material stiffness similar to the J2DT, for a range of loading paths, which further supported the use of J2DT in instability analyses.

This was the starting point for several simpler phenomenological ‘corner’ theories which employed J2DT stiffness for a range of loading paths and introduced modifications to incorporate a yield surface corner (Figure 2.3) and elastic unloading for stress rates directed within it, thus overcoming a significant limitation of J2DT. The resulting yield function, assuming it exists, is not smooth, so it cannot be differentiated. Hence the yield criterion as described in paragraph 2.2.2 cannot be used to identify whether the material behaves elastically or plastically for a given stress rate $\dot{\boldsymbol{\sigma}}$. Instead, some measure of non-proportionality is employed which relates the direction of the stress increment in

comparison with the geometry of the yield surface corner. This is a key component of corner and pseudo-corner models, and various candidate measures have been suggested. Some measures with clear geometric meaning are the angles formed between the axis of the corner and the stress rate (β), or the strain rate (θ) or even the plastic strain rate (θ^p), all schematically shown in Figure 2.3.

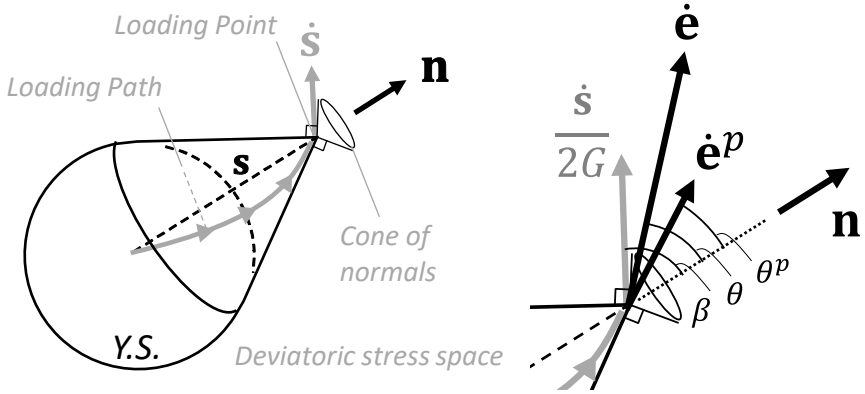

Figure 2.3: Yield surface with conical vertex; direction of plastic strain rate dependent on the total strain rate**.**

Christoffersen & Hutchinson (1979) developed a phenomenological plasticity theory called J_2 Corner Theory (J2CT). The elastic domain is initially bounded by a Von Mises yield surface, but when yielding initiates, at the point of loading a conical vertex develops, rather than the yield surface expanding, and the axis of the cone is in the direction defined by tensor $\mathbf{n} = \mathbf{s}/\|\mathbf{s}\|$. As the yield surface is not smooth, plastic strain rates in several directions are possible, depending on the direction of the strain or stress rate. All such directions are enclosed by the vertex's forward cone of normals: this is a surface defined by the normal tensors to the conical yield surface at the point of loading, shown in Figure 2.3. This demand comes from Drucker's postulate that in stable materials the plastic work is non-negative positive ($\dot{\boldsymbol{\sigma}} \cdot \dot{\mathbf{e}}^p \geq 0$)

Without going into detail, the J2CT postulates the existence of a plastic potential Ω_{CH} of the stress rate $\dot{\boldsymbol{\sigma}}$, which can be differentiated to obtain the plastic strain rate.

$$\dot{\mathbf{e}}^p = \frac{\partial \Omega_{CH}}{\partial \dot{\boldsymbol{\sigma}}} \tag{2.29}$$

After some tensor algebra, the plastic strain rate can be expressed is a format remarkably similar to the J2DT, as:

$$\dot{\mathbf{e}}^p = \frac{1}{1 + h_{CH}/3G} (\mathbf{I}^{dev} - \mathbf{n} \otimes \mathbf{n})\, \dot{\mathbf{e}} + \frac{1}{1 + H_{CH}/3G} (\mathbf{n} \otimes \mathbf{n})\, \dot{\mathbf{e}} \tag{2.30}$$

In place of hardening moduli H, h augmented functions H_{CH}, h_{CH} are defined:

$$H_{CH} = \frac{H}{f(\theta_{CH}) - f'(\theta_{CH}) \tan(\theta_{CH})/2} \tag{2.31}$$

$$h_{CH} = \frac{h}{f(\theta_{CH}) + f'(\theta_{CH}) \cot(\theta_{CH})/2} \tag{2.32}$$

They are connected to and angular measure θ_{CH} and they can be expressed in relation to direction of the stress rate (angle β) and the material properties as

$$\tan\theta_{CH} = \sqrt{H/h}\ \tan\beta \tag{2.33}$$

The purpose of θ_{CH} is to define the direction of the stress rate relative to the yield surface and use it to control the stiffness of the model, through an explicit function $f(\theta_{CH})$. Two types of function f are given in Table 2.4. The main features of this function are:

- $f = 1$ for a range of 'near' proportional stress rates ($\theta_{CH} \leq \theta_0$), so that the plastic strain rate and the material stiffness are identical to the J2DT.
- f reduces smoothly for increasing values of θ_{CH} (relating to increasing non-proportionality in the loading)
- $f = 0$ for strain rates directed tangent to or inward the cone vertex. As a result, moduli $H_{CH}, h_{CH} \to \infty$ and no plastic strain is produced, ensuring elastic unloading is implemented

The stiffness and compliance moduli of the J2CT can be expressed by eq.(2.27), (2.28), respectively, by substituting the hardening moduli H, h with their modified counterparts H_{CH}, h_{CH}.

The J2CT was successfully used in problems of shear band development (Christoffersen & Hutchinson, 1979; Needleman & Tvergaard, 1984). This model was, later, used for buckling problems and problems of structural instability of cylinders under axial compression and pressure loads (Tvergaard, 1983a, 1983b; Giezen, 1988; Tvergaard & Needleman, 2000). It was found to produce good bifurcation load estimates and was used to investigate the post-buckling of shells.

The formulation of J2CT is mathematically elegant but introduces several complexities in modelling the material behaviour, which is clear already from the overly simplified description offered above. A main difficulty in J2CT refers to the calibration of material parameters that control the corner behaviour. The model's stiffness is governed by the angular parameter θ_{CH} which relates to both the material hardening and the direction of the stress rate. The difficultly directly controlling θ_{CH} in an experimental setup creates

challenges in the calibration of function f, which has not been thoroughly clarified.

Less complicated corner models were developed by Gotoh (1985), Goya & Ito (1991) who adopted the flow rule of J2DT and elastic unloading within the yield surface vertex, but eliminated the complications of $f(\theta_{CH})$, and directly used the direction of the stress rate (angle β) to explicitly define the direction θ^p of the plastic strain rate and its size. Similar to the J2CT, the plastic strain rate and the material moduli can be expressed in a form akin to (2.26) and (2.27), by appropriate defining stress-rate-dependent functions for the modified hardening moduli H, h. Additionally, Gotoh (1985) introduced a plastic strain history variable, similar to ε_q in J2FT, which permitted consideration of materials with no strain hardening. The model by Goya & Ito (1991) was a generalization of previously proposed corner models (Christoffersen & Hutchinson, 1979; Gotoh, 1985) and was extended to account for kinematic hardening (translations of the yield surface).

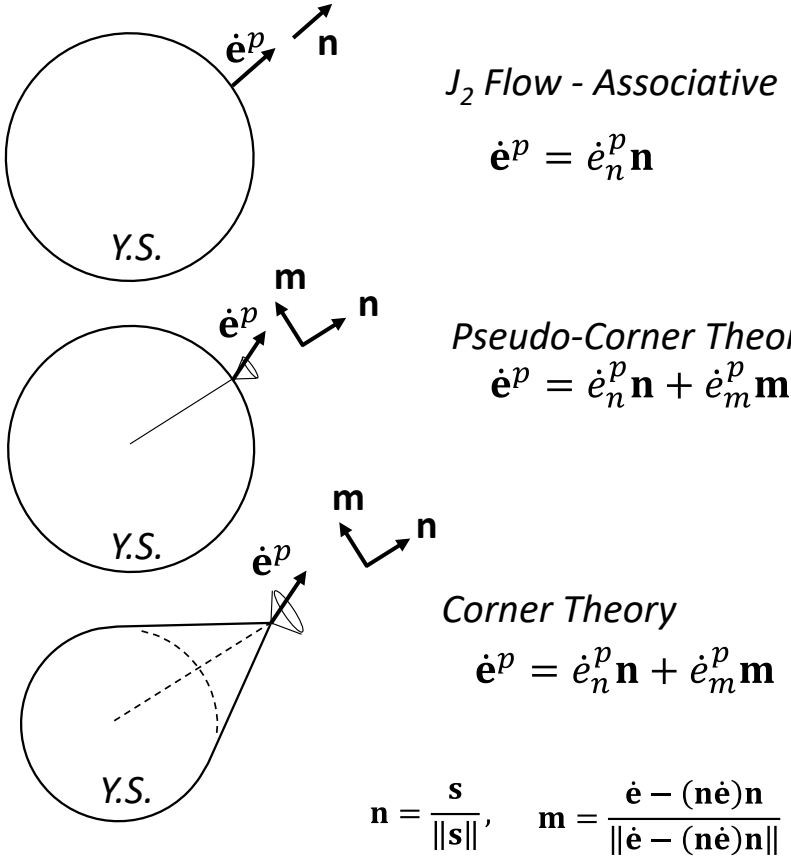

Figure 2.4: Yield surface and flow rules for associative plasticity, pseudo-corner and corner models

Nevertheless, the implementation of the corner models in an implicit finite element environment (integration and linearization -see Chapter 4-) is non-trivial. Ambiguities in the loading/unloading conditions arise in the lack of traditional yield criterion. Incorporating the conical yield surface poses challenges in efficiently monitoring the

evolution of all corners that form under complex loading histories, where several stress paths changes occur.

2.6 Pseudo-corner models

A simpler solution is offered in pseudo corner models, which mimic the effect of a yield surface corner by reducing the stiffness of the material, but employ a smooth Von Mises yield surface which can be implemented efficiently. A schematic comparison between these types of models is made in Figure 2.4.

Hughes & Shakib (1986) developed a 'pseudo-corner' model, which adopts an associative flow rule -eq. (2.15)- and a modified hardening modulus $\overline{H}$ explicitly dependent on the direction of the strain rate (angle θ in Figure 2.3). Appropriate definition of $\overline{H}$ allows for lower material stiffness and increased plastic flow for non-proportional loading paths compared to J2FT, having an effect similar to a corner forming in the yield surface. However, Appendix 2 shows that this model allows for very small increase in plastic flow, and it is not applicable for materials without strain hardening, while no instance of its application is identified in the literature.

A key contribution is the model by Simo (1987), who postulated that a defined conical vertex of semi angle θ_c forms in the yield surface, and plastic strain rates may occur in any direction within this vertex, but not outside it. Simo argued that for any strain rate directed within this simulated vertex ($\theta \leq \theta_c$), plastic strain will be codirectional to the strain rate, while for strain rates directed outside the vertex, the respective plastic strains would lie along the cone of the vertex (forming an angle θ_c with the yield surface normal **n**). This behaviour is demonstrated in Figure 2.5. As a Von Mises yield surface is adopted, for strain directions tangent and inward the yield surface, no plastic strain is produced.

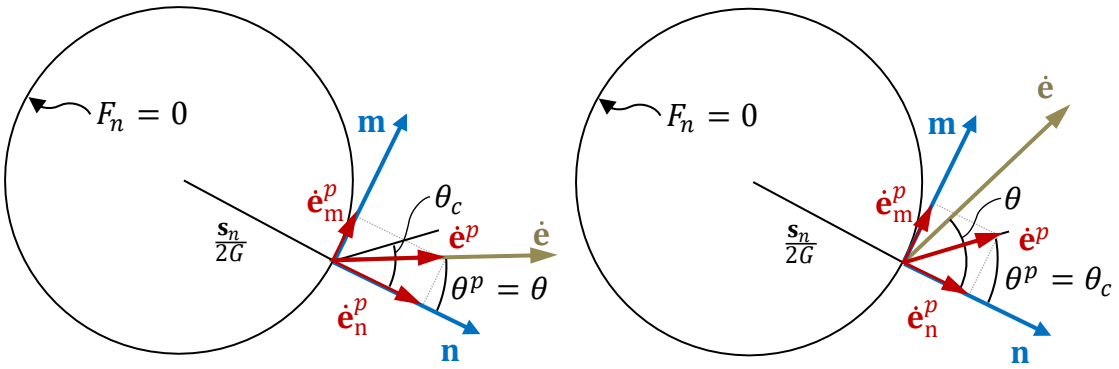

Figure 2.5: Plastic strain rate depending on the direction of the strain rate in the flow rule by Simo (1987)

This flow rule is non-associative, in the sense that the plastic strain rate has a component perpendicular to the yield surface, in the direction **n**, and one tangent to the yield surface, in a direction **m**, defined by the strain rate. The plastic flow rule is expressed as:

$$\dot{\mathbf{e}}^p = \sqrt{3/2}\ \dot{\varepsilon}_q\left[\mathbf{n} + \hat{\delta}\ \mathbf{m}\right] \tag{2.34}$$

The behaviour of the 'vertex' is simply implemented using a function $\hat{\delta}$, which is equal to the tangent of angle θ^p formed by the plastic strain rate and the yield surface normal **n**, and it takes the form:

$$\hat{\delta} = \begin{cases} \tan\theta & , \quad 0 \le \theta \le \theta_c \\ \tan\theta_c & , \quad \theta_c \le \theta \le \pi/2 \end{cases} \tag{2.35}$$

An immediate advantage of Simo's approach is the clear and direct definition of material behaviour, based on natural arguments, not indirectly through abstract functions as in corner theories. This may facilitate the identification of the material corner parameter θ_c, though experimental investigations. Additionally, the material behaviour relates to the direction of the strain rate (angle θ), not the stress rate (angle β), and (Kuroda & Tvergaard, 2001; Yoshida, 2017) argued that this may be more representative as plasticity is strain driven. As a result, the vertex effect persists in materials without strain hardening, for which $\beta = \pi/2$ for all non-proportional strain paths, given the Von Mises yield function. Indeed, this model is applicable independent of the material hardening rule, contrary to the J2CT or the model by Hughes & Shakib (1986).

The elastoplastic rigidity of this model was not discussed in the original publication, but accounting for consistency ($\dot{F} = 0$) and after some tensor algebra, it may be expressed as:

$$\mathbf{D}_{ep} = 3K\mathbf{I}^{vol} + 2G\left[1 - \frac{\hat{\delta}/\tan\theta}{1 + H/3G}\right][\mathbf{I}^{dev} - \mathbf{n}\otimes\mathbf{n}] + \frac{2G}{1 + H/3G}(\mathbf{n}\otimes\mathbf{n}) \tag{2.36}$$

And it can be rewritten in the form (2.27) with

$$h_{SM} = H\tan\theta/\hat{\delta} + 3G\left(\tan\theta/\hat{\delta} - 1\right), \qquad H_{SM} = H \tag{2.37}$$

Simo's model predicts material stiffness that is lower than all mentioned 'corner' models that are based on the J2DT: assuming small deviations from proportionality ($\theta \le \theta_c$), for Simo's model eq. (2.37) defines hardening parameter $h_{SM} = H$, while in J2DT this hardening parameter is $h = k/\varepsilon_q > dk/d\varepsilon_q = H$. The difference in stiffness is particularly pronounced at first yield ($\varepsilon_q = 0$), where $h \to \infty$. This behaviour of Simo's model may be interpreted as the yield surface corner being fully formed, instantly at first

yield. In J2DT stiffness parameter h is the secant modulus of the $k(\varepsilon_q)$ curve, which reduces gradually.

2.6.1 Pseudo-corner models for buckling

The above types of models were suggested as candidates for investigating material and structural instability that occurs in the inelastic rage of the material. The corner theories offered the advantage of a J2DT stiffness, while accounting for unloading within a yield surface vertex, with a drawback of a difficult implementation and calibration. Pseudo-corner models offered a more direct implementation and calibration, but the suggested flow rules have been overly compliant for buckling calculations.

For inelastic instability of shells, plasticity models were proposed sharing the attractive features of both 'corner' and 'pseudo-corner' models: the stiffness of J2DT found to lead to realistic buckling estimates, and the applicability of a smooth yield surface. Nevertheless, this combination creates a discontinuity in the material behaviour for strain rates directed tangent to the yield surface (neutral loading): strain rates directed slightly inwards the yield surface would lead to a purely elastic material response, while ones directed slightly outwards would lead to elastic-plastic behaviour (Figure 2.6). This introduces a discontinuity in the material stiffness which is not representative for the material behaviour and can lead to numerical instability when such loading conditions occur in simulations. Two methods for addressing this issue are identified below.

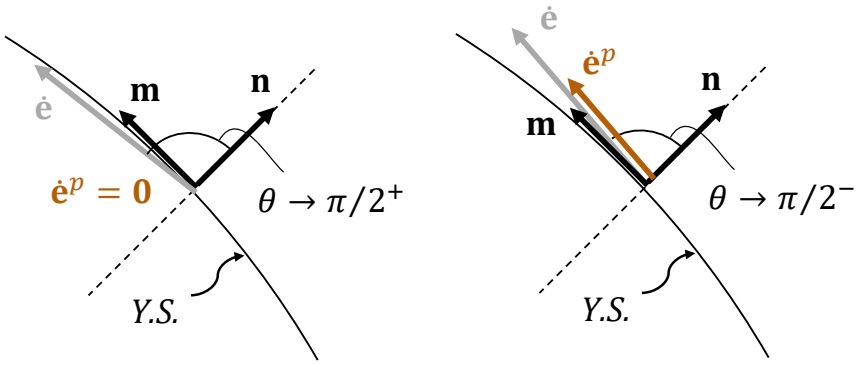

Figure 2.6: Discontinuity of plastic production for straining directions tangent to the yield surface

Peek (2000) developed an "incrementally continuous" deformation theory with unloading (ICUDT), which addressed this issue by relaxing the yield criterion, so that some amount of plastic strain can be produced for strain rates directed tangent to and inward the yield surface. Hence, continuity was established, but as a result, unloading is not elastic. This model is comparable to a 'corner' theory, with a very sharp corner formed in the yield

surface, but the relaxed yield criterion doesn't accurately describe the unloading behaviour of the material and complicates implementation.

In a different approach, Pappa & Karamanos (2016) eliminated the aforementioned discontinuity, and fully accounted for elastic unloading within the Von Mises yield surface. They modified the flow rule of J2DT, so that no plastic strain is produced for strain directions tangent to the yield surface. This effect was implemented by introducing a new measure $\bar{E}_S$, which is equal to the material secant modulus E_S for a wide range of direction angles, effectively mimicking the behaviour of J2DT, and it increases for higher levels of non-proportionality (higher angles θ) up to E for strain directions tangent to the yield surface, thus inhibiting production of plastic strain for such strain directions. Function $\bar{E}_S$ is defined as:

$$\bar{E}_S = E_S[1 - x(\theta)] + Ex(\theta) \tag{2.38}$$

where $x(\theta) = \sin^n \theta\,, n = 250 - 300$, so that the model follows the rate form of J2DT for angles $\theta \leq \theta_c = 75°$ (approximately) and is transitions to zero plastic production at $\theta = 90°$. The plastic strain rate was expressed as:

$$\dot{\boldsymbol{e}}^p = \frac{3}{2}\left(\frac{1}{E} - \frac{1}{\bar{E}_S}\right)\dot{\mathbf{s}} + \frac{3}{2}\frac{\dot{q}}{q}\left(\frac{1}{E_T} - \frac{1}{\bar{E}_S}\right)\mathbf{s} \tag{2.39}$$

which closely resembles eq.(2.22)b, accounting for the definitions of H, h. This model was considered a starting point for the present research due to its simplicity and comprehensiveness, incorporating elastic unloading and producing good buckling estimates. However, its numerical integration and linearization (see Chapter 4) are not trivial, and the originally suggested scheme did not fully account for the influence of angle θ in its implementation. This adversely affected the convergence of the FE model simulations, when it was examined in preliminary stages of the present research. Additionally, using function $x(\theta)$ to zero plastic strains for loading directions tangent to the yield surface may be effective, but other approaches may equally be adopted, more aligned with the definitions of hardening moduli in 'corner' theories, or the more geometric approach by Simo.

Incorporating such models motivates the development of a framework to systematically address non-associative and pseudo-corner behaviours. This is the aim for the development of the J_2 non-associative (J2NA) model, and care is taken to fully account for the influence of the strain rate direction angle θ, throughout the development. Focusing on simplicity and direct applicability in FE simulations, a specific behaviour is

considered, to allow for efficiently investigating the structural response of inelastic shells under compressive loads, accurately tracing their equilibrium paths and consistently assessing stability.

2.7 J_2 non-associative model

A framework is presented for developing non-associative metal plasticity models, employing a smooth Von Mises yield surface. Modifying the rate form of the J2DT and introducing a non-associative hardening function $\bar{h}$ dependent on the loading history and the direction of the strain rate, different amounts of allowable non-associative plastic straining can be implemented, resulting in stiffer or more compliant material behaviour, without negating the requirement of elastic unloading.

For simulating the structural behaviour and instability of thick-walled metal shells, a two branched definition is proposed for the function $\bar{h}$, so that the model can reliably trace the equilibrium path of compressed shells and consistently estimate bifurcation. The rate form of the J2DT is employed for small deviations from proportional loading (Peek, 2000; Pappa & Karamanos, 2016), to capitalize on the good bifurcation predictions of this model, which are in agreement with available experimental data. In addition, a branch following the approach by (Simo, 1987) is used to moderate the non-associative straining for more pronounced deviations from proportional loading. It is chosen due to its simplicity and geometric interpretation, that mimics the development of a yield surface vertex, and because it allows for fully elastic unloading for straining directions tangent to the yield surface.

Preliminary calculations indicated that the direct use of either the J2DT or Simo's model individually may not result in both: (a) estimating instability and (b) tracing post-buckling behaviour of thick-walled cylinders, an issue to be extensively discussed in paragraph 4.1. By combining both models, as presented in the following, their desirable attributes are endowed into the J_2 non-associative (J2NA) model.

2.7.1 Model description - rate form

In the framework of incremental small-strain metal plasticity, the rate of stress $\dot{\boldsymbol{\sigma}}$ is related to the elastic strain rate $\dot{\boldsymbol{\varepsilon}}^e$ as:

$$\dot{\boldsymbol{\sigma}} = \mathbf{D}\dot{\boldsymbol{\varepsilon}}^e = \mathbf{D}(\dot{\boldsymbol{\varepsilon}} - \dot{\boldsymbol{\varepsilon}}^p) = \mathbf{D}\dot{\boldsymbol{\varepsilon}} - \mathbf{D}\dot{\boldsymbol{\varepsilon}}^p \tag{2.40}$$

where $\mathbf{D}$ is the fourth-order elastic stiffness tensor, $\dot{\boldsymbol{\varepsilon}}$ is the rate of total strain, and $\dot{\boldsymbol{\varepsilon}}^p$ is

the (deviatoric) plastic strain rate, which for J2DT takes the following form - see eq. (2.22) & (Chakrabarty; 2006) -:

$$\dot{\mathbf{e}}^p = \frac{3}{2}\frac{\varepsilon_q}{q}\dot{\mathbf{s}} + \frac{3}{2}\left(\frac{\dot{\varepsilon}_q}{q} - \frac{\varepsilon_q \dot{q}}{q^2}\right)\mathbf{s} \tag{2.41}$$

where $\mathbf{s} = \mathbf{I}^{dev}\boldsymbol{\sigma}$ is the deviatoric part of the stress tensor, ε_q is the (accumulated) equivalent plastic strain, $q = \sqrt{3/2}\,\|\mathbf{s}\|$ is the equivalent Von Mises stress, with $\|\mathbf{s}\| = \sqrt{\mathbf{s}\cdot\mathbf{s}}$ being the norm of $\mathbf{s}$, and their rates, indicated by a superimposed dot: $\dot{\mathbf{s}}$, $\dot{\varepsilon}_q$ and $\dot{q}$. By further enforcing consistency with a Von Mises yield surface in (2.41), which implies ($\dot{\varepsilon}_q = \dot{q}/H$), the flow rule of the J2DT as presented by (Goya & Ito, 1991; Pappa & Karamanos, 2016) can be obtained.

Considering these definitions, one may readily show that $\dot{q} = \sqrt{3/2}\,\mathbf{s}\cdot\dot{\mathbf{s}}/\|\mathbf{s}\|$, and $\dot{\mathbf{s}} = 2G(\dot{\mathbf{e}} - \dot{\mathbf{e}}^p)$ with $\dot{\mathbf{e}} = \mathbf{I}^{dev}\dot{\boldsymbol{\varepsilon}}$. Inserting those in (2.41) and rearranging, the plastic strain rate can be expressed as:

$$\dot{\mathbf{e}}^p = \sqrt{3/2}\,\dot{\varepsilon}_q\mathbf{n} + \frac{[\mathbf{I}^{dev} - \mathbf{n}\otimes\mathbf{n}]\dot{\mathbf{e}}}{1 + h/3G} \tag{2.42}$$

where $\mathbf{n} = \mathbf{s}/\|\mathbf{s}\|$ is the unit tensor in the direction of $\mathbf{s}$ and $h = q/\varepsilon_q$ is a non-associative hardening function representing the secant modulus of the stress-plastic strain curve. The plastic strain rate comprises two components: one in the direction of the tensor $\mathbf{n}$ and one in the direction $[\mathbf{I}^{dev} - \mathbf{n}\otimes\mathbf{n}]\dot{\mathbf{e}}$, which is perpendicular to $\mathbf{n}$, in the direction defined by the strain rate. This consideration is employed in the previous paragraphs to develop a uniform expression for the rigidity tensor of the referenced models.

The present model adopts this form of plastic strain rate $\dot{\mathbf{e}}^p$, but replaces h with a different explicitly chosen function $\bar{h}$:

$$\dot{\mathbf{e}}^p = \sqrt{3/2}\,\dot{\varepsilon}_q\mathbf{n} + \frac{[\mathbf{I}^{dev} - \mathbf{n}\otimes\mathbf{n}]\dot{\mathbf{e}}}{1 + \bar{h}/3G} \tag{2.43}$$

The function $\bar{h}$ is a non-associative-hardening parameter, whose definition is discussed in paragraph 2.7.2, that moderates the amount of plastic straining perpendicular to $\mathbf{n}$. In (2.43), the rate of equivalent plastic strain is defined as $\dot{\varepsilon}_q = \sqrt{2/3}\,\mathbf{n}\cdot\dot{\mathbf{e}}^p$, a definition also adopted by Simo (1987), which is equivalent to its counterpart in J2FT ($\dot{\varepsilon}_q = \sqrt{2/3}\sqrt{\dot{\mathbf{e}}^p\cdot\dot{\mathbf{e}}^p}$) for proportional loading. The flow rule (2.43) can be rewritten in the following, more convenient, geometric form, which is similar to the one used by Simo

(1987) and is used more extensively in the numerical integration of the model, described in Chapter 3:

$$\dot{\mathbf{e}}^p = \sqrt{3/2}\,\dot{\varepsilon}_q\,\mathbf{n} + \frac{\|\dot{\mathbf{e}}\|\sin\theta}{1+\bar{h}/3G}\mathbf{m} \tag{2.44}$$

In (2.44), θ is the angle defined by the strain rate $\dot{\mathbf{e}}$ and the tensor $\mathbf{n}$, shown in Figure 2.7, analytically expressed as:

$$\cos\theta = \frac{\mathbf{n}\cdot\dot{\mathbf{e}}}{\|\dot{\mathbf{e}}\|} \tag{2.45}$$

and $\mathbf{m}$ is the unit deviatoric tensor perpendicular to $\mathbf{n}$, in the direction of the strain rate

$$\mathbf{m} = \frac{(\mathbf{I}^{dev} - \mathbf{n}\otimes\mathbf{n})\dot{\mathbf{e}}}{\|(\mathbf{I}^{dev} - \mathbf{n}\otimes\mathbf{n})\dot{\mathbf{e}}\|} = \frac{(\mathbf{I}^{dev} - \mathbf{n}\otimes\mathbf{n})\dot{\mathbf{e}}}{\|\dot{\mathbf{e}}\|\sin\theta} \tag{2.46}$$

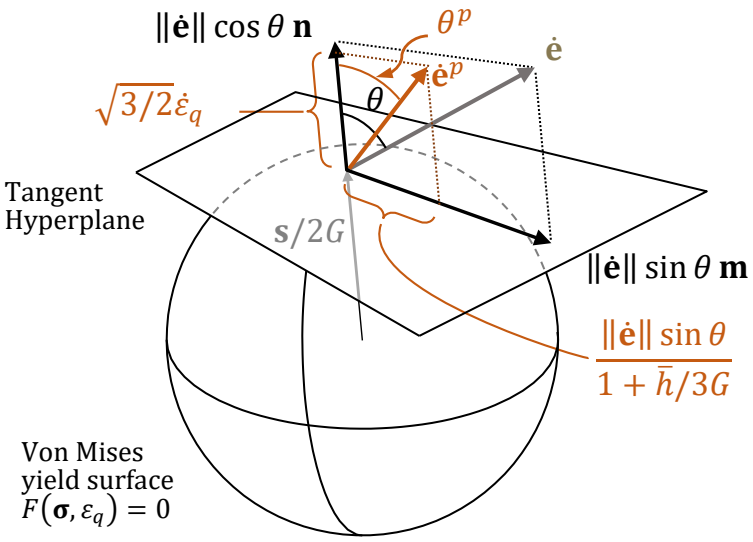

Figure 2.7: Schematic representation of the yield surface in the deviatoric plane, the normal tensor $\mathbf{n}$, the tangential tensor $\mathbf{m}$ in the direction of the strain rate $\dot{\mathbf{e}}$ and the plastic strain rate $\dot{\mathbf{e}}^p$, with components in both directions normal and tangent to the yield surface.

Yielding is defined with respect to a Von Mises yield function with nonlinear isotropic hardening:

$$F(\boldsymbol{\sigma},\varepsilon_q) = \frac{\sqrt{2/3}}{2G}\left[q - k(\varepsilon_q)\right] = \frac{\|\mathbf{s}\|}{2G} - \frac{\sqrt{2/3}\,k(\varepsilon_q)}{2G} = 0 \tag{2.47}$$

where $k(\varepsilon_q)$ is the material yield stress in uniaxial tension, that defines the size of the yield surface as a function of the (accumulated) equivalent plastic strain ε_q. The above expression for the Von Mises yield criterion is chosen because it scales down the yield surface to the deviatoric strain space, so that all the strain components, the shape of the

yield surface and their relative size and geometry can be presented in the same graph (e.g. Figures 2.7, 3.1, 3.2). Hence, tensors **n**, **m** are the unit tensors normal and tangent to the Von Mises yield surface respectively, and (2.43) demonstrates the non-associative nature of the present model, with the increased plastic flow moderated by $\bar{h}$.

Enforcing consistency $\left(\dot{F}=0\right)$, and using (2.4) and (2.43), the equivalent plastic strain rate is expressed similarly with the J2FT:

$$\dot{\varepsilon}_q = \sqrt{2/3}\frac{1}{1+H/3G}(\mathbf{n}\cdot\dot{\mathbf{e}}) \tag{2.48}$$

where $H = dk/d\varepsilon_q$ is the material isotropic hardening modulus. Ultimately, accounting for consistency ($\dot{F}=0$), the plastic strain rate is expressed as:

$$\dot{\mathbf{e}}^p = \left[\frac{\mathbf{I}^{dev}-\mathbf{n}\otimes\mathbf{n}}{1+\bar{h}/3G}+\frac{\mathbf{n}\otimes\mathbf{n}}{1+H/3G}\right]\dot{\mathbf{e}} \tag{2.49}$$

Using equations (2.4), (2.43) and (2.48), the instantaneous rigidity tensor (continuum tangent moduli) for this material model is readily calculated as

$$\mathbf{D}_{ep} = 3K\,\mathbf{I}^{vol}+\frac{2G}{1+3G/\bar{h}}\,\mathbf{I}^{dev}-\left(\frac{2G}{1+H/3G}-\frac{2G}{1+\bar{h}/3G}\right)(\mathbf{n}\otimes\mathbf{n}) \tag{2.50}$$

or

$$\mathbf{D}_{ep} = 3K\,\mathbf{I}^{vol}+\frac{2G}{1+3G/\bar{h}}[\mathbf{I}^{dev}-\mathbf{n}\otimes\mathbf{n}]+\frac{2G}{1+3G/H}(\mathbf{n}\otimes\mathbf{n}) \tag{2.51}$$

It may be rewritten equivalently as in (2.52), a more familiar form, akin to the rigidity tensor of the J2FT. However, it employs a reduced shear modulus $\bar{G}$, combined with an increased hardening modulus $\bar{H}$, which are dependent on the non-associative hardening parameter $\bar{h}$ and account for the straining-direction-dependency, characteristic of the model. As a result, the elastic-plastic instantaneous moduli of non-associative model are less stiff than the corresponding moduli of the J2FT, ultimately leading to a more compliant material behaviour under non-proportional strain paths.

$$\begin{aligned}\mathbf{D}_{ep} &= 3K\,\mathbf{I}^{vol}+2\bar{G}(\mathbf{I}^{dev}-\mathbf{n}\otimes\mathbf{n})+\frac{2\bar{G}}{1+3\bar{G}/\bar{H}}\,(\mathbf{n}\otimes\mathbf{n})\\ &= 3K\,\mathbf{I}^{vol}+2\bar{G}\mathbf{I}^{dev}-\frac{2\bar{G}}{1+\bar{H}/3\bar{G}}\,(\mathbf{n}\otimes\mathbf{n})\end{aligned} \tag{2.52}$$

where

$$\bar{G} = \frac{G}{1 + 3G/\bar{h}} \tag{2.53}$$

$$\bar{H} = \frac{1}{1/H - 1/\bar{h}} \tag{2.54}$$

Finally, the material compliance tensor $\mathbf{C}_{ep} = \mathbf{D}_{ep}^{-1}$ can be readily calculated as:

$$\mathbf{C}_{ep} = \frac{\mathbf{I}^{vol}}{3K} + \frac{\mathbf{I}^{dev}}{2\bar{G}} + \frac{3}{2\bar{H}}(\mathbf{n} \otimes \mathbf{n}) \tag{2.55}$$

2.7.2 Definition of the function $\bar{h}$

The choice of $\bar{h}$ is of key importance in this model, leading to stiffer or more compliant material behaviour. Table 2.2 shows that the appropriate selection of $\bar{h}$, allows the model to mimic different material models available in the literature.

To incorporate elastic unloading together with the selected non-associative flow rule, continuity of the production of plastic strain must be ensured, as noted by Peek (2000) and Pappa & Karamanos (2016). Without this provision, strain rates directed slightly inwards the yield surface would lead to elastic response, while ones directed slightly outwards would cause for elastoplastic straining, thus introducing an artificial numerical instability when such loading occurs (Figure 2.6). This implies that no plastic strain may be produced for strain rates directed tangent to the yield surface ($\theta \to \pi/2$), which created demand (2.56) for function $\bar{h}$ in J2NA:

$$\lim_{\theta \to \left(\frac{\pi}{2}\right)^-} \|\dot{\mathbf{e}}^p\| / \|\dot{\mathbf{e}}\| = 0 \;\; \Rightarrow \lim_{\theta \to \left(\frac{\pi}{2}\right)^-} \bar{h} \to +\infty \tag{2.56}$$

Therefore, $\bar{h}$ must depend on the direction of the strain rate (θ), which implies that the rigidity tensor (2.50) at a material point is not fully defined by its loading history, but the strain rate direction must also be known. This is a manifestation of the nonlinear dependence of the stress rate on the strain rate, characteristic in all mentioned corner and pseudo-corner models.

Table 2.1: Summary of the non-associative model

(1) Linear isotropic stress/strain relations

$$\mathbf{s} = 2G[\mathbf{e} - \mathbf{e}^p]$$
$$tr\ \boldsymbol{\sigma} = 3K\ tr\ \boldsymbol{\varepsilon}$$

(2) Yield condition

$$F(\boldsymbol{\sigma}, \varepsilon_q) = \frac{1}{2G}\left[\|\mathbf{s}\| - \sqrt{2/3}\, k(\varepsilon_q)\right]$$
$$\dot{\varepsilon}_q = \sqrt{2/3}\, \mathbf{n} \cdot \dot{\mathbf{e}}^p$$
$$\mathbf{n} = \mathbf{s}/\|\mathbf{s}\|$$

(3) Flow rule

$$\dot{\mathbf{e}}^p = \sqrt{3/2}\, \dot{\varepsilon}_q\, \mathbf{n} + \frac{\|\dot{\mathbf{e}}\| \sin\theta}{1 + \bar{h}/3G}\mathbf{m}$$
$$\mathbf{m} = \frac{(\mathbf{I}^{dev} - \mathbf{n} \otimes \mathbf{n})\dot{\mathbf{e}}}{\|(\mathbf{I}^{dev} - \mathbf{n} \otimes \mathbf{n})\dot{\mathbf{e}}\|}$$
$$\cos\theta = \mathbf{n} \cdot \dot{\mathbf{e}}/\|\dot{\mathbf{e}}\|$$
$$\cos\theta^p = \mathbf{n} \cdot \dot{\mathbf{e}}^p/\|\dot{\mathbf{e}}^p\|$$
$$h = k(\varepsilon_q)/\varepsilon_q$$

1st branch:	$\bar{h} = h \quad \& \quad \theta^p(\bar{h}) \le \theta_c$
2nd branch:	$\theta^p = \theta_c \rightarrow \bar{h}(\theta_c) > h$

(4) Kuhn-Tucker loading/unloading conditions

$$\dot{\varepsilon}_q \ge 0, \qquad F(\boldsymbol{\sigma}, \varepsilon_q) \le 0, \qquad \dot{\varepsilon}_q F(\boldsymbol{\sigma}, \varepsilon_q) = 0$$

(5) Plastic consistency in loading ($\dot{\varepsilon}_q > 0$)

$$\dot{\varepsilon}_q = \sqrt{2/3}\frac{1}{1 + H/3G}(\mathbf{n} \cdot \dot{\mathbf{e}})$$

The present model (J2NA) adopts a two-branch definition for the non-associative hardening parameter $\bar{h}$. For small deviations from proportional loading, $\bar{h} = h = k(\varepsilon_q)/\varepsilon_q$, and the model's flow rule coincides with the flow of the J2DT, aspiring to inherit its superiority in estimating bifurcation. A second branch is necessary to comply with the limitations imposed by elastic unloading, so for larger deviations from proportional loading, up to loading tangent to the yield surface, the model is chosen to follow the flow proposed by Simo (1987). This branch mimics the effect of a conical yield surface vertex of semi-angle θ_c in the direction of the stress deviator: it constrains the plastic strain rate to lie within the forward cone of normals of the vertex, as shown in Figure 2.9. This is interpreted as $(\theta^p \le \theta_c)$, where θ^p is the angle formed by the yield surface normal and the plastic strain rate (Figure 2.7), analytically expressed as:

$$\cos\theta^p = \frac{\mathbf{n} \cdot \dot{\mathbf{e}}^p}{\|\dot{\mathbf{e}}^p\|} \tag{2.57}$$

From (2.43) and (2.57), it is deduced that θ^p is a decreasing function of $\bar{h}$, which allows for the two branches of the model to be reduced to the following definition.

$$\{\bar{h} \geq h = k(\varepsilon_q)/\varepsilon_q \qquad \text{so that} \qquad \theta^p \leq \theta_c\} \tag{2.58}$$

A summary of the model is given in Table 2.1. In the rate form of the model, the definition of $\bar{h}$ in equation (2.58), can be equivalently expressed in the form presented in Table 2.2, which demonstrates its compliance with requirement for continuity of plastic production (2.56). This definition of $\bar{h}$ is computationally attractive, as it simplifies the implementation of the model in a finite element environment, and it is calibrated using a single scalar parameter. It further provides versatility in the range of behaviours that the model can represent, leading to stiffer or more compliant material responses.

Determining the value of parameter θ_c is a challenge, similar to 'corner' theories. This may be achieved conducting experiments that involve non-proportional loading, as the ones described by (Rønning et al., 2010; Yoshida & Tsuchimoto, 2018). In those experiments, axial deformation is applied to a tubular specimen beyond the yield point, e.g. up to strain 1%, followed by combined increments of axial strain ($\Delta\varepsilon$) and twist increments ($\Delta\gamma$), producing a non-proportional strain path. This path forms an angle ψ with the preloading path, which is calculated as $\psi = \text{atan}(\sqrt{3}\Delta\tau/\Delta\sigma)$, where $\Delta\sigma, \Delta\tau$ are calculated from the measured axial force and torque load increments. From the strain and load increments and using eq.(2.49), the values for $H, \bar{h}$ are estimated (Figure 2.9). In a preliminary approach, the model's angle parameter can be approximated as $\theta_c \approx \text{atan}\,(H/\bar{h}\tan\psi)$. It is noted that pure twisting ($\psi = 90^o$) may be inappropriate for calibrating θ_c, as the very small size of the resulting plastic strain increments may disallow reliably estimating their direction.

In an analogous manner, the parameter θ_c can also be calculated from biaxial experiments on cruciform specimens (Kuwabara, et al., 2000; Kuwabara, 2007), in which, after a proportional preloading stage, non-proportionality is induced in the second loading stage by applying different strain increments in the two directions.

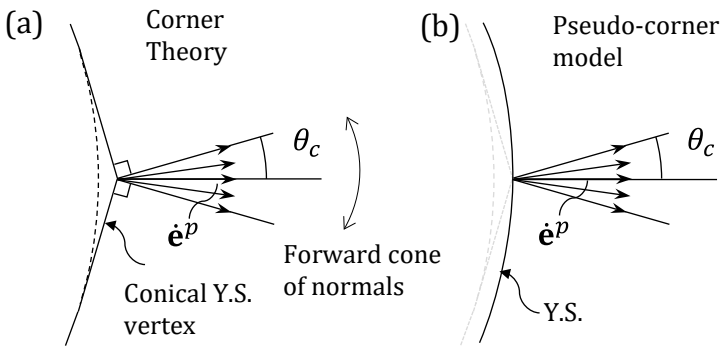

Figure 2.8: (a) Yield surface corner models and (b) Pseudo-corner model

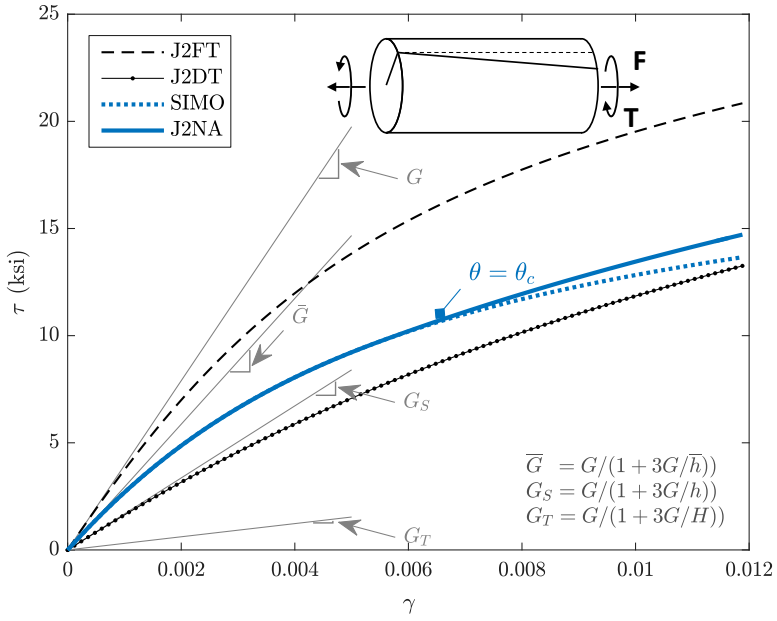

Figure 2.9: Model calibration under non-proportional loading ($\psi = 67.5^o$)

Table 2.2: Expressing different models* from the literature using parameter $\bar{h}$

J_2 Flow – Associative model	$\bar{h} \to +\infty$
J_2 Deformation Theory	$\bar{h} = h = k(\varepsilon_q)/\varepsilon_q$
Pappa & Karamanos (2016)	$\bar{h} = [E \sin^n \theta + h]/[1 - \sin^n \theta]$
Simo (1987)	$\bar{h} = Hc + 3G(c-1), \quad c = \tan\theta/\hat{\delta}(\theta),$ $\hat{\delta}(\theta) = \tan(\max(\theta, \theta_c))$
Present model	$\bar{h} = \max\begin{Bmatrix} k(\varepsilon_q)/\varepsilon_q \\ Hc + 3G(c-1) \end{Bmatrix}, c = \tan\theta \,/\, \tan\theta_c$

*rate form

2.7.3 Plastic production, comparisons with literature

A qualitative comparison between various corner and pseudo-corner models can be made using the plastic production $w^*(\theta, \varepsilon_q)$ and the plastic angle $\theta^p(\theta, \varepsilon_q)$ associated with each model. The first, introduced by Hughes & Shakib (1986), expresses the amount of plastic strain produced by a strain rate $\dot{\mathbf{e}}$ depending on its direction (angle θ). It is defined as:

$$w^*(\theta, \varepsilon_q) = \frac{\|\dot{\mathbf{e}}^p\|}{\dfrac{\|\dot{\mathbf{e}}\|}{1 + H/3G}} \tag{2.59}$$

The plastic angle θ^p is an additional measure for describing the behaviour of a model, stemming from the non-associative nature of the majority of the considered flow rules. It

expresses the angle the plastic strain rate $\dot{\boldsymbol{\varepsilon}}^p$ forms with the deviatoric stress $\mathbf{s}$, defined in (2.57) depending on the direction θ of the (total) strain rate $\dot{\boldsymbol{\varepsilon}}$. Analytical expressions for these measures, are provided in Table 2.4, for several flow rules in the literature.

The behaviour of each model is influenced by the loading history of the material; therefore, for the following comparison, a specific material point is considered, loaded well into the inelastic range to its current stress state. The material stress-strain behaviour is assumed to follow a Ramberg-Osgood (R-O) curve -eq.(2.60)- whose parameters are provided in Table 2.3, together with material properties and state variables of the point under consideration.

$$\varepsilon = \frac{\sigma}{E}\left[1 + \frac{3}{7}\left(\frac{\sigma}{\bar{\sigma}}\right)^{n-1}\right] \tag{2.60}$$

Table 2.3: Material properties and state variables at considered loading state

Young's Modulus	$E = 194\ GPa$
Poisson's Ratio	$\nu = 0.3$
R-O stress parameter	$\bar{\sigma} = 572\ MPa$
R-O exponent	$n = 10.8$
Equivalent plastic strain	$\varepsilon_q = 1.6\%$
Hardening modulus	$H/E = 2\%$
Angle parameter*	$\theta_c = \pi/4$

*Applicable for the models by Simo (1987), Hughes & Shakib (1986) and the J2NA

In Figures 2.10, 2.11 the plastic production and plastic angles are plotted with respect to the angle θ for the J2NA and several other models from the literature [2]. For proportional loading ($\theta = 0$), all models predict the same plastic production as the J2FT, since all models must be able to replicate identically a proportional loading experiment, e.g. a uniaxial test. As non-proportionality increases, plastic production in all models is higher than the one predicted by the J2FT, corresponding to more compliant responses. All models that account for fully elastic unloading produce zero plastic strain for strain rates directed tangent to their respective yield surfaces. Those directions correspond to $\theta = \pi/2$ for the models employing a Von Mises yield surface, and to $\theta = \pi - \theta_{c.CnH}$ for the models which incorporate a yield surface vertex, such as the J_2 corner theory [3].

[2] For the J_2 corner theory two curves are plotted, each one representing a family of flow rules proposed by Christoffersen & Hutchinson (1979)

[3] The value of $\theta_{c.CnH}$ is given in Table 2.4

The J_2 corner theory, the models by Peek (2000) and Pappa & Karamanos (2016) and the J2NA, all exhibit a response similar with the J2DT for a certain range of strain rate directions (θ). Each of them employs a dedicated branch with the purpose of gradually suppressing plastic production for strain rate directions that approach the tangent to the yield surface. This is a key feature that differentiates each model with respect to the others. All models incorporate a maximum allowable angle θ^p which the plastic strain rate may not exceed, but its value and the range of strain-rate directions θ for which this angle is activated vary for each model.

Figure 2.12 shows that, at first yield the J2DT has an essentially associative behaviour, allowing for plastic straining only in the direction of the deviatoric stress. Progressively, as plastic deformation accumulates, increasing amounts of non-associative plastic strain are produced for a given angle θ, meaning that both plastic production and plastic angle increase. For large values of accumulated plastic strain ε_q this behaviour becomes similar to the first branch of the model proposed by Simo (1987). This gradually more compliant behaviour of the J2DT leads to lower bifurcation estimates for thick-walled shells and explains its use in several constitutive models aiming at inheriting its capability for providing reliable buckling predictions.

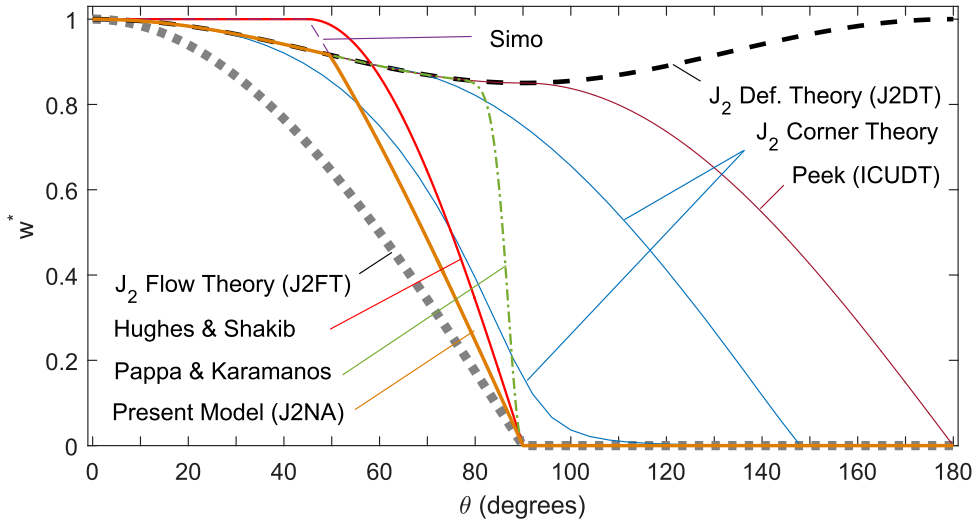

Figure 2.10: Plastic production ratio (w^*) with respect to the direction of the strain rate (angle θ)

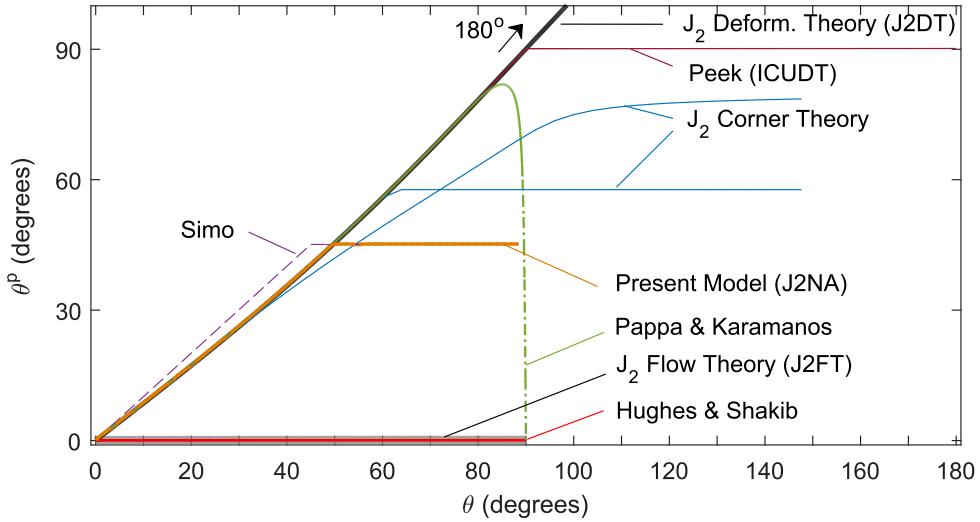

Figure 2.11: Direction of plastic strain rate (angle θ^p) with respect to the direction of the total strain rate (angle θ)

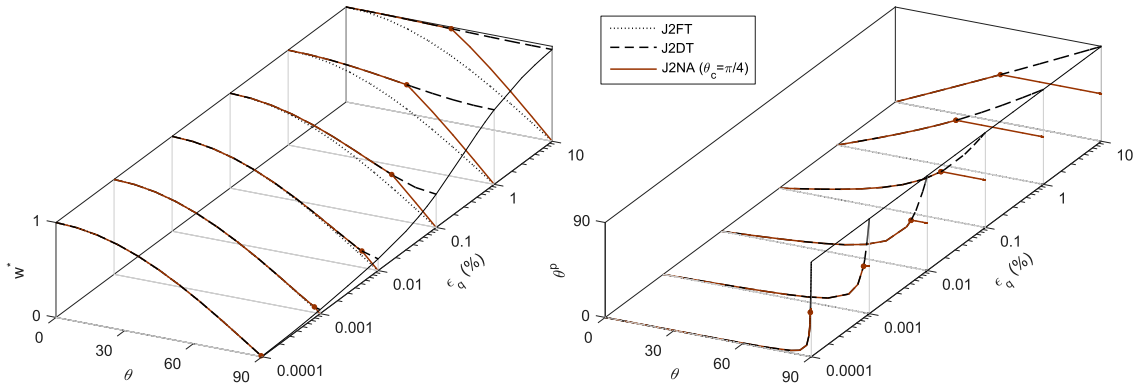

Figure 2.12: (a) Evolution of plastic production with increasing plastic deformation, (b) Evolution of angle θ^p, with increasing plastic deformation

Table 2.4: Plastic production and plastic angle for different models

	Plastic Production $w^*(\theta, \varepsilon_q)$	**Plastic Angle** $\tan\theta^p(\theta, \varepsilon_q)$	**Details**
J_2 Flow theory (associative model)	$\cos\theta$	0	
Hughes and Shakib (1987)	$\cos\psi$	0	$\psi = \max\left\{0,\ \frac{\pi}{2}\frac{(\theta-\theta_c)}{(\pi/2-\theta_c)}\right\}$
Simo (1987)	$\cos\theta\sqrt{1+\hat{\delta}^2}$	$\hat{\delta}(\theta)$	$\hat{\delta}(\theta) = \tan(\min\{\theta, \theta_c\})$
J_2 Deform. Theory (Total Strain Theory)	$\sqrt{\cos^2\theta + c^2\sin^2\theta}$	$c\tan\theta$	$c = [1+H/3G]\ /\ [1+h/3G]$ $H = dk/d\varepsilon_q\ ,\ \ h = k/\varepsilon_q$
Pappa & Karamanos (2016)	$\sqrt{\cos^2\theta + c^2\sin^2\theta}$	$c\tan\theta$	$c = [1+H/3G]\ /\ [1+h_{PnK}/3G]$ $h_{PnK} = [E\sin^n\theta + h]/[1-\sin^n\theta]$
Peek (2000)	$\sqrt{\cos^2\psi + c^2\sin^2\theta}$	$c\tan\psi$	$c = [1+H/3G]\ /\ [1+h/3G]$ $\psi = \min(\theta, \pi/2)$
J_2 Corner Theory Family 1 . Family 2 .	$\sqrt{\cos^2\theta + c^2\sin^2\theta}$ $f = \begin{cases} 1 & [0\,,\theta_o) \\ \cos^2\psi, & \theta^{CH}\in[\theta_o,\theta_c) \\ 0 & [\theta_c,\pi] \end{cases}$ $\psi = \pi/2\,[(\theta^{CH}-\theta_c)/(\pi/2-\theta_c)]$ $f(\theta^{CH}) = \left[g(\phi^{CH})[1+l(\phi^{CH})]\right]^{-1}$ with $g(\phi^{CH}) = \begin{cases} 1, & \phi^{CH}\in[0\,,\theta_0) \\ (1-\bar{\phi}^m)^{-2}, & \phi^{CH}\in[\theta_0,\theta_\pi] \end{cases}$ $\bar{\phi} = (\phi^{CH}-\theta_0)/(\theta_\pi-\theta_0), m \geq 2$ $l(\phi^{CH}) = g'/(2g)$	$c\tan\theta$	$c = [1+H/3G]\ /\ [1+h_{CH}/3G]$ with $H_{CH} = H/[f - f'\tan\theta^{CH}]$ $h_{CH} = h/[f + f'\cot\theta^{CH}]$ $\tan\theta^{CH} = \sqrt{H/h}\frac{h_{CH}}{H_{CH}}c\tan\theta$ $\tan\theta_c = -\sqrt{H/h}\frac{\sigma_0}{\sqrt{q_e^2-\sigma_0^2}}$ where σ_0 is the yield stress of the material and q_e is the current mises stress of the material and $\theta_0 \leq \theta_c - \pi/2$ is the angle cutoff, following which the model ceases to follow the flow rule of J2DT
J_2 Non-Associative Model (J2NA)	$\sqrt{\cos^2\theta + c^2\sin^2\theta}$	$\min\begin{Bmatrix} c\tan\theta \\ \tan\theta_c \end{Bmatrix}$	$c = [1+H/3G]\ /\ [1+\bar{h}/3G]$ $\bar{h} \leq h$ so that $\theta^p \leq \theta_c$

3 NUMERICAL IMPLEMENTATION

Towards the implementation of the presented special-purpose plasticity model (J2NA) in a finite element environment, a stress update algorithm (or integration scheme) is developed, accounting for the particular features of the non-associative flow. A geometric approach, similar to the one developed by Simo (1987), is adopted for the integration of the governing equations, while key modifications are introduced, intended to account for nonlinear material hardening, and for the dependence on the direction of the strain increment that J2NA exhibits. Appropriate mathematical manipulations reduce the integration of the model to the solution of a single manageable equation of a scalar unknown, irrespective of the material hardening rule, as in the case of J2FT. The resulting solution scheme is less complicated and more versatile compared to earlier approaches (Simo, 1987; Rønning et al., 2010; Pappa & Karamanos, 2016), while it fully accounts for the influence of the strain rate direction and for non-linear hardening, both in the integration and in the linearization scheme. The constitutive integration scheme is developed for brick elements and an extension for shell element analysis is included. The generalization to implement other benchmark models from the literature is discussed.

3.1 Backward-Euler stress update algorithm

For any material integration point at pseudo-time t_n the stress $\boldsymbol{\sigma}_n$ and strain $\boldsymbol{\varepsilon}_n$ are known, as well as the equivalent plastic strain $\varepsilon_{q|n}$ (internal variable). At pseudo-time $t_{n+1} = t_n + \Delta t$, a strain increment $\Delta\boldsymbol{\varepsilon} = \boldsymbol{\varepsilon}_{n+1} - \boldsymbol{\varepsilon}_n$ leads to changes in the material

stress state $\boldsymbol{\sigma}_{n+1}$ and internal variable $\varepsilon_{q|n+1}$, which are calculated by integrating the plasticity constitutive model in the pseudo-time increment Δt.

An elastic predictor–plastic corrector scheme (Simo & Taylor, 1986) is adopted: an elastic-predictor step, leading to a stress state outside the yield surface, is followed by a plastic-corrector step, which enforces consistency and returns the stress to the updated yield surface. The elastic predictor $\boldsymbol{\sigma}^e$ assumes a purely elastic trial stress and is split as follows:

$$\boldsymbol{\sigma}^e = \boldsymbol{\sigma}_n + \mathbf{D}\Delta\boldsymbol{\varepsilon} = -p^e\mathbf{I} + \mathbf{s}^e \tag{3.1}$$

where

$$p^e = -1/3\,(\mathbf{I}\cdot\boldsymbol{\sigma}^e) = p_n - K(\mathbf{I}\cdot\Delta\boldsymbol{\varepsilon}) \tag{3.2}$$

$$\mathbf{s}^e = \mathbf{I}^{dev}\boldsymbol{\sigma}^e = \mathbf{s}_n + 2G\Delta\mathbf{e} \tag{3.3}$$

Furthermore, $\Delta\mathbf{e} = \mathbf{I}^{dev}\Delta\boldsymbol{\varepsilon}$ is the deviatoric part of the strain increment**,** p_n and $\mathbf{s}_n$ are respectively the hydrostatic pressure and the deviatoric stress at the beginning of the increment ($\boldsymbol{\sigma}_n = \mathbf{s}_n - p_n\mathbf{I}$).

The Von Mises stress at the beginning of the strain increment (q_n) and at the elastic predictor state (q^e) are respectively defined as:

$$q_n = \sqrt{3/2}\sqrt{\mathbf{s}_n\cdot\mathbf{s}_n} = \sqrt{3/2}\,\|\mathbf{s}_n\| \tag{3.4}$$

and

$$q^e = \sqrt{3/2}\sqrt{\mathbf{s}^e\cdot\mathbf{s}^e} = \sqrt{3/2}\,\|\mathbf{s}^e\| \tag{3.5}$$

If the trial stress violates the yield condition, elastic-plastic straining is accounted for, and the new stress state is calculated by including the plastic correction phase

$$\boldsymbol{\sigma}_{n+1} = \boldsymbol{\sigma}_n + \mathbf{D}\,(\Delta\boldsymbol{\varepsilon} - \Delta\mathbf{e}^p) = \boldsymbol{\sigma}^e - 2G\Delta\mathbf{e}^p \tag{3.6}$$

The final stress $\boldsymbol{\sigma}_{n+1}$ at pseudo-time t_{n+1} is split into hydrostatic and deviatoric parts

$$\boldsymbol{\sigma}_{n+1} = -p_{n+1}\mathbf{I} + \mathbf{s}_{n+1} \tag{3.7}$$

where p_{n+1} is the hydrostatic pressure and $\mathbf{s}_{n+1}$ is the deviatoric stress defined as:

$$p_{n+1} = -\frac{1}{3}(\mathbf{I}\cdot\boldsymbol{\sigma}_{n+1}) = p^e \tag{3.8}$$

$$\mathbf{s}_{n+1} = \mathbf{I}^{dev}\boldsymbol{\sigma}_{n+1} = \mathbf{s}^e - 2\mathrm{G}\Delta\mathbf{e}^p \tag{3.9}$$

Enforcing the consistency condition (2.47) at the end of the increment (t_{n+1}):

$$F(\boldsymbol{\sigma}_{n+1}, \Delta\varepsilon_q) = \frac{\sqrt{\mathbf{s}_{n+1} \cdot \mathbf{s}_{n+1}}}{2G} - \frac{\sqrt{2/3}\, k(\varepsilon_{q|n} + \Delta\varepsilon_q)}{2G} = \sqrt{2/3}\frac{q_{n+1} - k_{n+1}}{2G} = 0 \tag{3.10}$$

where $\Delta\varepsilon_q$ is the equivalent plastic strain increment. The corresponding plastic strain increment $\Delta\mathbf{e}^p$ is calculated using a backward-Euler integration of equation (2.43):

$$\Delta\mathbf{e}^p = \sqrt{3/2}\,\Delta\varepsilon_q\,\mathbf{n}_{n+1} + \frac{\|\Delta\mathbf{e}\|\sin\theta}{1 + \bar{h}_{n+1}/3G}\,\mathbf{m}_{n+1} \tag{3.11}$$

where the index $n+1$ was dropped for the direction angle $\theta = \theta_{n+1}$ for simplicity. The unit deviatoric tensor normal to the yield surface and the one tangential to it, in the direction of the strain increment, at the beginning and at the end of the increment (see Figure 3.1) are respectively defined as:

$$\mathbf{n}_n = \frac{\mathbf{s}_n}{\|\mathbf{s}_n\|}, \qquad \mathbf{m}_n = \frac{[\mathbf{I}^{dev} - \mathbf{n}_n \otimes \mathbf{n}_n]\,\Delta\mathbf{e}}{\|[\mathbf{I}^{dev} - \mathbf{n}_n \otimes \mathbf{n}_n]\,\Delta\mathbf{e}\,\|} \tag{3.12}$$

$$\mathbf{n}_{n+1} = \frac{\mathbf{s}_{n+1}}{\|\mathbf{s}_{n+1}\|}, \qquad \mathbf{m}_{n+1} = \frac{[\mathbf{I}^{dev} - \mathbf{n}_{n+1} \otimes \mathbf{n}_{n+1}]\,\Delta\mathbf{e}}{\|[\mathbf{I}^{dev} - \mathbf{n}_{n+1} \otimes \mathbf{n}_{n+1}]\,\Delta\mathbf{e}\,\|} \tag{3.13}$$

while the unknown tensors $\mathbf{n}_{n+1}$, $\mathbf{m}_{n+1}$ can be expressed in terms of $\mathbf{n}_n$, $\mathbf{m}_n$ using the following geometric relation identified by Simo (1987):

$$\mathbf{n}_{n+1} = \cos\zeta\,\mathbf{n}_n + \sin\zeta\,\mathbf{m}_n \tag{3.14}$$

$$\mathbf{m}_{n+1} = -\sin\zeta\,\mathbf{n}_n + \cos\zeta\,\mathbf{m}_n \tag{3.15}$$

In the above expression, the angle ζ is represented geometrically in Figure 3.1, together with angles ζ^*, ζ^e, θ, θ_n, θ^e, θ^p, that are formed by the key tensors and are involved in subsequent operations. Furthermore, geometry dictates:

$$\zeta = \zeta^e - \zeta^* \tag{3.16}$$

$$\theta = \theta_{n+1} = \theta^e + \zeta^* = \theta_n - \zeta \tag{3.17}$$

where

$$\cos\zeta^e = \frac{\mathbf{s}_n \cdot \mathbf{s}^e}{\|\mathbf{s}_n\|\|\mathbf{s}^e\|}, \qquad \cos\theta^e = \frac{\Delta\mathbf{e} \cdot \mathbf{s}^e}{\|\Delta\mathbf{e}\|\|\mathbf{s}^e\|} \tag{3.18}$$

Multiplying (3.9) by $\mathbf{n}_{n+1}$ and $\mathbf{m}_{n+1}$, the following relations are obtained:

$$q^e\cos\zeta^* = q_{n+1} + 3G\Delta\varepsilon_q \tag{3.19}$$

$$q^e \sin\zeta^* = \sqrt{2/3}\,\frac{3G\|\Delta\mathbf{e}\|\sin\theta}{1+\bar{h}_{n+1}/3G} \tag{3.20}$$

Equations (3.10), (3.17), (3.19), (3.20) constitute a system of 4 equations with 5 unknowns: q_{n+1}, $\Delta\varepsilon_q$, ζ^*, θ, and $\bar{h}_{n+1}$. The extra equation necessary for the solution is the definition of $\bar{h}$, which is different in each branch of the J2NA model. The solution procedure for the system is described in the next paragraphs for each branch. The implementation of the above formulation for an explicitly chosen function $\bar{h}(\varepsilon_q,\theta)$, which may mimic the behaviour of various models in the literature, is further considered in Appendix 1. An enhancement of this solution procedure for implementation in shell elements is presented in paragraph 3.3.

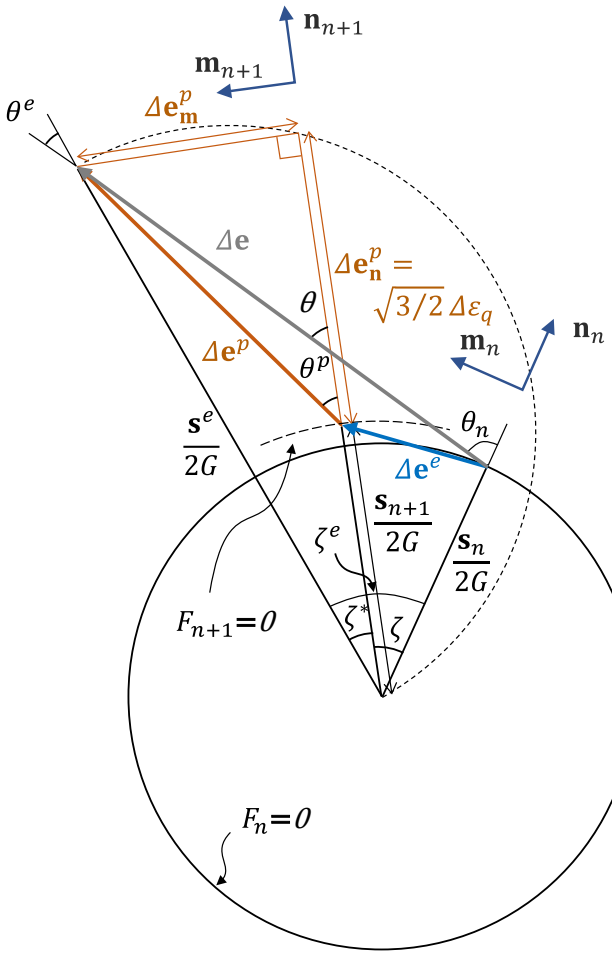

Figure 3.1: Geometric representation of the return mapping of a non-associative model

It should be noted that, at the beginning of the integration algorithm ($t = t_n$) the value of θ^p is unknown, and either branch of the model may be activated. In the proposed implementation, the first branch is assumed to be activated, and the respective plastic corrector is calculated. If the calculated plastic strain angle θ^p is smaller than the angle θ_c, the assumption was correct, and the integration procedure is complete. If not, the

solution is discarded, and the integration scheme of the second branch is used. A summary of this integration procedure is given in Table 3.1.

3.1.1 First branch of the model

In the first branch of the model, the parameter $\bar{h} = \bar{h}(\Delta\varepsilon_q)$, independent of angle θ, is defined as:

$$\bar{h}_{n+1} = k_{n+1}/\varepsilon_{q|n+1} \tag{3.21}$$

Thus, equation (3.20) together with (3.21) can be used to express $\zeta^*(\Delta\varepsilon_q)$ as a function of the equivalent plastic strain $\Delta\varepsilon_q$, as follows:

$$\tan\zeta^* - \frac{\sin\theta^e}{\frac{\|\mathbf{s}^e\|}{2G\|\Delta\mathbf{e}\|}\left[1+\frac{h_{n+1}}{3G}\right]-\cos\theta^e} = 0 \tag{3.22}$$

Treating $\Delta\varepsilon_q$ as the only primary unknown, equations (3.10) and (3.21) can be used to eliminate q_{n+1}, ζ^* from (3.20) resulting in a single scalar equation (3.23) of the equivalent plastic strain increment $F_{p1}(\Delta\varepsilon_q) = 0$, as in the case of J2FT.

$$F_{p1}(\Delta\varepsilon_q) = 1 + \left[\frac{\sin\theta^e}{\frac{\|\mathbf{s}^e\|}{2G\|\Delta\mathbf{e}\|}\left[1+\frac{h_{n+1}}{3G}\right]-\cos\theta^e}\right]^2 - \left[\frac{q^e}{k_{n+1}+3G\Delta\varepsilon_q}\right]^2 = 0 \tag{3.23}$$

The above equation (3.23) can be solved using a local Newton scheme and all necessary derivatives are provided in Appendix 1. When $\Delta\varepsilon_q$ is found, equations (3.21), (3.22), (3.16), (3.14) and (3.15) give respectively h_{n+1}, ζ^*, ζ, $\mathbf{n}_{n+1}$, and $\mathbf{m}_{n+1}$, and the plastic corrector is readily computed from (3.11). Next, it is checked whether the result of this branch satisfies the flow rule restriction $\theta^p_{br1} \leq \theta_c$, and the solution proceeds accordingly.

3.1.2 Second branch of the model

In cases where the first branch of the model leads to plastic strain increment angle θ^p_{br1} greater than the semi-angle θ_c of the simulated vertex ($\theta^p_{br1} > \theta_c$), the second branch is activated. In this case, the plastic strain increment is constrained to form an angle $\theta^p = \theta_c$ with the deviatoric stress in the converged state, so that:

$$\tan\theta^p = \frac{\mathbf{m}_{n+1}\cdot\Delta\mathbf{e}^p}{\mathbf{n}_{n+1}\cdot\Delta\mathbf{e}^p} = \tan\theta_c \tag{3.24}$$

Using (3.11), the above equation can be rewritten as

$$\frac{\|\Delta\mathbf{e}\|\sin\theta}{1+\frac{\bar{h}_{n+1}}{3G}} = \sqrt{3/2}\,\Delta\varepsilon_q \tan\theta_c \tag{3.25}$$

Substituting (3.25) into equation (3.20), the angle θ is eliminated and an explicit expression is found for $\zeta^*(\Delta\varepsilon_q)$:

$$\sin\zeta^* = \frac{\sqrt{3/2}\,\Delta\varepsilon_q \tan\theta_c}{\|\mathbf{s}^e\|/2G} = \frac{3G\Delta\varepsilon_q\,\tan\theta_c}{q^e} \tag{3.26}$$

Equation (3.26) may be used to eliminate ζ^* from (3.19), resulting in a scalar equation of the equivalent plastic strain increment $\Delta\varepsilon_q$:

$$F_{p2}(\Delta\varepsilon_q) = \left[\Delta\varepsilon_q + \frac{k_{n+1}(\Delta\varepsilon_q)}{3G}\right]^2 + \left[\Delta\varepsilon_q \tan\theta_c\right]^2 - \left(\frac{q^e}{3G}\right)^2 = 0 \tag{3.27}$$

which can be solved numerically. When the equivalent plastic strain increments $\Delta\varepsilon_q$ is calculated, equations (3.26), (3.16), (3.17), (3.14), (3.15) are used to calculate ζ^*, ζ, θ, $\mathbf{n}_{n+1}$, $\mathbf{m}_{n+1}$, respectively, and ultimately the plastic strain increment $\Delta\mathbf{e}^p$ and the new stress state $\boldsymbol{\sigma}_{n+1}$ are calculated using (3.11) and (3.6). Notably, in the presence of linear hardening, equation (3.27) reduces to a second-order polynomial of $\Delta\varepsilon_q$, which has a single positive solution given by (3.28), which coincides with the analytical solution obtained by Simo (1987), given below:

$$\Delta\varepsilon_q = \frac{q^e}{3G}\frac{1}{1+\frac{H}{3G}}\,\frac{\sqrt{1+a^2(1-r^2)}-r}{1+a^2} \tag{3.28}$$

with

$$a = \frac{\tan\theta_c}{1+H/3G} \tag{3.29}$$

$$r = \frac{k_n}{q^e} < 1.0 \tag{3.30}$$

In Figure 3.2 a qualitative comparison is made for the integration process using the classical J2FT and the J2NA model. For a given stress state $\mathbf{s}_n$ and non-proportional strain increment $\Delta\mathbf{e}$, when employing the J2FT the converged state corresponds to a greater rotation of the stress deviator and a larger expansion of the yield surface than when using the J2NA, which denote the comparatively less stiff behaviour of J2NA.

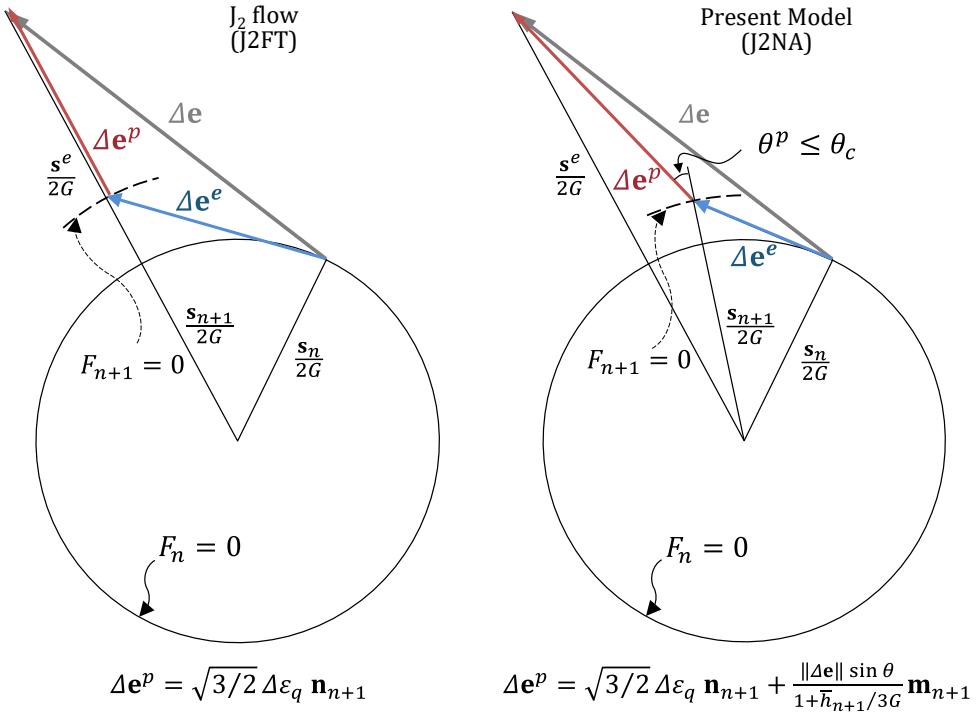

Figure 3.2: Comparison of the return mapping in J2FT and J2NA

Remark: In equation (3.25), the parameter $\bar{h}\left(\theta, \varepsilon_q, \|\Delta\mathbf{e}\|\right)$ is defined for the second branch of the model, by demanding $\theta^p = \theta_c$. This is not interchangeable with the form $\bar{h}\left(\theta, \varepsilon_q\right)$ given in Table 2.2, which refers only to infinitesimal strain increments (rate form), obtained by further demanding $\|\Delta\mathbf{e}\| \to 0^+$.

Nevertheless, it is possible to develop models which employ an explicit expression for the function $\bar{h}\left(\theta, \varepsilon_q\right)$, as in the case of by Pappa & Karamanos (2016). In these models the integration algorithm cannot be reduced to a single equation as above, in the general case. Instead, the system of equations (3.14), (3.15), (3.16), (3.17), (3.26) needs to be solved. However, using (3.10), (3.17), the unknowns q_{n+1} and θ can be eliminated from (3.19) and (3.20) resulting in a system of two equations with two unknowns ($\Delta\varepsilon_q$ and ζ^*) to be solved numerically:

$$F_{p\bar{h}}\left(\Delta\varepsilon_q, \zeta^*\right) = q^e \cos\zeta^* - \left[k_{n+1} + 3G\Delta\varepsilon_q\right] = 0 \tag{3.31}$$

$$L_{p\bar{h}}\left(\Delta\varepsilon_q, \zeta^*\right) = q^e \sin\zeta^* - \sqrt{2/3}\frac{3G\|\Delta\mathbf{e}\|\sin(\theta^e + \zeta^*)}{1 + \bar{h}_{n+1}/3G} = 0 \tag{3.32}$$

with

$$\bar{h}_{n+1} = \bar{h}\left(\Delta\varepsilon_q, \theta = \theta^e + \zeta^*\right) \tag{3.33}$$

Table 3.1: Integration algorithm for three-dimensional element analysis

1. Compute trial elastic stress (elastic prediction)

$$\boldsymbol{\sigma}^e = \boldsymbol{\sigma}_n + \mathbf{D}\Delta\boldsymbol{\varepsilon} \quad , \qquad \mathbf{s}^e = \mathbf{I}^{dev}\boldsymbol{\sigma}^e \quad , \qquad p^e = -1/3\,(\mathbf{I}\cdot\boldsymbol{\sigma}^e)$$

$$q^e = \sqrt{3/2}\,\|\mathbf{s}^e\|\,, \qquad k_n = k\big(\varepsilon_{q|n}\big), \qquad F_{n+1}^{trial} = \frac{1}{2G}\Big[\|\mathbf{s}^e\| - \sqrt{2/3}\,k_n\Big]$$

2. IF $F_{n+1}^{trial} \le 0$ THEN

$$\Delta\mathbf{e}^p = \mathbf{0} \qquad , \qquad \Delta\varepsilon_q = 0$$

ELSE ($F_{n+1}^{trial} > 0$)

$$\mathbf{n}_n = \frac{\mathbf{s}_n}{\|\mathbf{s}_n\|} \qquad , \qquad \mathbf{m}_n = \frac{[\mathbf{I}^{dev} - \mathbf{n}_n \otimes \mathbf{n}_n]\,\Delta\mathbf{e}}{\|[\mathbf{I}^{dev} - \mathbf{n}_n \otimes \mathbf{n}_n]\,\Delta\mathbf{e}\,\|}$$

$$\cos\theta_n = \frac{\mathbf{n}_n \cdot \Delta\mathbf{e}}{\|\Delta\mathbf{e}\|}, \qquad \cos\theta^e = \frac{\Delta\mathbf{e}\cdot\,\mathbf{s}^e}{\|\Delta\mathbf{e}\|\|\mathbf{s}^e\|}, \qquad \cos\zeta^e = \frac{\mathbf{s}_n\cdot\,\mathbf{s}^e}{\|\mathbf{s}_n\|\|\mathbf{s}^e\|}$$

(2a) Assume 1st branch is activated

To calculate $\Delta\varepsilon_q$ solve:

$$F_{p1}\big(\Delta\varepsilon_q\big) = 1 + \tan^2\zeta^* - \left[\frac{q^e}{k_{n+1} + 3G\Delta\varepsilon_q}\right]^2$$

with

$$\zeta^*(\Delta\varepsilon_q) = \tan^{-1}\left[\frac{\sin\theta^e}{\frac{\|\mathbf{s}^e\|}{2G\|\Delta\mathbf{e}\|}\left[1 + \frac{h_{n+1}}{3G}\right] - \cos\theta^e}\right]$$

Compute:

$$\bar{h}_{n+1} = h_{n+1} \quad , \qquad \theta = \theta^e + \zeta^*$$

$$\theta^p = \tan^{-1}\left[\frac{\frac{\|\Delta\mathbf{e}\|\sin\theta}{1 + \bar{h}_{n+1}/3G}}{\sqrt{3/2}\,\Delta\varepsilon_q}\right]$$

(2b) If $\theta^p > \theta_c$: the second branch is activated

To calculate $\Delta\varepsilon_q$ solve:

$$F_{p2}\big(\Delta\varepsilon_q\big) = \left[\Delta\varepsilon_q + \frac{k_{n+1}\big(\Delta\varepsilon_q\big)}{3G}\right]^2 + \big[\Delta\varepsilon_q \tan\theta_c\big]^2 - \left(\frac{q^e}{3G}\right)^2 = 0$$

Compute:

$$\zeta^*\big(\Delta\varepsilon_q\big) = \sin^{-1}\left[\frac{3G\Delta\varepsilon_q\,\tan\theta_c}{q^e}\right], \qquad \theta = \theta^e + \zeta^*, \qquad \theta^p = \theta_c$$

$$\bar{h}_{n+1} = 3G\left(\frac{\|\Delta\mathbf{e}\|\sin\theta}{\sqrt{3/2}\,\Delta\varepsilon_q\tan\theta_c} - 1\right)$$

(2c) Calculate the plastic strain increment

$$\zeta = \zeta^e - \zeta^*$$

$$\mathbf{n}_{n+1} = \quad \cos\zeta\,\mathbf{n}_n + \sin\zeta\,\mathbf{m}_n, \qquad \mathbf{m}_{n+1} = -\sin\zeta\,\mathbf{n}_n + \cos\zeta\,\mathbf{m}_n$$

$$\Delta\mathbf{e}^p = \sqrt{3/2}\,\Delta\varepsilon_q\,\mathbf{n}_{n+1} + \frac{\|\Delta\mathbf{e}\|\sin\theta}{1 + \bar{h}_{n+1}/3G}\mathbf{m}_{n+1}$$

3. Update stress tensor and state variables

$$\boldsymbol{\sigma}_{n+1} = \boldsymbol{\sigma}^e - 2G\Delta\mathbf{e}^p$$

$$\varepsilon_{q|n+1} = \varepsilon_{q|n} + \Delta\varepsilon_q$$

3.2 Consistent algorithmic moduli

To preserve Newton's quadratic rate of convergence in finite element codes, material stiffness operators that are consistent with the developed integration scheme must be implemented for the constitutive models. In this paragraph, the basis for obtaining the consistent algorithmic moduli is presented for the chosen radial return integration scheme, based on the procedure proposed by (Simo & Taylor, 1985), enhanced to account for the particular characteristics of models incorporating strain angle dependent behaviours.

The consistent (algorithmic) material stiffness moduli, are computed from the following fundamental equation:

$$\mathbf{D}_{ep}^{c} = \frac{\partial \boldsymbol{\sigma}_{n+1}}{\partial \boldsymbol{\varepsilon}_{n+1}} \tag{3.34}$$

In the context of pressure-independent metal plasticity, it is convenient to isolate the volumetric and the deviatoric part of stress and strain and treat them separately:

$$\mathbf{D}_{ep}^{c} = 3K\,\mathbf{I}^{vol} + \frac{\partial \mathbf{s}_{n+1}}{\partial \mathbf{e}_{n+1}} \tag{3.35}$$

The fourth-order tensor $\partial \mathbf{s}_{n+1}/\partial \mathbf{e}_{n+1}$ is obtained for each model branch, by expressing the differential of the stress deviator as a function of the differential of the strain increment:

$$d\mathbf{s}_{n+1} = \frac{\partial \mathbf{s}_{n+1}}{\partial \mathbf{e}_{n+1}} d\Delta\mathbf{e} \tag{3.36}$$

The stress deviator at the converged state is expressed as follows:

$$\begin{aligned} \mathbf{s}_{n+1} &= \mathbf{s}_{n+1}\left(\Delta\varepsilon_q, \zeta^*, \Delta\mathbf{e}\right) = \sqrt{2/3}\, k_{n+1}\mathbf{n}_{n+1} \\ &= \sqrt{2/3}\, k_{n+1}[\cos(\zeta^e - \zeta^*)\,\mathbf{n}_n + \sin(\zeta^e - \zeta^*)\,\mathbf{m}_n] \end{aligned} \tag{3.37}$$

Therefore, differentiating using the chain rule, one obtains:

$$d\mathbf{s}_{n+1} = \mathbf{s}_{n+1,\Delta\varepsilon_q} d\Delta\varepsilon_q + \mathbf{s}_{n+1,\zeta^*} d\zeta^* + \mathbf{s}_{n+1,\Delta\mathbf{e}} d\Delta\mathbf{e} \tag{3.38}$$

where a comma followed by a variable implies partial derivative with respect to that variable, e.g., $\mathbf{s}_{n+1,\Delta\varepsilon_q} = \partial \mathbf{s}_{n+1}/\partial\Delta\varepsilon_q$. Variables $\Delta\varepsilon_q$ and ζ^* are expressed differently for each model branch, but in all cases are calculated for a given strain increment ($\Delta\mathbf{e}$) by solving the system of equations $F_1,\ F_2$:

$$F_1\left(\Delta\varepsilon_q, \zeta^*, \Delta\mathbf{e}\right) = 0 \tag{3.39}$$

$$F_2\left(\Delta\varepsilon_q, \zeta^*, \Delta\mathbf{e}\right) = 0 \tag{3.40}$$

The functions F_1, F_2 are given in Table 3.2 for the two branches of the model. The dependence of the internal variables $d\Delta\varepsilon_q, d\zeta^*$ in (3.38) on the strain increment in the converged state can be found by linearizing functions $F_1$and F_2, as follows.

$$\begin{bmatrix} dF_1 \\ dF_2 \end{bmatrix} = \begin{bmatrix} 0 \\ 0 \end{bmatrix} \tag{3.41}$$

This is equivalent to

$$\begin{bmatrix} F_{1,\Delta\varepsilon_q} & F_{1,\zeta^*} \\ F_{2,\Delta\varepsilon_q} & F_{2,\zeta^*} \end{bmatrix} \begin{bmatrix} d\Delta\varepsilon_q \\ d\zeta^* \end{bmatrix} + \begin{bmatrix} F_{1,\Delta\mathbf{e}} \\ F_{2,\Delta\mathbf{e}} \end{bmatrix} d\Delta\mathbf{e} = \begin{bmatrix} 0 \\ 0 \end{bmatrix} \tag{3.42}$$

so that

$$\begin{bmatrix} d\Delta\varepsilon_q \\ d\zeta^* \end{bmatrix} = \begin{bmatrix} \Delta\varepsilon_{q\,,\Delta\mathbf{e}} \\ \zeta^*{}_{,\Delta\mathbf{e}} \end{bmatrix} d\Delta\mathbf{e} \tag{3.43}$$

where

$$\begin{bmatrix} \Delta\varepsilon_{q\,,\Delta\mathbf{e}} \\ \zeta^*{}_{,\Delta\mathbf{e}} \end{bmatrix} = -\begin{bmatrix} F_{1,\Delta\varepsilon_q} & F_{1,\zeta^*} \\ F_{2,\Delta\varepsilon_q} & F_{2,\zeta^*} \end{bmatrix}^{-1} \begin{bmatrix} F_{1,\Delta\mathbf{e}} \\ F_{2,\Delta\mathbf{e}} \end{bmatrix} \tag{3.44}$$

Expressions for all the above derivatives are provided in Appendix 1. Ultimately, equation (3.38) may be rewritten as:

$$d\mathbf{s}_{n+1} = \left[\mathbf{s}_{n+1,\Delta\varepsilon_q} \otimes \Delta\varepsilon_{q,\Delta\mathbf{e}} + \mathbf{s}_{n+1,\zeta^*} \otimes \zeta^*{}_{,\Delta\mathbf{e}} + \mathbf{s}_{n+1,\Delta\mathbf{e}}\right] d\Delta\mathbf{e} \tag{3.45}$$

and therefore

$$\frac{\partial\mathbf{s}_{n+1}}{\partial\mathbf{e}_{n+1}} = \mathbf{s}_{n+1,\Delta\varepsilon_q} \otimes \Delta\varepsilon_{q,\Delta\mathbf{e}} + \mathbf{s}_{n+1,\zeta^*} \otimes \zeta^*{}_{,\Delta\mathbf{e}} + \mathbf{s}_{n+1,\Delta\mathbf{e}} \tag{3.46}$$

The tensor $\partial\mathbf{s}_{n+1}/\partial\mathbf{e}_{n+1}$may be expressed in terms of $\mathbf{n}_{n+1}, \mathbf{m}_{n+1}$ as follows:

$$\begin{aligned} \frac{\partial\mathbf{s}_{n+1}}{\partial\mathbf{e}_{n+1}} = D^{dev}\mathbf{I}^{dev} + D^{nn}\left(\mathbf{n}_{n+1} \otimes \mathbf{n}_{n+1}\right) + D^{nm}\left(\mathbf{n}_{n+1} \otimes \mathbf{m}_{n+1}\right) \\ + D^{mn}\left(\mathbf{m}_{n+1} \otimes \mathbf{n}_{n+1}\right) + D^{mm}\left(\mathbf{m}_{n+1} \otimes \mathbf{m}_{n+1}\right) \end{aligned} \tag{3.47}$$

where

$$D^{dev} = \sqrt{2/3}\, k_{n+1} \frac{\sin\zeta}{\|\Delta\mathbf{e}\| \sin\theta_n} \tag{3.48}$$

and

$$\begin{bmatrix} D^{nn} & D^{nm} \\ D^{mn} & D^{mm} \end{bmatrix} = \begin{bmatrix} A_{nn} & A_{nm} \\ A_{mn} & A_{mm} \end{bmatrix} - \begin{bmatrix} \mathbf{s}^{\mathbf{n}}_{n+1,\Delta\varepsilon_q} & \mathbf{s}^{\mathbf{n}}_{n+1,\zeta^*} \\ \mathbf{s}^{\mathbf{m}}_{n+1,\Delta\varepsilon_q} & \mathbf{s}^{\mathbf{m}}_{n+1,\zeta^*} \end{bmatrix} \begin{bmatrix} F_{1,\Delta\varepsilon_q} & F_{1,\zeta^*} \\ F_{2,\Delta\varepsilon_q} & F_{2,\zeta^*} \end{bmatrix}^{-1} \begin{bmatrix} F^{\mathbf{n}}_{1,\Delta\mathbf{e}} & F^{\mathbf{m}}_{1,\Delta\mathbf{e}} \\ F^{\mathbf{n}}_{2,\Delta\mathbf{e}} & F^{\mathbf{m}}_{2,\Delta\mathbf{e}} \end{bmatrix} \tag{3.49}$$

In the above expression $\mathbf{X^n} = \mathbf{n}_{n+1} \cdot \mathbf{X}$, and $\mathbf{X^m} = \mathbf{m}_{n+1} \cdot \mathbf{X}$, are the components in the directions of tensors $\mathbf{n}_{n+1}$ and $\mathbf{m}_{n+1}$ respectively of a tensor $\mathbf{X}$ which belongs on the $(\mathbf{n}, \mathbf{m})$ hyperplane, hence:

$$\begin{bmatrix} \mathbf{s}^{\mathbf{n}}_{n+1,\Delta\varepsilon_q} & \mathbf{s}^{\mathbf{n}}_{n+1,\zeta^*} \\ \mathbf{s}^{\mathbf{m}}_{n+1,\Delta\varepsilon_q} & \mathbf{s}^{\mathbf{m}}_{n+1,\zeta^*} \end{bmatrix} = \sqrt{2/3}\, k_{n+1} \begin{bmatrix} H_{n+1}/k_{n+1} & 0 \\ 0 & -1 \end{bmatrix} \tag{3.50}$$

and

$$\begin{bmatrix} A_{nn} & A_{nm} \\ A_{mn} & A_{mm} \end{bmatrix} = D^{dev} \begin{bmatrix} -1 & 0 \\ -B\sin\zeta^* & -1 + B\cos\zeta^* \end{bmatrix}, \quad B = \frac{2G\|\Delta\mathbf{e}\|\sin\theta_n}{\|\mathbf{s}^e\|\sin\zeta} \tag{3.51}$$

The above linearized moduli are non-symmetric, as the multipliers D^{mn} and D^{nm} of the non-symmetric terms $\mathbf{m}_{n+1} \otimes \mathbf{n}_{n+1}$ and $\mathbf{n}_{n+1} \otimes \mathbf{m}_{n+1}$ respectively, are not equal. Thus, $D^c_{ep(ijkl)} \neq D^c_{ep(klij)}$, while the symmetries $D^c_{ep(ijkl)} = D^c_{ep(ijlk)} = D^c_{ep(jikl)} = D^c_{ep(jilk)}$ are preserved. In the limit $\|\Delta\mathbf{e}\| \to 0$, the linearized moduli reduce to the material tangent moduli.

Table 3.2: Functions necessary to define internal variables $\Delta\varepsilon_q, \zeta^*$

model / branch	$F_1 = 0$	$F_2 = 0$
1st branch - $\bar{h} = k(\varepsilon_q)/\varepsilon_q$	Eq. (3.23)	Eq. (3.22)
2nd branch - $\theta^p = \theta_c$	Eq. (3.27)	Eq. (3.26)
Explicit choice: $\bar{h} = \bar{h}(\theta, \Delta\varepsilon_q)$	Eq. (3.32)	Eq. (3.31)

3.3 Algorithm for shell element analysis

In shell element analysis, for a given strain increment $\Delta\bar{\boldsymbol{\varepsilon}}$ (which has no $\Delta\varepsilon_{33}$ component), the stress at the converged state $\bar{\boldsymbol{\sigma}}_{n+1}$ (which has no $\bar{\sigma}_{n+1(33)}$ component) must be calculated, accounting for the traction component perpendicular to the shell laminae (assumed to be direction 3 in Figure 3.3) to be zero throughout the analysis:

$$\sigma_{n+1(33)} = 0 \tag{3.52}$$

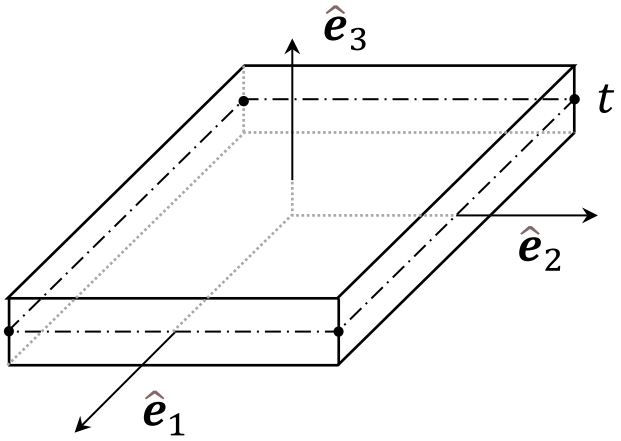

Figure 3.3: Representation of a shell element and the direction perpendicular to its laminae

The constraint (3.52), is used to calculate the unknown component of the strain increment perpendicular to the shell laminae $\Delta\varepsilon_{33}$. The total strain increment $\Delta\boldsymbol{\varepsilon}$, is decomposed as follows:

$$\Delta\boldsymbol{\varepsilon} = \Delta\bar{\boldsymbol{\varepsilon}} + \Delta\varepsilon_{33}\mathbf{a} \tag{3.53}$$

where $\mathbf{a} = \hat{\boldsymbol{e}}_3 \otimes \hat{\boldsymbol{e}}_3$. Enforcing (3.52), at the end of the strain increment, one obtains:

$$\mathbf{a} \cdot \mathbf{s}_{n+1} - p_{n+1}\mathbf{a} \cdot \mathbf{I} = 0 \tag{3.54}$$

Herein, (3.54) is updated using (3.37):

$$F_{shell}\left(\Delta\varepsilon_q, \zeta^*, \Delta\varepsilon_{33}\right) = \sqrt{2/3}\, k_{n+1}\left[\cos(\zeta^e - \zeta^*)\, n_{n(33)} + \sin(\zeta^e - \zeta^*)\, m_{n(33)}\right] - p_{n+1} = 0 \tag{3.55}$$

The internal variables $\left(\Delta\varepsilon_q, \zeta^*, \Delta\varepsilon_{33}\right)$ are computed by solving the system of three equations (3.39), (3.40), (3.55) (defined in Table 3.2 depending on the model branch). This system can be reduced to a 2x2 system since for either model branch, equation (3.40) can easily be rewritten as an analytic expression $\zeta^*\left(\Delta\varepsilon_q, \Delta\varepsilon_{33}\right)$ and used for eliminating ζ^* from the remaining two equations. This results in a system of nonlinear equations $\hat{F}_1\left(\Delta\varepsilon_q, \Delta\varepsilon_{33}\right) = 0$ and $\hat{F}_{shell}\left(\Delta\varepsilon_q, \Delta\varepsilon_{33}\right) = 0$. More details on the solution of this system are given in Table 3.3.

The above formulation can be easily adjusted to account for plane stress conditions by additionally demanding zero out-of-plane shear stresses ($\sigma_{13} = \sigma_{23} = 0$), which directly translates to $\Delta\varepsilon_{13} = \Delta\varepsilon_{23} = 0$. Under plane stress conditions, the above algorithm is directly applicable.

Table 3.3: Integration algorithm for shell element analysis – $\sigma_{33} = 0$

1. Compute trial elastic stress (elastic prediction)

$$\boldsymbol{\sigma}^e = \boldsymbol{\sigma}_n + \mathbf{D}_{con}\Delta\bar{\boldsymbol{\varepsilon}}, \qquad \mathbf{s}^e = \mathbf{I}^{dev}\boldsymbol{\sigma}^e \ , \qquad p^e = -1/3\,(\mathbf{I}\cdot\boldsymbol{\sigma}^e)$$

$$q^e = \sqrt{3/2}\,\|\mathbf{s}^e\| \ , \qquad k_n = k\left(\varepsilon_{q|n}\right), \qquad F_{n+1}^{trial} = \frac{1}{2G}\left[\|\mathbf{s}^e\| - \sqrt{2/3}\,k_n\right]$$

2. IF $F_{n+1}^{trial} \le 0$ THEN

$$\Delta\mathbf{e}^p = \mathbf{0} \qquad , \qquad \Delta\varepsilon_q = 0$$

ELSE $(F_{n+1}^{trial} > 0)$

$$\mathbf{n}_n = \mathbf{s}_n/\|\mathbf{s}_n\|$$

(2a) Assume 1st branch is activated

Find $\Delta\varepsilon_q, \Delta\varepsilon_{33}$, solving the following 2x2 system (details in Table 10.1):

$$\hat{F}_1\left(\Delta\varepsilon_q, \Delta\varepsilon_{33}\right) = F_{p1}\left(\Delta\varepsilon_q, \zeta^*\left(\Delta\varepsilon_q, \Delta\varepsilon_{33}\right), \Delta\varepsilon_{33}\right) = 0$$

$$\hat{F}_{shell}\left(\Delta\varepsilon_q, \Delta\varepsilon_{33}\right) = F_{shell}\left(\Delta\varepsilon_q, \zeta^*\left(\Delta\varepsilon_q, \Delta\varepsilon_{33}\right), \Delta\varepsilon_{33}\right) = 0$$

with

$$\tan\zeta^* = \frac{\sin\theta^e}{\frac{\|\mathbf{s}^e\|}{2G\|\Delta\mathbf{e}\|}\left[1 + \frac{h_{n+1}}{3G}\right] - \cos\theta^e}$$

Calculate:

$$\Delta\boldsymbol{\varepsilon} = \Delta\bar{\boldsymbol{\varepsilon}} + \Delta\varepsilon_{33}\mathbf{a}, \qquad \boldsymbol{\sigma}^e = \boldsymbol{\sigma}_n + \mathbf{D}\Delta\boldsymbol{\varepsilon}, \qquad \mathbf{s}^e = \mathbf{I}^{dev}\boldsymbol{\sigma}^e = \mathbf{s}_n + 2G\Delta\mathbf{e}$$

$$\cos\theta^e = \frac{\Delta\mathbf{e}\cdot\mathbf{s}^e}{\|\Delta\mathbf{e}\|\|\mathbf{s}^e\|}, \qquad \bar{h}_{n+1} = h_{n+1}, \qquad \theta = \theta^e + \zeta^*$$

$$\tan\theta^p = \frac{\|\Delta\mathbf{e}\|\sin\theta}{1 + \bar{h}_{n+1}/3G}\Big/\left(\sqrt{3/2}\,\Delta\varepsilon_q\right)$$

(2b) If $\theta^p > \theta_c$: the second branch is activated

Find $\Delta\varepsilon_q, \Delta\varepsilon_{33}$, solving the following 2x2 system (details in Table 10.1):

$$\hat{F}_1\left(\Delta\varepsilon_q, \Delta\varepsilon_{33}\right) = F_{p2}\left(\Delta\varepsilon_q, \zeta^*\left(\Delta\varepsilon_q, \Delta\varepsilon_{33}\right), \Delta\varepsilon_{33}\right) = 0$$

$$\hat{F}_{shell}\left(\Delta\varepsilon_q, \Delta\varepsilon_{33}\right) = F_{shell}\left(\Delta\varepsilon_q, \zeta^*\left(\Delta\varepsilon_q, \Delta\varepsilon_{33}\right), \Delta\varepsilon_{33}\right) = 0$$

with

$$\zeta^*\left(\Delta\varepsilon_q\right) = \sin^{-1}\left[\frac{3G\Delta\varepsilon_q\,\tan\theta_c}{q^e}\right]$$

Calculate:

$$\Delta\boldsymbol{\varepsilon} = \Delta\bar{\boldsymbol{\varepsilon}} + \Delta\varepsilon_{33}\mathbf{a}, \qquad \boldsymbol{\sigma}^e = \boldsymbol{\sigma}_n + \mathbf{D}\Delta\boldsymbol{\varepsilon}, \qquad \mathbf{s}^e = \mathbf{I}^{dev}\boldsymbol{\sigma}^e = \mathbf{s}_n + 2G\Delta\mathbf{e}$$

$$\cos\theta^e = \frac{\Delta\mathbf{e}\cdot\mathbf{s}^e}{\|\Delta\mathbf{e}\|\|\mathbf{s}^e\|}, \quad \theta = \theta^e + \zeta^*\left(\Delta\varepsilon_q, \Delta\mathbf{e}(\Delta\varepsilon_{33})\right)$$

$$\bar{h}_{n+1} = 3G\left(\frac{\|\Delta\mathbf{e}\|\sin\theta}{\sqrt{3/2}\,\Delta\varepsilon_q\tan\theta_c} - 1\right)$$

(2c) Calculate the plastic strain increment

$$\mathbf{m}_n = \frac{[\mathbf{I}^{dev} - \mathbf{n}_n\otimes\mathbf{n}_n]\,\Delta\mathbf{e}}{\|[\mathbf{I}^{dev} - \mathbf{n}_n\otimes\mathbf{n}_n]\,\Delta\mathbf{e}\,\|}, \qquad \cos\zeta^e = \frac{\mathbf{s}_n\cdot\mathbf{s}^e}{\|\mathbf{s}_n\|\|\mathbf{s}^e\|}, \qquad \zeta = \zeta^e - \zeta^*$$

$$\mathbf{n}_{n+1} = \cos\zeta\,\mathbf{n}_n + \sin\zeta\,\mathbf{m}_n, \qquad \mathbf{m}_{n+1} = -\sin\zeta\,\mathbf{n}_n + \cos\zeta\,\mathbf{m}_n$$

$$\Delta\mathbf{e}^p = \sqrt{3/2}\,\Delta\varepsilon_q\,\mathbf{n}_{n+1} + \frac{\|\Delta\mathbf{e}\|\sin\theta}{1 + \bar{h}_{n+1}/3G}\,\mathbf{m}_{n+1}$$

3. Update stress tensor and state variables:

$$\boldsymbol{\sigma}_{n+1} = \boldsymbol{\sigma}^e - 2G\Delta\mathbf{e}^p \qquad \textbf{Note:} \text{ at this stage it is } \sigma_{n+1(33)} = 0$$

$$\varepsilon_{q|n+1} = \varepsilon_{q|n} + \Delta\varepsilon_q$$

3.3.1 Consistent moduli for shell element analysis

For shells, an equivalent three-dimensional integration scheme was presented above which accounts for the constraint (3.52) to calculate the dependent strain increment component $\Delta\varepsilon_{33}(\Delta\bar{\boldsymbol{\varepsilon}})$. It follows that the total strain increment is readily available after the integration, and the consistent moduli $D^{c}_{ep|\kappa\lambda\mu\nu}$ for an equivalent 'brick' element can be found as in paragraph 3.2, disregarding the dependence $\Delta\varepsilon_{33}(\Delta\bar{\boldsymbol{\varepsilon}})$. For shell elements this dependence needs to be reintroduced in the algorithmic moduli, and the know stress component σ_{33} needs to be eliminated by static condensation. The shell algorithmic moduli are expressed as:

$$\mathbf{D}^{c,shell}_{ep} = \frac{d\bar{\boldsymbol{\sigma}}}{d\bar{\boldsymbol{\varepsilon}}} = \frac{\partial\bar{\boldsymbol{\sigma}}}{\partial\bar{\boldsymbol{\varepsilon}}} + \frac{\partial\bar{\boldsymbol{\sigma}}}{\partial\Delta\varepsilon_{33}}\frac{\partial\Delta\varepsilon_{33}}{\partial\bar{\boldsymbol{\varepsilon}}} \tag{3.56}$$

The derivative $\partial\Delta\varepsilon_{33}/\partial\bar{\boldsymbol{\varepsilon}}$ is obtained by demanding the differential of constraint (3.52) to be zero:

$$d\Delta\varepsilon_{33} = -\frac{\partial\sigma_{n+1(33)}/\partial\bar{\boldsymbol{\varepsilon}}}{\partial\sigma_{n+1(33)}/\partial\Delta\varepsilon_{33}}d\bar{\boldsymbol{\varepsilon}} \tag{3.57}$$

and finally, the condensed material moduli, employed in shell analyses can be calculated as:

$$D^{c.shell}_{ep}\big|_{\kappa\lambda\mu\nu} = D^{c}_{ep}{}_{\kappa\lambda\mu\nu} - \frac{D^{c}_{ep}{}_{\kappa\lambda 33}D^{c}_{ep}{}_{33\mu\nu}}{D^{c}_{ep}{}_{3333}} \tag{3.58}$$

where $\kappa,\lambda,\mu,\nu = 1,2,3$ but not $\kappa=\lambda=3$ or $\mu=\nu=3$. In equation (3.58), one should note that $D^{c}_{ep|\kappa\lambda\mu\nu} \neq D^{c}_{ep|\mu\nu\kappa\lambda}$ so that the algorithmic moduli for shells are non-symmetric. For plane stress elements the rigidity moduli can be expressed by (3.58), with $\kappa,\lambda,\mu,\nu = 1,2$, and they are also non-symmetric.

3.4 Theoretical testing of the model properties

In this paragraph, using benchmark tools from the literature, key features of the behaviour and properties of the developed non-associative constitutive model are illustrated.

3.4.1 Behaviour under non-proportional strain paths

Various loading scenarios are employed to demonstrate the behaviour of the J2NA model juxtaposed with the results adopting J2FT, J2DT and the model by Simo (1987). The three-dimensional element formulation is presented first, demonstrating the more compliant behaviour of the non-associative models with respect to J2FT and their relation with J2DT, depending on the strain angle θ. The J2NA model exhibits a somewhat stiffer response than Simo's model when the strain angle is small enough ($\theta \leq \theta_c$), while the two models have the same behaviour in load strain histories where $\theta > \theta_c$, shown in Figure 3.5. A further demonstration of the two models is offered for plane stress conditions (Figure 3.6), which exhibit behaviours akin to their three-dimensional counterparts.

3.4.1.1 Three-dimensional formulation

To illustrate the behaviour of the models, the loading scenarios introduced by Hughes and Shakib (1987) and further used by Simo (1987) are adopted. A one-parametric family of non-proportional deviatoric strain paths is considered, expressed analytically by eq. (3.59). The strain paths consist of a preloading proportional branch, followed by a non-proportional one, forming an angle ψ with the preloading path (Figure 3.4).

$$\mathbf{e}(t) = \mathbf{e}_0 t + (\mathbf{e}_1 - \mathbf{e}_0)\langle t-1\rangle, \quad t \in [0,2] \tag{3.59}$$

In the above $\langle \cdot \rangle = \max\{(\cdot), 0\}$ is the Macaulay bracket and $\mathbf{e}_0, \mathbf{e}_1$ are expressed as:

$$\mathbf{e}_0 = \bar{\varepsilon}\begin{bmatrix} -1/2 & 0 & 0 \\ 0 & -1/2 & 0 \\ 0 & 0 & 1 \end{bmatrix} \tag{3.60}$$

$$\mathbf{e}_1 = \bar{\varepsilon}\begin{bmatrix} -1/2\cos\psi & 0 & 0 \\ 0 & -1/2\cos\psi & \sqrt{3}/2\sin\psi \\ 0 & \sqrt{3}/2\sin\psi & \cos\psi \end{bmatrix} \tag{3.61}$$

With $\bar{\varepsilon} = 7.5 \times 10^{-3}$, and four significant non-proportionality cases are displayed:

$$\psi = \pi/8\,, 2\pi/8\,, 3\pi/8\,, 4\pi/8 \;\text{ or }\; 22.5°, 45.0°, 67.5°, 90.0° \tag{3.62}$$

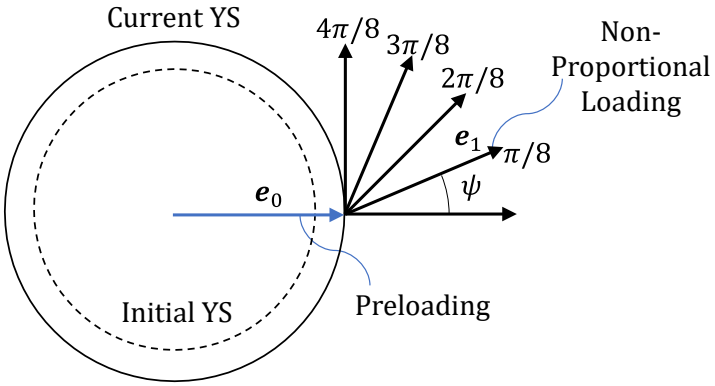

Figure 3.4: Schematic representation of the one-parameter, non-proportional deviatoric strain path family considered

A material with linear hardening and the material properties in Table 3.4 are adopted, to allow for comparisons to previous works, in conjunction with four cases for the angle parameter:

$$\theta_c = 0,\ \pi/12\,, 2\pi/12\,, 3\pi/12\,, 4\pi/12 \ \text{ or } \ 0°, 15°, 30°, 45°, 60° \tag{3.63}$$

Table 3.4: Material properties

Young's Modulus	$E(ksi)$	10.5×10^3
Shear Modulus	$G(ksi)$	3.95×10^3
Plastic Modulus/Hardening	$H(ksi)$	10^3
Yield stress	$\sigma_y(ksi)$	33.65

The numerical calculations were performed with pseudo-time increment $\Delta t = 0.01$ and the plotted results refer to the second phase of the deformation (non-proportional phase), summarized in Table 3.5

Table 3.5: Notation of the plotted results

$e(t) = \|\mathbf{e}_1\|\,\langle t-1\rangle$
$= \sqrt{3/2}\,\bar{\varepsilon}\,\langle t-1\rangle$
$\sigma(t) = \sigma_{33}(t)$
$\bar{\varepsilon}^{pl}(t) = e^p_{33}(t) - e^p_{33}(1)$
$\tau(t) = \sigma_{23}(t)$
$\gamma^{pl}(t) = 2e^p_{23}(t)$

In Figure 3.5, the stress and plastic strain evolution is given for the selected strain path family for discrete angles ψ, employing J2NA, and the model Simo (1987), accounting for several values for the angle parameter θ_c. The material responses employing J2FT and J2DT under these strain paths are also included, to facilitate comparisons.

Under non-proportional straining, the stress tensor rotates towards the direction of the non-proportionality, and the angle (θ) it forms with the successive strain increments

gradually decreases, irrespective of the material model. It follows that if non-proportionality angle $\psi < \theta_c$, in the non-associative models considered, only one branch is activated, leading to a behaviour unaffected by parameter θ_c. For such combinations ($\theta_c > \psi$), a single line is offered in the following figures for each of the models. In these cases, the behaviours of the J2DT and the J2NA are very similar, somewhat stiffer than the model by Simo, and less stiff that the J2FT.

Comparably, in cases that $\psi \gg \theta_c$, it is possible that throughout the analysis $\theta_c < \theta$, so that only the second branch of the J2NA model is activated. In such cases, the J2NA and Simo's model has the same response for given values θ_c, which is stiffer than the J2DT, and less stiff than the J2FT.

In a final case, $\psi > \theta_c$ only for part of the deformation history. Hence, the second model branch is activated initially, producing similar behaviours for the two non-associative models. However, angle θ decreases with deformation and $\theta \leq \theta_c$ develops onward, activating the first branch of each model, hence differentiating their responses. Such points are clearly identifiable in Figures 3.5 , 3.6 .

3.4.1.2 Plane Stress

For plane stress a one-parameter strain path expressed by (3.59) is also used, with

$$\mathbf{e}_0 = \bar{\varepsilon}\begin{bmatrix} 1 & 0 \\ 0 & 0 \end{bmatrix} \tag{3.64}$$

$$\mathbf{e}_1 = \bar{\varepsilon}\begin{bmatrix} \cos\psi & \sqrt{3}/2\sin\psi \\ \sqrt{3}/2\sin\psi & 0 \end{bmatrix} \tag{3.65}$$

This strain path is not deviatoric, as in the three-dimensional case, but it represents the tension and torsion of a tube who is fixed in the radial direction, for example by being filled with a very stiff material. It follows that, in the preloading at first yield there is a small non-proportionality which reduces with deformation, but in all considered cases smaller than θ_c. Hence, angle ψ is approximate representation of the angle formed between the two consecutive strain paths. The material parameters in Table 3.4 are used. The behaviours are very similar to the non-proportional paths in brick elements, discussed above.

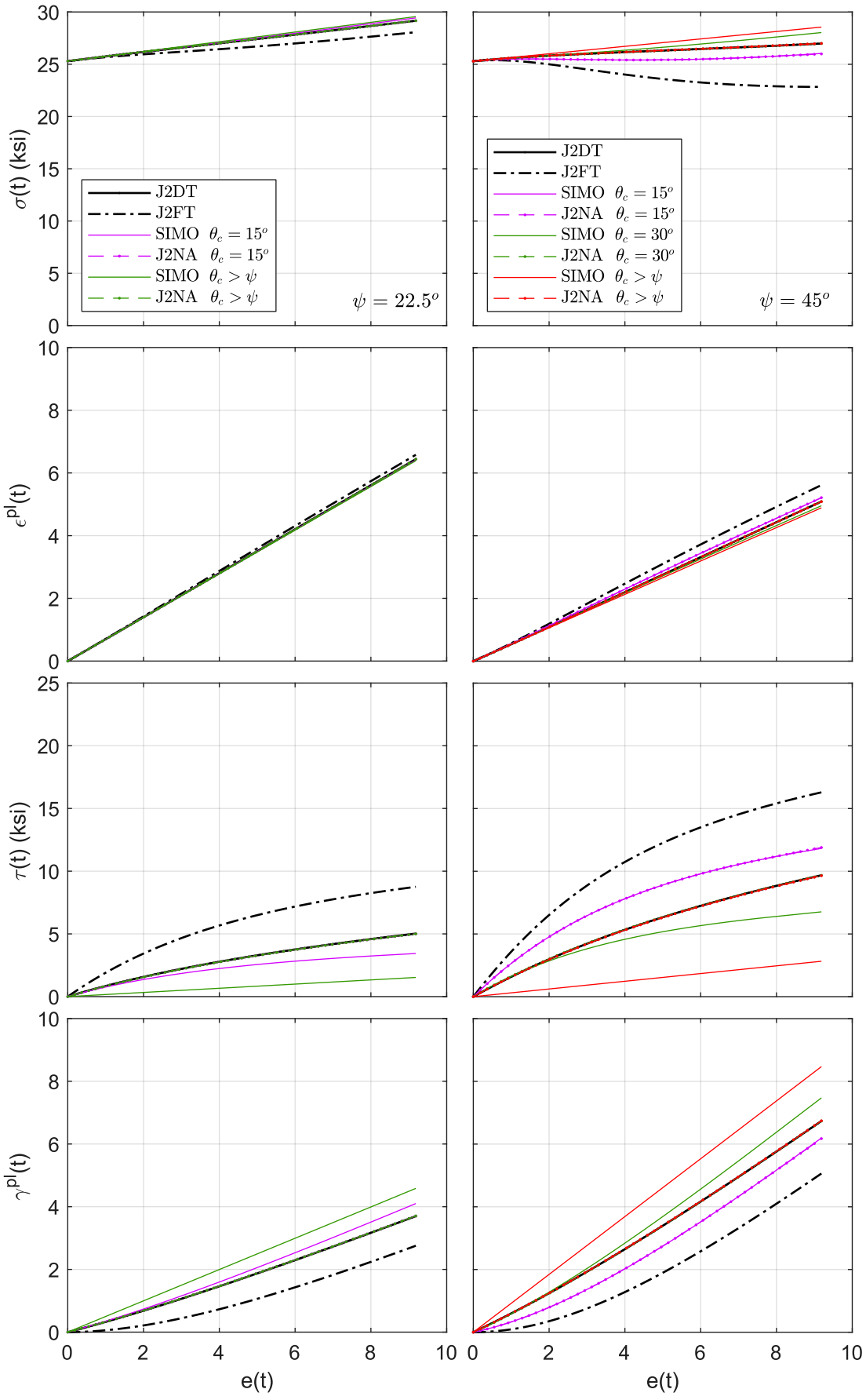

Figure 3.5: Stress and plastic strain under non-proportional strain family (3.59) (a) $\psi = \pi/8$ (22.5°), (b) $\psi = 2\pi/8$ (45°)

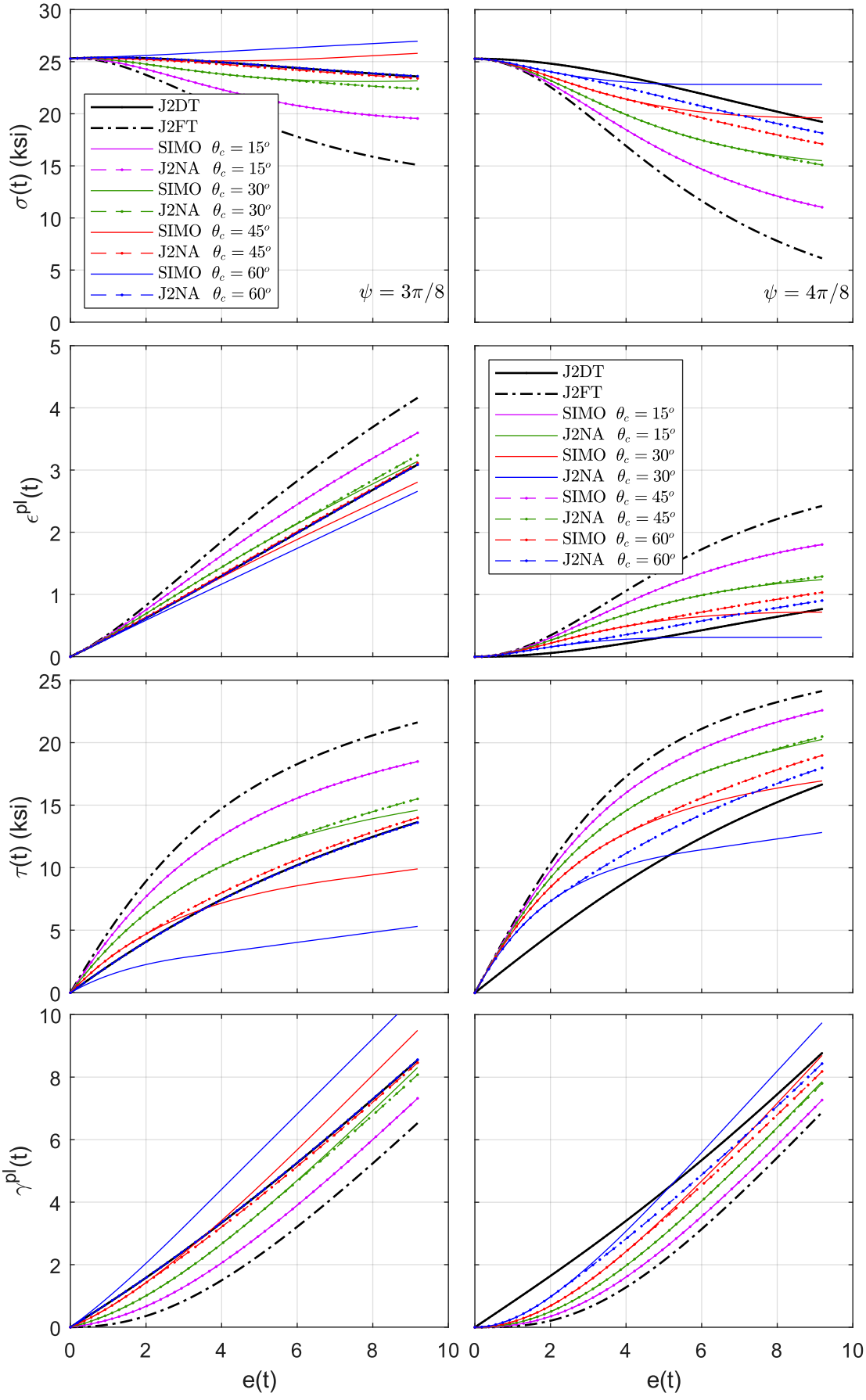

Figure 3.5: Stress and plastic strain under non-proportional strain family (3.59) (c) $\psi = 3\pi/8$ (67.5°), (d) $\psi = 4\pi/8$ (90°)

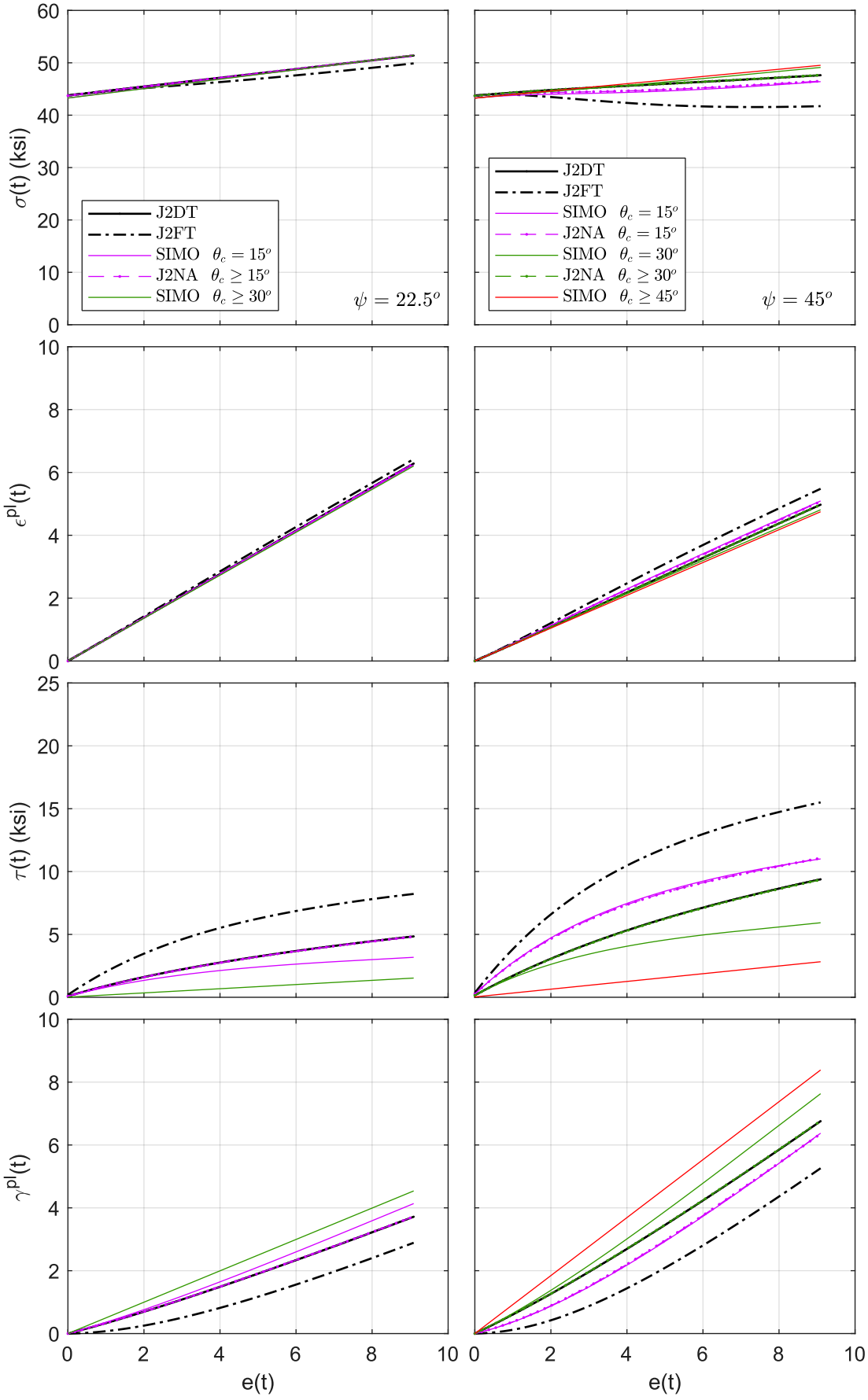

Figure 3.6: Plane stress - Stress and plastic strain under non-proportional strain family (3.59) (a) $\psi = \pi/8$ (22.5°), (b) $\psi = 2\pi/8$ (45°)

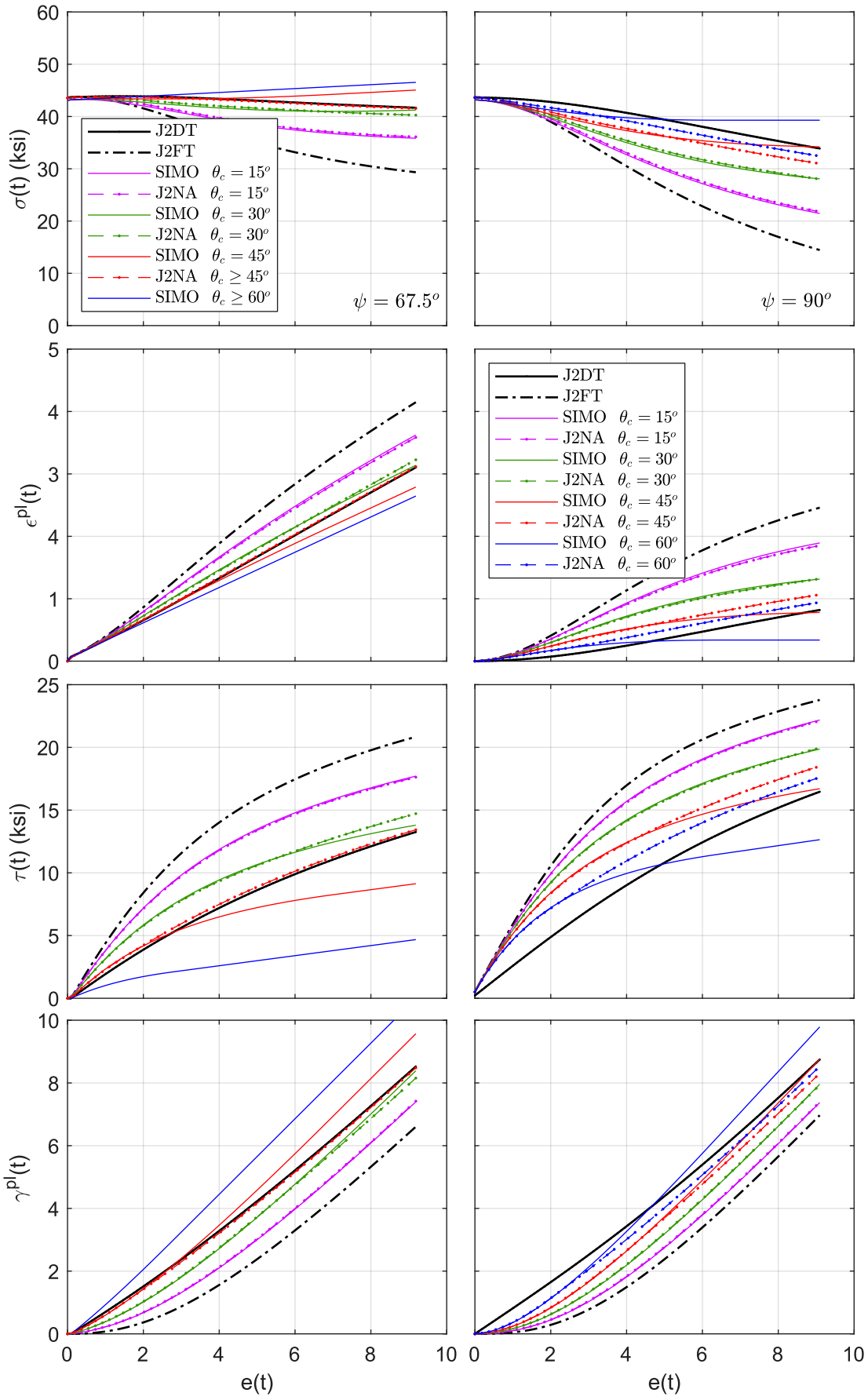

Figure 3.6: Plane stress - Stress and plastic strain under non-proportional strain family (3.59) (c) $\psi = 3\pi/8$ (67.5°), (d) $\psi = 4\pi/8$ (90°)

3.4.2 Accuracy Analysis - Iso-error Maps

To numerically evaluate the accuracy of the developed algorithm, iso-error maps are constructed for a material point under strain-controlled loading. The iso-error maps offer a schematic representation of the accuracy of the integration algorithm under a variety of loading paths. In the present study, the loading cases suggested by Simo & Taylor (1986) are used to test the accuracy of the J2NA model, considering shell elements in plane stress loading conditions ($\sigma_{33} = \sigma_{13} = \sigma_{23} = 0$).

Starting from a stress state on the yield surface (points A,B,C in Figure 3.7), the new stress state $\boldsymbol{\sigma}(\Delta\boldsymbol{\varepsilon})$ is calculated for a range of strain increments (combinations of $\Delta\varepsilon_{11}$ and $\Delta\varepsilon_{22}$), employing the developed integration scheme in a single integration step. Subsequently, the 'exact' solution $\boldsymbol{\sigma}^*(\Delta\boldsymbol{\varepsilon})$ is obtained by incrementally applying $\Delta\boldsymbol{\varepsilon}$ in sufficiently small sub-increments and employing the developed integration scheme. The number of sub-increments is increased until convergence of $\boldsymbol{\sigma}^*$. The error of the integration is estimated based on the deviatoric part for the stress, according to the expression:

$$e = \frac{\|\mathbf{s} - \mathbf{s}^*\|}{\|\mathbf{s}^*\|} \cdot 100\% \tag{3.66}$$

Three initial stress states are considered: (A) uniaxial, (B) biaxial and (C) pure shear loading, which represent a wide range of initial loading conditions. The strain increments are normalized with the yield strain parameter $\varepsilon_y = \sigma_y/E = 0.1\%$. In all iso-error maps the shear stress is taken as zero ($\sigma_{12} = 0$). In line with literature, the unfavourable case of rigid plasticity is considered, with the properties in Table 3.6

Table 3.6: Material properties and state variables for iso-error maps

Poisson's Ratio	$\nu = 0.3$
Young's Modulus	$E = 207\ GPa$ (30000 ksi)
Von Mises Stress	$\sigma_y = 207\ MPa$ (30 ksi)
Hardening modulus	$H = 0\ GPa$
Equivalent plastic strain	$\varepsilon_q = 0.00\%$
Angle parameter	$\theta_c = 2°$

The level of error for this model is similar to that reported previously in the literature and the J2FT, which is up to 8% for strain increments of the size of the yield strain. Increasing the hardening modulus leads to somewhat smaller error, because the denominator of equation (3.66), that expresses the size of the yield surface, increases. The algorithm

exhibits no error for the case of proportional loading, namely, along the line $\Delta\varepsilon_{22}/\,\Delta\varepsilon_{11} = 0.5$ in Figure 3.7(A), and lines $\Delta\varepsilon_{22}/\Delta\varepsilon_{11} = 1$, in Figure 3.7(B, C).

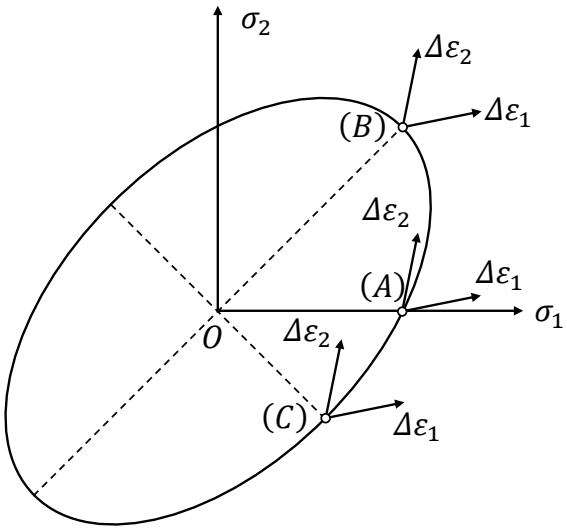

Plane stress yield surface, points A, B, C used for constructing iso-error maps.

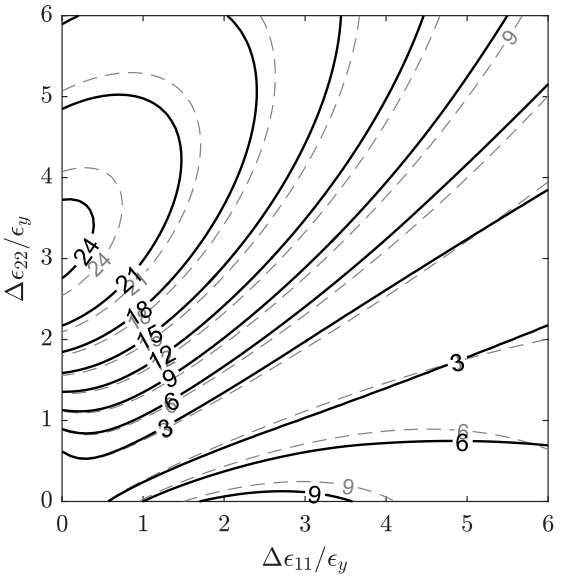

(A) Point A – Uniaxial loading initial state

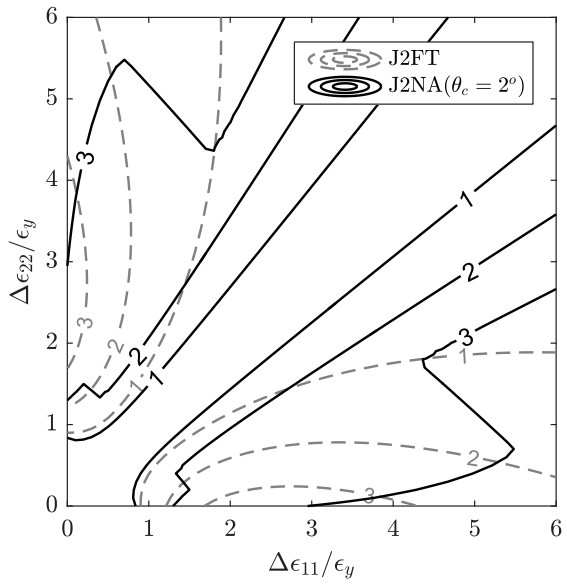

(B) Point B – Biaxial loading initial state

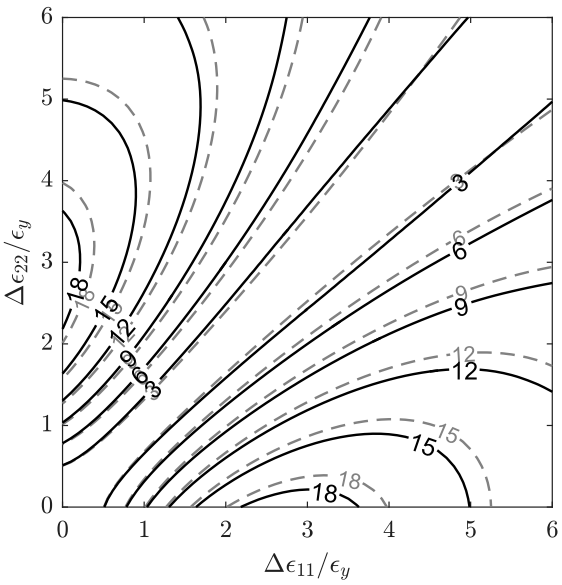

(C) Point C – Pure Shear initial state

Figure 3.7: Iso-error maps for different points A, B and C on the yield surface.

3.5 Shell buckling calculations

This paragraph addressed the application of the J2NA model in the context of finite element analyses, to perform buckling calculations, discussing the influence of its non-associative character in the way instability calculations are executed.

3.5.1 Implementation in finite element programs

Lower bound estimates of the bifurcation load from the pre-buckling equilibrium path can be obtained using Hill's 'comparison solid' concept. Hutchinson (1974) described in detail its implementation and Tvergaard (1983a) discussed its application using the J_2 corner theory by Christoffersen and Hutchinson (1979), which employs material moduli dependent on the direction of the strain rate.

The comparison solid concept introduces a quadratic functional, based on the virtual work principle, whose positiveness ensures stability, while the occurrence of non-positive values indicates bifurcation. For a discretized finite element model, the functional takes the form:

$$F = \mathbf{\Delta U}^T \ [\mathbf{K}'] \ \mathbf{\Delta U} \tag{3.67}$$

where $[\mathbf{K}']$ is the global stiffness matrix that employs the tangent material moduli of the constitutive model, and $\mathbf{\Delta U}$ is the vector with the unconstrained degrees of freedom. The elastoplastic tangent moduli are used for material points whose loading state is on the surface of their respective yield surfaces and the elastic moduli in all other cases. This expression implies that stability is ensured by the positive definiteness of the stiffness matrix $[\mathbf{K}']$, or equivalently, instability occurs when a non-positive eigenvalue of $[\mathbf{K}']$ is encountered.

Using the implicit finite element environment in ABAQUS/Standard, the global stiffness matrix $[\mathbf{K}']$ can be extracted using a dedicated step and a material subroutine UMAT to apply the material elastoplastic tangent moduli. Eliminating the constrained degrees of freedom, the eigenvalues may be calculated externally, and bifurcation is identified at the first zero eigenvalue. Alternatively, using a linear perturbation step, the smallest eigenvalues and the respective eigenmodes can be obtained to detect bifurcation. In a static analysis, by default, ABAQUS records the occurrence of non-positive eigenvalues in the stiffness matrix, which is an alternative way of identifying bifurcation. However, implicit analyses, employ the algorithmic moduli of the constitutive models in their calculations, which differ from the tangent moduli. Therefore, they may lead to non-

accurate bifurcation estimates, especially when large strain increments are used. Nonetheless, in all cases analysed in the present study, the above methods produced the same bifurcation estimates.

For non-associative and corner models, the material tangent moduli depend on the direction (angle θ) of the strain increment at bifurcation, which is not a priori known, as loading path changes may occur. On an assumption of strain direction continuity, the instantaneous moduli associated with the angle θ of the last strain increment are used, adopting an ‘alternative comparison solid’, a concept introduced by Tvergaard (1983a).

4 COMPRESSION OF THICK-WALLED METAL CYLINDERS

The structural behaviour of long thick-walled cylinders under uniform axial compression is addressed in this chapter, demonstrating several key aspects of inelastic instability of shells. The buckling and post-buckling behaviours of the cylinders are treated employing analytical and numerical tools. Local instability and its evolution are considered, accounting for the effect of initial geometric imperfection to investigate the influence of constitutive modelling in the structural performance of the simulated cylinders. Comparisons are performed successfully with experiments from the literature.

4.1 Axisymmetric buckling

Thick-walled metal cylinders (pipes or tubes), when adequately restrained laterally e.g buried pipelines, if subjected to axial compression, they shorten uniformly and are loaded well into the plastic range of the material before a bifurcation point is met and the tube wall exhibits local buckling. Gellin (1979) showed that the resulting buckling mode is axisymmetric, characterized by the development of periodic wrinkles uniform along the cylinder (Figure 4.1) - assuming the absence of significant boundary effects or imperfections which lead to localized effects.

The critical bifurcation stress (σ_c) and the corresponding halfwave length (λ_c), can be

calculated analytically using the following well-known equations (a proof is also provided in Appendix 3):

$$\sigma_c = \left[\frac{D_{11}D_{22} - D_{12}^2}{3}\right]^{1/2} \left(\frac{t}{R}\right) \tag{4.1}$$

$$\lambda_c = \left[\frac{D_{11}^2}{12(D_{11}D_{22} - D_{11}^2)}\right]^{1/4} (Rt)^{1/2} \tag{4.2}$$

where R is the radius of the tube, t is the thickness and $D_{\alpha\beta} = \partial\sigma_{\alpha\beta}/\partial\varepsilon_{\alpha\beta}$ (no summation on α, β) is the condensed material stiffness tensor $D_{ep\,(\alpha\beta\alpha\beta)}^{c.shell}, \alpha, \beta = 1,2$ presented in equation (3.58), employing the (instantaneous) material tangent moduli (2.50) (not the linearized moduli, as discussed in paragraph 3.5).

The bifurcation strain ε_c, stress σ_c and the corresponding halfwave length λ_c are obtained by solving the nonlinear equation (4.1), which has the equivalent plastic strain ε_q or the equivalent stress q_e as the only unknown. In the absence of initial geometric imperfection, the pre-buckling average stress-shortening response follows the material compression curve, independently of the material model, while the various models provide significantly different bifurcation estimates, as they employ different stiffness moduli.

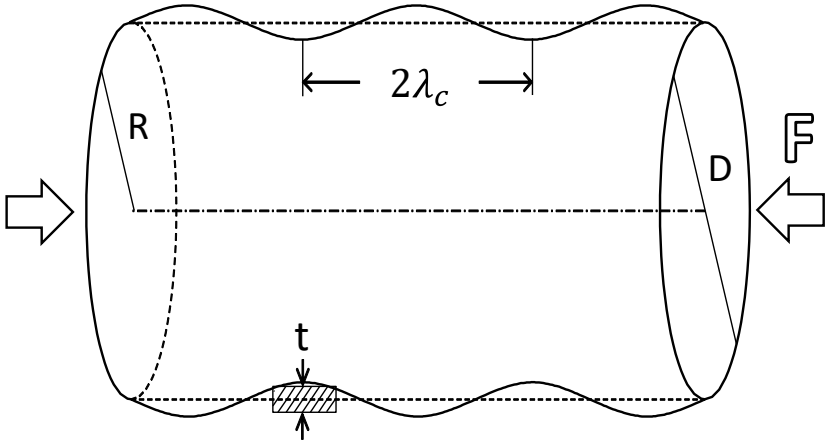

Figure 4.1: Axisymmetric buckling of cylinder under uniform compression

Key features of the presented methodology are demonstrated below in numerically simulating buckling experiments of thick-walled duplex stainless steel tubes reported in (Bardi & Kyriakides, 2006; Bardi et al., 2006). Those experiments were designed to mitigate the influence of edge supports and represent the bifurcation behaviour of long shells, as opposed to older investigations on axially-compressed cylinders (Lee, 1962;

Batterman, 1965), where specimen length and support conditions prevented the clear identification of wrinkling onset, which may result in misleading comparisons between bifurcation and ultimate loads.

In Figure 4.2b,c,d, the axisymmetric bifurcation stress (σ_c), strain (ε_c) and the corresponding halfwave length (λ_c) are displayed for tubes in terms of the diameter-to-thickness ratio (D/t). Bifurcation from the pre-buckling path is identified by solving expression (4.1), employing the material moduli for different constitutive models and the material curve Figure 4.2a. The predictions for J2NA and J2DT are identical as the preloading is proportional, and both models employ the same material moduli. The J2FT, marked with dotted lines, over-predicts the bifurcation stresses by a significant amount, in the entire range considered, while J2NA generally provides predictions in better agreement with experimental values by (Bardi & Kyriakides, 2006), marked with circles and squares.

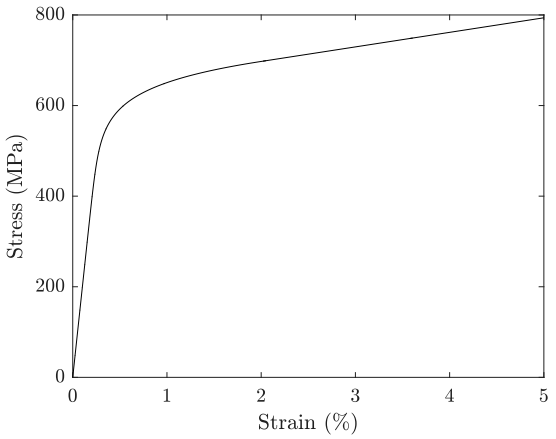

(a) Material stress-strain curve

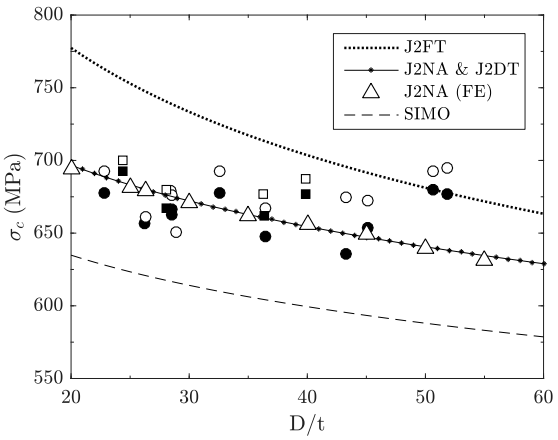

(b) Bifurcation stress σ_c vs D/t

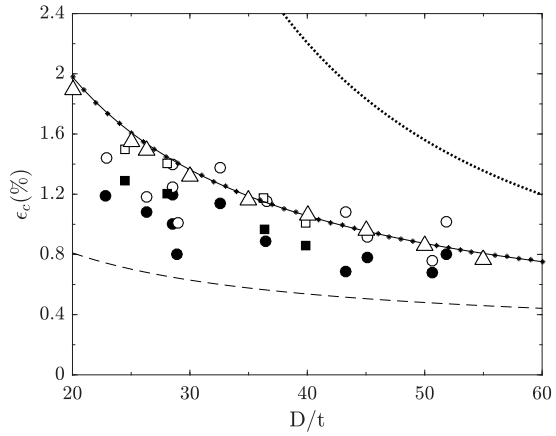

(c) Bifurcation strain ε_c vs D/t

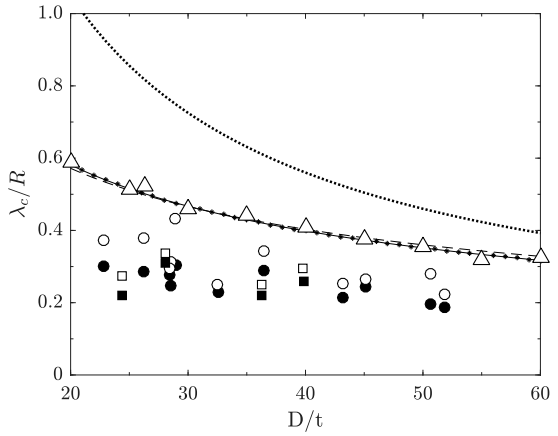

(d) Wrinkling halfwave length $\lambda_c$vs D/t

Figure 4.2: Influence of constitutive modelling in the bifurcation stress, strain and halfwave length for thick-walled tubes. Experimental data are included

On the other hand, the non-associative model by Simo (1987) predicts bifurcation at

significantly lower load than experiments indicate. The differences are more salient when considering the values of strain at bifurcation in Figure 4.2c. In that case, the J2FT grossly over-predicts bifurcation strains, whereas the J2NA is in better agreement with experiments. Finally, the model by Simo leads to significant underpredictions of the bifurcation strain, particularly for tubes with larger values of D/t ratio.

The buckling halfwave length is overestimated by all models. Simo's model yields predictions similar to the ones by J2NA, which are more consistent with experimental results compared to those of J2FT, but still over-predict the reported halfwave values by a factor of two. The differences can be alleviated when yield anisotropy is taken into account (Bardi & Kyriakides, 2006; Corona et al., 2006; Kyriakides et al., 2005) which was reported in these experiments, but this is outside the scope of the present study.

Bifurcation predictions are also obtained using finite element models via static analyses in Abaqus, employing the user-material-subroutine (UMAT) for J2NA. Axisymmetric and three-dimensional shell element models with different lengths were used, under a displacement-controlled analysis scheme (modelling details and mesh properties were as described in the paragraphs 4.1.1 and 4.2). A series of analyses was performed to identify the length that leads to the lowest bifurcation stress, which also supplied the relevant strain and halfwave length parameters. The finite element results are included with triangular marks in Figure 4.2b,c,d, and they are in excellent agreement with the analytical predictions. It is noted that in FE analyses the hardening behaviour is introduced as pairs of values of true stress – logarithmic plastic strain. These values are calculated from the material hardening curve Figure 4.2a, considering it represents the uniaxial behaviour under compression (the standard formulas are used on the material curve under tension).

4.1.1 Non-axisymmetric buckling modes

To investigate the development of non-axisymmetric bifurcation modes, models of length $L = 2\kappa\lambda_c$ (κ is an integer) are used, following the argument by (Gellin, 1979; Koiter, 1963). Models employ 12 S4 elements per halfwave and 120 around the circumference, together with periodic symmetry support conditions. Shortening (axial displacement at the cylinder ends) is imposed incrementally and at 0.1% strain increments, the eigenvalues of the stiffness matrix are monitored, to identify structural instability. The first zero eigenvalue corresponds to an axisymmetric buckling mode, and the relevant bifurcation stress, strain, and wavelength are in line with the analytical solution. At increasing deformations, bifurcation into non-symmetric modes with e.g. two and three

circumferential waves was also recorded (Figure 4.3). Longer finite element models, with κ equal to 2, 3,… replicated the bifurcation modes and the corresponding strains obtained by their shorter two-halfwave counterparts ($\kappa = 1$).

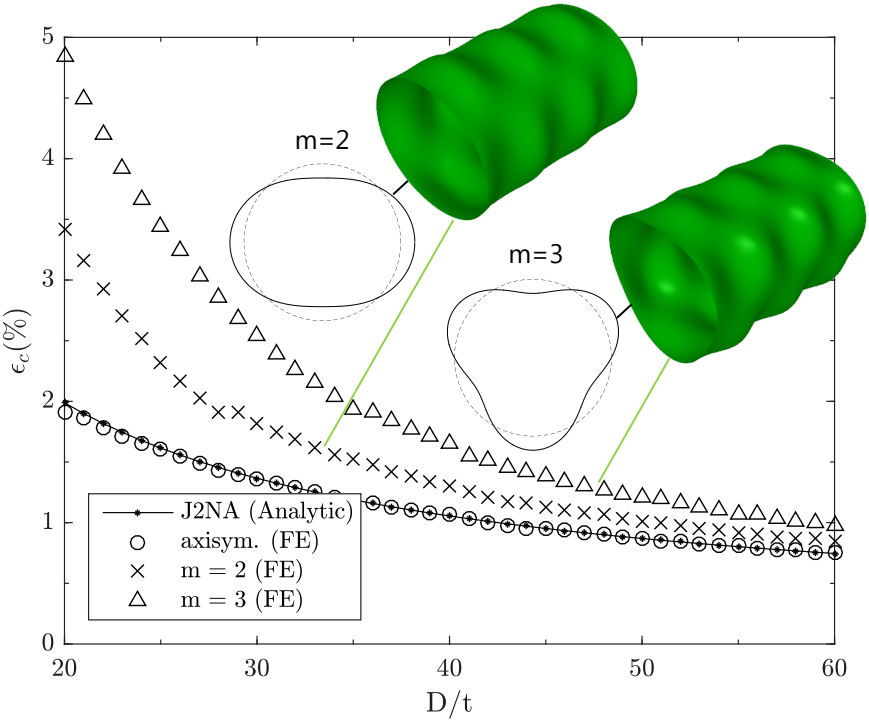

Figure 4.3: Bifurcation into non-axisymmetric bucking modes

4.2 Evolution of uniform wrinkling

Initial geometric imperfection leads to non-uniform stress distribution along the tube and non-proportionality arises, surfacing the influence of various constitutive models. The average stress (F/A) - normalized shortening -or average strain- ($\Delta L/L$) diagrams of initially imperfect cylinders demonstrate this influence (Figures 4.5- 4.7).

Displacement-controlled axisymmetric analyses are performed, employing twenty, two-node axisymmetric shell elements, denoted as SAX1 in Abaqus, simulating a one halfwave long segment of the cylinder, with seven integration points across the wall thickness. To enforce periodicity along the cylinder (uniform wrinkling), the rotation of the top and the bottom of the model is restrained, while the cylinder is free to expand radially (Figure 4.4).

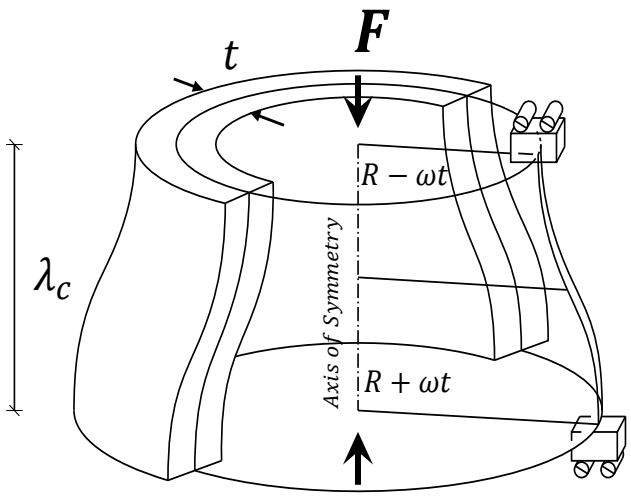

Figure 4.4: Geometry and boundary conditions of an axisymmetric one-halfwave model of an imperfect thick-walled cylinder under compression

Initial geometric imperfection is introduced in the shape of the first (axisymmetric) eigenmode of the shell, and the radial displacement along the tube can be written as:

$$w = \omega t \cos\frac{\pi x}{\lambda_c} \tag{4.3}$$

where parameter ω refers to the amplitude of the imperfection as a fraction of the shell thickness. For simplicity, onward ω is simply referred to as imperfection amplitude. The behaviour of the imperfect cylinder is presented in Figure 4.5, using the J2NA with angle values θ_c equal to $2°, 5°, 10°, 15°, 30°$, as well as the J2FT and J2DT models for comparison purposes. A small imperfection of amplitude $\omega = 10^{-4}$ is used, which enables the solution to follow the secondary path, without an abrupt transition at the bifurcation point. In all analyses, a maximum shortening increment of 0.01% is used.

The J2FT model follows the primary path, which is practically the material compression curve, for axial shortening up to 5%, and develops a load maximum at about 6%. On the contrary, the J2DT model develops a load maximum at the bifurcation point of the perfect system, immediately followed by a decreasing branch, behaviour in line with arguments by Peek (2000). The J2NA leads to behaviours bounded by these two models. At bifurcation, the cylinder starts diverging from the primary path with increasing load. The parameter θ_c influences the load maximum of the tube, with larger values of θ_c leading to lower load maxima, and behaviours that approach the J2DT. As the angle θ_c becomes very small, the response of J2NA model approaches that of the J2FT. It is important to notice that a small value of angle θ_c, e.g., 2°, can lead to a response which is quite different to that of J2FT. Such small values of θ_c may be hard to measure experimentally,

which would explain the difficulties in past investigations (Hecker,1972) to observe yield surface corners.

For a large imperfection amplitude ($\omega = 10^{-1}$), the equilibrium path is smoother (Figure 4.6). Similarly, the J2NA leads to behaviours bounded by the J2FT and the J2DT curves, but for high imperfection amplitudes, all these models lead to rather similar behaviours. The equilibrium path obtained using the model by Simo (1987) diverges from the material curve very close to the corresponding point of bifurcation, as calculated in Figure 4.2c, which is a significantly lower level of deformation than the J2DT and experimental data indicate. Increasing values of angles θ_c lead to progressively earlier load maxima and more accentuated deviations from the material compression curve. Numerical instabilities were met when employing Simo's model with low values of angle θ_c and imperfection ω, which is attributed the model's full vertex formation effect immediately at first yield, as noted in paragraph 2.6. This abruptly reduces material stiffness and hinders convergence.

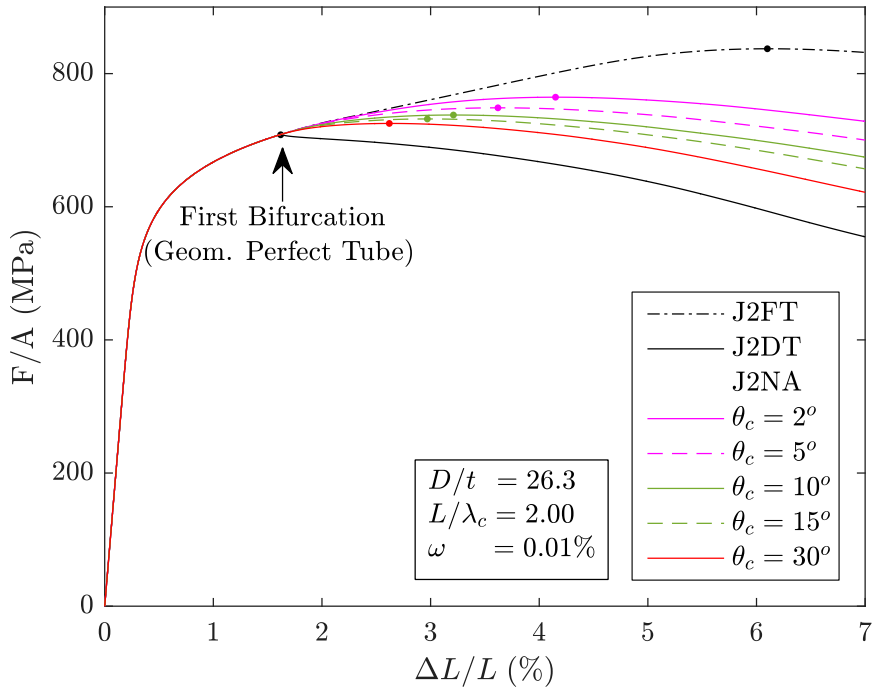

Figure 4.5: Influence of constitutive modelling in the wrinkling of the axially compressed tube ($\omega = 10^{-4}$)

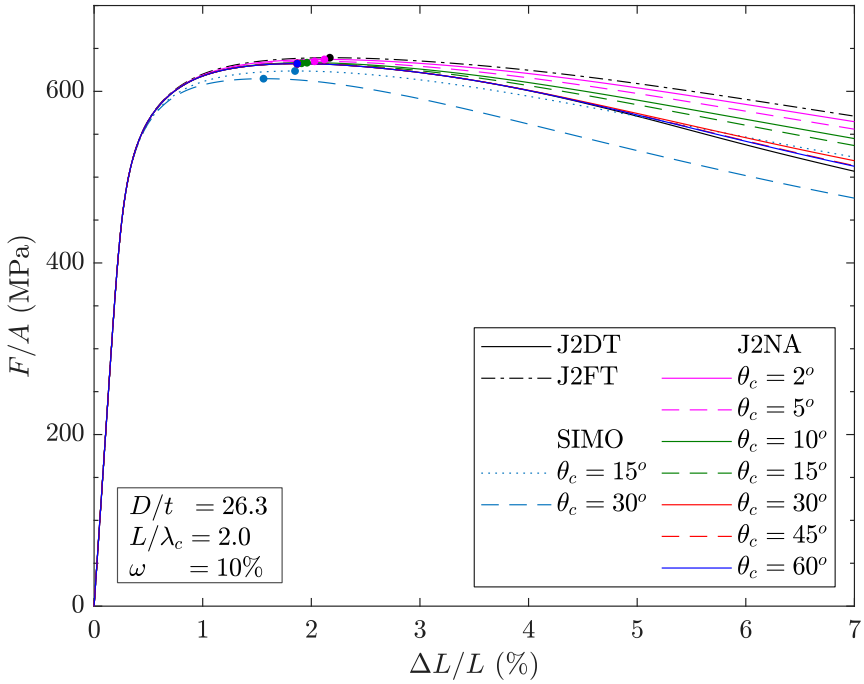

Figure 4.6: Influence of constitutive modelling in the wrinkling of the axially compressed tube ($\omega = 10^{-1}$)

In Figure 4.7, an overview is given of the influence of imperfection amplitude ω in the wrinkling behaviour of the cylinders, when using the J2FT and J2NA models. The use of progressively smaller imperfection while employing the J2NA has little influence on the simulated response of the cylinder. The equilibrium path diverges from the material compression curve soon after the bifurcation strain of the perfect tube, and the secondary path is followed. For small values of imperfection $\omega \leq 0.05\%$ the stress-strain curve is practically unaffected by the imperfection amplitude, it exhibits a clear load maximum which occurs at a discernible limit strain $\varepsilon_L \cong 4\%$.

On the other hand, the sensitivity of the J2FT to initial imperfection is seen: increasingly small imperfection amplitudes enable the cylinder to follow the primary path (material compression curve) up to high values of axial shortening, leading to increasingly high load maxima at increasing average strains, while for a small imperfection ($\omega = 10^{-5}$), no maximum load is identified for shortening up to 7%. For larger imperfection amplitudes $\omega > 0.1\%$ the two constitutive laws produce increasingly similar behaviours, while they become almost identical for $\omega = 10\%$. The influence of imperfection amplitude in the axial load capacity and the respective average strain of the cylinder are summarized in Figure 4.8, using the J2FT and J2NA.

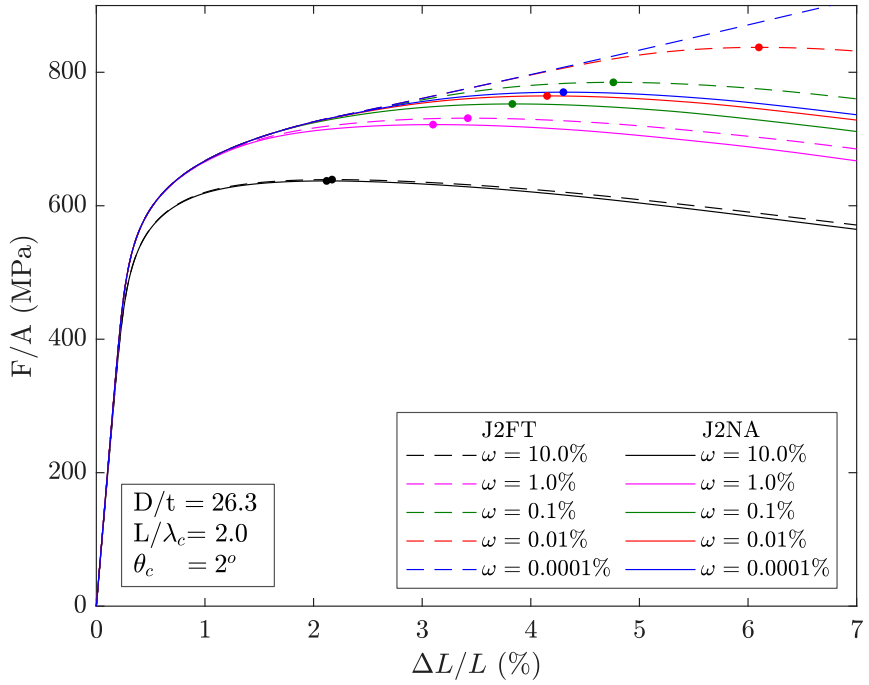

Figure 4.7: Influence of imperfection amplitude in uniform wrinkling, using the J2FT and J2NA

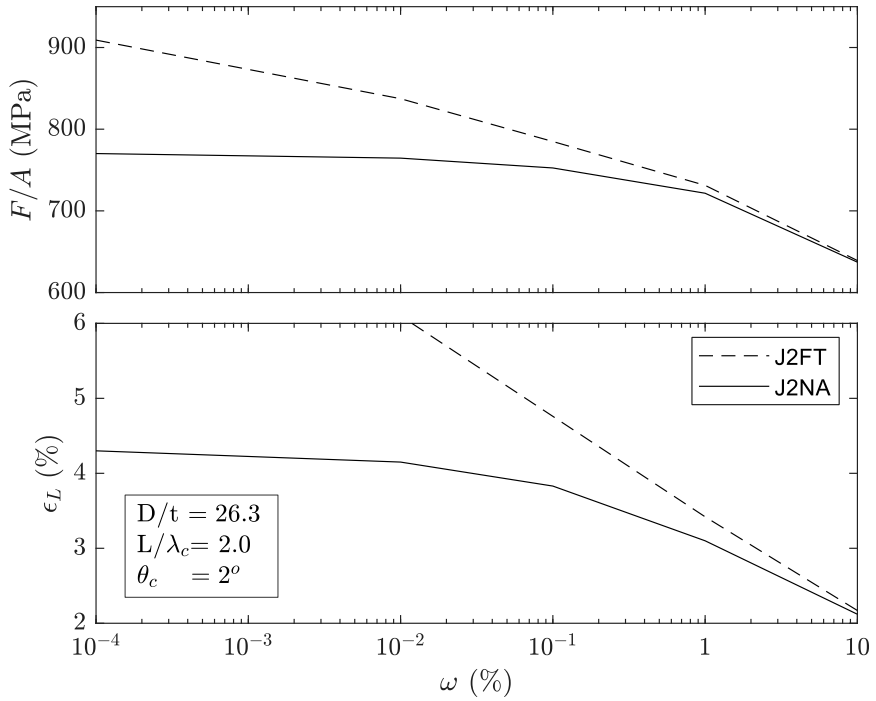

Figure 4.8: Influence of imperfection amplitude in cylinder's axial load capacity

In Figure 4.9 the values of angle θ are given across the cylinder thickness in the uniform wrinkling model. In the neighbourhood of 2% shortening values of θ exceed 40º, indicating significant non-proportionality in the loading path. The highest values of θ are recorded in locations with biaxial compression, caused by wrinkling due local bending

across thickness (σ_x), but also hoop stresses along the cylinder (σ_θ).

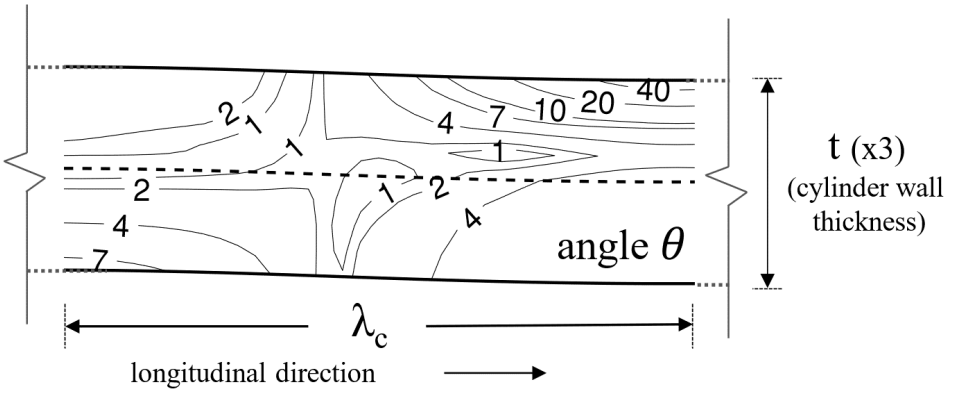

Figure 4.9: Non proportionality angle θ along a wavelength at $\varepsilon = 2\%$, $\omega = 10^{-5}$

Figure 4.10 depicts the limit strain ε_L, when the maximum load capacity of the compressed cylinder is reached, plotted with respect to the diameter-to-thickness ratio, assuming uniform axisymmetric wrinkling. Three initial imperfection levels are considered, namely $\omega = 0.1, 1.0, 5.0\%$ which are in line with investigations by the experimenters, suggested to be consistent with the levels of imperfection in the tested specimens, and two constitutive models: J2FT and J2NA. Uniformly, the J2FT leads to higher limit strains for all levels of imperfection, with more pronounced differences at low imperfections. Numerical results are in agreement with the experimental values reported by Bardi & Kyriakides (2006), included in the graph, particularly for higher D/t values.

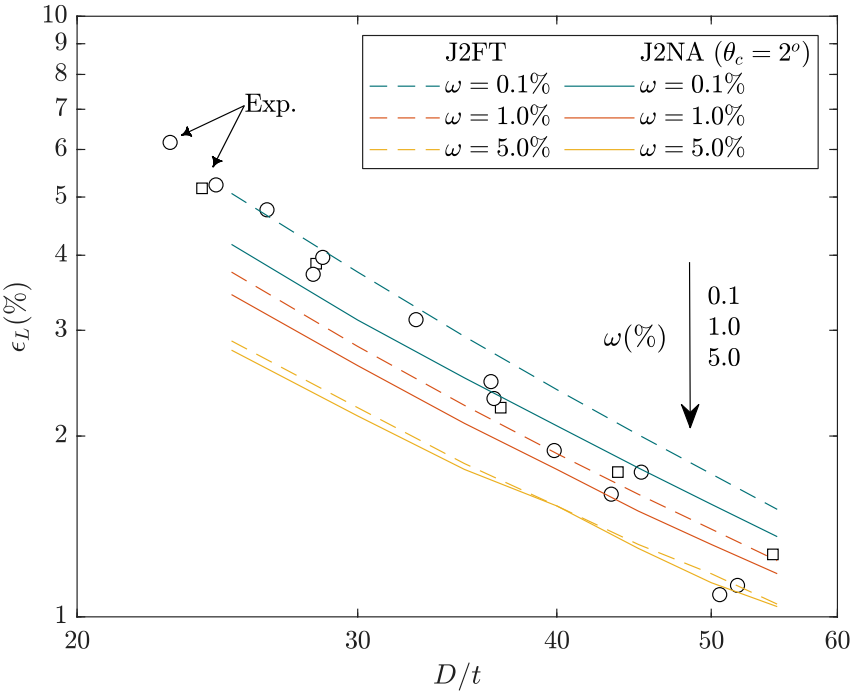

Figure 4.10: Limit strain versus diameter-to-thickness ratio D/t; uniform wrinkling

4.3 Localization of wrinkling

To simulate the localization of the axisymmetric buckling pattern, finite element models of multiple halfwaves are used. The length L is assumed equal to $N\lambda_c$, where λ_c is the critical halfwave length calculated from equation (4.1), and N an integer. The mesh employs twenty axisymmetric shell elements (SAX1) per halfwave and seven integration points across the shell thickness. The geometric imperfection is assumed as a stress-free initial radial displacement field of the form:

$$w = -t\left[\omega + \omega_1 \cos\frac{2\pi x}{N\lambda_c}\right]\cos\frac{\pi x}{\lambda_c} \tag{4.4}$$

Parameter ω represents the uniform amplitude of the axisymmetric imperfection, while parameter ω_1 is used to modulate the imperfection amplitude along the tube segment under consideration and enforce localization at the centre of the 14-halfwave-long model ($N = 14$). At the two ends of the model, symmetry conditions are imposed: the rotation is restrained, while the radial displacements of the cross-section are free, as in Figure 4.4.

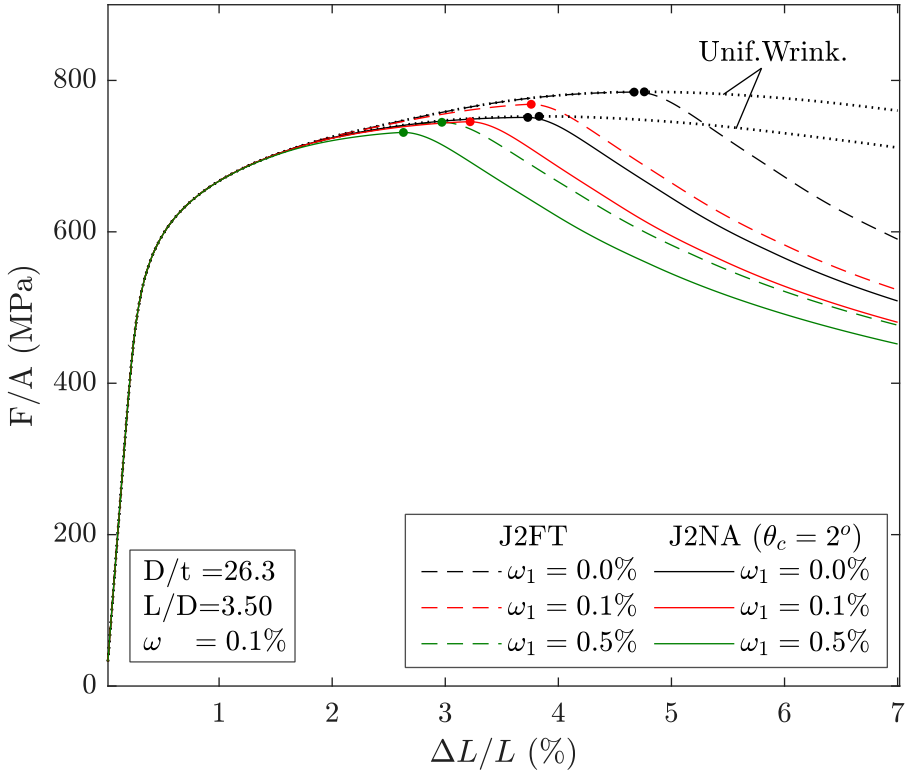

Figure 4.11: Effect of the imperfection amplitude ω_1 in the average stress- average strain response of the imperfect tube employing the J2FT and J2NA

Figure 4.11 shows the effect of imperfection bias ω_1 on the response of the compressed tube for a value of uniform imperfection amplitude $\omega = 0.1\%$ and for values of ω_1 equal

to 0.0 %, 0.1%, and 0.5%. When no imperfection amplitude bias ($\omega_1 = 0$) is employed, the cylinder closely follows the same equilibrium path as in uniform wrinkling, but after the limit load formation, additional shortening is distributed non-uniformly along the cylinder, localizing in a single wrinkle, and the load capacity reduces rapidly. The limit load for the localization model and the uniform wrinkling model are very close. The imperfection amplitude bias ω_1 causes localization to initiate at lower levels of stress and strain, for both the J2FT and F2NA models, the limit load in these models is similar to the uniform wrinkling limit load for imperfection amplitude $\omega + \omega_1$, as noted (Bardi et al., 2006). The tube maintains structural rigidity up until greater deformations when the J2FT is employed.

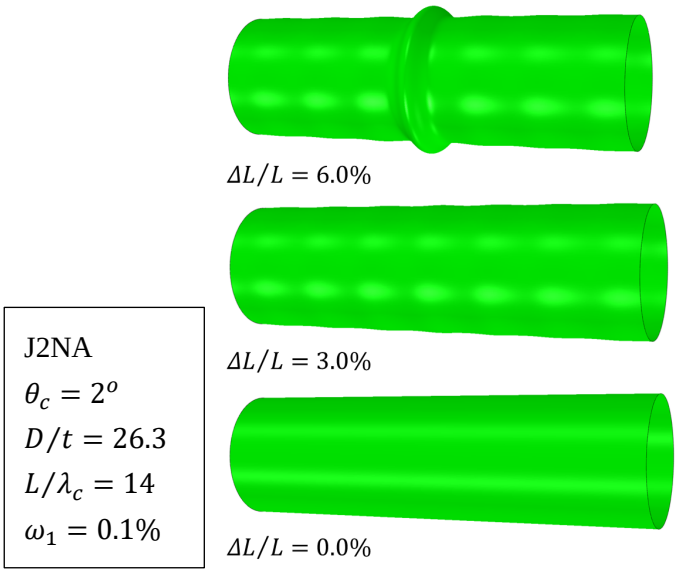

Figure 4.12: Deformed configuration at increasing strains

An interesting observation refers to the orientation of the maximum initial imperfection, as for either inward or outward maximum imperfection, the wrinkling localizes in an outward bugle following the limit load. When initial imperfection has a maximum outward wrinkle, the imperfection pattern initially increases almost uniformly in a controlled manner when compression is applied. At the load maximum localization commences at the wrinkle with the maximum initial amplitude, the displacements start increasing rapidly locally, while regions far from the buckle area start to unload (Figures 4.12 & 4.13b). When the imperfection maximum is in an inward wrinkle, a similar response is recorded at early stages of deformation. However, localization takes place at one of the outward wrinkles on the side of the maximum inward wrinkle (Figure 4.13b). This effect on the orientation of the initial imperfection was found using both the J2FT model and the J2NA and it is in line with observations by Tvergaard (1983). In Figure

4.13b the increase in diameter along the tube is further given for different stages of the analysis. In Figure 4.14 the strain direction angle θ is plotted along a tube section in an advanced stage of the post-buckling ($\Delta L/L = 6\%$). Great variations are seen in θ, and values greater than 90^o signify the unloading of parts of the tube length.

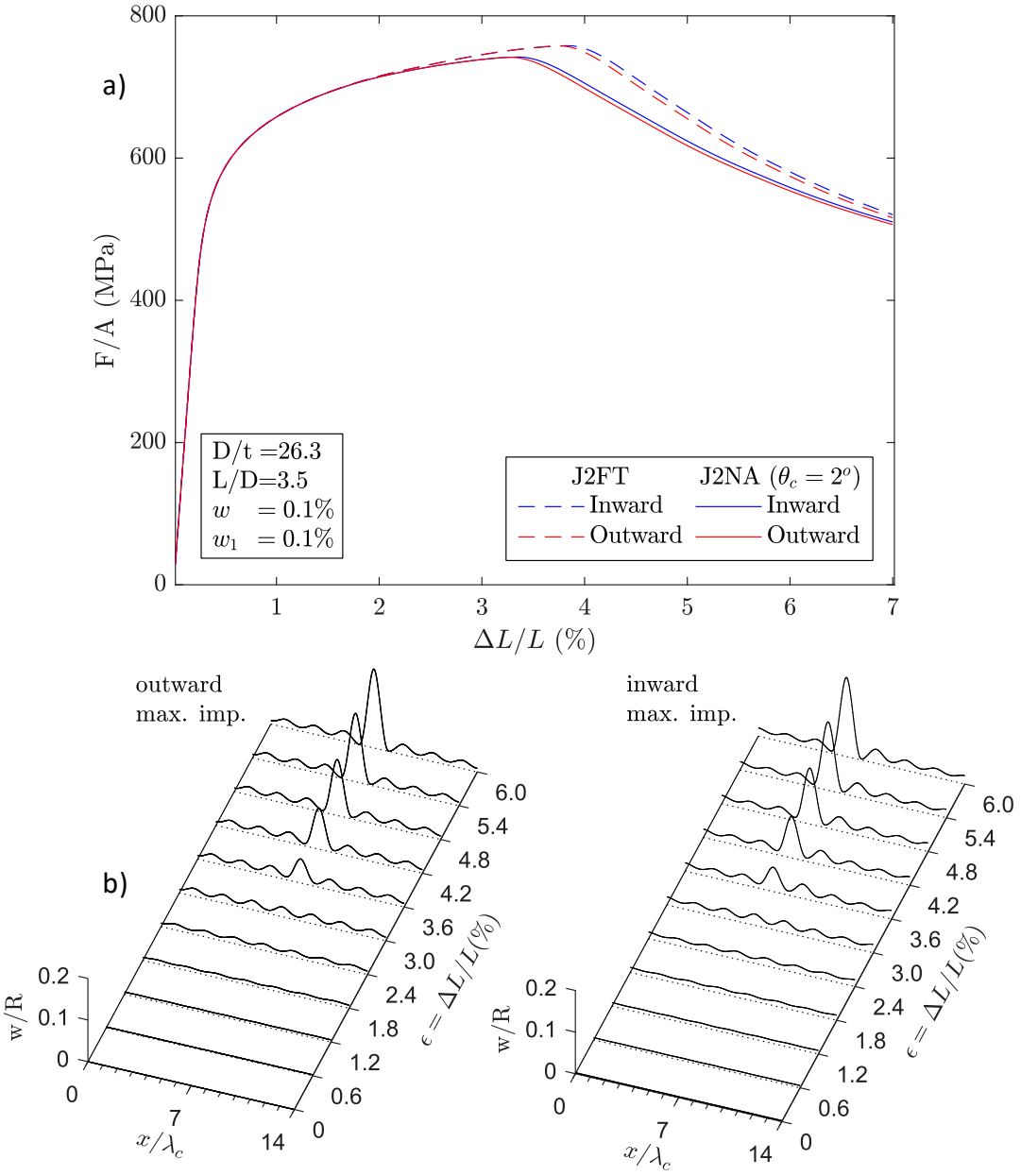

Figure 4.13: Influence on the direction of the maximum imperfection in (a) the average stress- average shortening of compressed cylinders; (b) the displacement profile along cylinder generator

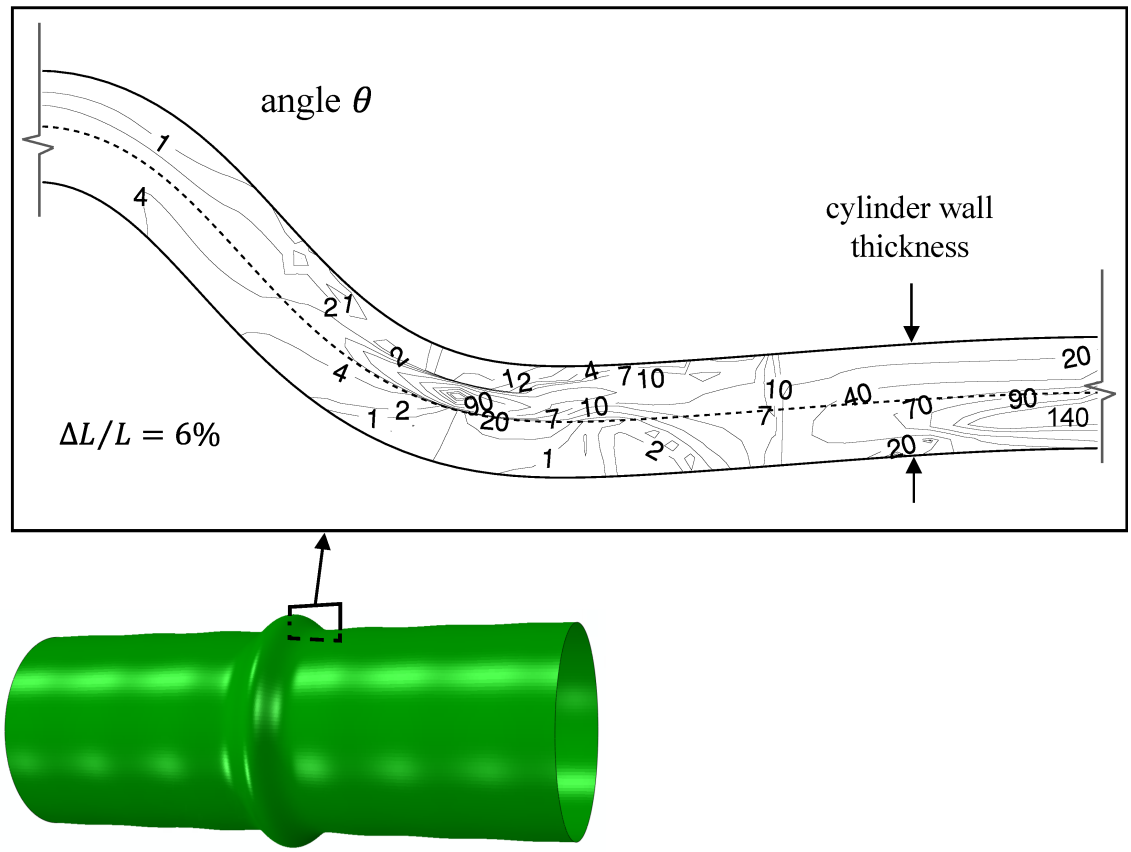

Figure 4.14: Angle θ across the thickness in the cylinder after localization of wrinkling.

4.3.1 Non axisymmetric modes

By developing fully 3D shell element models, failure into non-symmetric modes is modelled, characteristic in the more thin-walled shells. Additional non-symmetric imperfection is introduced expressed as:

$$w_m = -t\omega_m \cos\frac{\pi x}{2\lambda_c}\cos m\theta \tag{4.5}$$

where $t\omega_m$ is the amplitude of the buckling mode with m waves developing in the circumference. The number m of circumferential waves developing at buckling depends on the D/t ratio of the cylinder, with more waves developing in more thin-walled cylinders, in general, but in real shells it is also affected by the imperfection that is present. In Figure 4.15 the influence of non-axisymmetric imperfection in the failure of the cylinder with $D/t = 43.3$ is presented, considering the J2FT and J2NA. Analyses with $m = 2$ demanded higher imperfection amplitude and failed to incite pronounced non-symmetric buckling, so $m = 3$ is considered critical and the influence of ω_3 in the wrinkling localization is given below. This observation is in line with the analysis in (Bardi et al., 2006), indicating that three waves develop circumferentially for cylinders

with $D/t > 39$ and further suggesting imperfection amplitudes $\omega = 0.05\%$ and $\omega_3 = 6\%$ are representative for this cylinder.

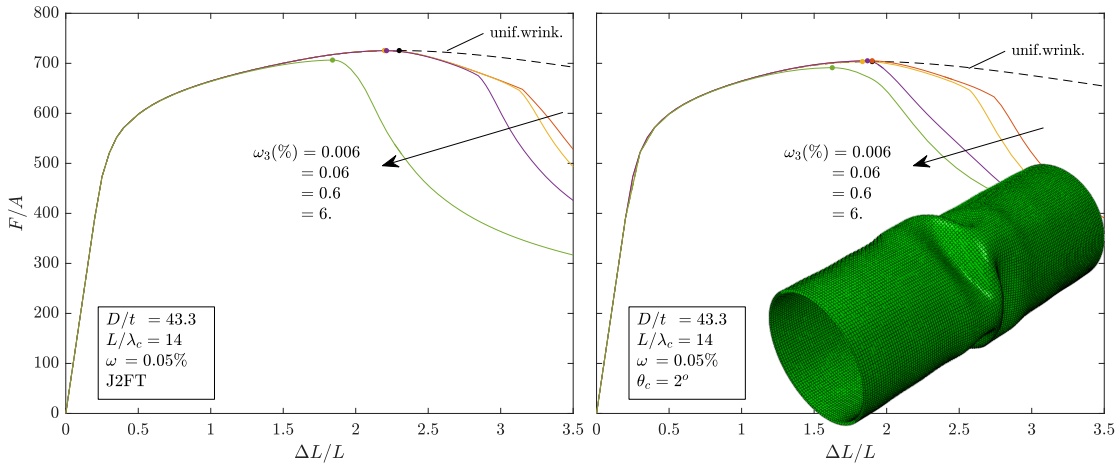

Figure 4.15: Localization into a non-symmetric mode

Employing the axisymmetric imperfection amplitude $\omega = 0.05\%$, along with various levels of non-symmetric imperfection ω_3, analyses show that for amplitudes $\omega_3 \leq 10\omega$, the equilibrium path up to the limit load is unaffected. The maximum force and the respective average shortening are the same as in the axisymmetric case and wrinkling in the cylinder is essentially axisymmetric. Wrinkling is initially quite uniform and at the limit load the centre wrinkles become more pronounced, begin to localize axisymmetrically, and load capacity reduces. With further shortening, a distinct bifurcation point is met, the shell stiffness drops abruptly, and circumferential buckles develop. This transition occurs at additional shortening of 0.5% for low values of ω_3 and it occurs progressively earlier in the post-limit-load equilibrium path for increasing values of ω_3.

Higher amplitudes of non-axisymmetric imperfection (e.g., $\omega_3 = 6\%$) are quite significant and reduce the limit load and the average strain when it occurs. In this case, wrinkling localizes directly in a single buckle at the centre of the cylinder, but shows signs of circumferential waves even before the limit point is reached. The circumferential waves are dominant in the cylinder profile immediately after the maximum load. This behaviour is found using both the J2FT and J2NA, with the latter leading to more compliant responses, as in the axisymmetric case, and allowing for transitions to the secondary path (non-symmetric buckling) for lower imperfection amplitudes.

In Figure 4.16 this behaviour is compared to the experimental curve by (Bardi et al., 2006). Simulation follows very closely the experiment up to the limit point when it shows

a smoother post limit load behaviour. In the experiment, the shortening was measured in a segment of the tube of length $L = 1.25D$, while the curves in Figure 4.15 measure it in a length of $3.42D(14\lambda_c)$, so the two are not directly comparable. An appropriate curve is included in the graph, measuring the shortening from the relative displacements of two cross sections $1.24D$ apart, located on either side of the buckle, and it exhibits the same smooth behaviour as the experiment.

Following the limit point, deformation localizes in the buckles and additional shortening is not distributed uniformly along the cylinder. It follows that after the limit point any shortening measures are dependent on the length that was used, with longer sections leading to a seemingly more abrupt loss of stiffness. So, comparisons with the experiment in shortening terms must be made based on metrics in the same model length.

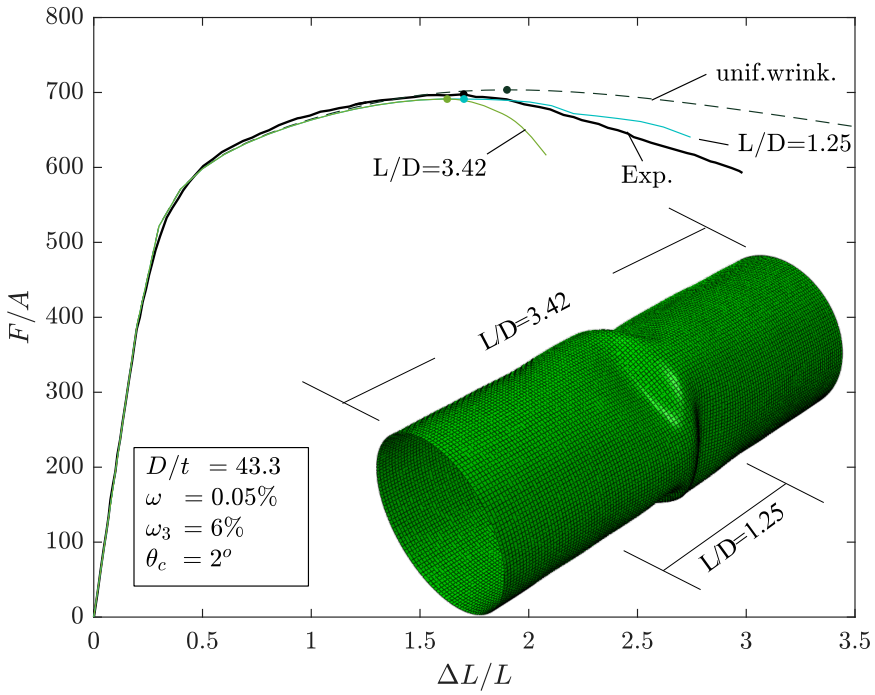

Figure 4.16: Model length and comparison with experiment

4.4 Conclusions

The inelastic instability of thick-walled cylinders under uniform compression is reviewed using analytic tools and nonlinear numerical analyses. Several constitutive models are employed to investigate local buckling. Analytic calculations demonstrate that the J2NA can reliability estimate instability, while estimates using the J2FT or the model by Simo (1987) show a disparity with experimental data, producing overly high and low predictions, respectively. Finite element models are developed in Abaqus and using the

software capabilities they are used to validate the bifurcation estimates based on the ‘alternative’ comparison solid. They verify that local instability onsets in the form of periodic axisymmetric wrinkling, when J2NA is employed.

The influence of constitutive modelling in the post-buckling response is examined using implicit FE analyses. Low values of parameter θ_c are shown to measurably affect the post-buckling response of the cylinders and are used in further buckling calculations. The evolution of uniform wrinkling shows the J2NA leads to lower limit loads than J2FT, with lower sensitivity to the amplitude of initial imperfection. Comparisons are made with experimental data, and models are extended to investigate the local growth of wrinkles. Analyses demonstrate the nature of the wrinkle localization process leading to folding of the section and to a limit load instability, which can occur well after the onset of wrinkling. The presence of imperfection reduces the load capacity of cylinders and instigates localization. Analyses demonstrate the complexity of the load paths in the post-buckling of shells, which necessitates the cautious model implementation scheme described in the previous chapter.

Finite element analyses employing J2NA address key features of inelastic shell buckling and demonstrate the capabilities of these modelling tools to reliably simulate inelastic buckling of thick-walled cylinders under compression. In the following chapter, they are employed to investigate cylinder instabilities under more demanding bending loads.

5 PURE BENDING OF LONG THICK-WALLED METAL CYLINDERS

The structural performance of thick-walled metal cylinders under pure bending is examined in this chapter. Contrary to the case of compression, under bending the prebuckling equilibrium path is non-trivial, involving double opposite curvatures in the hoop and meridional direction of the cylinder, leading to biaxial, non-proportional loading, prior to bifurcation. The influence of constitutive modelling in these more complicated loading paths is examined, modelling the structural behaviour of cylinders with various D/t ratios, addressing their pre- and post-buckling response.

Overview

The structural behaviour of thick-walled cylindrical shells under bending is characterized by the interaction of geometric and material nonlinearities. Ovalization and bifurcation instabilities determine the bending load tubulars can sustain, and the elastic-plastic material properties further influence the structural performance of tubes, as significant inelastic deformations may precede buckling and failure. This chapter focuses on the simulation of the mechanical behaviour of thick-walled cylinders, employing the J2NA constitutive law to account for the above phenomena.

Brazier (1927) showed that bending of elastic cylinders induces ovalization of the cross section, which has a prominent role in their structural behaviour. With increasing bending deformation, the cross section gradually ovalizes and tends to flatten (Figure 5.1). As the distance between the compression and tension side of the tube reduce, a gradual reduction of the section's bending stiffness is recorded and ultimately a moment maximum develops (ovalization limit load instability). Further bending deformation leads to a reduction in moment the tube section sustains. This geometric destabilization (second order deformation effects) is not addressed by the beam theory. Its influence in the performance of elastic tubes has been studied by, e.g. (Reissner, 1959) who investigated ovalization instability of elastic cylinders further considering pressure with semi-analytic methods, and more recently (Karamanos, 2002) who employed a nonlinear finite element formulation.

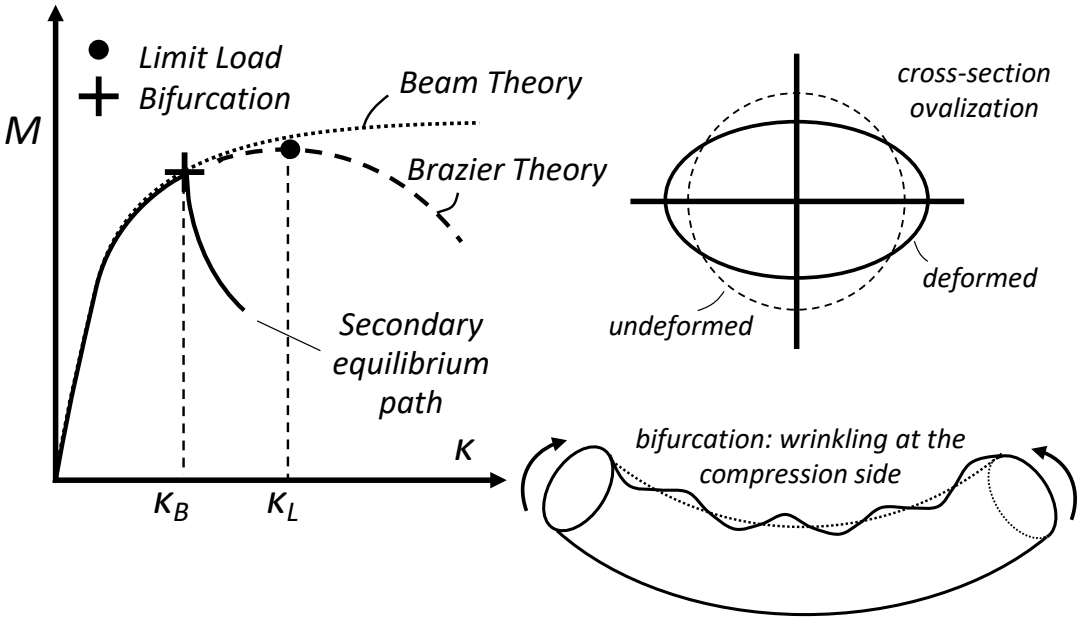

Figure 5.1: Moment-curvature response of elastic-plastic tube under bending

Relatively thick-walled cylinders fail while loaded in the plastic range of the material, so the ovalization-induced loss of bending stiffness is further exacerbated by the low stiffness of the material in the plastic range. The significant combined global and hoop bending create a biaxial state of stress in the cylinder wall, which leads the material to yield at lower curvatures, further reducing stiffness. As a result, tubulars members may be unable to sustain the full plastic moment of the initial cross section ($M_o = \sigma_o D_o^2 t$). The interaction of material and ovalization instabilities is important for metal cylinders with a diameter/thickness ratio (D/t) of less than, say, 60, when the effects of the inelastic material behaviour are more prominent. Particularly in shells with $D/t \leq 25$, this

interaction dominates their structural response, which is characterized by ovalization of the tube section, formation of a limit load, followed by a gradual failure with significant post-limit-load strength. (Figure 5.2c).

Ades (1957) analysed the ovalization of tubulars in the inelastic range, assuming that the cross-section deforms into an elliptical shape, and employing the J2DT to describe inelastic material behaviour. This study found the limit (ovalization) moment and curvature of elastic-plastic long cylinders, to be lower compared to predictions assuming elastic material properties. Gellin (1980) further considered limit loads and curvatures of bent tubes, together with nonlinear kinematics from ring deformation theory, enforcing the condition of inextentionality employing the J2DT to model material behaviour. Fabian (1981) employed similar kinematics and used the J2FT. Motivated by the mechanical behaviour of offshore pipelines Kyriakides & Shaw (1982) extensively examined the inelastic bending response of relatively thick-walled tubes ($15<D/t<80$), accounting for the influence of external pressure. They employed analytical ovalization models based on an inextensional non-linear theory (Brush & Almroth, 1975), using the J2DT to model material plasticity.

Shaw & Kyriakides (1985) and Corona & Kyriakides (1987) extended this study, by adopting an improved kinematic formulation, allowing for large changes of hoop curvatures, and using J2FT as a constitutive model. Karamanos & Tassoulas (1991) investigated the problem using employing “tube” finite elements and offered further numerical verification of the experimental data reported in (Corona & Kyriakides, 1987). Elchalakani et al. (2002) through theoretical models and experiments further demonstrated the role of ovalization instability in the behaviour of thick-walled cylinders. They indicated that for reliable modelling of the ovalization behaviour of thick-walled cylinders, closed form solutions may be insufficiently detailed. Wang et al. (2018) considered the influence of ovalization in the moment resistance of thick-walled under bending in the inelastic range using finite elements.

Experiments by (Kyriakides & Ju, 1992; Reddy, 1979) indicated that ovalization analyses may be inadequate to investigate the bending behaviours for metal tubes with D/t values higher than about 45. These cylinders may experience local buckling in the form of tube-wall wrinkling, before reaching the ovalisation limit moment. During bending, axial stresses increase at the compression side of the cylinder can lead to a shell-type instability, characterized by the formation of a wave pattern, referred to as ‘local bucking’ or ‘wrinkling’. This is a bifurcation problem, and the developed buckling mode is

characterized by short-wavelength wrinkles forming periodically along the cylindrical shell (Figure 5.1). They have a maximum amplitude at the compression side of the cross section and gradually diminish around the circumference. The wrinkle development reduces the section rigidity, while its interaction with geometric imperfections can have a significant influence in the buckling of the cylinders. Bifurcation instability in bending is more pronounced in long cylinders, free from boundary conditions.

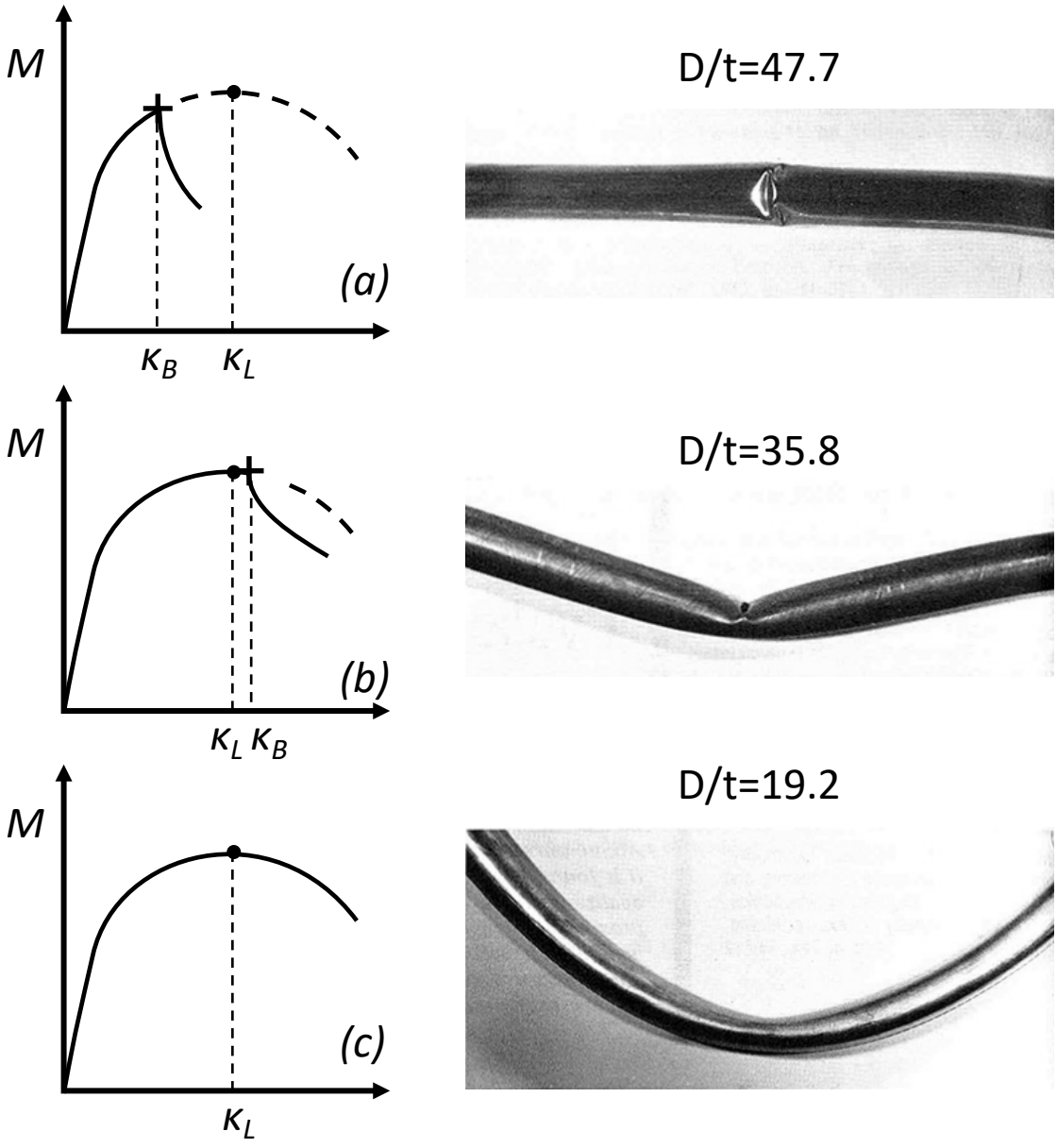

Figure 5.2: Typical moment curvature behaviours and bucking modes of thick-walled tubes, images from Kyriakides & Shaw (1987)

Bifurcation from the ovalization primary path may occur either before or beyond the ovalization limit load instability, depending on cylinder's D/t ratio. For the less thick-walled shells under consideration (D/t>45), bifurcation and short wavelength wrinkling

precede limit load instability, and occur at progressively lower curvatures for increasing values of D/t. For the more thin-walled shells, the wrinkle development is followed by an immediate drop in the moment capacity of the shell, localized deformation in one main buckle and failure in a "diamond" mode (Figure 5.2a), similar to thin-walled elastic cylinders.

Numerical studies on the uniform wrinkling of bent cylinders were reported by (Gellin, 1980), where bifurcation in the inelastic range was detected at loads lower than the ovalization limit point. Fabian (1981) further considered inelastic stability under combined bending and pressure, employing the J2FT for the moment-curvature path and J2DT for bifurcation calculations. The experimental work by Reddy (1979) elucidates the plastic buckling of thick-walled steel and aluminium cylinders ($30< D/t <80$) under monotonic pure bending. He observed considerable scatter in terms of critical strains, and noted variations in the wrinkling wavelengths when comparing between experimental values and estimates obtained using both J2DT and J2FT, based on the tubes' bifurcation under compression.

Ju & Kyriakides (1992) investigated experimentally the bending, ovalization and wrinkling of cylinders with $20< D/t <60$. They performed carefully controlled experiments on aluminium cylinders, and monitored their structural behaviour until failure. Bifurcation instability in the plastic regime was recorded before or after the ovalization limit point, dependent on the cylinders D/t ratio. Ju & Kyriakides (1992b) followingly successfully modelled these experiments employing a semi-numerical model and considered the main parameters that influence the failure of cylinders. The inelastic material behaviour was modelled using J2FT to trace the moment-curvature response (equilibrium path) and the J2DT moduli were employed to estimate bifurcation. This approach was used by (Houliara, 2008) in the bending of relatively thick cylinders using a finite-element formulation.

Karamanos & Tassoulas (1996) & Limam et al. (2010) examined the structural response of tubes under monotonic bending and pressure. Sadowski & Rotter (2013) investigated the non-linear plastic buckling behaviour of thick-walled tubes under bending and demonstrated the computational efficiency and the reliability of shell elements. The disparity between experimental values and numerical predictions on the wrinkling wavelength noted by (Ju & Kyriakides, 1992; Reddy, 1979) was re-examined in the work of (Corona et al., 2006) and was attributed to the effects of anisotropy. The book by (Kyriakides & Corona, 2007) provides a concise overview of the problem of buckling

and collapse of inelastic cylinders, and summarizes the previous experimental and semi-numerical studies.

To reliably predict the behaviour of cylinders under bending, the intrinsic issue of describing accurately the uniform ovalization induced by bending need to be addressed, in a consistent manner with bifurcation instabilities. More specifically, the study of the buckling and the subsequent post-buckling behaviour, leading to failure, demand accounting for the onset, growth and localization of wrinkling which is significantly affected by the ovalization process. Towards this purpose, the importance of the constitutive modelling becomes clearer, as considerable inelastic deformations and non-proportional loading take place. Prediction of ovalization localization, associated with the natural limit load for thicker shells, and its interaction with wrinkling, for shells with a wide range of D/t values, must be addressed in the analyses.

5.1 Finite Element Modelling

Geometrically and materially nonlinear analyses are performed using the implicit static solver in Abaqus 2016 to simulate the structural response of the thick-walled circular cylinders under bending. Four-node thick shell elements (S4) with finite membrane strains are employed. The inelastic material properties are introduced into Abaqus in the form of true stress and logarithmic plastic strain and used in the context of a material user subroutine UMAT, employing the non-associative constitutive law (J2NA) developed in previous paragraphs. Several low values are considered for parameter θ_c, leading to the use of a value of 2^o which provided good results in both problems of compression and bending.

Finite element meshes are chosen to employ approximately 12 elements per $\sqrt{Dt}$ of length, and 144 elements around the circumference, with 7 integration points across the thickness, found sufficient to accurately capture the buckling behaviour of the cylinders, while maintaining computational efficiency. To study both (a) initial instability in the form of wrinkling and (b) post-buckling and depending on the geometry the transition into non-symmetric buckling modes with circumferential waves, characteristic in the less thick-walled shells, an entire cylindrical shell segment is modelled, without half-symmetry assumptions. Initial geometric imperfection is accounted for, in the form of the wrinkled shape eigenmode, obtained at the bifurcation point of the geometrically perfect shells, appropriately modulated.

The finite element models are subjected to pure bending, under a rotation-controlled loading scheme. A simply supported static system is adopted. Reference points are placed at the geometric centres of the two ends of the model. The end-cross-section-nodes are kinematically coupled to the reference nodes, as in Figure 5.3, imposing kinematic constrains that keep the end cross sections plane, while allowing for the cross section to ovalize in its rotated plane. This simulates the response of a long cylinder, minimizing the influence of the mesh length. A few models were developed with capped ends (assuming rigid plates at the models ends, obstructing all-sectional deformation in the rotated section plane), which are named appropriately in the following paragraphs.

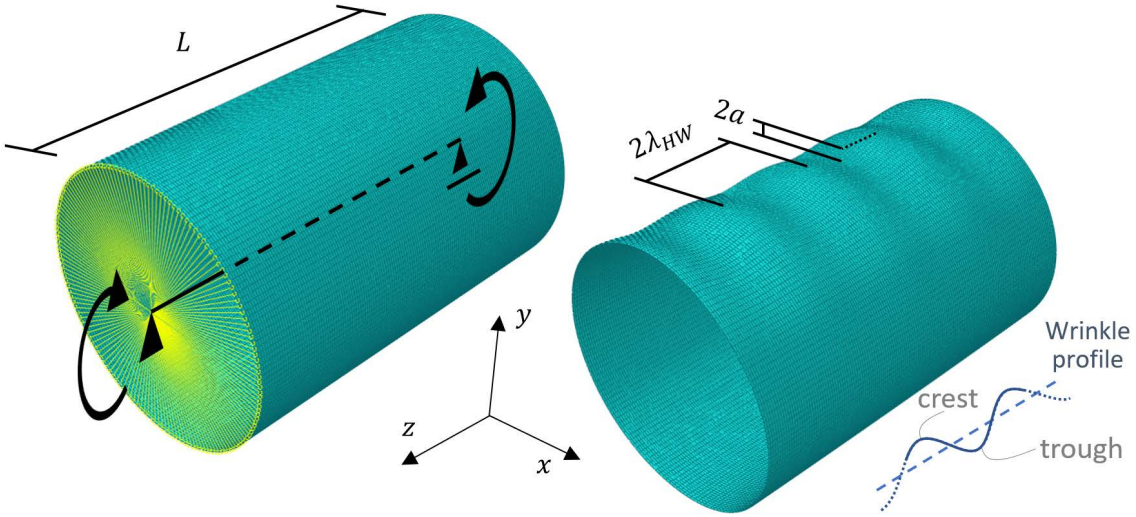

Figure 5.3: Wrinkling of geometrically perfect tube segment under bending

5.2 Uniform ovalization and non-proportionality

A primary requirement for predicting accurately the structural response of long cylindrical shells under bending, is tracing the prebuckling equilibrium path. In the absence of initial geometric imperfection, their length ovalizes uniformly, as their cross section is bent due to the loading. The longitudinal uniformity implies that the length of the employed meshes has little influence in the predicted response, assuming appropriate end conditions. Simulations employing meshes with length ranging from 10% to 300% of the tube diameter display virtually no differences in the overall moment-curvature ($m - k$) behaviour of the shells, when no buckling or wrinkle development take place (Figure 5.4), provided that the chosen meshes are fine enough in the circumferential direction to adequately describe the deformation of the tube. Hence, the influence of the constitutive law in the ovalization of the cylinders is investigated in this stage and the extend of non-proportionality that is encountered.

Table 5.1: Geometric and mechanical definitions

t	Cylinder wall thickness
a	Initial geometric imperfection amplitude
D	Cylinder outside diameter
$D_o = D - t$	Cylinder mean diameter
σ_o	0.2% offset yield strength
$M_o = \sigma_o D_o^2 t$	Plastic Moment
$\kappa_1 = t/D_o^2$	Curvature-type normalization parameter

Table 5.2: Material and geometric data for cylindrical shells tested by Ju & Kyriakides (1992)

Exp.No.	D (mm)	D/t	E (GPa)	σ_o (MPa)	$\bar{\sigma}$* (MPa)	n*
1	31.82	60.5	68.95	299.0	298.6	28
2	38.10	52.6	69.64	299.0	298.6	33
3	25.40	50.0	70.67	307.0	307.5	29
4	31.78	44.0	67.20	304.0	303.4	25
5	35.00	38.5	71.02	287.0	285.4	25
6	31.75	35.7	67.36	283.4	282.0	28
7	28.63	32.2	71.16	288.0	286.1	26
8	25.34	28.2	66.20	304.0	303.0	35
9	31.80	25.3	69.16	286.0	284.8	30
10	31.78	21.2	71.16	285.0	284.1	28
11	31.78	19.5	68.67	309.0	308.9	37

*Ramberg-Osgood parameters in eq.(2.60)

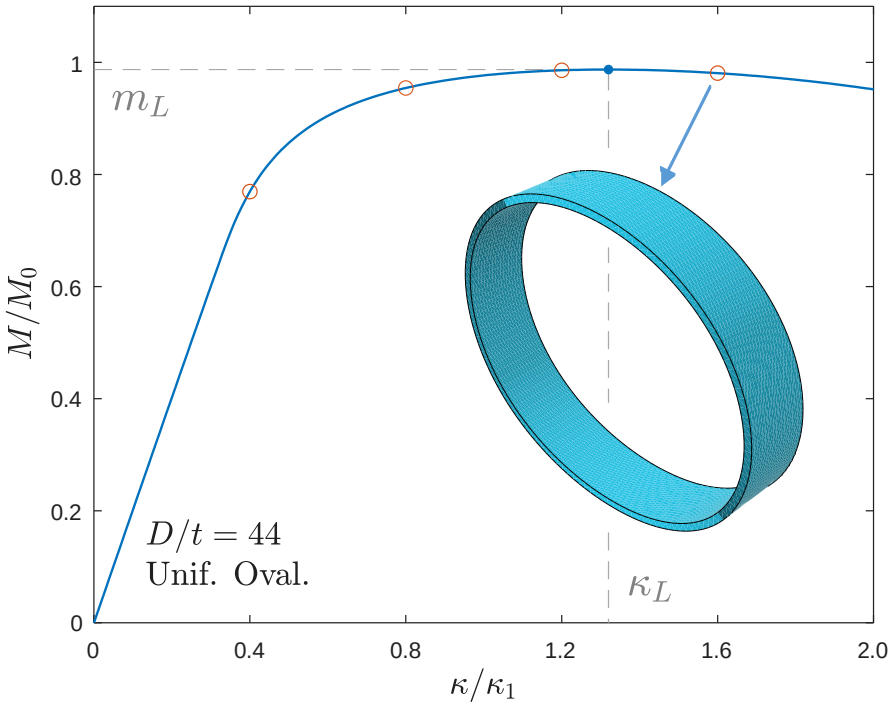

Figure 5.4: Moment-curvature response thick-walled cylinder under bending

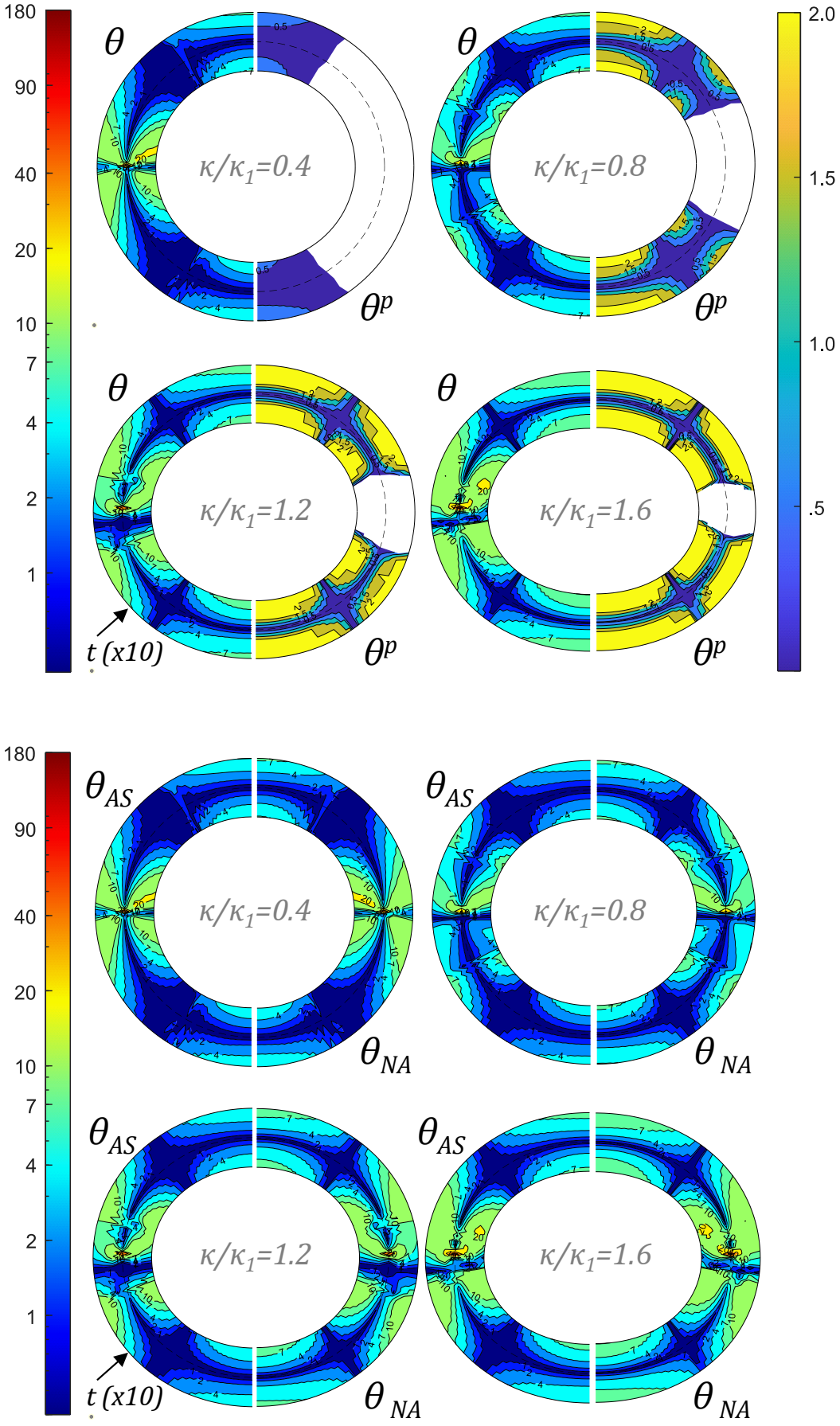

Figure 5.5: Angles θ and θ^p over the cross section of the cylinder; Comparison of angle θ employing the associative (J2FT) versus the non-associative model (J2NA)

In Figure 5.5a angles θ and θ^p are presented at increasing curvatures when employing the J2NA ($\theta_c = 2^o$) in a mid-range cylinder (D/t=44). Geometric and material data for this cylinder and others referenced followingly are provided in Table 5.1. Initially, both the direction angles θ and plastic angle θ^p take small values. At approximately $\kappa/\kappa_1 = 0.6$ ($\kappa_1 = t/D_o^2$ - see Table 5.1), at the intrados (compressed side - top) and the extrados (tensioned side - bottom) of the cross section, ovalization-induced local bending leads to more pronounced non-proportionality, and the second branch of the model is activated so that $\theta^p = \theta_c$, both the inner and outer surface of the cylinder. In contrast, at the mid-surface, the angles θ^p remain small throughout the analysis, implying almost proportional loading. Hence, the main contributor to the non-proportionality is the ovalization-induced hoop bending. As curvature increases, ovalization and hoop bending increase, so that non-proportional load paths develop in a larger part of the cross section. The area about the cylinder's neutral axis where material remains elastic (no θ^p values / marked as white) reduces with increasing curvature, and the greater part of the cross-section experiences non-proportional elastoplastic loading.

In Figure 5.5b a comparison is made at different stages of deformation for the strain angles θ, obtained with J2FT and J2NA models displayed on left- and right-hand-side of the cylinders, respectively. For both constitutive laws, angles θ are initially quite small all around the cross section, apart from the area around the neutral axis where, as expected, the combination of meridional bending and ovalization-induced hoop bending leads to more pronounced non-proportionality. With increasing deformation angles θ increase initially in the 'flattening' top and bottom of the cross section reaching values smaller than $10°$ for both models. Slightly smaller deviations from proportionality are encountered for the J2FT with angles barely exceeding $8°$. The loading paths are more complicated around the neutral zone where the biaxial bending leads to angle θ values in the range up to $20° - 40°$. However, those are encountered mainly in the elastic zone of the material and are of limited interest.

5.2.1 The effect of constitutive model angle θ_c

The plastic angle parameter θ_c of the non-associative constitutive law influences the pre-buckling structural response of the simulated bent cylindrical shell in a limited manner (Figure 5.6). Increasing values of θ_c lead to higher non-associative plastic deformation, which facilitates ovalization of the cross section, lowering somewhat limit moments and deformations in the loaded shells. The prebuckling equilibrium paths are relatively

unaffected by θ_c and all are in agreement with the J2FT and the experiments. The differences are more pronounced at curvatures in the neighbourhood of the cylinder's limit loads. The material is loaded well into the inelastic range and exhibits reduced stiffness, allowing for greater plastic deformations in the presence of the non-proportional loading. This ultimately leads to higher ovalization of the cross section.

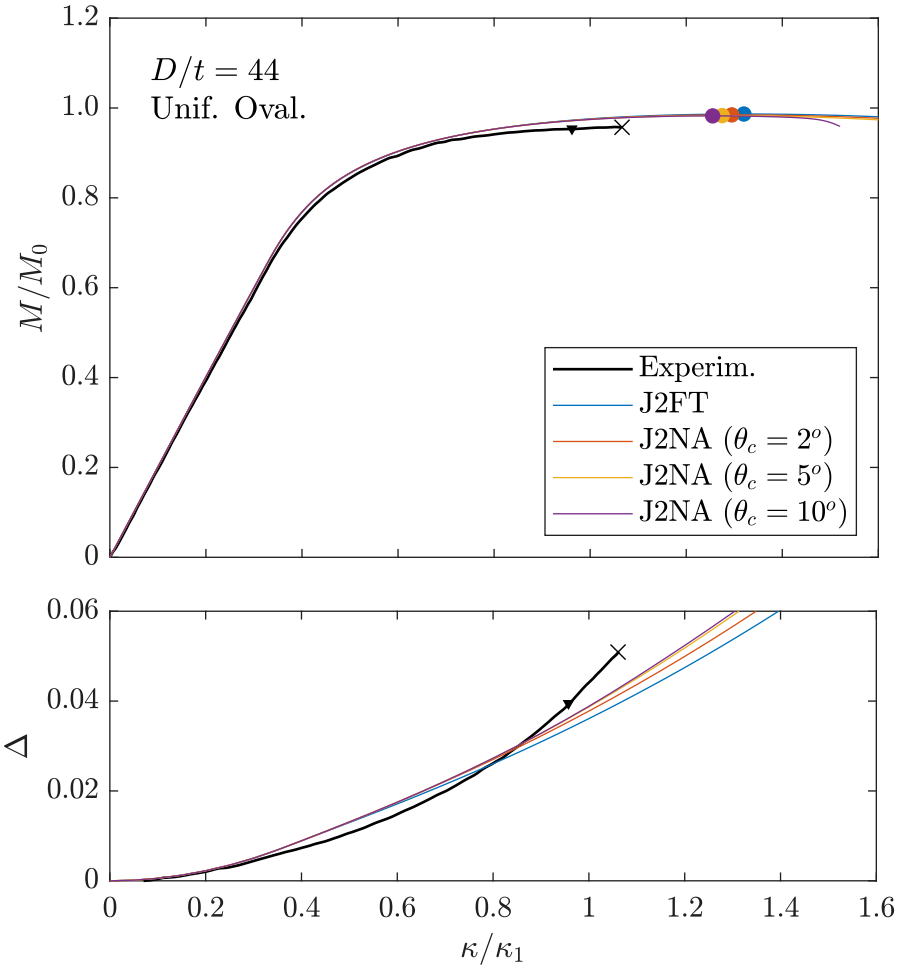

Figure 5.6: Influence of constitutive modelling in the structural response of a cylinder under bending

Figure 5.6 demonstrates the effect of increasing values for the angle $\theta_c = 2^o, 5^o, 10^o$ in the prebuckling equilibrium path, characterized by uniform ovalization of a moderately thick aluminium shell with $D/t = 44$. The experimental curve of this cylinder by (Ju & Kyriakides, 1992) is included. The reported wrinkling and failure are indicated with (▾) and (x), respectively. As in the case of compression, in bending a low value $\theta_c = 2°$ leads to slightly more compliant responses than the J2FT in the overall behaviour of the cylinder, in line with experiments. For all angles θ_c, the pre-limit-load path is practically unaffected, while increasing values θ_c gradually reduce the limit load m_L and limit

curvature κ_L for the cylinders. Differences with respect to J2FT become noticeable at deformations levels in the neighbourhood of the limit moment m_L.

Similarly, the J2NA leads to more pronounced ovalization, defined in (5.1), of the bent cylinders' cross-section. Higher values of θ_c lead to higher ovalization throughout the curvature range in Figure 5.6, approaching marginally more the trend of the experimental curve.

$$\Delta = \frac{D_{max} - D_{min}}{D_{max} + D_{min}} \tag{5.1}$$

A similar influence of θ_c is encountered in the entire range of D/t under consideration, when geometrically perfect shells are addressed. In Figure 5.7 the moment-curvature response of tubes with D/t values of 25.3 and 60.5 are given for a wider range for the semi-angle parameter θ_c ($2^o - 18^o$). Its influence is limited in the initial moment-curvature response of the cylinder, assuming uniform ovalization, but it becomes more pronounced at higher curvatures, following the formation of the limit load.

For D/t=60.5, following the limit load m_L, more pronounced differences are predicted in the structural response of the tube segment, depending on the adopted value θ_c. For all θ_c values, the response is less stiff compared to the J2FT, but for $\theta_c = 2°$, the differences are modest. Intermediate angles θ_c lead to more compliant behaviours, while for values of $\theta_c \geq 10°$, the predicted structural responses group together with minimal differences. In these cases, similar to the contours in Figure 5.5 for D/t=44, the loading path of the material in several locations is non-proportional. However, non-proportionality is limited and does not lead to direction angles θ in excess of 10°, so for models with $\theta_c \geq 10^o$ only one branch of the model is activated, and they all produce practically identical behaviours, as shown in paragraph 3.4.1. Less pronounced differences are found in the uniform ovalization behaviour of the more thick-walled shell D/t=25.3 (Figure 5.7).

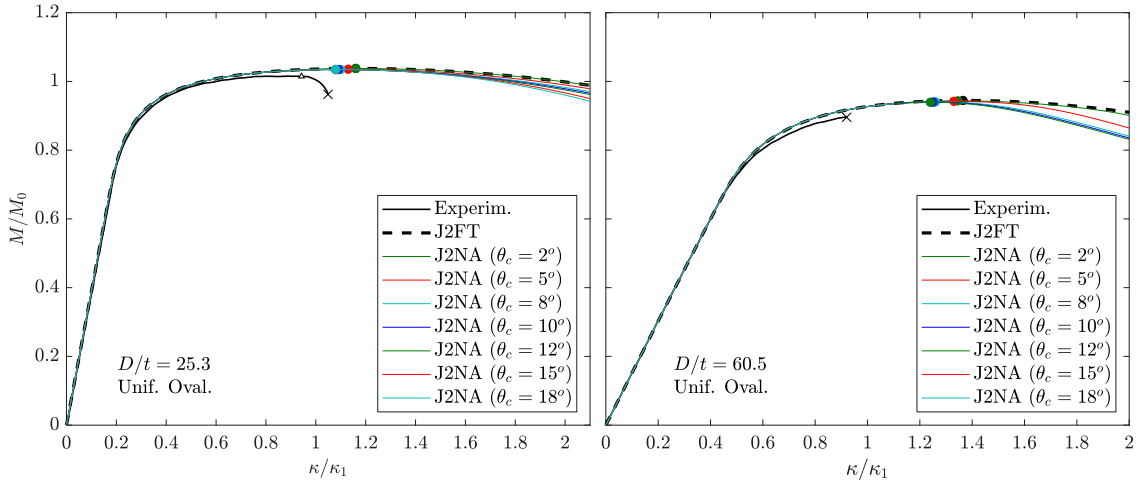

Figure 5.7: Effect of constitutive modelling parameter θ_c in the structural response of cylinders under bending

5.3 Bifurcation analysis and uniform wrinkling

Perturbation analyses are performed at regular deformation intervals to identify the lowest eigenvalues of the cylinder model. The occurrence of non-positive eigenvalues denotes instability, and the curvature at which the first non-positive eigenvalues occur is the shell's bifurcation curvature κ_b. The associated eigenmode is characterized by wrinkling of the compressed side of the cylinders (Figure 5.3). The number of halfwaves N_{HW} is used to define the wrinkling halfwave length of the shell $\lambda_{HW} = L/N_{HW}$.

In simulating 'long' tube segments any stiffening influence from the support conditions should be alleviated in order to obtain accurate bifurcation estimates. Indeed, considering bending of models with length $L = 3D$ and monitoring their eigenvalues at curvature intervals of $0.01\kappa_1$, the bifurcation curvature and the halfwave are identified for several cylinders tested by (Ju & Kyriakides, 1992). At bifurcation, these models develop 1-3 non-positive eigenvalues simultaneously, with associated eigenmodes of 11-19 halfwaves forming along the compressed side of the shells (Table 5.3). Hence, long models can provide a range for the wrinkling wavelength, which in Figure 5.8 is seen to be consistent with the predictions by Ju & Kyriakides (1992), indicating the effectiveness of this method. The predicted λ_{HW} are uniformly longer than the ones measured experimentally. This discrepancy was also met in tubes under compression, and it can be addressed by further accounting for material anisotropy due to the manufacturing process (Bardi & Kyriakides, 2006; Corona et al., 2006; Kyriakides et al., 2005). In Figure 5.8 the ratio of the experimentally calculated to the numerically estimated halfwave length is given.

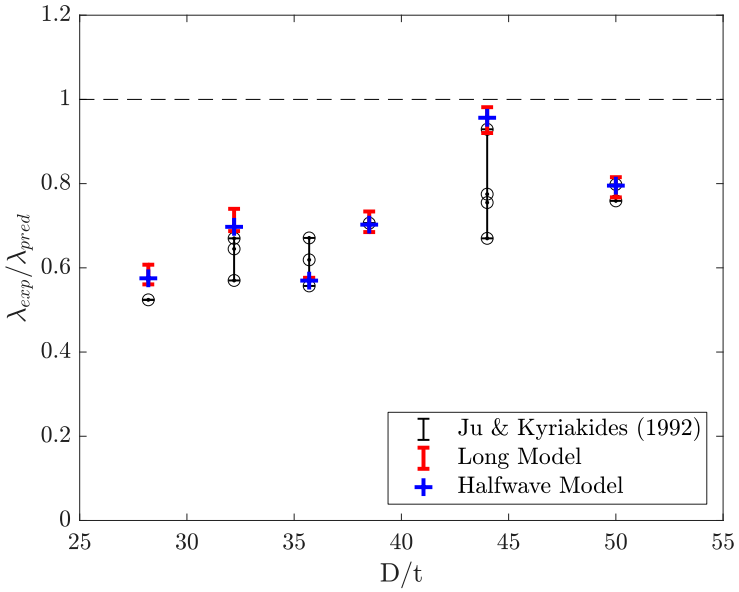

Figure 5.8: Comparison of predicted and experimental wavelength of long thick-walled cylinders under bending

Table 5.3: Bifurcation data for cylinders tested by Ju & Kyriakides (1992)

No	D/t	$\frac{\kappa_b}{\kappa_1}$	$\frac{\kappa_b}{\kappa_1}\Big\vert_{exp}$	$\frac{N_{HW}}{L}$	$\frac{\lambda_{HW}}{\sqrt{Dt}}$	$\frac{\lambda_{HW}\vert_{exp}}{\sqrt{Dt}}$
1	60.5	1.05		18, 19	1.21 - 1.27	
2	52.6	1.03		18, 17, 16	1.19 -1.33	
3	50.0	1.05	0.91	17, 16	1.22 -1.30	0.997
4	44.0	1.09	0.95	16, 15	1.22 -1.30	1.193
5	38.5	1.10	0.95	15, 14	1.21 -1.30	0.887
6	35.7	1.09	0.96	14	1.24	0.717
7	32.2	1.13	0.94	14, 13	1.18 -1.27	0.872
8	28.2	1.11	0.89	13, 12	1.18 -1.28	0.718
9	25.3	1.17		12	1.21	
10	21.2	1.26		11	1.20	
11	19.5	1.26		11	1.14	

Similar bifurcation calculations using the J2FT yield unrealistically high values of critical moments, curvatures and longer critical λ_{HW}. Such a result is also reported in for thick-walled shells under axial compression in Chapter 4. Moderate variations of the model length L do not affect the bifurcation curvature κ_b, but can affect the number of negative eigenvalues and the number of forming waves. Therefore, no single value can be obtained for λ_{HW} from long models. A more precise investigation on λ_{HW} may be performed by adopting 'short' meshes of approximately one halfwave. The wavelength is not known a priori and, therefore, a sequence of analyses is conducted, assuming for several trial wavelength values. The critical wavelength corresponds to the 'earliest' bifurcation point

on the primary path, occurring at the lowest moment capacity (Karamanos & Tassoulas, 1996).

The periodicity of winkling can be modelled accurately by the assumed support conditions when the model length is an integer multiple of λ_{HW}. As shown in Figure 5.9, for the shell with D/t=44 and models with length raging between $0.8\sqrt{Dt}$ and $1.8\sqrt{Dt}$, have been analysed to identify bifurcation halfwave of the shell. All meshes with length of $1.18\sqrt{Dt}$ up to $1.32\sqrt{Dt}$, experience bifurcation at the critical curvature $1.08\,\kappa_1$, which was also identified by longer simulated segments. This is the lowest recorded value by the one-halfwave models. Slightly shorter and longer meshes experience bifurcation at higher curvatures up to 23% higher ($0.25\kappa_1$), as the non-critical lengths together with the symmetry conditions stiffen the model's response.

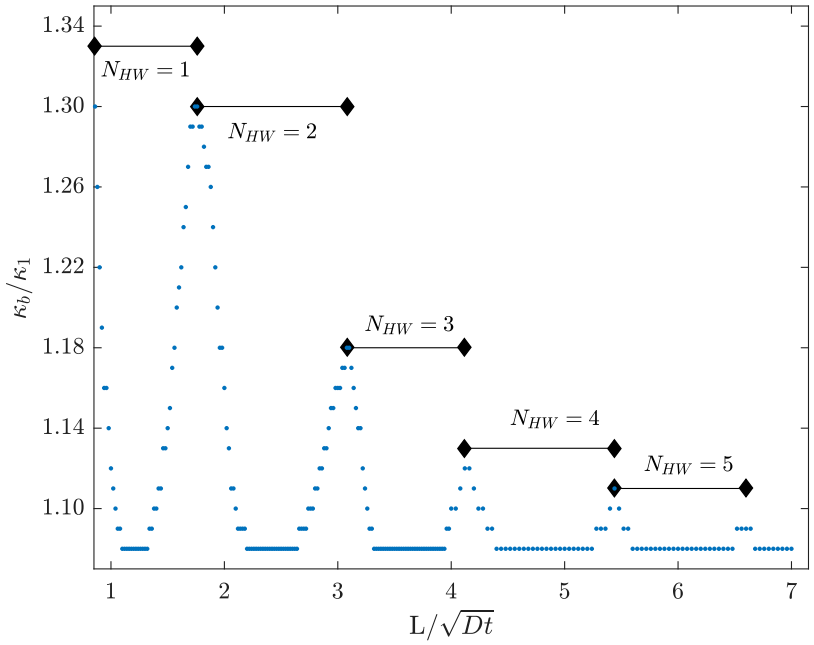

Figure 5.9: Bifurcation curvature versus the length of the simulated tube segment

Considering longer shell segments with $L/\sqrt{Dt}$ ranging from 1.8 to 7.0, while maintaining the element size approximately constant, the earliest bifurcation is similarly recorded at $\kappa_b = 1.08\kappa_1$. For segments with $L/\sqrt{Dt} \geq 6$, the bifurcation curvature κ_b is relatively insensitive to the segment length and it quickly converges to the value obtained for long shells ($L = 3D$). At bifurcation these meshes develop two or more halfwaves along the tube segment. As expected, the λ_{HW} values computed by the longer modes are always within the length range calculated by the one-halfwave models.

It is algebraically calculated that any model length $L \geq 10\sqrt{Dt}$ is an integer multiple of a

value in the range of critical λ_{HW} obtained by the shorter halfwave models, and as a result has the same bifurcation curvature κ_b, under a fixed frequency of bifurcation checks. This further supports the concept of using long models to produce accurate estimates for κ_b, and explains the occurrence of multiple negative eigenmodes: the long model's length can be an integer multiple of different values in the range calculated by the one halfwave models.

Further accuracy in the calculation of κ_b is obtained by performing bifurcation analyses at smaller deformation intervals, i.e., $0.001\kappa_1$, leading to more precise values for λ_{HW}. In Figure 5.8, the 'precise' λ_{HW} obtained from one-halfwave models in this way is included and is always within the expected ranges. The exaggerated buckling mode in the cross section of two cylinders is shown in Figure 5.10. The part of the cross section affected by buckling is larger for thicker cylinders (lower values of D/t). The same effect was found in elastic shells by (Houliara & Karamanos, 2006).

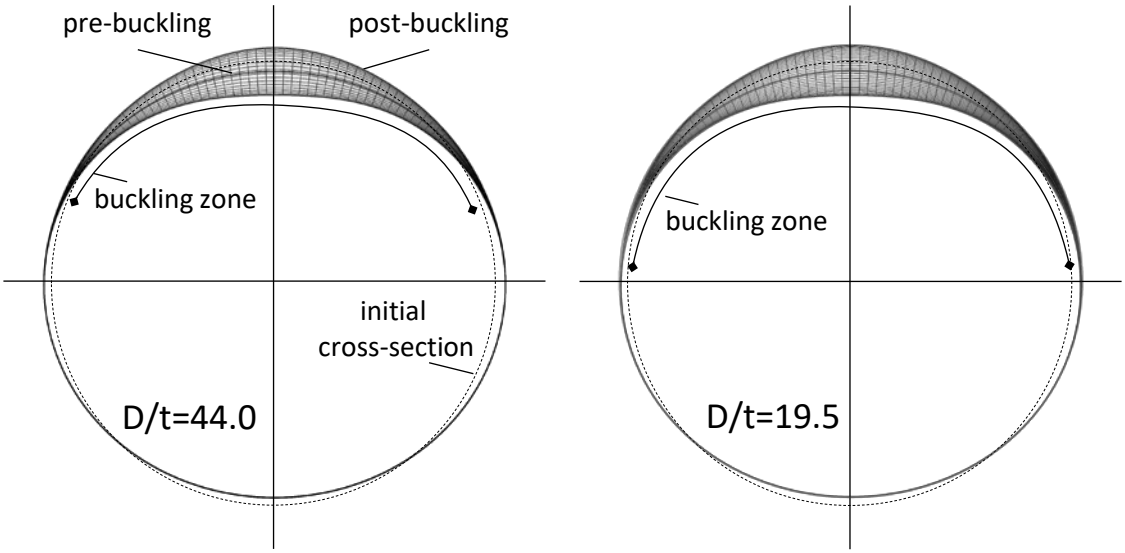

Figure 5.10: Buckling in the cylinder cross section under pure bending

5.3.1 Influence of imperfection

Buckling includes non-uniform deformation along the shell, which grows in the developing wrinkles at the compressed side. In a first approach, axial wrinkles are assumed to grow periodically along the bent shell, and therefore a single halfwave segment ($L = \lambda_{HW}$) may be analysed. Considering λ_{HW} values in the above calculated range has very limited influence on the uniform wrinkling response of the shell, irrespective of the level of initial geometric imperfection (Figure 5.11). The imperfection is in the shape of the eigenmode obtained from the perturbation analyses in the previous paragraph, and three amplitudes are considered with respect to the shell radius: $\omega_R =$

$a/R = 0.5,\ 1,\ 3‰$, which are similar to the ones used in compression and they were considered by the experimenters as representative. For any given imperfection amplitude, using wrinkling wavelengths in the obtained range produces very small differences in the limit moment m_L and curvature κ_L, less than 1% (Figure 5.11b).

The imperfection amplitude affects the moment-curvature response of the cylinders, as in the case of compression, mainly in the inelastic part of the response and as bending deformation increases, the imperfect cylinder response becomes more compliant. Both the value of the maximum moment m_L and the curvature κ_L at which it develops progressively reduce for increasing imperfection amplitudes.

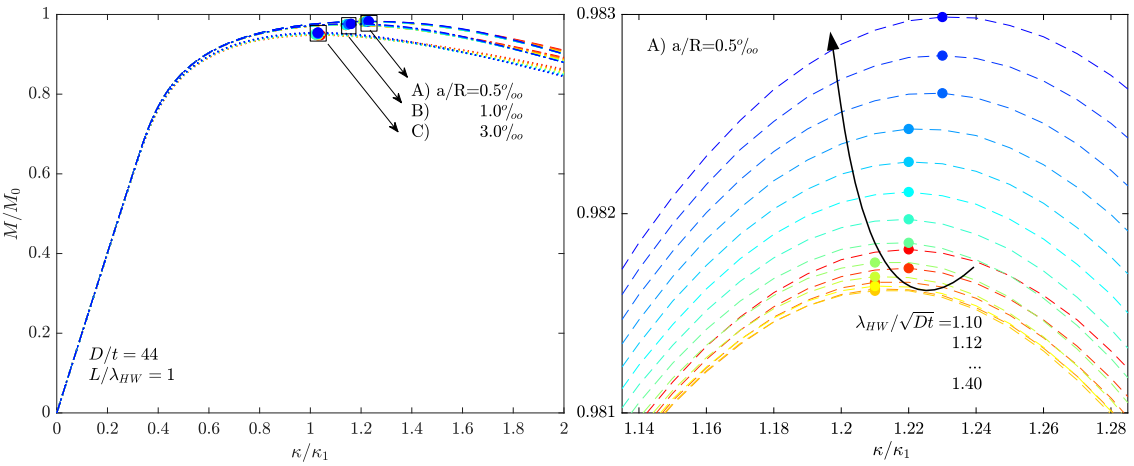

Figure 5.11: Influence of imperfection amplitude and wavelength in the uniform wrinkling of a cylinder under bending

5.3.2 Non-proportional loading

In the imperfect cylinders, non-proportionality, as expressed by angle θ, is higher than in the geometrically perfect uniform ovalizing shell, and it varies along the cylinder depending on the position of the cross section. At the crests and troughs of the wrinkles, material experiences complicated stress paths due to biaxial local bending and the meridional compression from global bending. Figure 5.12 shows the values of angle measures θ and θ^p around the cross-section at these two critical positions, at various levels of deformation in the wrinkled cylinder (D/t=44). For visualization purposes, the shell thickness is magnified ten times in the plots.

At a low curvature ($\kappa/\kappa_1 = 0.4$), values of θ in the wrinkled shell are significantly higher, compared to the uniform ovalizing case, and they are not symmetric with respect to the cylinder mid surface. In particular, at the position of the wrinkle trough, non-

proportionality angle θ reaching values of more than $10°$ in an extended part of the section intrados. Therefore, higher plastic strains are predicted than J2FT and the second branch of the constitutive law ($\theta^p = 2^o$) is activated already at this stage. Higher values θ are encountered at the inner surface of the shell at this position, yet the angles θ^p do not reach θ_c. This is caused by the non-uniform stress distribution across the thickness of the shell. The inner surface experiences lower compression because of wrinkling-induced local bending and as a result it has not deformed plastically as much as the outside surface, and the material response is stiffer at lower plastic deformations. At the crest of the wrinkles, lower values of θ are seen across the cylinder thickness. At material points located about the bending axis, insignificant differences are encountered between the two cross sections, though angles θ take somewhat higher values.

In the wrinkle trough, at curvature $\kappa/\kappa_1 = 0.8$ the compressed side of the cylinder shows direction angles θ as high as $20°$ at the outer surface. Angles larger than $90°$ are found at the inner surface, implying unloading has initiated in this part of the section. Non-proportionality is high enough, so that the second branch of the model is activated almost in the entire compressed side of the shell, both at the crest and at the trough of the imperfection.

By curvature $\kappa/\kappa_1 = 1.2$, the moment capacity of the section has begun to decrease and ovalization is visible in Figure 5.12. Unloading occurs in an extended area of the inner surface at the wrinkle trough, but also at the outer surface of the wrinkle crest starting at the symmetry axis and expanding circumferentially with increasing deformation. Throughout the deformation, in the neutral axis, the material remains elastic, so the high values θ are of no interest.

In the bottom part of the cylinder, (extrados) which is loaded in tension due to flexural bending, the loading paths are practically unaffected by the wrinkling. Angles θ are very similar to the uniform ovalization case particularly before κ_b, with slight increases of up to 2^o for $\kappa/\kappa_1 \geq 1.2$.

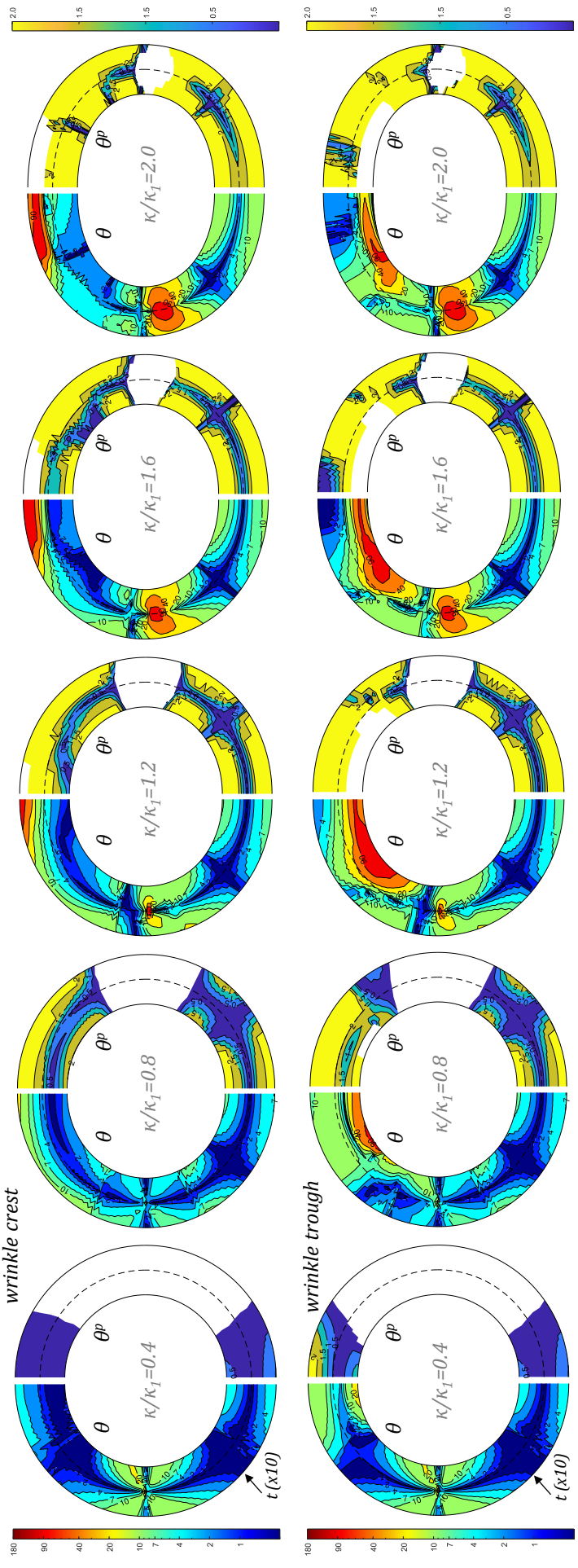

Figure 5.12: Angles θ and θ^p around the cross section of the imperfect cylinder, at the crest and trough of wrinkles.

5.3.3 Non-symmetric bifurcation modes

The thinner shells under consideration ($D/t \geq 44$) develop wrinkles at an increasing load, soon followed by buckling into a diamond mode, developing one sharp local buckle characterized by a number of circumferential waves. To investigate bifurcation into non-symmetric buckling modes, these are assumed to be periodically repeated along a cylinder with an axial wavelength twice that of the uniform wrinkling value (Gellin, 1979). Hence a two-halfwave ($L = 2\lambda_{HW}$) geometrically perfect model is subjected to bending under a rotation-controlled regime and the occurrence of negative eigenvalues is monitored, as in the previous section. Figure 5.13 presents the curvatures at which the cylinder segment experiences bifurcation, together with the corresponding bifurcation modes.

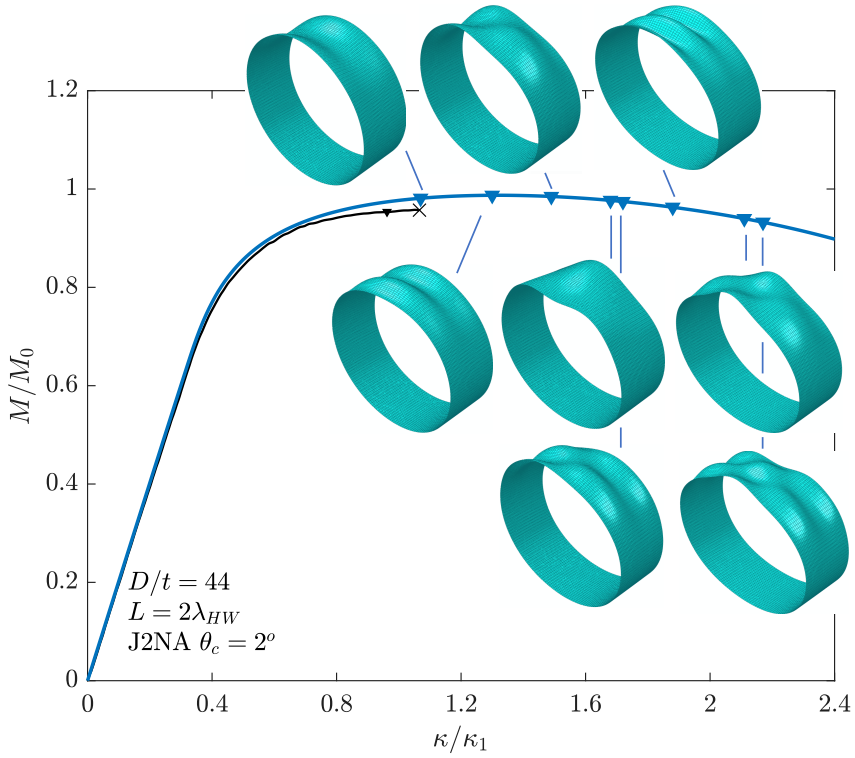

Figure 5.13: Bifurcation into non-symmetric modes

Following the first bifurcation, several negative eigenvalues are recorded with increasing curvature, both before and after the load maximum of the cylinder. The sequence of the buckling modes is similar to the one obtained from analyses of compressed cylinders. The first eigenmode is associated with uniform wrinkling of the compressed side of the shell, developing longitudinal waves of halfwave λ_{HW} at the bifurcation curvature κ_b, which was obtained from previous simpler analyses. At progressively higher curvatures, buckling modes develop, characterized by increasing numbers of circumferential waves and smaller longitudinal wavelengths.

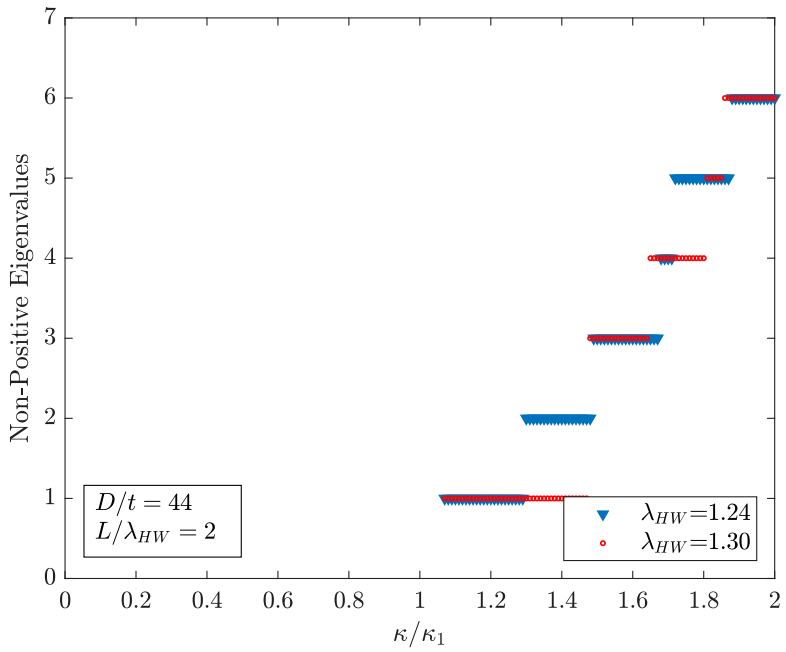

Figure 5.14: Effect of the simulated halfwave length λ_{HW} in the development of non-symmetric bifurcation modes

Small perturbations on the model length do not affect the first bifurcation into uniform wrinkling, as shown in Figure 5.14. However, they may affect the curvature at which the following eigenmodes might occur. They can somewhat delay or accelerate the occurrence of following bifurcation mode shapes. The curvature difference is not substantial, and the sequence of which buckling modes is not altered. Estimating bifurcation directly in much longer cylinder segments (several halfwaves long) is considerably more computationally expensive, and it can be more complicated. The first bifurcation occurs at the calculated curvature κ_b in a uniform wrinkled mode. Yet, additional eigenmodes may be obtained followingly, that do not always directly relate to the ones obtained by the two halfwave models but may represent superposition of several eigenmodes.

When employing the two-halfwave model, estimating bifurcation of cylinders, with imperfection in the shape of the first bifurcation mode, leads to secondary bifurcation generally recorded at somewhat higher curvatures than the respective ones in the geometrically perfect shell. In imperfect shells, the obtained eigenmodes are similar to the respective of the geometrically perfect cylindrical shell, with the imperfection profile superimposed, as shown in Figure 5.15. The sequence of the eigenmodes of the imperfect cylinder segments is not altered.

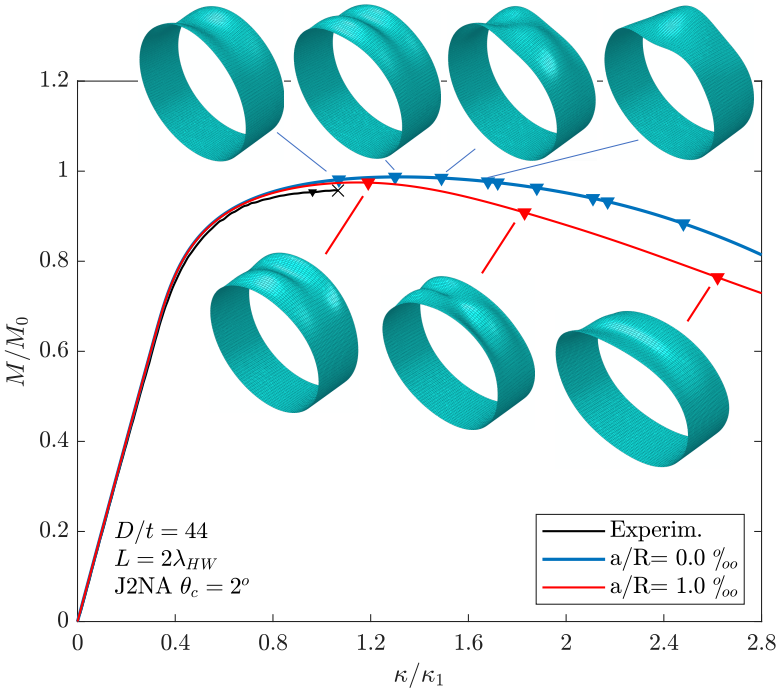

Figure 5.15: Buckling of imperfect cylinders into non-symmetric modes

5.4 Wrinkling localization and influence of imperfection

To investigate localization of wrinkling, long models ($L \geq 16\lambda_{HW}$) are subjected to bending. Symmetry support conditions are used, as described earlier. Imperfection in the form of the uniform wrinkling eigenmode is employed, which was obtained from a bifurcation analysis of the perfect shell. Three imperfection amplitudes are considered $\omega_R = a/R = 0.5,\ 1,\ 3$ ‰. Results are obtained using two constitutive models: the developed J2NA juxtaposed with the J2FT. A $3\%\omega_R$ imperfection bias is implemented midway along the cylinder, to incite localization far from the end supports. Maximum imperfection directed both inward and outward the shell is considered and its influence in the structural response of the cylinders is presented.

In Figure 5.16, the characteristic structural response of the thinner cylinder ($D/t = 60.5$) is demonstrated. Initially the shell ovalizes uniformly and ovalization grows non-linearly with curvature, in agreement with the behaviours from shorter models. In the neighbourhood of the perfect shell's bifurcation curvature κ_b, at increasing moment, the wrinkles at compressed side of the shell grow in amplitude uniformly and bending rigidity is reduced. Followingly, deformation localizes at the mid-length wrinkles: the amplitude of the wrinkles and the ovalization of the cross section increases rapidly and locally. A maximum moment develops, and a steep drop is recorded in the cylinder's $m - k$ response. The load maximum is slightly lower to the one obtained for uniform wrinkling,

due to the slightly higher imperfection amplitude, and significantly lower to the uniform ovalization limit load of the shell, as induced by the Brazier effect alone.

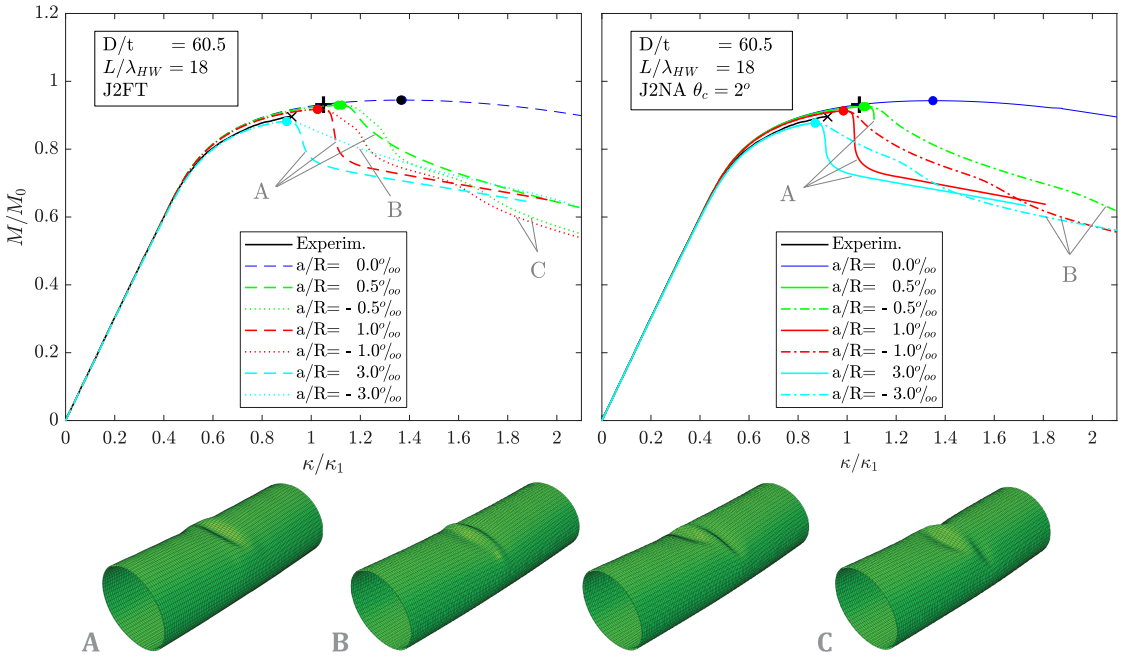

Figure 5.16: Effect of imperfection in the structural response of a thin-walled cylinder under bending using J2FT and J2NA.

Maximum inward imperfections (wrinkle troughs) lead to buckled shapes where a single symmetric inward buckle develops at the position of the deepest wrinkle, see Figure 5.16A. The deformation is localized, leading to a dropping branch in the moment-curvature behaviour of the shell. Increasing imperfection amplitudes leave the shells maximum moment relatively unaffected, but the curvatures at which they occur become smaller and the developing buckles become more pronounced. Following the load maximum, the recorded drop in the moment capacity of the cylinder is precipitous.

Maximum outwards imperfection produces a somewhat stiffer behaviour. When deformation localizes at the (mid-length) location of the maximum outward wrinkle, it allows for imperceptibly higher load maxima and limit curvatures, and the cylinder moment capacity reduces less abruptly. At the moment maximum, the outward imperfection stops developing as rapidly and two inward buckles start forming eccentrically, either both on one side of the buckle, or one in each side of the outward wrinkle begin to develop anti-symmetrically and, on the two sides of the maximum wrinkle Figure 5.16B.

Similarly, buckling in a diamond shape occurs, forming one inward buckle centrally on one side of the localizing maximum imperfection, and two eccentric buckles in the other

side. These modes of buckling are observed experimentally in the thinner tubes with $D/t \geq 50$ by (Ju & Kyriakides, 1992). In analyses the transition to diamond buckling modes can be incited earlier by the addition of small non-symmetric geometric imperfections corresponding to the buckling shape.

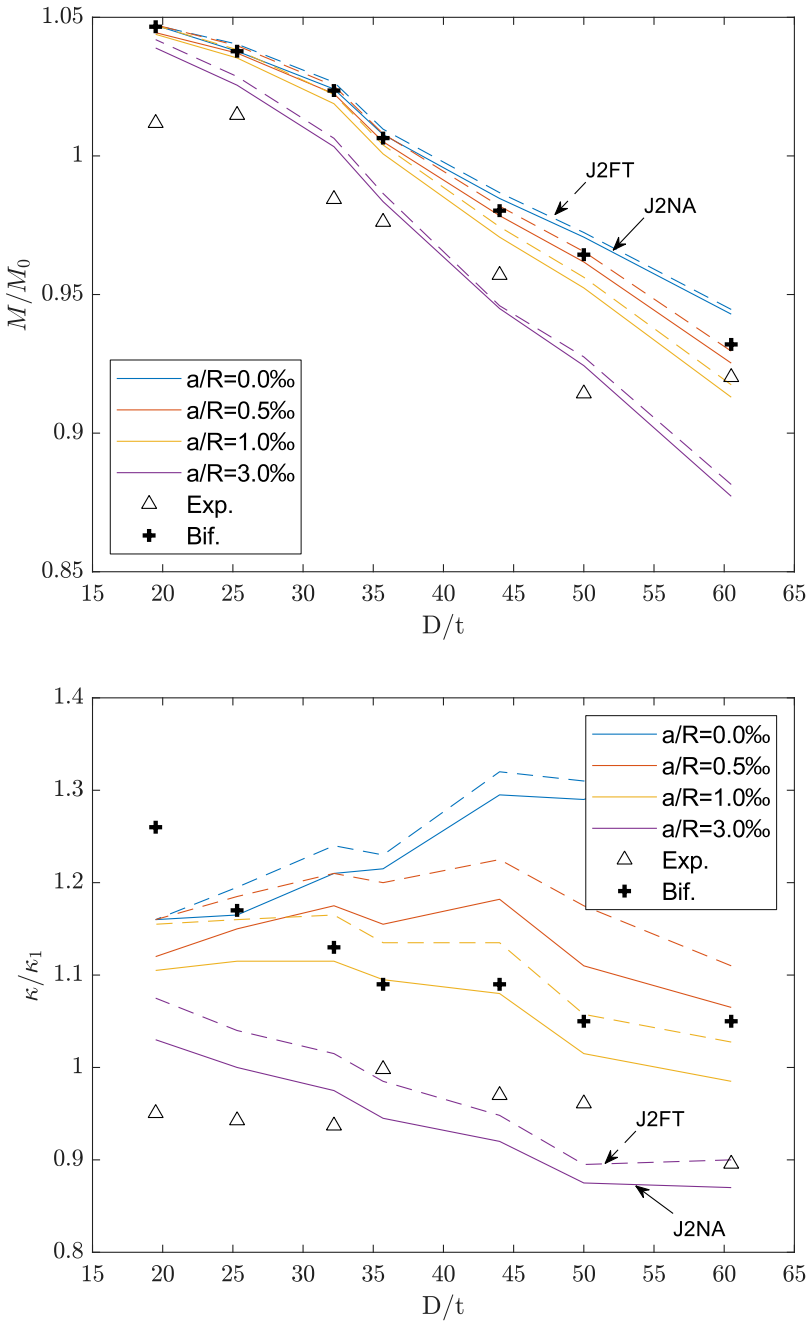

Figure 5.17: Limit moment and curvature of cylinders versus D/t ratio

In Figure 5.17 the influence of the wrinkling imperfection amplitude in the limit (maximum) load and curvature of the cylinders is plotted with respect to the D/t ratio. Significant reduction is found in the cylinder ultimate moment capacity and limit curvature with increasing imperfection for the thinner cylinders ($D/t \geq 40$). In these cylinders bifurcation instability precedes the ovalization instability, and localization initiates immediately, close to the wrinkling bifurcation point. Following the moment maximum, the drop in the moment capacity of the cylinder is also very abrupt. Section failure (marked in Figure 5.18 when the moment capacity in the cylinder drops by 5%) occurs immediately after the limit point in thin cylinders but not in the thicker cylinders ($D/t < 30$). In those, the overall effect of outward geometric imperfection is similar: leading to a maximum inward dent developing at the location of maximum imperfection trough where ovalization localizes and deformations increase rapidly, but significant additional bending deformation is sustained before section failure. Imperfection has small influence in the $m-k$ response of the thicker cylinders, only slightly affecting the ultimate moment capacity and the limit curvature. This is justified by the bifurcation point shown to occur after the limit load instability in thick cylinders, so ultimate load capacity is mainly the result of ovalization and demands additional investigation in the next paragraph.

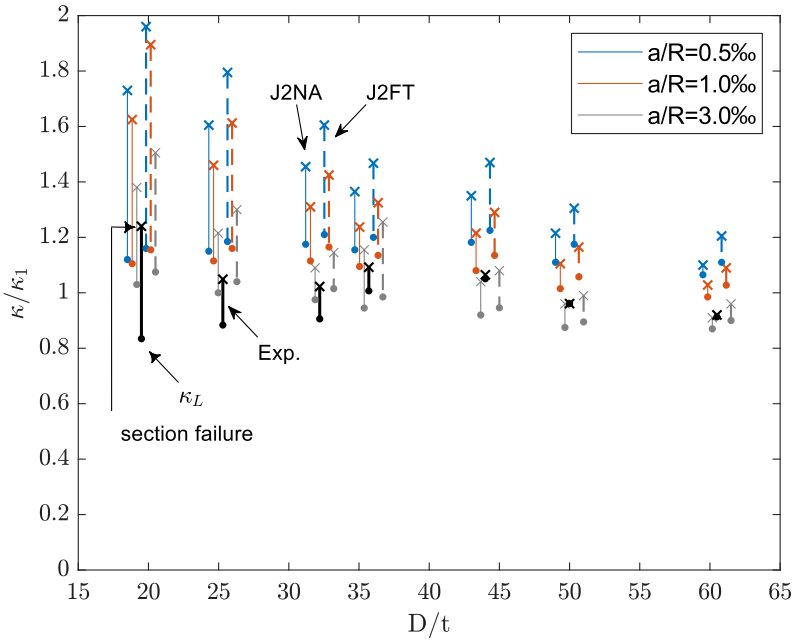

Figure 5.18: Influence of imperfection amplitude in the limit curvature and failure of the cylinders depending on the D/t ratio

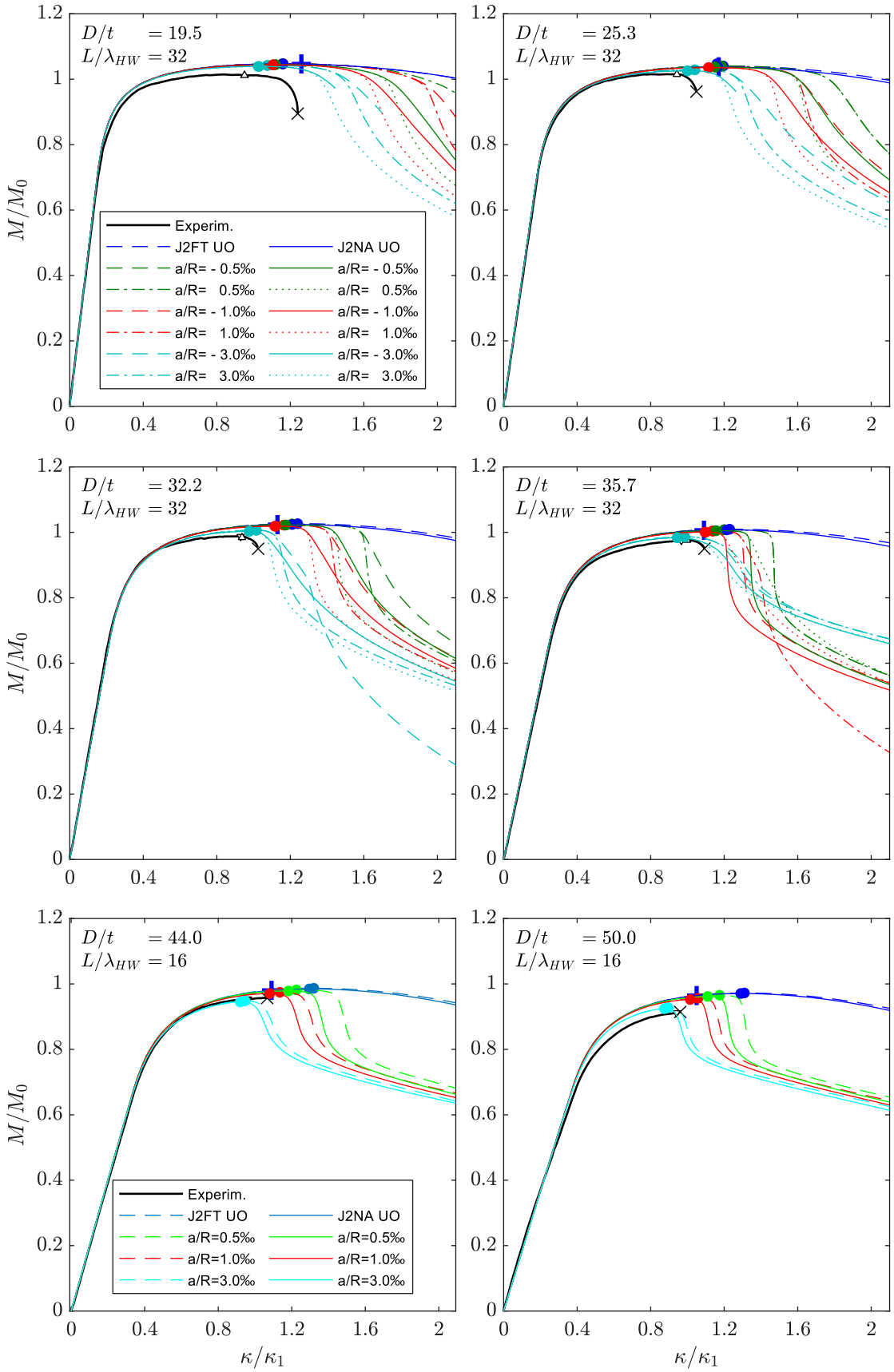

Figure 5.19: Effect of imperfection and constitutive modelling in the structural response of thick-walled cylinders under bending

Overall, the two constitutive models produce similar behaviours for the cylinders, with the J2FT leading to somewhat higher moment and deformation capacities, compared to the more compliant J2NA. Using the non-associative model, the structural response is more compliant, and localization leads to lower moment maxima, developing at curvatures uniformly lower, compared to the ones obtained using the J2FT. In addition, the load drop is more abrupt and deformations are more localized after the maximum load, particularly in the thinner cylinders. Models employing the J2FT follow the primary loading path up to higher curvatures before localization initiates. Differences between the J2FT and J2NA are more pronounced for the lower imperfection amplitude. Employing larger values for θ_c, decreases the overall stiffness of the tube's response and the curvature when diamond-shaped buckles develop. The $m-k$ response of cylinders with $D/t = 19.5 - 50$ is presented in Figure 5.19 for the two constitutive models and these imperfection amplitudes, along with experimental curves.

5.4.1 Support conditions and model length

For the thicker shell under consideration (D/t=19.5), employing the long cylinder conditions and the range of imperfections described earlier, the section failure is calculated at curvatures higher than experiments reported. Considering higher imperfection amplitude results in localization at lower curvatures, they have small influence on the limit moment of the shell, but the behaviour following the maximum moment is smoother than the one observed in experiments. An explanation lies in the influence of model length, which is investigated next. As shown in Figure 5.20a, considering increasingly long segments, leads to similar limit loads and curvatures, while the post-limit-moment response becomes more abrupt. Considering length and support conditions similar to the ones used in experiments, a structural behaviour in line with the experimental response is obtained for the thicker tubes as well.

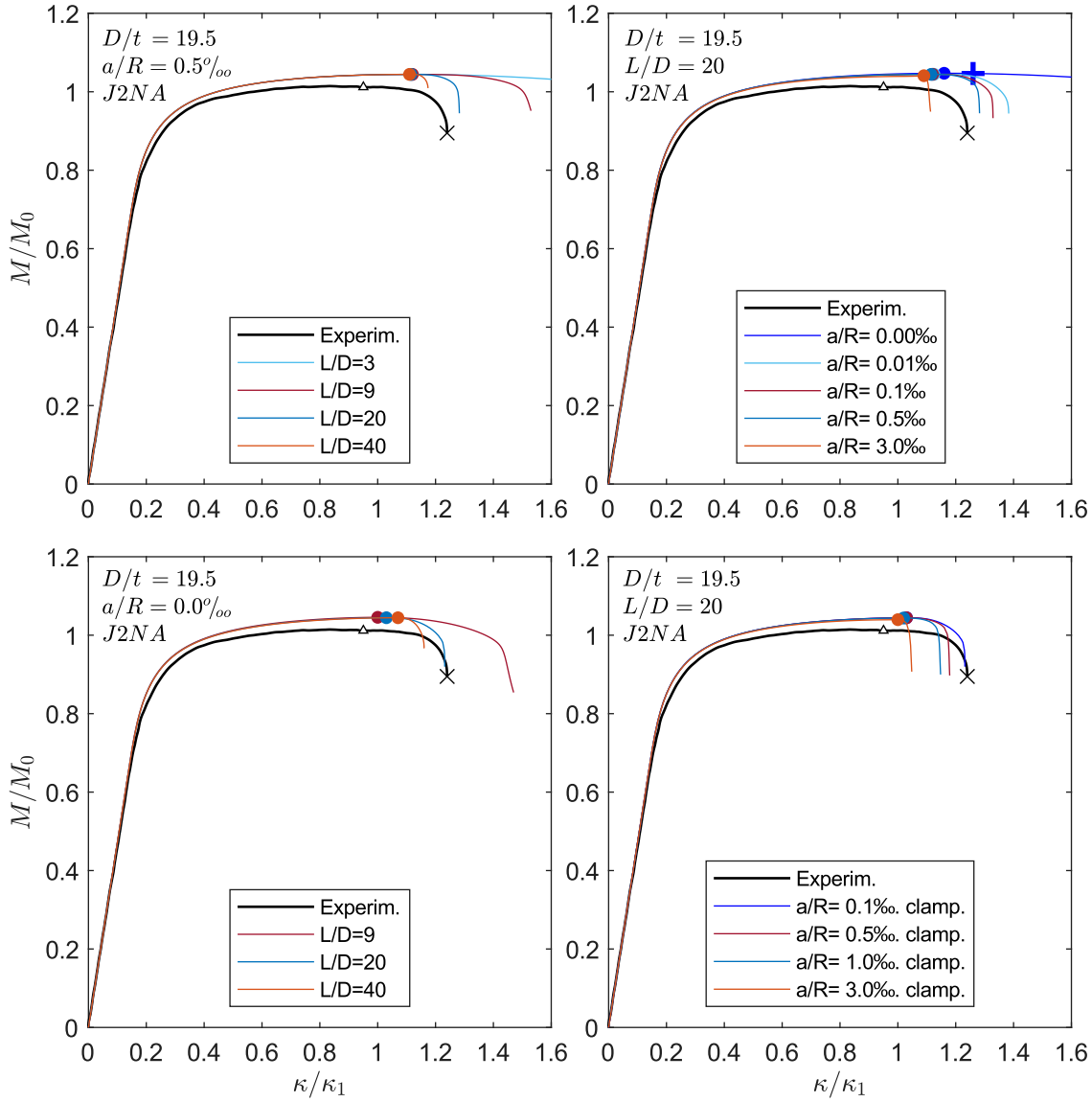

Figure 5.20: Effect of end conditions and imperfection in the bending response of thick-walled cylindrical shell

The ovalization profile along the tube segment is given in Figure 5.21 (V), and it follows a similar trend as the experiments indicate. The ovalization, increases uniformly at the early stages of deformation. At curvature values approximately equal to κ_1, ovalization begins to localize in a section about 6D long at the centre of the tube segment.

When the edges are clamped, the ovalization of the tube is influenced locally at the models ends, while wrinkling localization occurs in the middle of the model and its behaviour is similar to the infinite shell as obtained using shorter models with symmetry conditions.

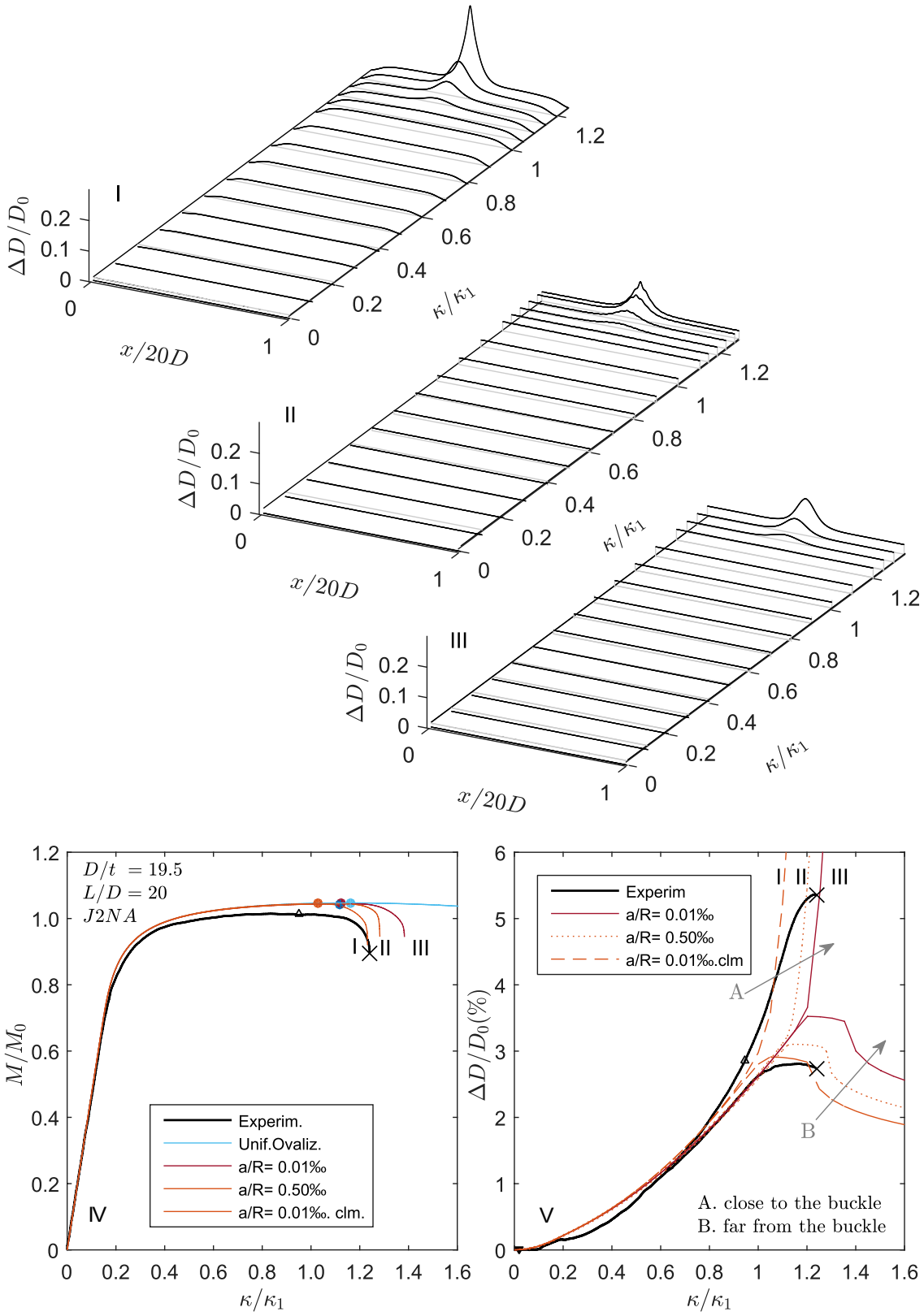

Figure 5.21: Evolution of the ovalization along the cylinder for different support conditions and imperfection; moment-curvature graph; ovalization-curvature graph

5.5 Conclusions

The structural performance of long thick-walled inelastic cylinders ($D/t < 60$) under pure bending is examined using nonlinear finite element analyses, accounting for imperfection and material nonlinearity. Ovalization and bifurcation instabilities are shown to control the behaviour of the cylinders. These instabilities occur while the material is loaded in the inelastic range, so the elastoplastic properties of the material, and its representation through constitutive modelling influence the simulated cylinder's structural behaviour. Depending on the D/t ratio of the cylinder one of these instability modes becomes dominant and leads to the structural failure.

The prebuckling response of the cylinders shows considerable deformations and biaxial compressive stresses in the tube wall caused by global and hoop bending, leading to a non-trivial prebuckling equilibrium path and non-proportional loading in the cross section. Ovalization and bifurcation instabilities are identified, and the post-buckling equilibrium path is traced.

Rather thick cylinders ($D/t \leq 30$), ovalize uniformly until progressively forming a region of localized ovalization. They develop a limit load (maximum moment) but maintain significant post-limit load strength and fail gradually. Wrinkling type bifurcation is identified after the limit load and such imperfection was found to have limited influence in the limit load but may accelerate the behaviour leading to an earlier failure of the section. Stiff support conditions can have a similar effect. The section ovalizes in an extended segment of the tube, verifying the observations of previous researchers. Therefore, long models are necessary to simulate these behaviours.

For the thinner cylinders ($D/t \geq 45$), the bifurcation into short-wavelength wrinkling precedes the development of a limit load. Cylinder wall wrinkling and initial geometric imperfection reduce the ultimate moment capacity of the cylinders and lower the curvature when it is reached. For these cylinders, the local buckling leads to wrinkling localization, followed by an abrupt loss of bending stiffness of the cross-section and local deformations leading to non-symmetric 'diamond' buckling modes.

For intermediate values of D/t the two instability modes occur at similar curvatures and interact so limit load instability may somewhat precede catastrophic failure which can be more gradual.

The non-associative model parameter θ_c reduces somewhat the limit load of the simulated cylinder and the influence of imperfection amplitude. Similar to compression,

a small value of 2^o leads to behaviours aligned with experimental data from the literature. The developed constitutive model is found to accurately reproduce the structural behaviour of the cylinders under pure bending leading to reasonable instability estimates, but also in reliably tracing the pre- and post-buckling equilibrium path of cylinders.

6 BENDING UNDER INTERNAL PRESSURE

This chapter investigates the stability of long inelastic thick-walled cylinders subjected to bending under constant internal pressure. The combined loading creates an inherently non-proportional loading path, and the following analysis showcases the capability of the developed constitutive model to accurately simulate the structural behaviour, buckling and post-buckling of thick-walled cylinders under complex loading conditions. The influence of internal pressure in the ovalization and buckling of the cylinders is examined. The post-buckling response of the cylinder is traced, considering the influence of imperfection, and aspects of the structural failure are addressed. Comparisons with experimental data from the literature are performed successfully.

6.1 Modelling details

The mechanical behaviour of thick-walled cylindrical shells subjected to internal pressure and bending is numerically investigated using finite element simulations within the general-purpose finite element software Abaqus. Geometrically nonlinear static analyses are conducted employing the static and Rik's arc-length solvers. The material is considered to be elastic-plastic with isotropic hardening, defined by the stress –strain response of the material in uniaxial tension, and it is introduced in the analyses as true stress – logarithmic plastic strain values. The developed J_2 non-associative constitutive model ($\theta_c = 2^o$) is employed to simulate metal material behaviour, implemented through

a material user subroutine (UMAT). Initial geometric imperfection, when included, is introduced in the form of the buckling mode of the cylinders (wrinkling). Buckling modes are obtained from perturbation analyses accounting for the elastic-plastic moduli of the material, which are performed at the bifurcation point.

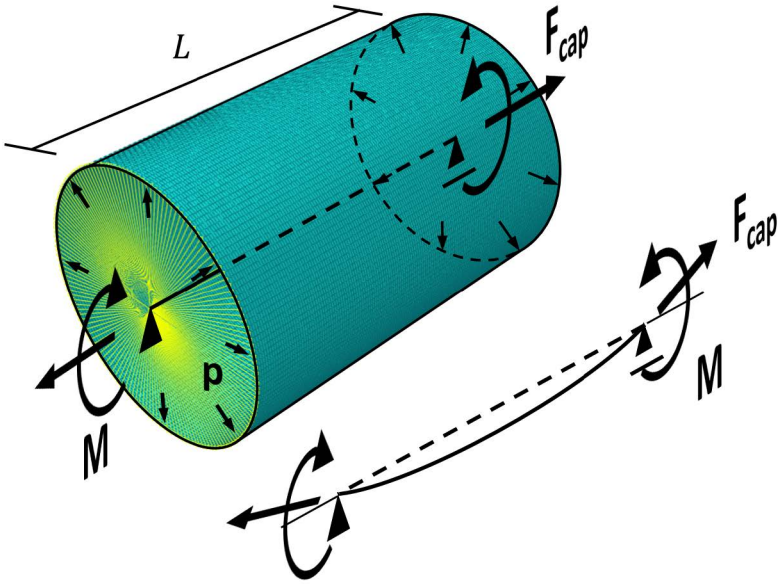

Figure 6.1: Boundary conditions, reference points and kinematic constraints at the end cross section for cylinders under bending and pressure.

Three-dimensional finite element meshes of variable lengths L are employed: short models ($L < D$) are used to accurately identify the shell's instability, the wrinkle development, sensitivity to initial imperfection and initial post-buckling, while longer models are employed to simulate wrinkling localization and structural failure of the cylinders. The cylinders are discretized with four-noded general-purpose shell elements (S4), with 7 integration points across the thickness. Around the cylinder circumference 144 elements are employed; mesh density in the longitudinal direction varies with the analysis type.

The cylinder is modelled as simply supported, and symmetry conditions are employed at the ends to represent continuity of a long cylinder. At each end of the mesh, a reference node is placed, and it is coupled with the nodes of respective end cross sections, constraining them to remain plane and follow the rotation of the reference node. The nodes of end cross section are permitted to slide on the rotated plane, allowing for cross sectional deformation. Support conditions eliminate rigid body motions of the model.

Loading is applied in two stages. Initially, internal pressure is applied by prescribing on the shell's surface a distributed force p, which is a fraction of the yield pressure $p_0 = 2\sigma_0 t/D_0$. Simultaneously, end-cap forces $F_{cap} = p\pi D_0^2/4$ are applied as concentrated

loads at the reference nodes at the end cross sections, defined as follower forces, which remain perpendicular to the cross section throughout the analysis (Figure 6.1). In a second stage, bending is induced by incrementally prescribing a relative angle of rotation ϕ between the reference nodes of the end cross sections. The pressure loads are kept constant during bending. The moment M is obtained from the reaction at these nodes and normalized by $M_0 = \sigma_0 t D_0^2$. The cylinders average curvature is calculated as $\kappa = \phi/L$, where ϕ is the relative rotation of the end cross sections, and it is normalized by the curvature-like quantity $\kappa_1 = t/D_0^2$.

6.2 Uniform Ovalization

The previous chapter demonstrated that the response of cylinders under bending is governed by the interaction of ovalization, bifurcation instabilities and inelastic material behaviour. In a first stage, the influence of internal pressure in axially uniform ovalization is addressed. A moderately thick-walled (D/t=52) stainless steel cylinder is analysed, chosen to allow for comparisons with the experimental investigation by (Limam et al., 2010). The Rambert-Osgood material curve fit, and geometry parameters of the cylinder are listed in Table 6.1.

A pseudo two-dimensional ovalization analysis is performed using a short cylinder segment with length equal to 5% of the cylinder's diameter. Ten (10) elements are employed in the longitudinal direction, to effectively exclude lengthwise non-uniform (wall wrinkling) phenomena from the response of the shell, while accurately describing the lengthwise curvature.

Table 6.1: Geometry and material properties

D(mm)	38.15
t(mm)	0.737
E(GPa)	186
$\bar{\sigma}$ (MPa)*	227
σ_o(MPa)	262
ε_t(%)	2.1
n *	9.3

*Ramberg-Osgood parameters in eq.(2.60)

The influence of internal pressure p/p_0 in the moment-curvature response of the uniformly ovalizing cylinder is shown in Figure 6.2a. For low curvatures, the behaviour is linear, independent of the pressure, until yielding initiates when bending stiffness reduces, a knee develops in the $m-k$ response of the cylinder and it smoothly diverges

from the initial elastic branch. Under pure bending, the Brazier effect gradually leads to the development of a limit load m_L at curvature $\kappa_L/\kappa_1 = 1.5$ followed by a dropping branch instigated by the rapid ovalization of the cross section and flattening.

Low levels of pressure have a stiffening effect and move upward the $m - k$ curve of the cylinder, while they curb significantly the growth-rate of cross-sectional ovalization Δ (Figure 6.3a). Furthermore, limit load instability is delayed: the limit (maximum) moment and the corresponding limit curvature increase. For a pressure value $p/p_0 = 0.10$, the limit moment increases by 10% and the respective curvature doubles. Pressurization introduces axial and circumferential tension in the cylinder, which interact with the compression at the top of the cylinder and tension at the bottom due to global bending and the hoop bending stresses due to ovalization, causing earlier material yielding. The complex biaxial loading path of the material into the inelastic range lead to high plastic deformations and low material stiffness, which reduce the bending rigidity of the cylinder. The influence of early yielding is clear for pressure levels $p/p_0 \geq 0.30$ for which the $m - k$ response of the cylinder moves downwards and diverges earlier form the initial linear branch. Yet, it maintains a hefty slope up to rather high curvatures as internal pressure counteracts the distortion of the cross section.

Internal pressure delays ovalization and the cylinder remains rounder (Figure 6.5a, b), so it sustains rather high values of moment and curvature before limit load instability. Indeed, for pressure levels greater than $0.3p_0$ no limit load was identified for curvatures up to $10\kappa_1$. In Figure 6.8 the ovalization limit curvatures are shown to increase unrealistically rapidly with pressure, compared to experimental data, indicating that the cross-section failure is governed by local buckling, non-uniform localized deformations which precede ovalization instability.

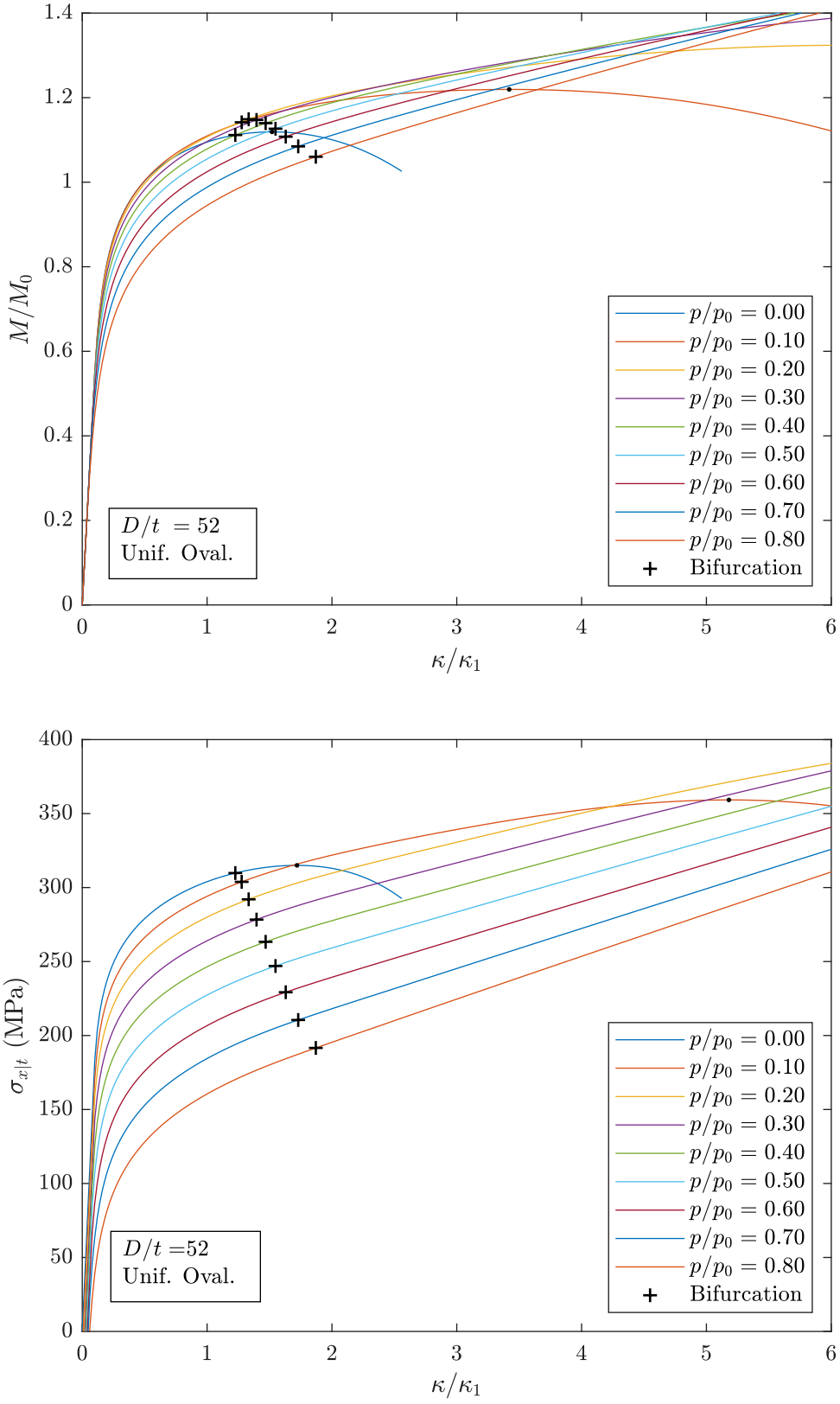

Figure 6.2: (a)Moment-curvature response, (b) Axial stress at the intrados of the uniformly ovalizing shell for various values of internal pressure

Figure 6.2b shows the evolution of the average axial stress $\sigma_{x|t}$ at the intrados of the shell where maximum compression occurs. It follows a similar trend with respect to curvature

as the cylinder's moment. The maxima of the two do not coincide, and stress maximizes at somewhat higher curvatures than κ_L . Following the ovalization limit point, compressive stresses at the intrados continue to increase while the moment capacity reduces driven by the rabidly reducing section height. The axial stress curve is seen to reduce uniformly (move downwards) with internal pressure for all curvature levels, which is the result of the axial tension ($pR/2t$) due to end-cap forces. The evolution of ovalization -eq.(5.1)- with respect to bending curvature, is provided in Figure 6.5a showing the beneficial influence of internal pressure. The change in the local hoop radius R_{eq} at the intrados of the cylinder (Figure 6.4) relative to the initial radius R is further given in Figure 6.5(b) under various pressure levels. R_{eq} is calculated from the coordinates of the three most compressed nodes of the cross section and its value increases more rapidly than ovalization. R_{eq} is associated with buckling resistance of the cylinder, and it is used in Chapter 7 together with $\sigma_{x|t}$ to estimate the bifurcation in a semi-analytical manner.

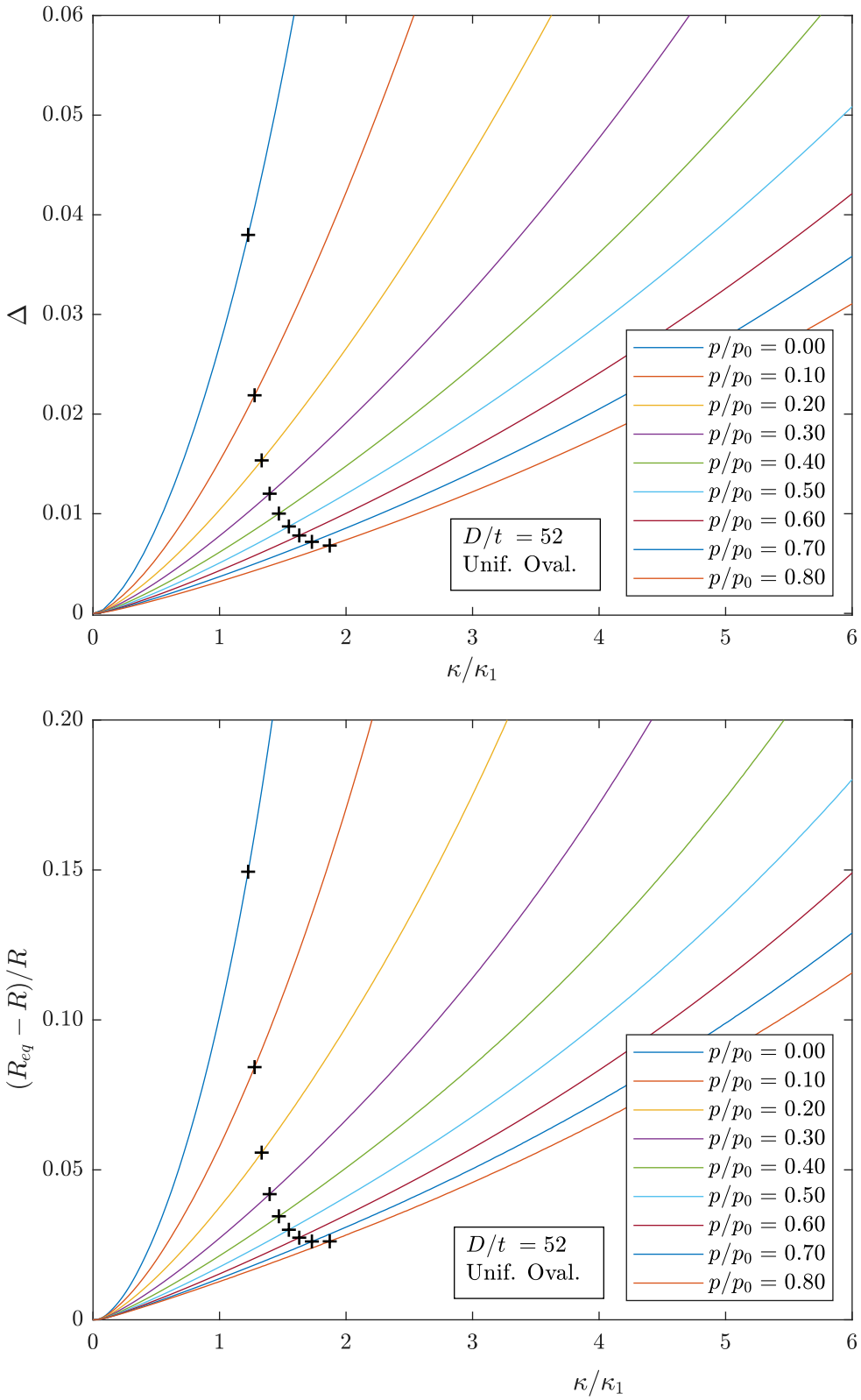

Figure 6.3: (a) Ovalization-curvature diagram of the pressurized shell (b) Change in the local hoop radius at the intrados of the shell at various levels of internal pressure

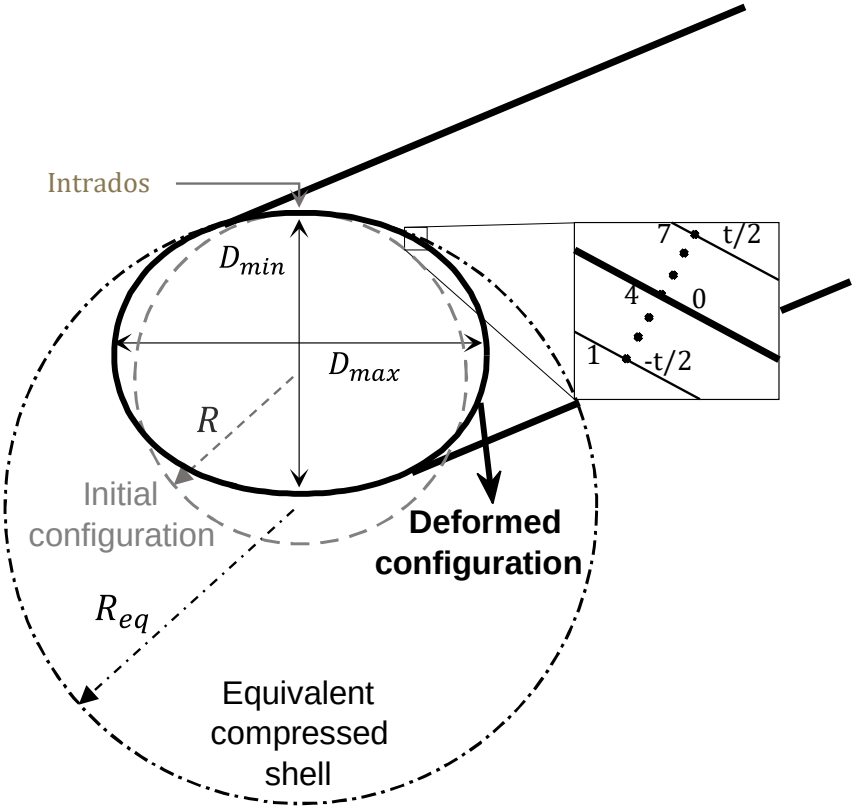

Figure 6.4: Ovalization due to bending, local hoop radius at the intrados of the cylinder and equivalent compressed cylinder

Limam et al. noted that in the presence of internal pressure, plastic deformation due to bending leads to expansion of the section. Figure 6.5a depicts the average change in diameter in the shell, expressed in (6.1), which approximates the average hoop strain. It clearly indicates an expansion of the cross section for high pressures, but it also shows some shrinking under pure bending. In Figure 6.5b, the average hoop strain in the cross section is calculated using (6.2). It verifies that section expands under bending for high levels of internal pressure, with expansion reaching 1.7% for $p/p_0 = 0.80$. It also shows that ovalization is almost inextensional under pure bending, and the simplified formula (6.1) is not representative for this case.

$$\Delta D = \frac{D_{max} - D_{min}}{2D} \tag{6.1}$$

$$\varepsilon_{\theta|avg} = \oint_C \bar{\varepsilon}_{\theta|t}\, dC/C \tag{6.2}$$

Above, $\bar{\varepsilon}_{\theta|t}$ is the cross-thickness average hoop strain and C is the shell's circumference in the deformed configuration.

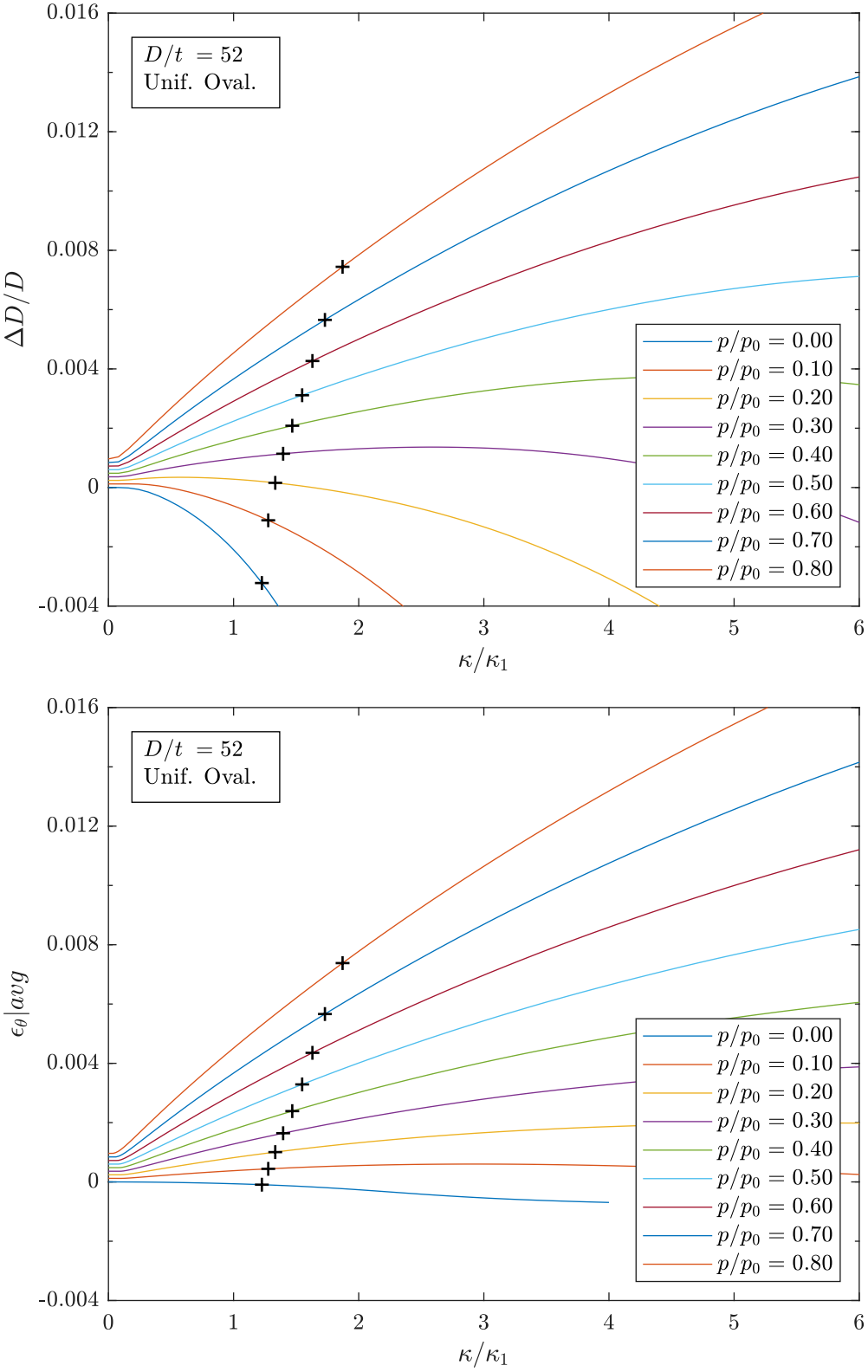

Figure 6.5: (a) Change in diameter (b) Average hoop strain of the shell versus curvature at various levels of internal pressure

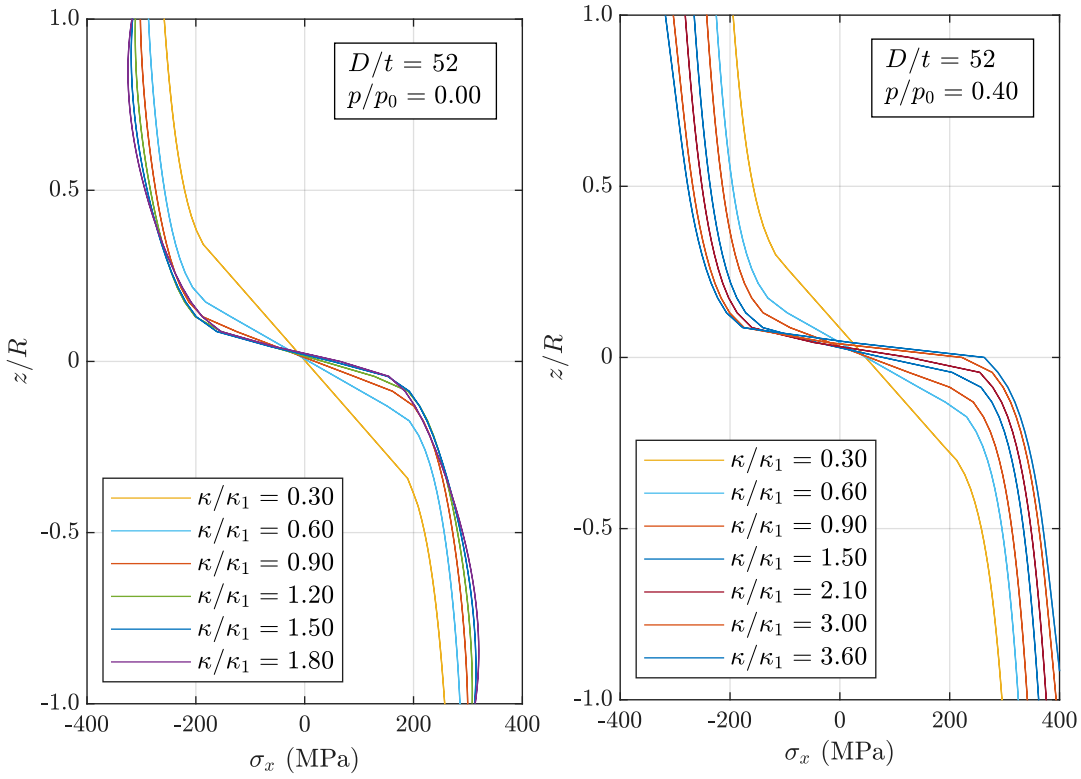

Figure 6.6: Axial stress distribution around the cross section of the cylinder (a) under pure bending $p/p_0 = 0.00$, (b) under internal pressure $p/p_0 = 0.40$

Figure 6.6 presents the axial stress distribution across the height of the shell at various levels of curvature, for two levels of pressure: $p/p_0 = 0.00$ and $p/p_0 = 0.40$. At low curvatures, ovalization is limited and the stress distribution follows the material curve. After the limit load, the maximum axial stress is not found at the intrados of the shell under pure bending. The bending stress distribution for pressure $p/p_0 = 0.40$ is qualitatively similar but is lower than the material curve due to the axial tension (cap forces) and the interaction with hoop stresses through the Von Mises yield criterion.

Further focusing on the intrados, the evolution of axial and hoop stress across the thickness of the cylinder is given in Figure 6.7 for different stages of deformation, and two levels of pressure. For $p/p_0 = 0.00$, at small curvatures, the distribution of σ_x is approximately uniform across the thickness. At higher curvatures, the ovalization-induced hoop bending causes significant hoop stresses, non-uniform across the thickness. These interact with axial stresses through the Von Mises yield criterion due to inelastic material response, resulting in a non-uniform profile of σ_x across the thickness. This effect is particularly pronounced in the absence of internal pressure, while even low levels of pressure limit this influence, by reducing hoop bending.

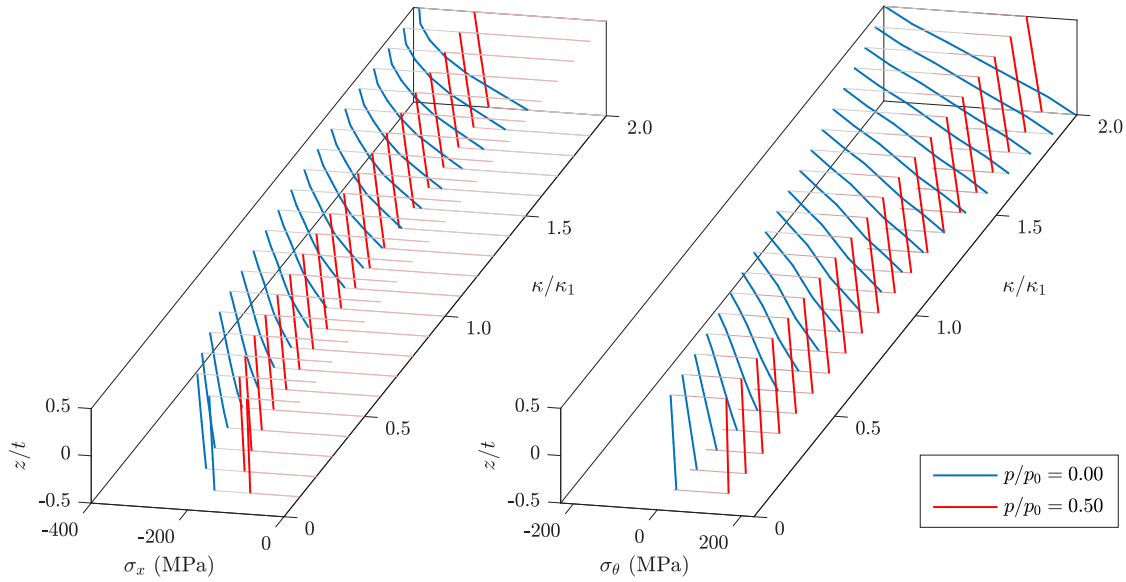

Figure 6.7: (a) Axial and (b) Hoop stress distribution across the thickness at the intrados of the cylinder versus curvature under pure bending $p/p_0 = 0.00$ and internal pressure $p/p_0 = 0.50$

6.3 Bifurcation using Abaqus

The onset of bifurcation from the axially uniform ovalizing prebuckling state is identified by the development of non-positive eigenvalues in the stiffness matrix of the model ('alternative comparison solid', as employed in the previous chapters). Using 'short' models of various lengths, the length leading to bifurcation at the lowest curvature κ_b is identified as the characteristic wavelength of the shell λ_{HW}, and a perturbation analysis at bifurcation provides the buckling eigenmode. To achieve accuracy of 1% in defining λ_{HW}, eigenvalue checks are necessary at deformation intervals $\sim 0.01\% \kappa_b$ in the vicinity of bifurcation. Similar to the case of pure bending, κ_b is found to be relatively insensitive to small length variations. The bifurcation points obtained by 'halfwave' models in Abaqus are marked with a '+' in Figures 6.2-6.5. Considering four- and eight-times smaller elements leads to smaller than 1% changes in the predicted κ_b and λ_{HW}. Consideration of smaller curvature increment size had no further influence.

Bifurcation occurs before the limit point from ovalization analyses for all pressure levels. Increasing pressure levels somewhat delay the bifurcation, which occurs at higher curvatures. The delay in the ovalization instability is considerably more pronounced, which is demonstrated in Figure 6.8 where both are plotted with respect to the level of internal pressure. The bending moment at bifurcation M_b increases for low values of pressure, reaching a 4.5% increase for $p/p_0 = 0.20$. For higher values of internal

pressure, the moment-curvature response of the shell moves downwards, and M_b follows the same trend.

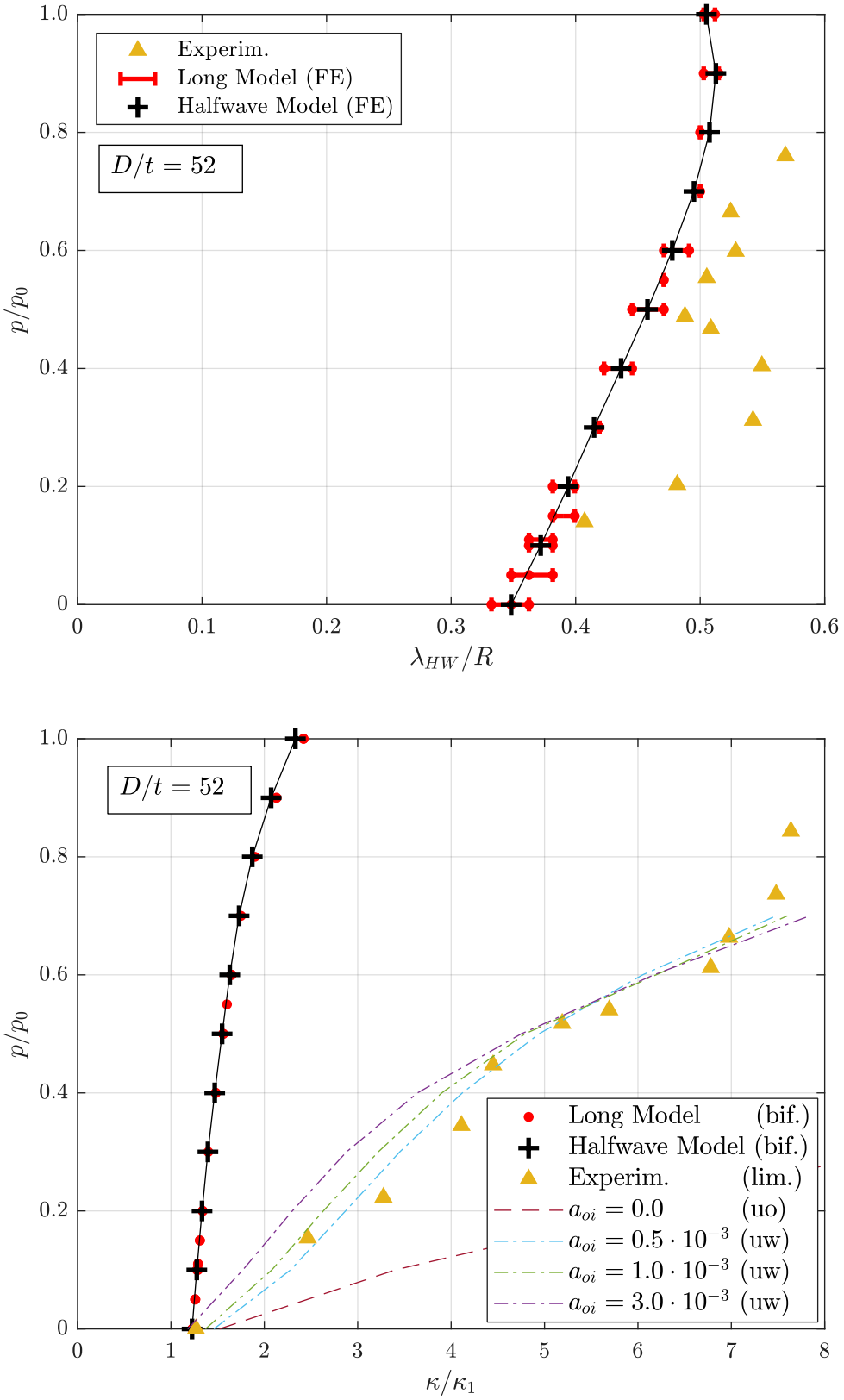

Figure 6.8: Buckling wavelengths of cylinders under bending versus internal pressure (b) Curvature at buckling versus internal pressure

The prebuckling (prior to bifurcation) and post-buckling configuration of the deformed cylinder are depicted in Figure 6.9 for two levels of internal pressure. Buckling displacements are obtained from perturbation analyses in Abaqus and for visualization purposes are amplified. The buckling mode includes deformations in an extended portion of the compressed side of the cylinder, centred at the intrados, while deformations zero towards the mid-height and the tension side of the section. The size of the 'buckling zone' increases with pressure: for pure bending it is $2R$, increasing to $2.4R$ for $p/p_0 = 0.60$. The 'buckling zone' is considered here as the arc along the cross-section circumference, where buckling displacements are greater than say 5% of the maximum displacement in the buckling mode (at the intrados).

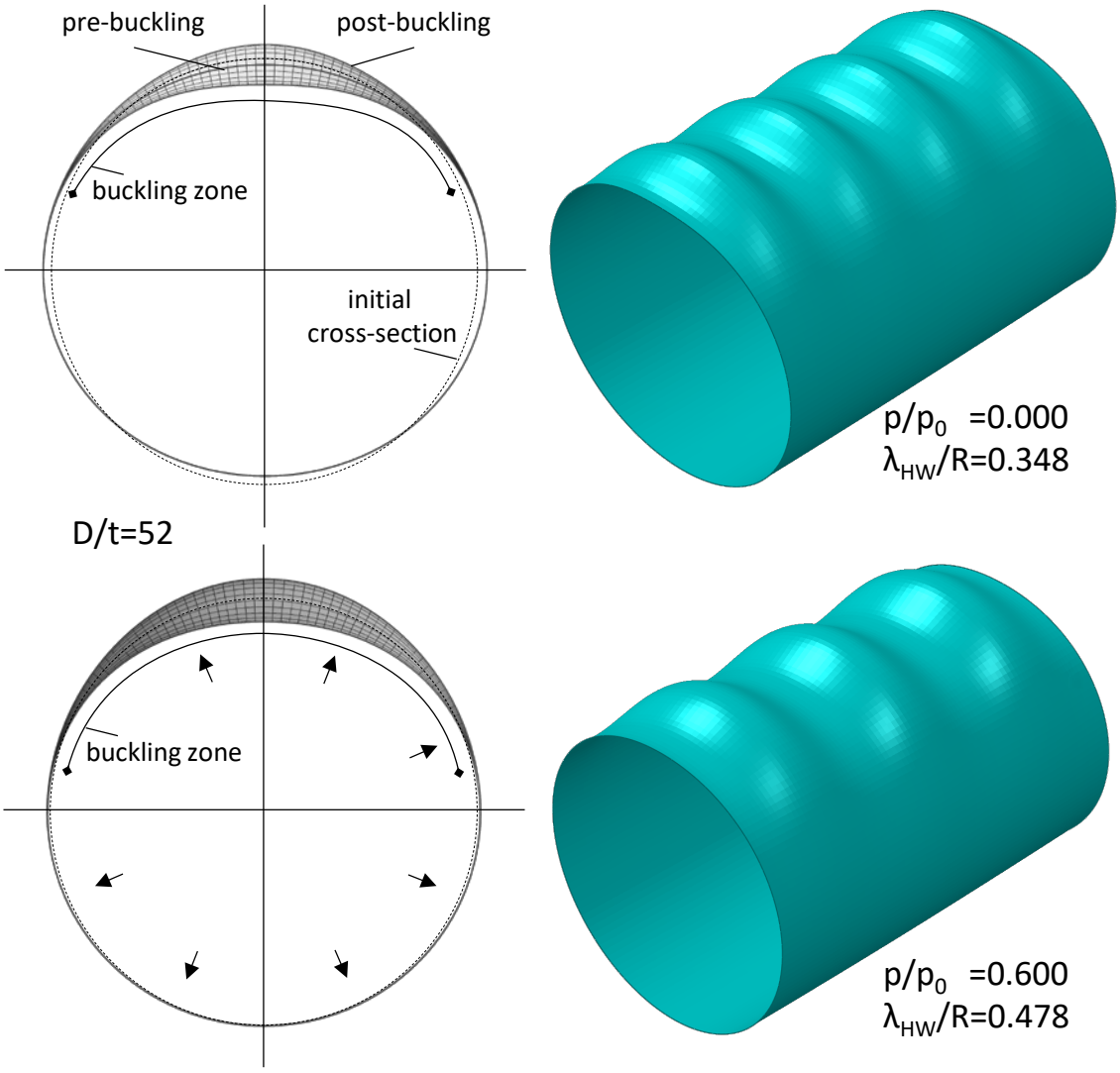

Figure 6.9: Exaggerated buckling mode of cylinder for two levels of internal pressure

An increasing trend for the 'buckling zone' width with respect to pressure was also found for elastic cylinders by (Houliara & Karamanos, 2006). For inelastic cylinders the buckling zone is more extended, not localized at the intrados. This is attributed to the

'relatively uniform' stress values in the material that has yielded and the lower ovalization compared to elastic shells, which results in buckling of a wider part of the section, as it approaches the local critical stress (see also Chapter 7).

In Figure 6.8, the values of κ_b, λ_{HW} are plotted with respect to the level of internal pressure. The exact calculations using 'halfwave' models are marked with a '+', while estimates obtained using 'long' models are plotted with dots, with several provided for each level of pressure, reflecting the number of non-positive eigenvalues obtained at κ_b, and measured from the corresponding eigenmodes. The buckling wavelength increases with internal pressure. Figure 6.9b displays the exaggerated buckling modes for $p/p_o = 0.00$, and $p/p_o = 0.47$, causing a 31% increase in λ_{HW}. This behaviour was observed experimentally in pressurized inelastic cylinders under bending by (Limam et al., 2010), and under uniform compression by (Paquette & Kyriakides, 2006). The opposite effect, was found by (Houliara & Karamanos, 2006) in elastic cylinders under bending, who found wrinkling wavelength to decrease with the level of internal pressure.

These seemingly incompatible behaviours are explained in Chapter 7, using the 'Local Buckling Hypothesis' drawing on similarities to the buckling of cylinders subjected to axial compression. It is shown that internal pressure lowers ovality at buckling (Figure 6.3) which tends to lower wavelength, as reported for elastic cylinders. However, in elastoplastic shells, yielding under biaxial loading leads to a considerable increase in wavelength and this ultimately governs the trend of λ_{HW} with respect to internal pressure. The obtained wavelength estimates are uniformly lower than the experimental values, as the influence of the reported anisotropy (Kyriakides et al., 2005) is not accounted for in the context of the present work.

The bifurcation curvature κ_b increases with the level of internal pressure (Figure 6.8), which is explained by the stabilizing influence of pressure: it keeps the section rounder and lowers compressive loads by introducing axial tension. Even at low pressure values, bifurcation occurs well before ovalization limit instability, which for p/p_0 =0.10, develops well after κ_b, following additional bending deformations of several κ_1 (Figure 6.8b). This comes in agreement with the reported experimental observations by (Limam et al., 2010) who identified wrinkling early in the bending history.

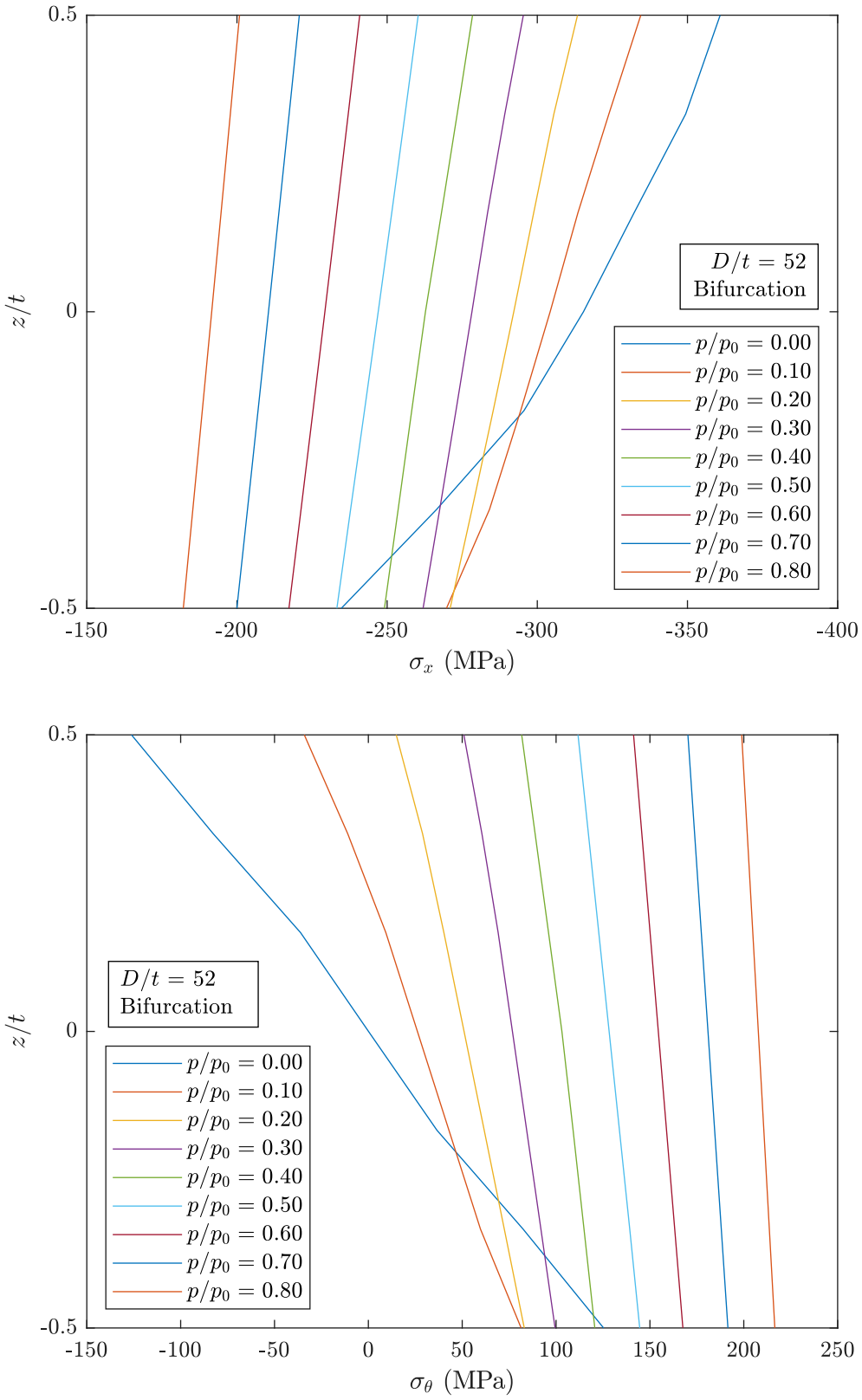

Figure 6.10: Distribution of (a) axial stress σ_x, (b) hoop stress σ_θ across the thickness at the intrados of the cylinder at bifurcation for various levels of internal pressure

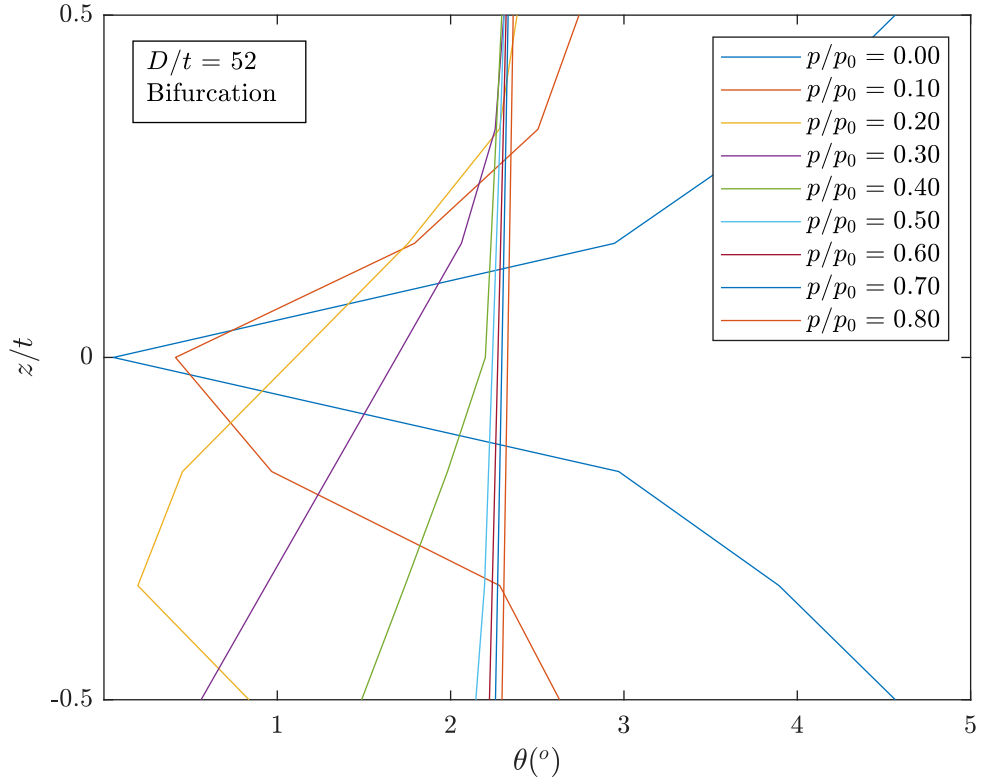

Figure 6.11: Non-proportionality angle θ across the thickness in the intrados at bifurcation for various levels of internal pressure

Figure 6.10 displays the distribution of the axial and hoop stress across the cylinder thickness at the intrados when bifurcation occurs. Apart from the case of pure bending ($p/p_o = 0.00$), both stress distributions are quasi-linear. The axial stress σ_x decreases with pressure across the cross section, while the hoop stress σ_θ increases. The non-proportionality angle θ at bifurcation is presented in Figure 6.11, and records small values $\sim 2.3^o$ for all pressure levels. For high values of pressure, θ is quasi-uniform across the thickness, while for low pressure values, it varies across the thickness, affected by hoop bending.

6.4 Uniform wrinkling

The onset of buckling from the ovalization prebuckling $m-k$ path is investigated for the pressurized cylinders. Uniform wrinkling is considered using one-halfwave long models, employing 10 elements along the halfwave. Imperfection in the shape of the obtained buckling mode is used to enable the model to follow the secondary equilibrium path. Several imperfection levels are considered with respect to the tube radius $a_{oi} = a/R$, ranging from 10^{-8} to 10^{-3}. Similarly to pure bending, wrinkling of the shell's

compressed side leads to a more compliant $m-k$ response. Increasing initial imperfection amplitude leads to progressively lower limit load values m_L, developing at lower curvatures.

Initial imperfection amplitude has a more pronounced influence in pressurized bending of cylinders, than under pure bending (p/p_0 =0.00). Particularly low values of imperfection suffice to affect measurably the shells behaviour. In Figure 6.12 the moment curvature response of the cylinder is given for two levels of internal pressure. For $p/p_0 = 0.138$, the behaviour deviates from the uniform ovalization response for imperfection values of $a_{oi} = 10^{-6}$, and limit loads reduce considerably for higher imperfection values. This effect becomes increasingly pronounced at higher levels of internal pressure e.g., $p/p_0 = 0.467$, where imperfection levels as low as $a_{oi} = 10^{-8}$ lead to a load maximum, at much lower curvature than estimates from ovalization analyses. Under pure bending, imperfection values of $a_{oi} = 10^{-4}$ are needed for the cylinder to follow the secondary equilibrium path, reducing its limit load. The imperfection sensitivity of the pressurized cylinder is depicted in Figure 6.13, showing the limit loads obtained from uniform wrinkling analyses, plotted with respect to the imperfection amplitude for various levels of internal pressure.

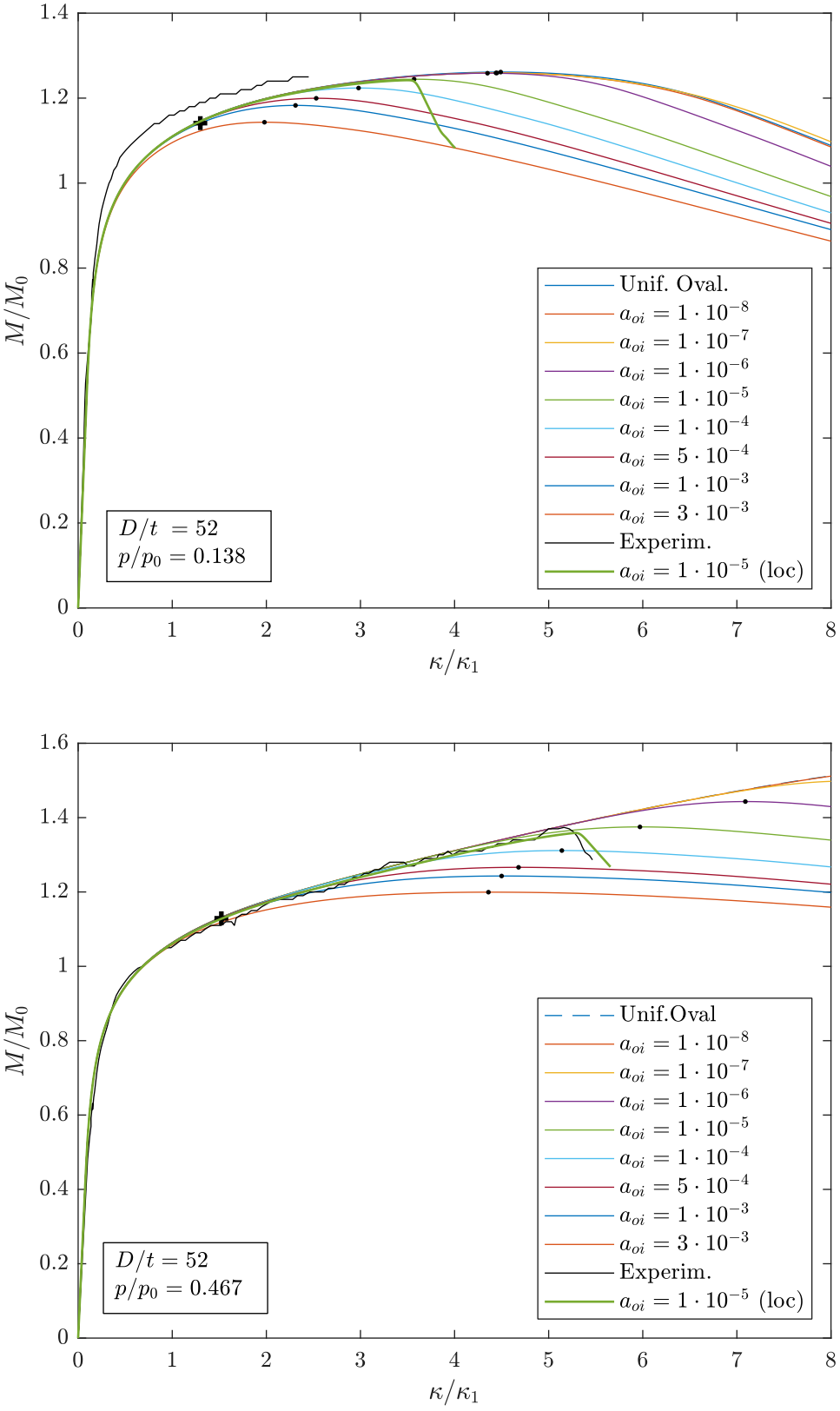

Figure 6.12: Moment-curvature response of pressurized cylinder with various levels of initial geometric imperfection

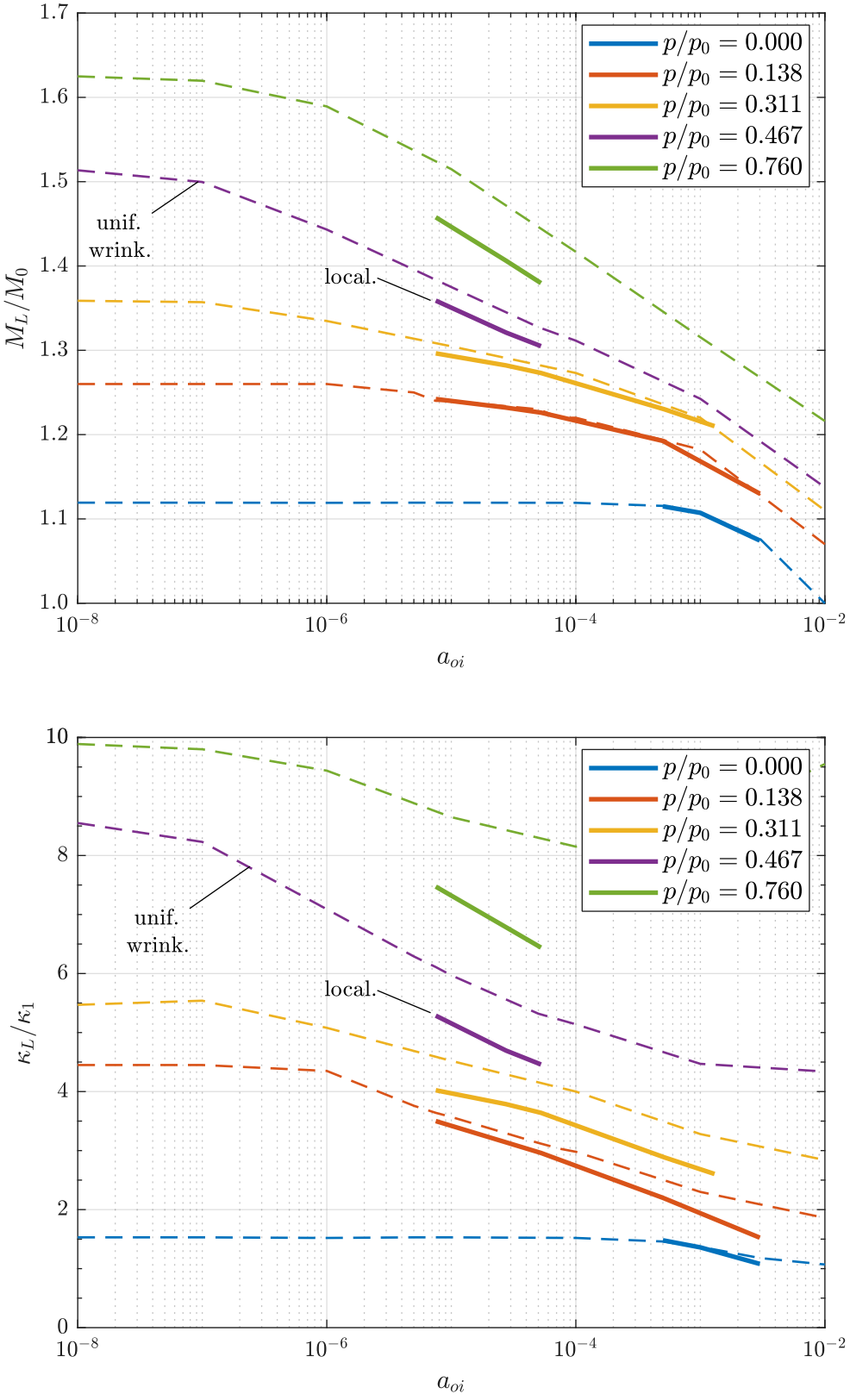

Figure 6.13: Influence of imperfection amplitude in the maximum moment of the shell and the respective curvature for various levels of internal pressure

6.5 Localization of wrinkling

To investigate the localization of deformation and failure of the pressurized cylinders under bending, models of length $L = 30\lambda_{HW}$ are employed with 10 elements per λ_{HW} in the axial direction. Initial geometric imperfection is introduced in the models in the shape of the eigenmode of pressurized cylinder. Imperfection bias is introduced in the mid-length of the cylinder, so that localization may initiate far from the supports: the eigenmode profile along the cylinder is multiplied by factor f

$$f = 1 + a_i/|a_{oi}| \sin^2 \pi x/L \tag{6.3}$$

where a_{oi} is the amplitude of uniform wrinkling of the shell and a_i offers a preference in the amplitude. Positive values of a_{oi} introduce a maximum outward (bulging) imperfection at the midspan, and negative imply a maximum inward (dent) imperfection.

6.5.1 Imperfection

In Figure 6.13 the maximum moment and respective curvature of the long cylinders under various levels of pressure are plotted versus the maximum amplitude of initial geometric imperfection, considering a preference $a_i = 3\%\, a_{oi}$. The imperfection sensitivity identified in uniform wrinkling is further exacerbated particularly at high pressures. For $p/p_0 = 0.760$ wrinkling localization is seen to occur well before the limit load from wrinkling analyses with the same amplitude. For lower pressures, the limit loads and curvatures from the full 3D analysis are somewhat lower but compare reasonably well with the limit loads from uniform wrinkling.

The direction of the maximum imperfection has small influence in the pre-maximum-load behaviour of the cylinder but influences the collapse configuration. Figure 6.14 shows the $m - k$ response of the cylinder under pressure level $p/p_0 = 0.138$. Both inward and outward imperfection leads to practically identical behaviours in the initial post-buckling, up until and including the development of the limit moments and curvatures. Before the development of the limit load, the wrinkle amplitude increases uniformly along the shell. At the vicinity of the limit load, the deformation localizes in the location of the maximum imperfection (Figure 6.15).

Immediately after the limit moment, an abrupt loss of bending resistance denotes the section failure. In the case of outward imperfection, a primary bulging buckle develops, and as collapse is initiated, at one of its sides an inward buckle develops which deepens rapidly and deformation localizes. On the other side of the initial bulging buckle, two

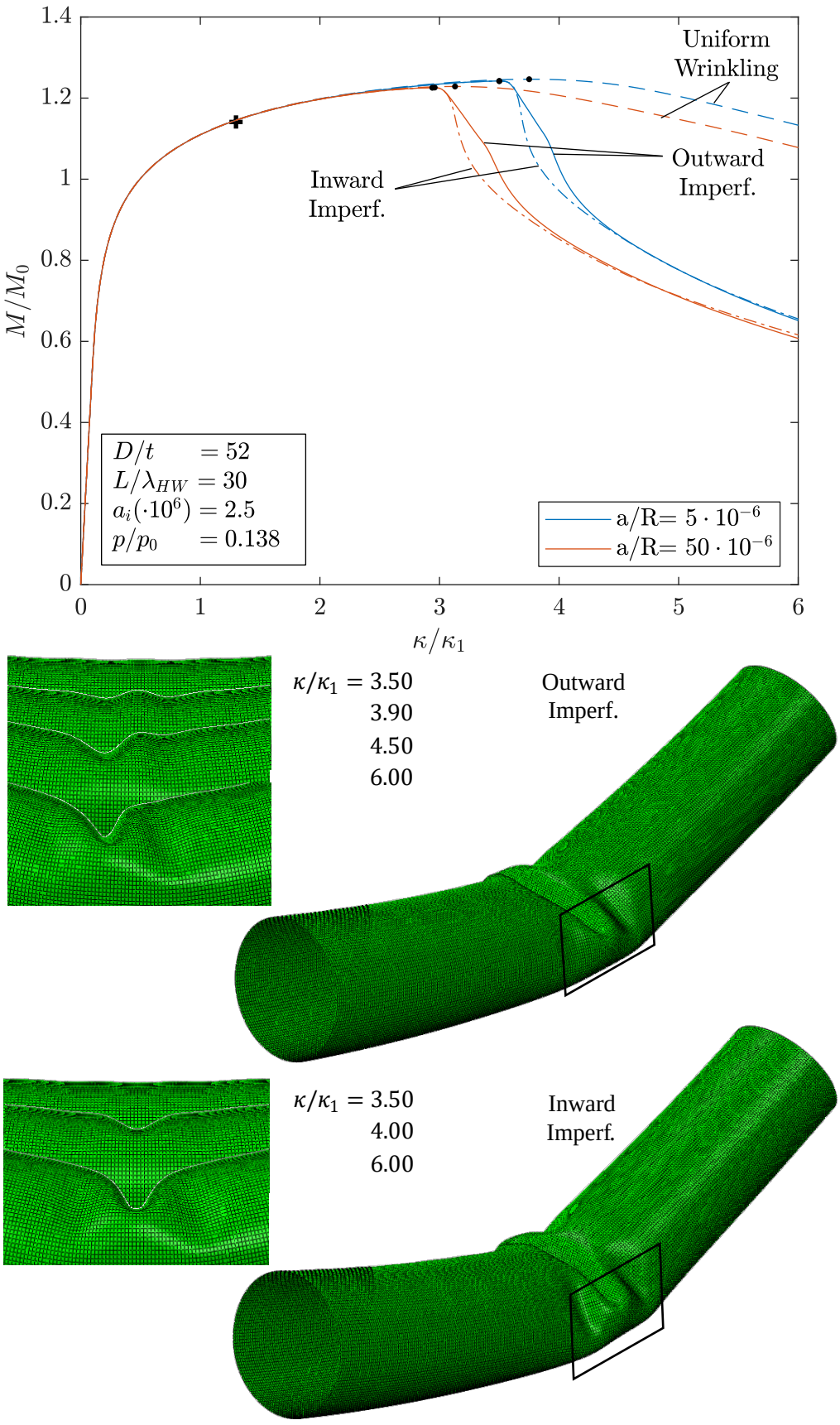

Figure 6.14: Influence of the direction of the maximum imperfection in the failure of the pressurized shell (a) Moment-curvature response (b) Ultimate configuration.

eccentric secondary buckles may be formed, leading to a diamond buckling mode.

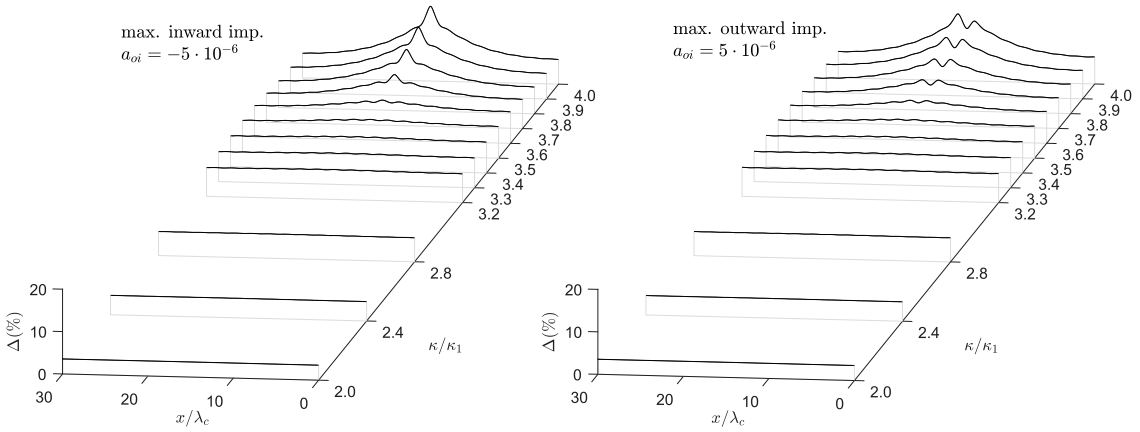

Figure 6.15: Evolution of ovalization along the pressurized cylinder ($p/p_0 = 0.138$) for (a) inward, (b) outward maximum initial geometric imperfection

In the case of inward imperfection, a primary inward buckle forms, whose depth increases rapidly following the limit load, while eccentric secondary buckles may develop one or both the side of its neighbouring imperfection crests. In this case, the post-limit load moment reduction is more precipitous. It is noted that the secondary non-symmetric buckles became visible at curvature just before $4\kappa_1$, by which stage the cylinder moment capacity was already reduced by 15%. These differences, dependent on the direction of imperfection, arise immediately after the limit load but soon afterwards the $m-k$ behaviours converge again and become very similar for both types of imperfection.

For a high internal pressure, the post-buckling behaviour is altered, as an outward buckle forms and deformation localizes symmetrically on the two adjacent wrinkle crests further pronouncing the main outward buckle. This leads to the symmetric buckling mode in (Figure 6.16), in agreement with the experiments at high pressure.

Figure 6.16 focuses on the deformation locally at the buckle in the vicinity of the maximum moment and well after it (at $\kappa = 7\kappa_1$). It further depicts the evolution of ovalization along the simulated cylinder segment at increasing values of curvature. Compared to the lower pressure in Figure 6.14, the wrinkle amplitude increases more uniformly up to larger values before localization. Despite bifurcation being estimated at $\kappa_c = 1.5\kappa_1$ the wrinkle evolution is curbed by pressurization, so wrinkle amplitude remains benign up to large curvatures $\kappa = 3.2\kappa_1$ (configuration 1) as noted by (Limam et al., 2010). Before the limit load (configuration 2) wrinkles are visible and the greatest amplitude is seen at the mid-length, where imperfection bias was applied. Figure 6.17 further shows the axial stress level in the pressurized cylinder at four stages of deformation, which are also marked in Figure 6.16

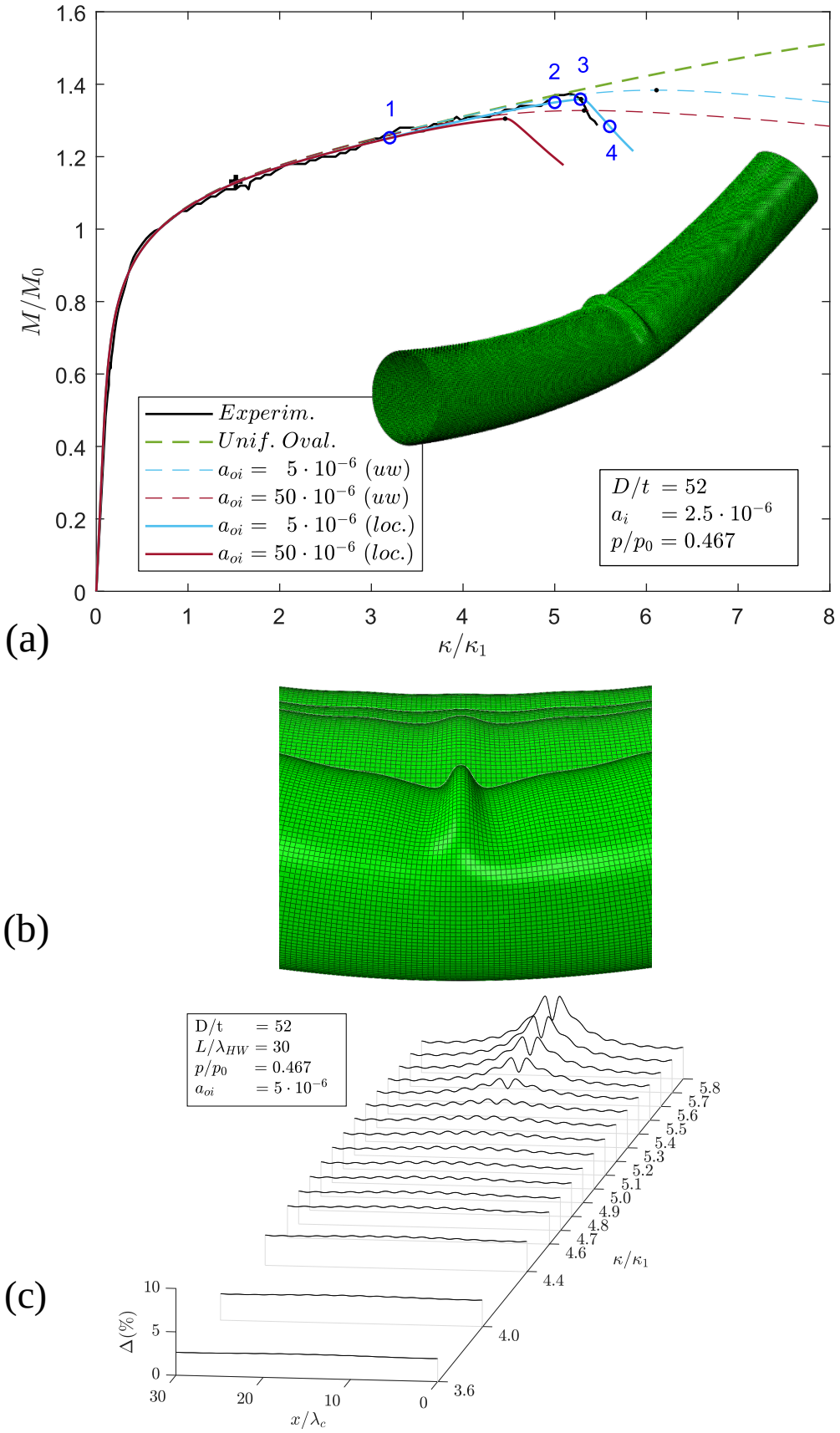

Figure 6.16: (a) Moment-curvature response of pressurized shell ($p/p_0 = 0.467$), (b) localization of wrinkling in an outward 'bulge', (c) Ovalization along the cylinder

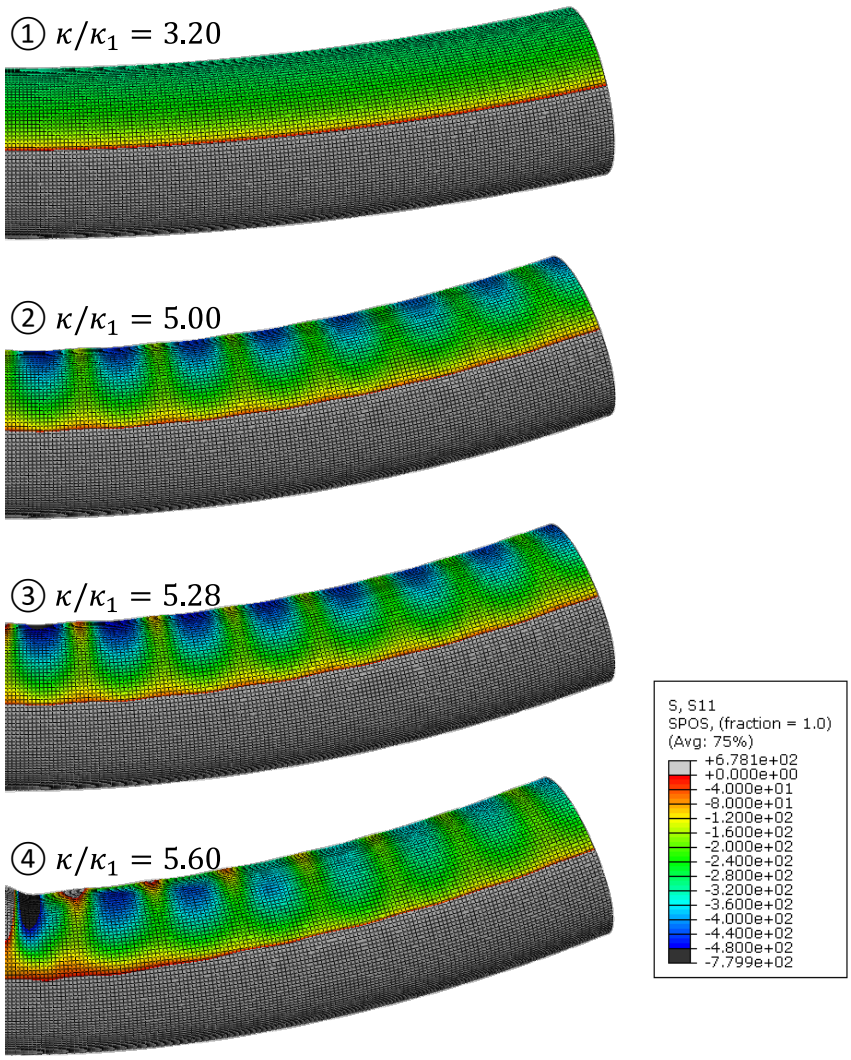

Figure 6.17: Axial stress in the buckled cylinder at different stages of deformation

A good comparison with the experimental response is seen for $p/p_0 = 0.467$ for imperfection amplitudes of order 10^{-5}. This was indicated in Figure 6.13 and it is consistent with the conclusions in (Limam et al., 2010). In Figure 6.18 the influence of imperfection amplitude in the ultimate moment capacity of the cylinder and the respective limit curvature are plotted versus the level of internal pressure.

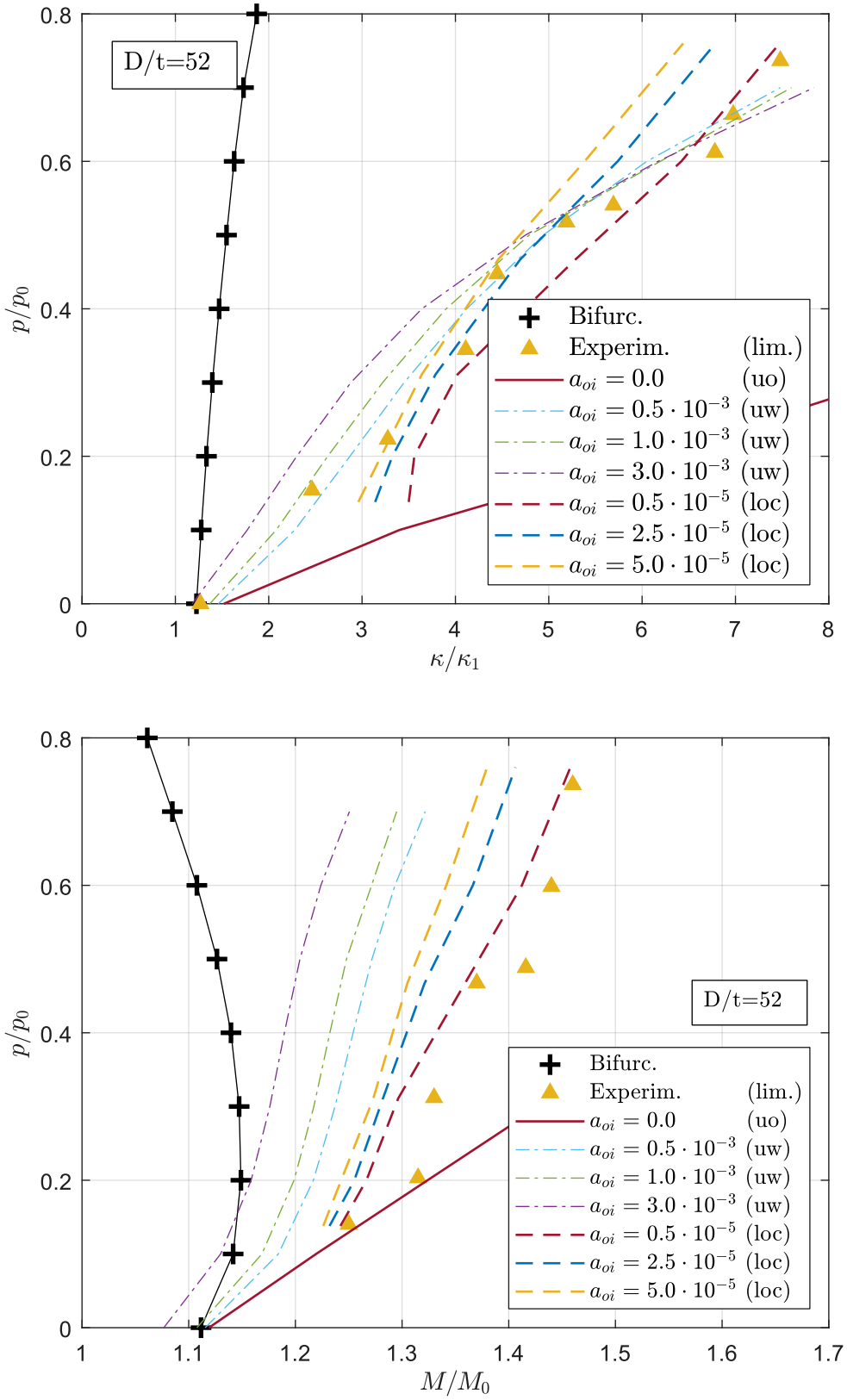

Figure 6.18: Limit curvatures and moments for various levels of imperfection and comparison with experimental data

6.5.2 Constitutive modelling

The influence of the constitutive model parameter θ_c in bending under pressure is similar to that in pure bending. Small values can lead to substantial differences in the limit curvature of the shell, and less pronounced changes in the limit load. The sequence of events leading to failure is not altered: (a) initially the shell ovalizes almost uniformly, (b) the onset of wrinkling is established, and the amplitude of the wrinkles increases uniformly along the shell (c) wrinkling localizes, a limit moment resistance develops and (d) collapse follows.

In Figure 6.19 the behaviour of the cylinder is given for pressure $0.138p_0$ and two imperfection amplitudes. For the associative model, the smaller imperfection amplitude $(5 \cdot 10^{-6})$ does not instigate collapse immediately after the limit load, as additional bending deformation of $0.8\kappa_1$ is applied before abrupt loss of stiffness. For the larger imperfection both take place concurrently, and this behaviour is also recorded with the non-associative model: bending rigidity drops immediately after the limit load formation. Limit loads develop earlier in the deformation history for increasing values of θ_c. Additionally, for $\theta_c = 5^o$, limit load develops at very similar deformation and load, for both imperfection amplitudes.

In all cases, the steep reduction of stiffness in the shell's behaviour signifies the transition to the localized wrinkling configuration, characterized by a main bulging buckle. Well into the dropping branch another bifurcation takes place, signified by the formation of secondary buckles on either side of the main one, which develop gradually within the dropping branch. In the cases of the J2FT and J2NA ($\theta_c = 2^o$), the cylinder ultimately transitions to a diamond mode, while buckles grow more rapidly when the non-associative model is used. By increasing the constitutive model's angle to $\theta_c = 5°$, a different secondary buckle profile is recorded, with eccentric buckles developing anti-symmetrically on either side of the main outward buckle (Figure 6.19).

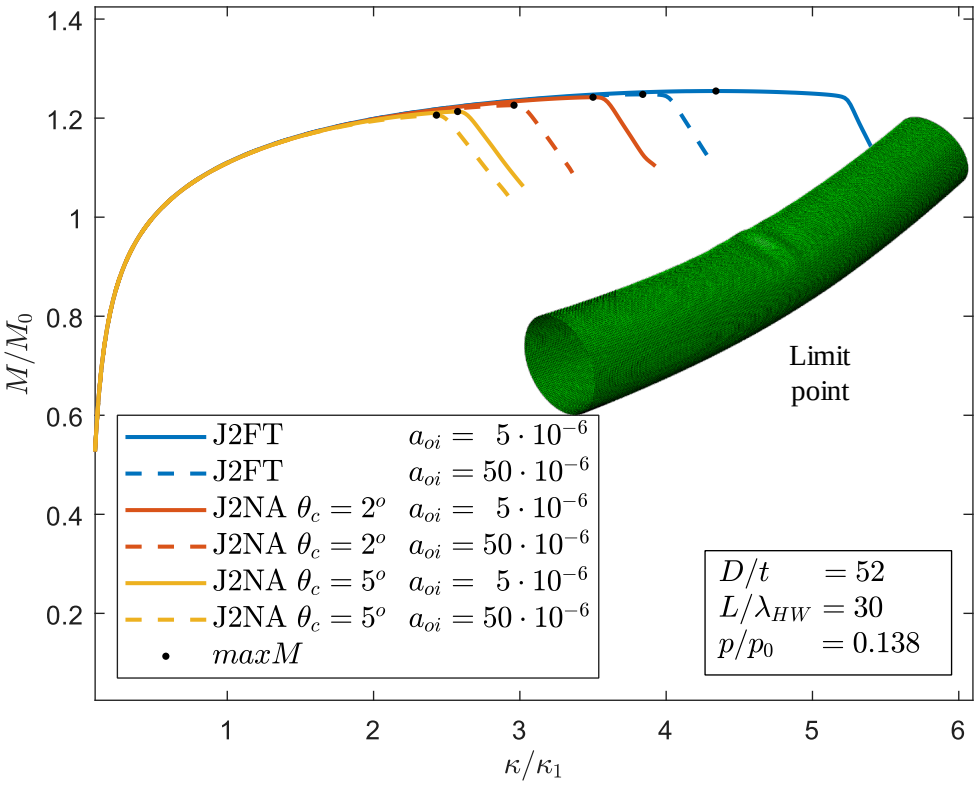
1.4
1.2
1
0.8
0.6
0.4
0.2
M/M_0
1
2
3
4
5
6
κ/κ_1
Limit
point
J2FT $a_{oi} = 5 \cdot 10^{-6}$
J2FT $a_{oi} = 50 \cdot 10^{-6}$
J2NA $\theta_c = 2^o$ $a_{oi} = 5 \cdot 10^{-6}$
J2NA $\theta_c = 2^o$ $a_{oi} = 50 \cdot 10^{-6}$
J2NA $\theta_c = 5^o$ $a_{oi} = 5 \cdot 10^{-6}$
J2NA $\theta_c = 5^o$ $a_{oi} = 50 \cdot 10^{-6}$
$maxM$
$D/t = 52$
$L/\lambda_{HW} = 30$
$p/p_0 = 0.138$

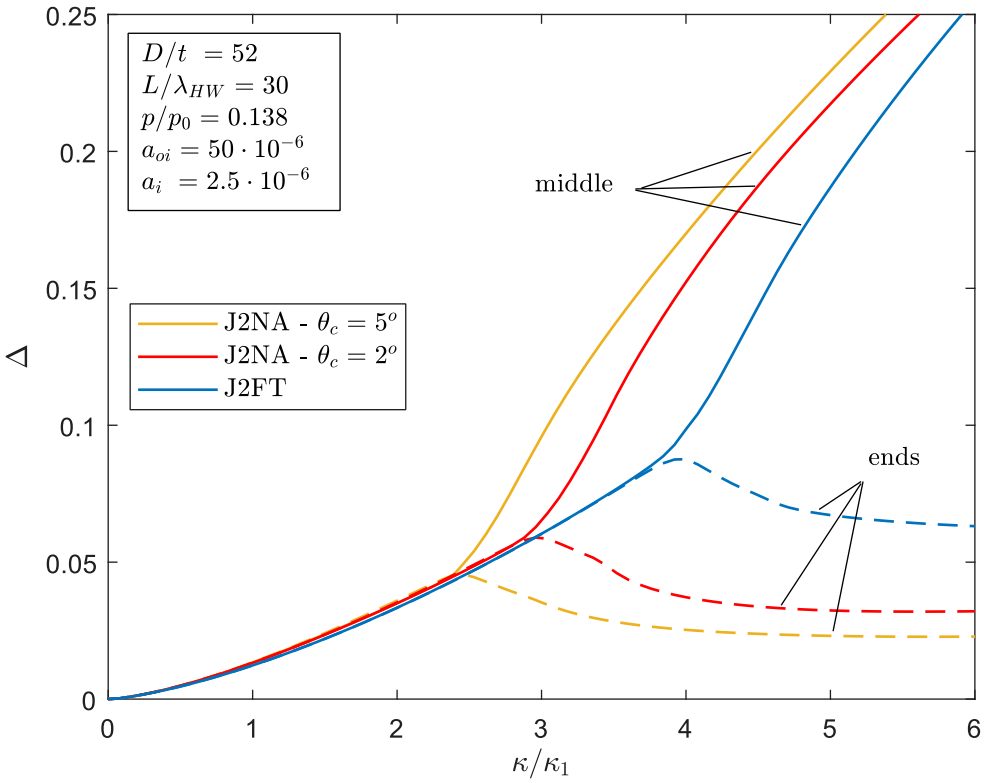
0.25
0.2
0.15
0.1
0.05
0
Δ
0
1
2
3
4
5
6
κ/κ_1
$D/t = 52$
$L/\lambda_{HW} = 30$
$p/p_0 = 0.138$
$a_{oi} = 50 \cdot 10^{-6}$
$a_i = 2.5 \cdot 10^{-6}$
middle
ends
J2NA - $\theta_c = 5^o$
J2NA - $\theta_c = 2^o$
J2FT

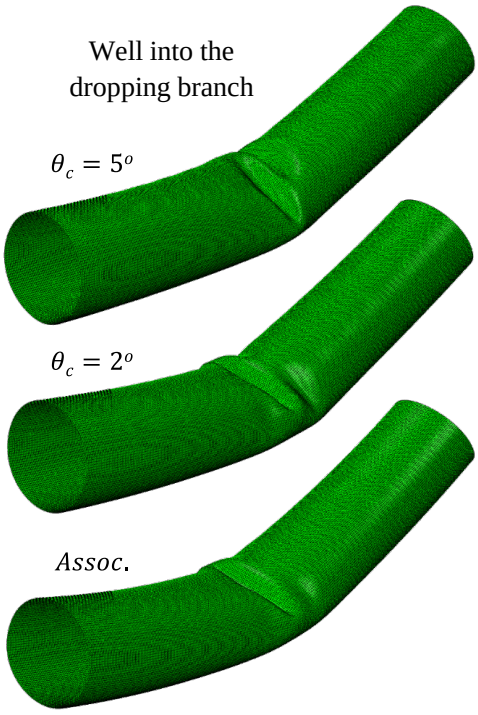

Figure 6.19: Influence of constitutive modelling in the moment-curvature and ovalization response of pressurized cylinder; exaggerated failure profile

6.5.3 Modelling of experiments

Simulations of the experiments by (Limam et al., 2010) are given in Figure 6.20 showing agreement with the experimental curves for the levels of imperfections that were suggested by the experimenters and investigated above.

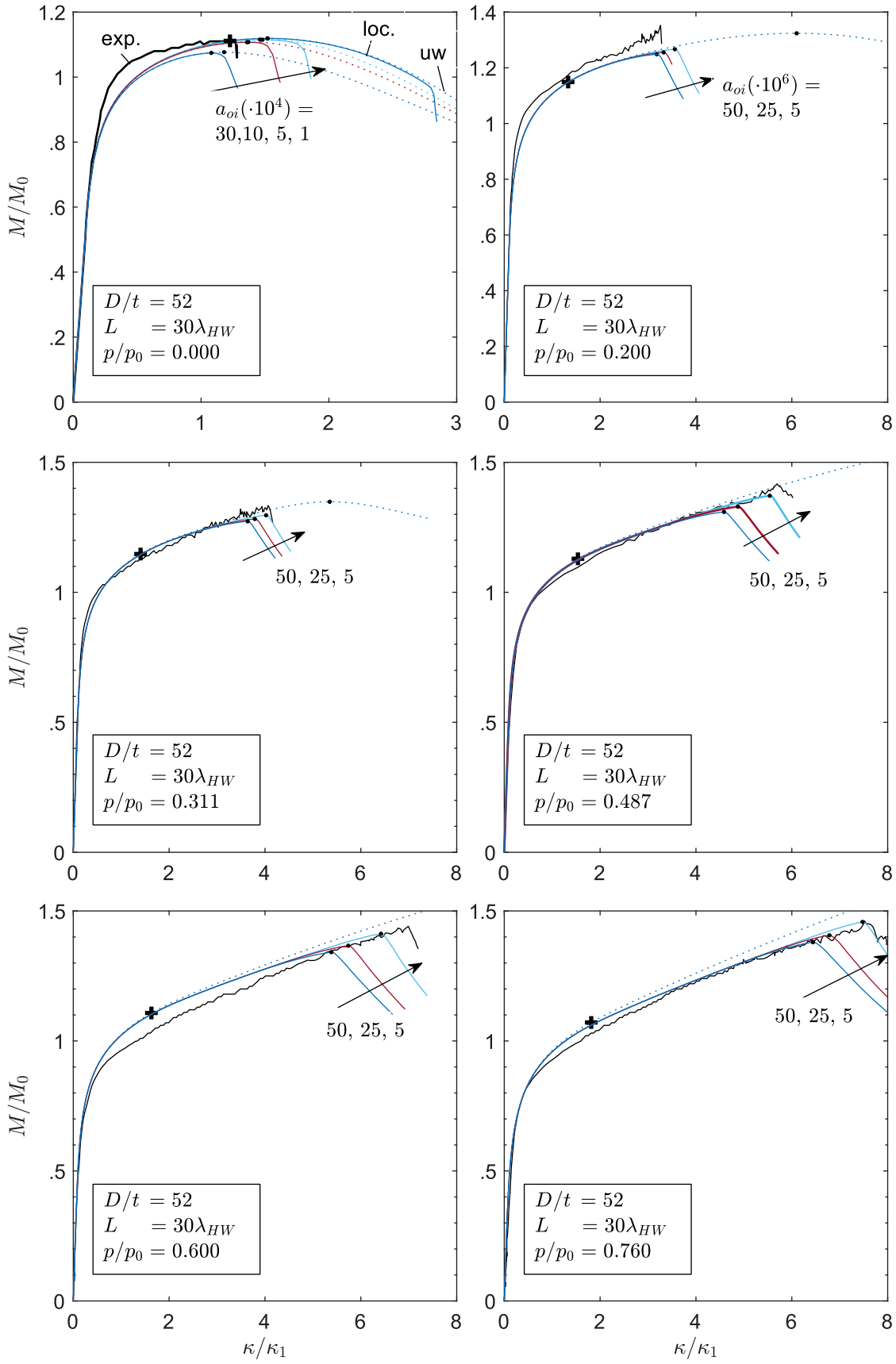

Figure 6.20: Comparisons with experimental data of bending under various levels of internal pressure

6.6 Conclusions

The structural response of a long internally pressurized thick-walled inelastic cylinder ($D/t = 52$) is examined using nonlinear finite element analyses, employing the developed non-associative flow rule. Results demonstrate the influence of two instability modes (ovalization and bifurcation) in the ultimate capacity and deformation of inelastic cylinder and verify the observation of previous researchers about the effects of pressure. The J2NA constitutive model is found to accurately reproduce the structural behaviour of the pressurized shell, including ovalization, buckling, wrinkle evolution and localization, ultimately leading to structural failure.

Bending tends to ovalize the cross section but internal pressure curbs the growth of ovalization. A low internal pressure (less than say $0.20p_0$) has a stiffening effect in the tube response, increasing the moment capacity and drastically delaying the ovalization limit point. Increasing values of pressure cause earlier yielding, and as a result the moment-curvature response of the shell develops a knee at progressively lower curvatures for increasing pressure. This lowers the moment sustained by the cylinder at any curvature, however, the maximum load at the ovalization limit point increases. It reaches uncharacteristic levels, denoting that local instability governs the cylinder failure.

Bifurcation instability (buckling) occurs in the form of wrinkles developing in the compressed side of the bent tube. Internal pressure delays somewhat the bifurcation point, which, however, in all cases is estimated well before ovalization instability. Wrinkle wavelength and width increase for increasing pressure loads. The secondary equilibrium path is smooth, and wrinkles develops stably. Significant post-buckling bending deformations may precede the localization of wrinkling, particularly for high values of pressure. Localization of wrinkling causes the development of a maximum load, followed by an abrupt loss of bending stiffness, which signifies the failure of the cylinder.

In the resulting dropping branch of the moment-curvature response, gradually with additional deformation, a transition into non symmetric modes may occur for low values of pressure, similar to the case of pure bending for cylinders with $D/t > 45$. For high values of pressure, the pressurization's stabilizing effect leads to buckling localization in an outward bulge at considerably higher loads and curvatures, consistent with experimental results. Comparisons with data by Limam et al. (2010) indicate good agreement with the analyses for the imperfection levels that were suggested.

The maximum load under uniform wrinkling shows sensitivity to imperfection, which

increases for higher pressure levels. The ‘long’ models indicate that wrinkle localization occurs significantly earlier that the limit point in uniform wrinkling models. The parameter θ_c of the constitutive model somewhat reduces sensitivity to imperfection amplitude, but also leads to less stiff behaviours, similar to observations in pure bending and compression, indicating small values are more representative for the material. The adopted approach is found to reliably model the cylinder behaviour, under the non-proportional loading scheme due to the internal pressure.

7 BENDING-COMPRESSION ANALOGY

Early investigations by (Seide & Weingarten, 1961) in bifurcation instability of elastic tubes under pure bending identified similarities to their bifurcation under uniform compression. They concluded that bifurcation onsets when the nominal bending stress is very close to the critical stress of the cylinder under uniform compression -eq. (7.1)-. This similarity offered a practical way to estimate bifurcation of the elastic cylinders under bending, yet, the resulting bifurcation moments were uncharacteristically high, so that buckling was estimated to occur after the ovalization limit point obtained by Brazier.

In an improved approach, Axelrad (1965) postulated that bifurcation is determined by the stress and deformation locally, inside the zone of an initial buckle. Based on this 'local buckling hypothesis' (LBH), instability under bending occurs when the compressive stress inside the buckle zone reaches the critical stress value of an 'equivalent compressed cylinder' with radius R_{eq} equal to the local hoop radius of the ovalized shell (Figures 6.4 & 7.1). This approach produces bifurcation estimates at moments which are lower than the ovalization limit load and more consistent with experimental results. Onward, LBH was successfully employed in investigations on bifurcation instabilities of elastic cylinders under bending, accounting for the influence of support conditions (Stephens, et al., 1975), pressure, initial curvature and non-circular cross sections (Fabian, 1977; Karamanos, 2002; Houliara & Karamanos, 2006). Similarities between the buckling behaviours under compression and bending were also considered for cylindrical shells

loaded into the inelastic range by e.g. (Reddy, 1979; Ju & Kyriakides, 1992; Vasilikis, 2012).

This paragraph demonstrates the use of LBH in estimating bifurcation of elastic-plastic cylinders under bending and internal pressure, based on their ovalization response. It further explains the mismatch in behaviour of the bending wavelengths in elastic and elastoplastic cylinders with respect to internal pressure: in inelastic cylinders pressure tends to increase wavelength, while it has the opposite effect in elastic cylinders.

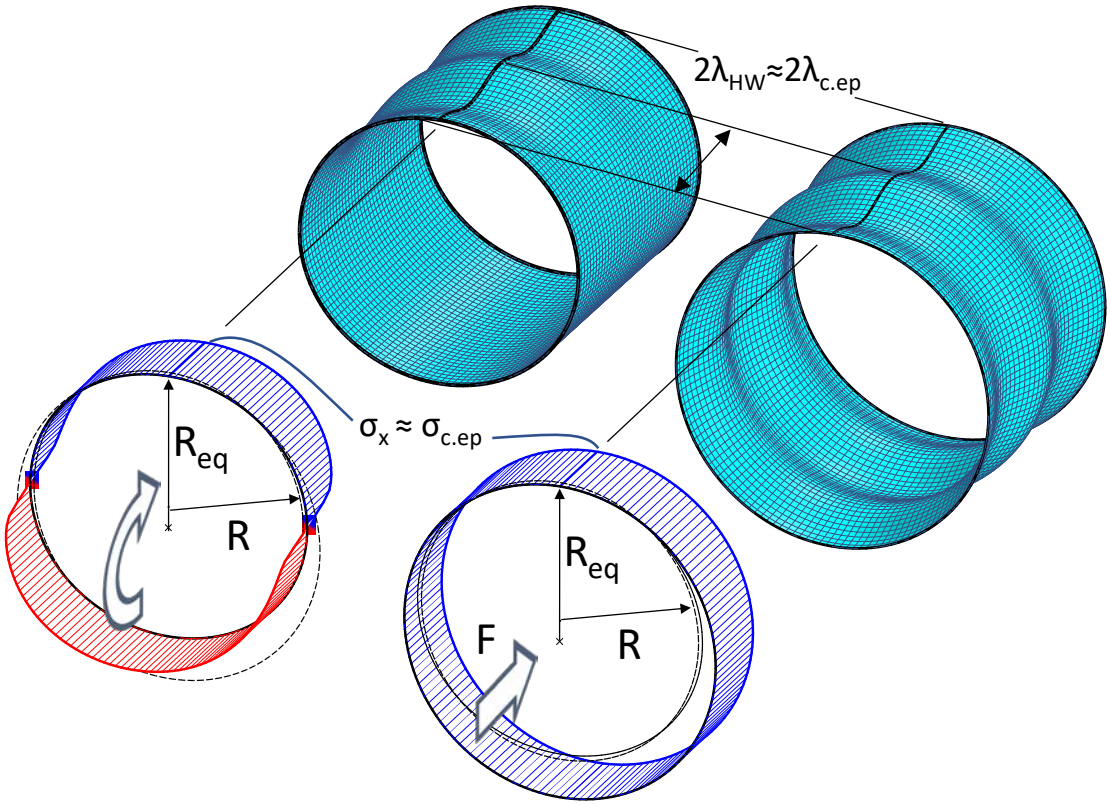

Figure 7.1: Schematic representation of the local buckling hypothesis (LBH) or bending-compression analogy in elastic plastic cylinders

7.1 Simplified bifurcation estimates

Using LBH in bending, bifurcation from the primary equilibrium path occurs when the compressive stress σ_x at the intrados of the ovalized cylinder reaches the critical stress value σ_c of an equivalent cylinder with radius R_{eq}, equal to the local hoop radius of the ovalized cross section. The wrinkling wavelength of the two cylinders is very similar. For elastic cylinders, this hypothesis is written as:

$$\sigma_x = \sigma_{c.el|EQ} = \frac{E}{\sqrt{1-\nu^2}} \frac{1}{R_{eq}/t} \tag{7.1}$$

$$\lambda_{HW} = \lambda_{c.el|EQ} = \frac{\pi}{\sqrt[4]{12(1-\nu^2)}}\sqrt{R_{eq}t} \tag{7.2}$$

where R_{eq} is the local hoop radius at the most compressed location (intrados) of the ovalized shell. Figure 7.1 shows a generalization of this analogy for inelastic cylinders. Previous researchers adopted a simplified ovalization displacement field for linear elastic materials and developed an analytic expression for the ovalization response of pressurized elastic shells under bending. This was used in (7.1) to obtain closed-form solutions for the critical bifurcation curvature κ_c and stress σ_c , and eq. (7.2) provided the corresponding halfwave length λ_{HW}. These bifurcation estimates were found to be in excellent agreement with estimates obtained using more sophisticated finite element models.

Extending this approach to inelastic shells demands accounting for the interaction of ovalization, pressure and the nonlinear, history-dependent material behaviour. This complexity disallows the obtainment of a closed form expression for κ_c. Instead, a semi-analytic approach is adopted, where the time histories of stress and local hoop radius are sourced from the initial nonlinear ovalization analyses in Abaqus. Throughout the bending history, the average axial stress at the intrados $\sigma_{x|t}$ is compared to the bifurcation stress $\sigma_{c.ep}$ of the equivalent elastic-plastic cylinder with hoop radius R_{eq} and the same level of pressure. Bifurcation from the primary (ovalization) equilibrium path is assumed at curvature κ_c, when $\sigma_{x|t}$ reaches $\sigma_{c.ep}$.

$$\sigma_{x|t}(\kappa_c) = \sigma_{c.ep}(\kappa_c) = \sigma_{c.ep|EQ} \tag{7.3}$$

$$\sigma_x = \sigma_{c.ep}\left(\sigma_x, \sigma_\theta, R_{eq}/t\right) = \sqrt{\frac{1 - C_{\theta\theta}\sigma_\theta}{3(C_{xx}C_{\theta\theta} - C_{x\theta}C_{\theta x})}}\frac{t}{R_{eq}} \tag{7.4}$$

To calculate the elastoplastic bifurcation stress $\sigma_{c.ep}$ at any stage of bending, a local iterative scheme is employed to solve eq. (7.4) in terms of σ_x, which is the generalized form of eq. (4.1) accounting for the influence of internal pressure - a detailed analysis on the obtainment of this formula is provided in Appendix 3. C_{ij} are the moduli of the material compliance tensor C, the inverse of the stiffness tensor D, which is dependent on the stress state $(\sigma_x, \sigma_\theta)$ and the adopted material model. The average value of hoop stress across the thickness at the intrados $(\sigma_{\theta|t})$ is used in calculations as hoop stress σ_θ, sourced from the ovalization analysis in Abaqus, or alternatively the simpler approximation $\sigma_\theta = pR/t$ which leads to the same results. The local hoop radius R_{eq} is calculated from the

displacement field at the cylinder intrados for each increment of the analysis (the $R_{eq} - \kappa$ history is given in Figure 7.3). In the adopted non-associative constitutive model, the flexibility tensor is further dependent on the non-proportionality angle θ, which is further sourced by the FE analyses. Figure 6.11 shows that θ takes low values at bifurcation for all levels of pressure, hence the material moduli are similar to the moduli of the J2DT. After the bifurcation point κ_c is identified by solving (7.3), the wrinkling halfwave $\lambda_{HW} = \lambda_{c.ep|EQ}$ is obtained using (7.5):

$$\lambda_{c.ep|EQ} = \pi \left[\frac{(C_{\theta\theta})^2}{12(C_{xx}C_{\theta\theta} - C_{x\theta}C_{\theta x})(1 - C_{\theta\theta}\sigma_{\theta})} \right]^{1/4} \left(R_{eq}t\right)^{1/2} \tag{7.5}$$

The above procedure of applying LBH in the buckling of inelastic cylinders under bending is presented in Figure 7.2 for pure bending and internal pressure $p/p_0 = 0.4$. Solving eq. (7.3) for all values of curvature, the critical stress $\sigma_{c.eq}$ of the equivalent compressed shell is calculated and plotted in with a black dashed line throughout the bending history. It reduces slowly with ovalization of the studied thick-walled cylinder. The average axial stress $\sigma_{x|t}(\kappa)$ increases with curvature and its intersection with line $\sigma_{c.eq}$ denotes bifurcation using LBH, it identifies $\sigma_{c.ep|EQ}$ and it is marked with (·) on the graph. Bifurcation estimated in Abaqus is marked with (+). Generally, $\sigma_{x|t}(\kappa)$ is very similar to axial stress at the integration point 4, positioned at the mid surface of the shell which is included in Figure 7.2, that further shows the stress history of all 7 integration points across the shell thickness. The same procedure is employed for pressurized bending.

Using LBH, the estimates for the critical curvature κ_c are somewhat lower than the ones obtained by the perturbation analyses in Abaqus, for all values of pressure. On the other hand, the bifurcation stress and halfwave estimates closely agree with the numerical results from the FE analyses (differences up of 1% in Figure 7.4).

An alternative, simpler approach to identifying the bifurcation using LBH is made by using $\sigma_{x|t}(\kappa)$, $\sigma_{\theta|t}(\kappa)$ from the ovalization analysis to identify the ratio $R_{c.ep}/t$ of the equivalent compressed cylinder that bifurcates under the current stress combination, by direct substitution of $\sigma_{x|t}$, $\sigma_{\theta|t}$ in eq. (7.4). Bifurcation is identified when R_{eq}/t from the ovalization analysis of the shell reaches the value $R_{c.ep}/t$, as shown in Figure 7.3. Bifurcation estimates employing this expression of the LBH are identical to the estimates using the more standard stress-based formulation used above. However, in this approach,

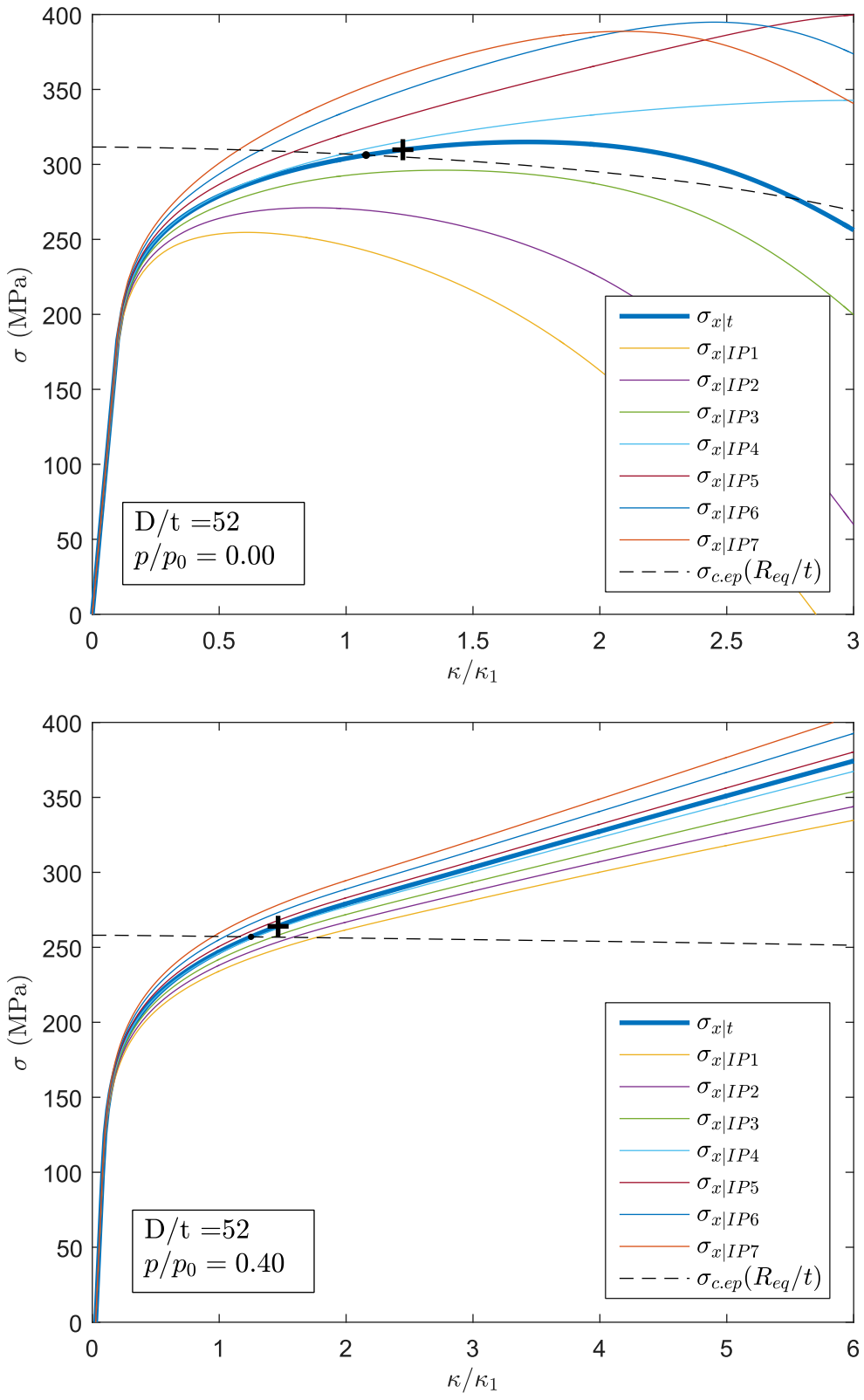

Figure 7.2: Axial stress $\sigma_{x|t}$, and the bifurcation stress $\sigma_{c.ep}$ of the equivalent compressed cylinder versus curvature under pure bending $p/p_0 = 0.00$ and internal pressure $p/p_0 = 0.40$.

no iterative solution of eq. (7.3) is necessary, making calculations simpler and more efficient.

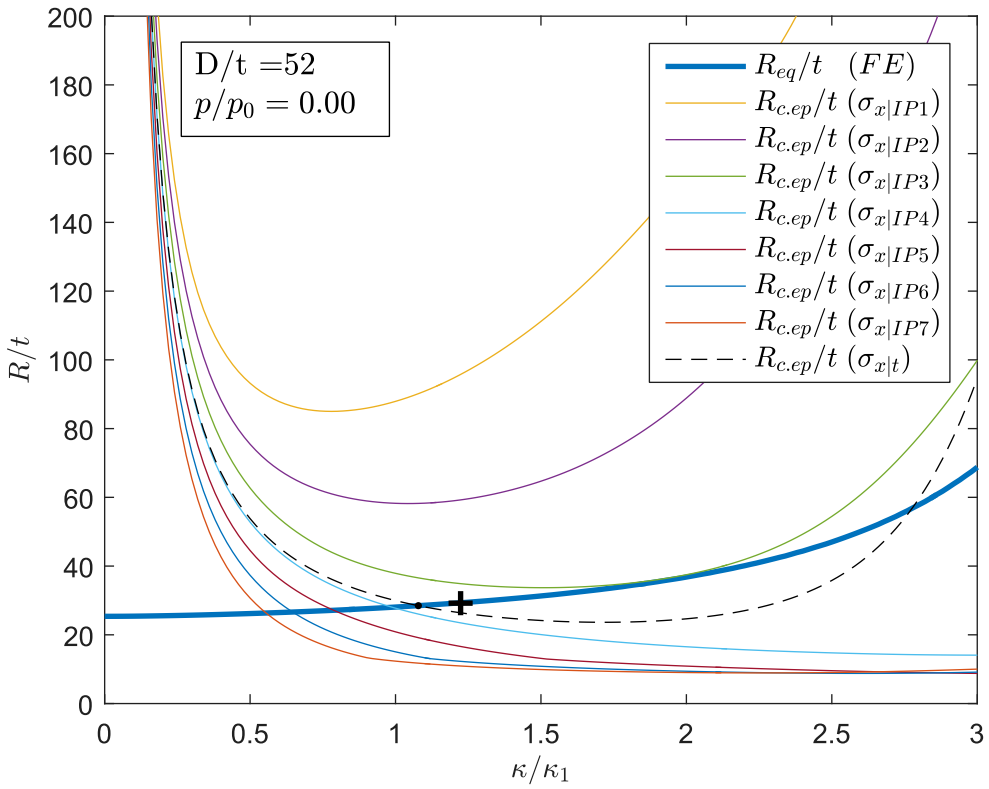

Figure 7.3: Hoop radius at the intrados over thickness R_{eq}/t vs curvature and the $R_{c.ep}/t$ of the compressed shell that bifurcated under the loading $\sigma_{x|t}$, $\sigma_{\theta|t}$, a simpler use of LBH.

In Figure 7.4 the estimated wrinkling wavelengths are plotted for the cylinder $(D/t = 52)$, subjected to bending and various levels of internal pressure. The wavelength predictions from LBH, using the data from the ovalization analyses are further marked with 'x'. They are in line with predictions obtained using the FE models for all pressure levels (differences up of 1%). It is noted that the compression material curve is used in these calculations, which was found to produce identical estimates with Abaqus in the problem of uniform compression. Estimated wavelengths follow the same trend as the FE estimates: the wavelengths increase with pressure. For high levels of pressure, close to the yield pressure p_0, this increasing trend is curbed and reversed. This is caused by the change of material behaviour at strain $\epsilon = 2.1\%$ (the stress-strain curve transitions from a Ramberg-Osgood curve to a linear hardening branch).

The wavelength of the pressurized elastic-plastic cylinder under uniform compression is further included in Figure 7.4, which follows a similar increasing trend with pressure, but as it neglects ovalization it displays higher differences to the Abaqus estimates, that reach 8% for pure bending. The wavelength of the axially compressed cylinder, when assuming elastic material behaviour (blue dashed line), does not accurately describe the influence of pressure in the inelastic cylinder.

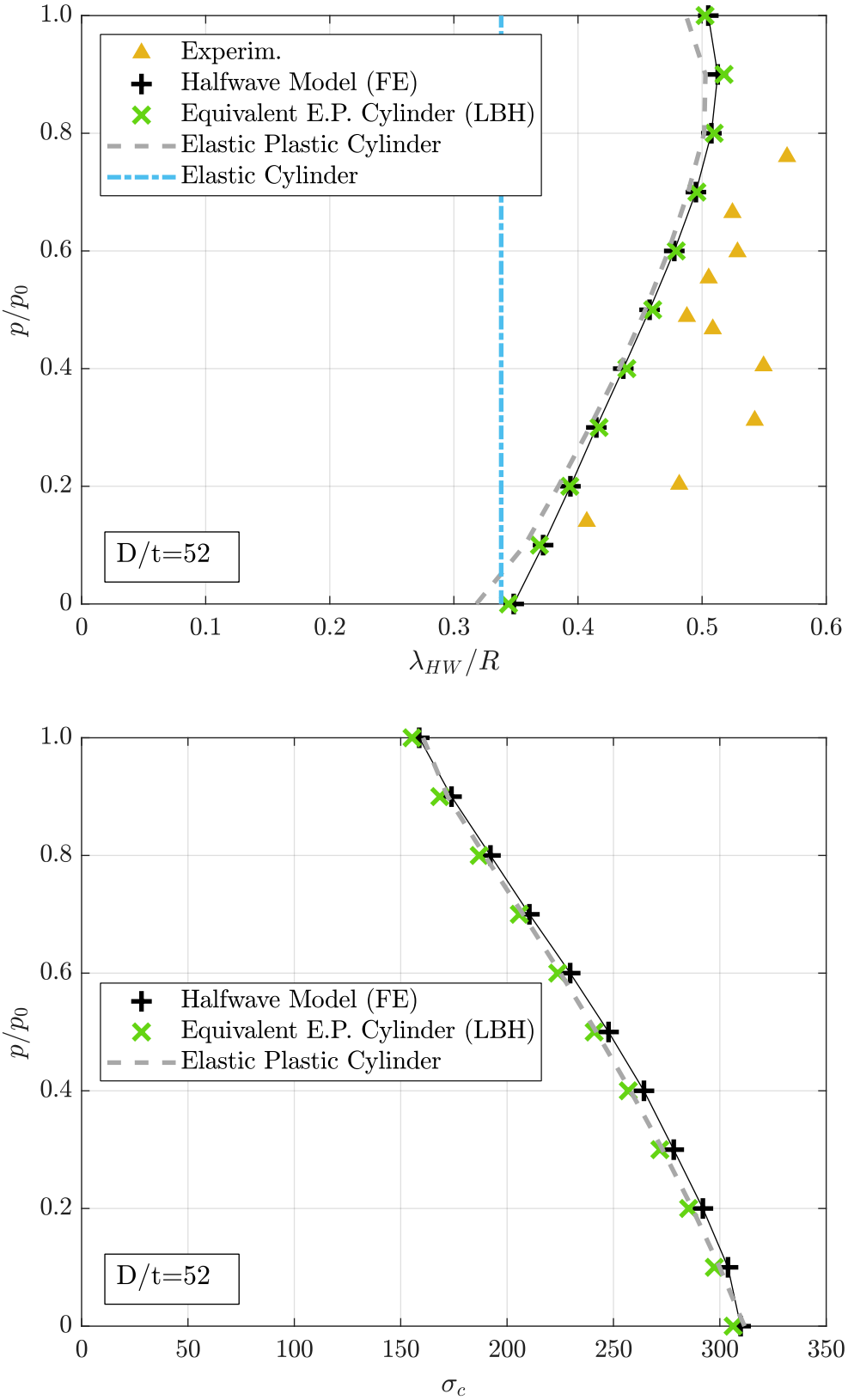

Figure 7.4: Wrinkling halfwave lengths and critical stress of the cylinder under bending versus internal pressure using Abaqus and LBH.

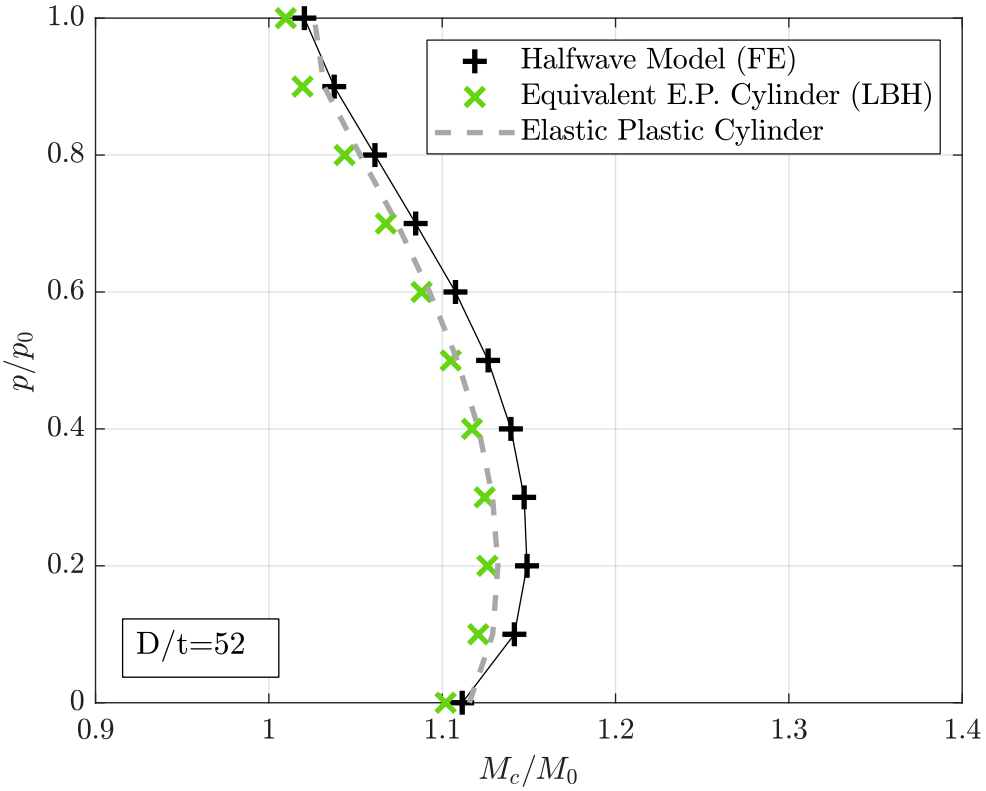

Figure 7.5: Critical moment of cylinder under bending versus internal pressure from FE analyses and using LBH.

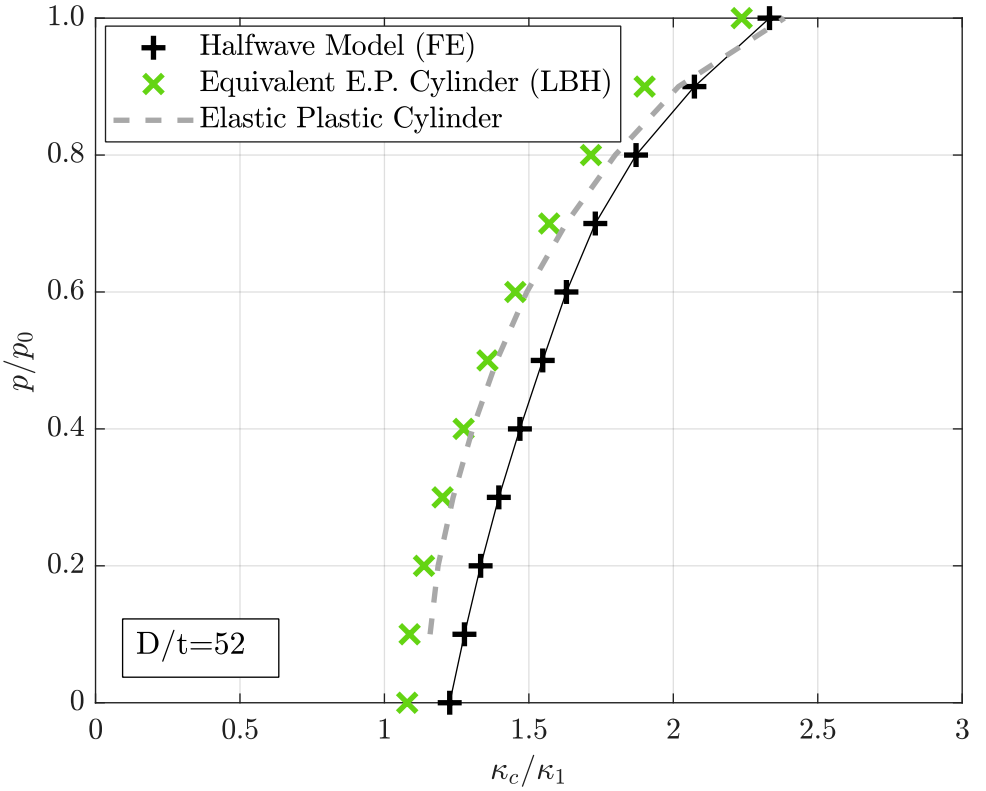

Figure 7.6: Critical bending curvature of cylindrical shell under bending versus internal pressure, calculated from FE analyses and LBH.

Very close agreement, between the LBH and the FE calculations is seen in the estimated critical axial stress $\sigma_x = \sigma_{c.ep|EQ}$ in Figure 7.4, and in the moment M_c in Figure 7.5 with differences up to 2% and 5%, respectively. The LBH estimated bifurcation curvature κ_c shows differences of $\sim$15% to the ones calculated using Abaqus, thus offering a conservative estimate.

The above analysis verifies that the bifurcation behaviour of inelastic cylinders under bending exhibits similarities with the instability of cylinders under compression, which persist in the presence of internal pressure. Using LBH and accounting for the material elastic-plastic material behaviour, accurate semi-analytical approximations of buckling stresses and wavelengths can be obtained, along with reasonable estimates of the bifurcation moment and curvature, based on simple pseudo-2D ovalization analyses.

7.1.1 Application in bending under external pressure

Similar agreement is found in the bifurcation of cylinders ($D/t = 49$), investigated by (Ju & Kyriakides, 1992) which are subjected to bending under external pressure. The LBH is employed to estimate wrinkling-type bifurcation for low values of external pressure, fractions of the cylinders collapse pressure p_c, which if applied on the cylinder leads to collapse in an ovalization mode. Its value is expressed as:

$$p_c = \frac{D_{\theta\theta}}{4(1 + (1/12)(t/R)^2)}\left(\frac{t}{R}\right)^3 \tag{7.6}$$

where $D_{\theta\theta} = C_{xx}/(C_{xx}C_{\theta\theta} - C_{x\theta}C_{\theta x})$ is a component of inelastic material stiffness tensor, and t, R the cylinder thickness and radius (proof and discussion in Appendix 3).

In Figure 7.7 the LBH is employed to estimate bifurcation for a low value of external pressure $p/p_c = -0.1$, producing reasonable agreement with FE results. For a higher external pressure ($p/p_c = -0.3$) the cylinder bending stress does not reach the buckling stress of the equivalent compressed shell and no instability estimates are obtained from the LBH.

This behaviour is verified from buckling analyses performed in Abaqus for the externally pressurized cylinder under bending, using finite element models as described in paragraph 6.1 loaded with external pressure (negative values of internal pressure). In Figure 7.8 the ovalization behaviour and bifurcation point are given for various levels of external pressure. For small fractions of p_c the obtained bifurcation mode is characterized by wrinkling in the compressed side of the tube (bifurcation points marked in '+'). For higher

values of external pressure, a bifurcation point is found (marked with 'o') associated with an ovalization buckling mode. However, the LBH fails to produce instability estimates for p/p_c values between -0.3 and -0.4 in which cases, Abaqus estimates instability after the moment maximum.

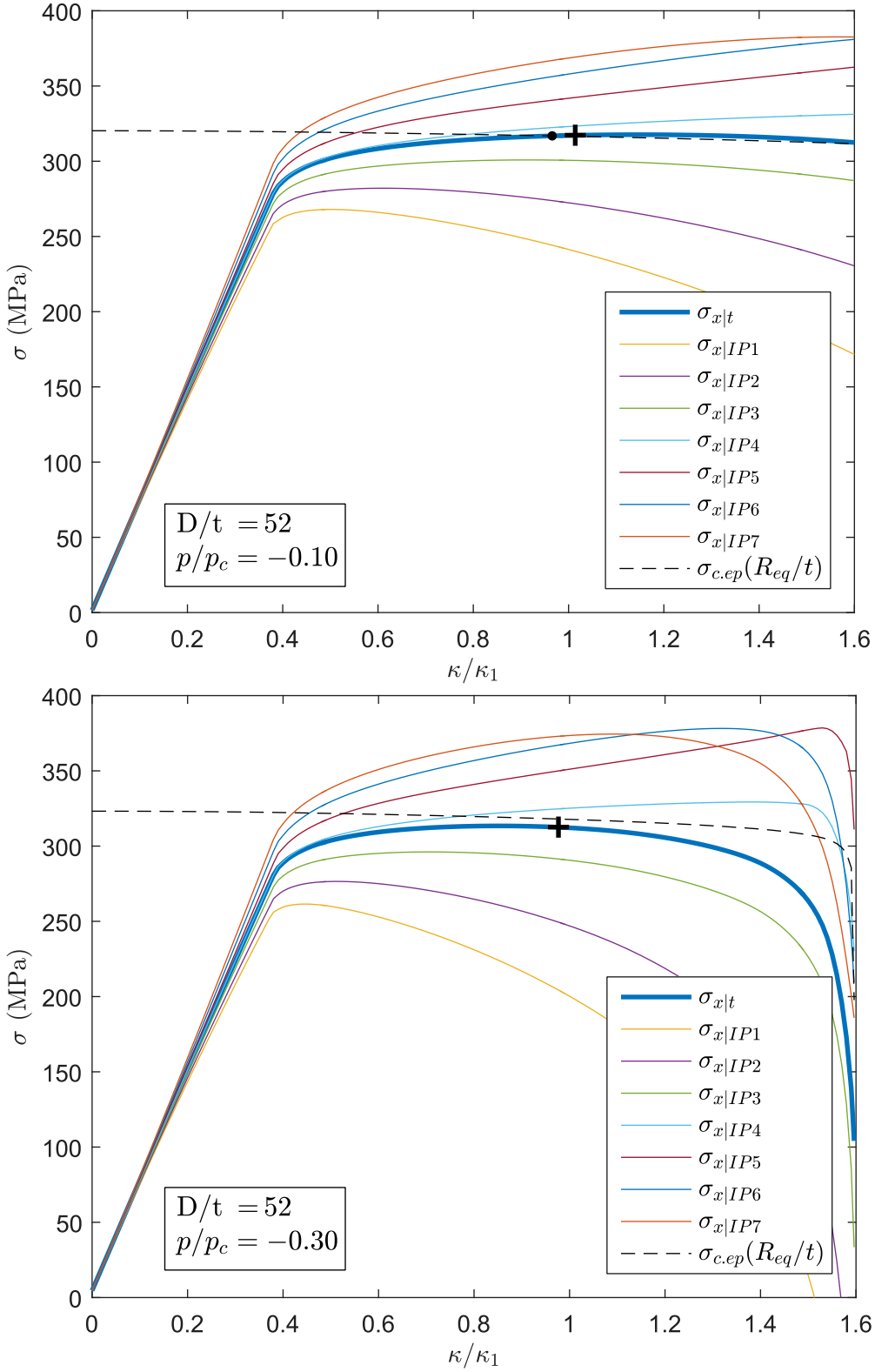

Figure 7.7: Axial stress $\sigma_{x|t}$, and bifurcation stress $\sigma_{c.ep}$ of the equivalent compressed cylinder versus curvature for cylinder bending under external pressure

Fully three-dimensional (localization) analyses further demonstrate that wrinkling-type imperfection has small influence is in the limit curvature of bent cylinders, loaded with high levels of external pressure (Figure 7.8), as ovalization instability dominates the cylinders behaviour. In contrast, for high values of internal pressure, in Figure 6.18, the role of imperfection is dominant in the performance of the cylinder, while ovalization analyses grossly overpredict its load capacity.

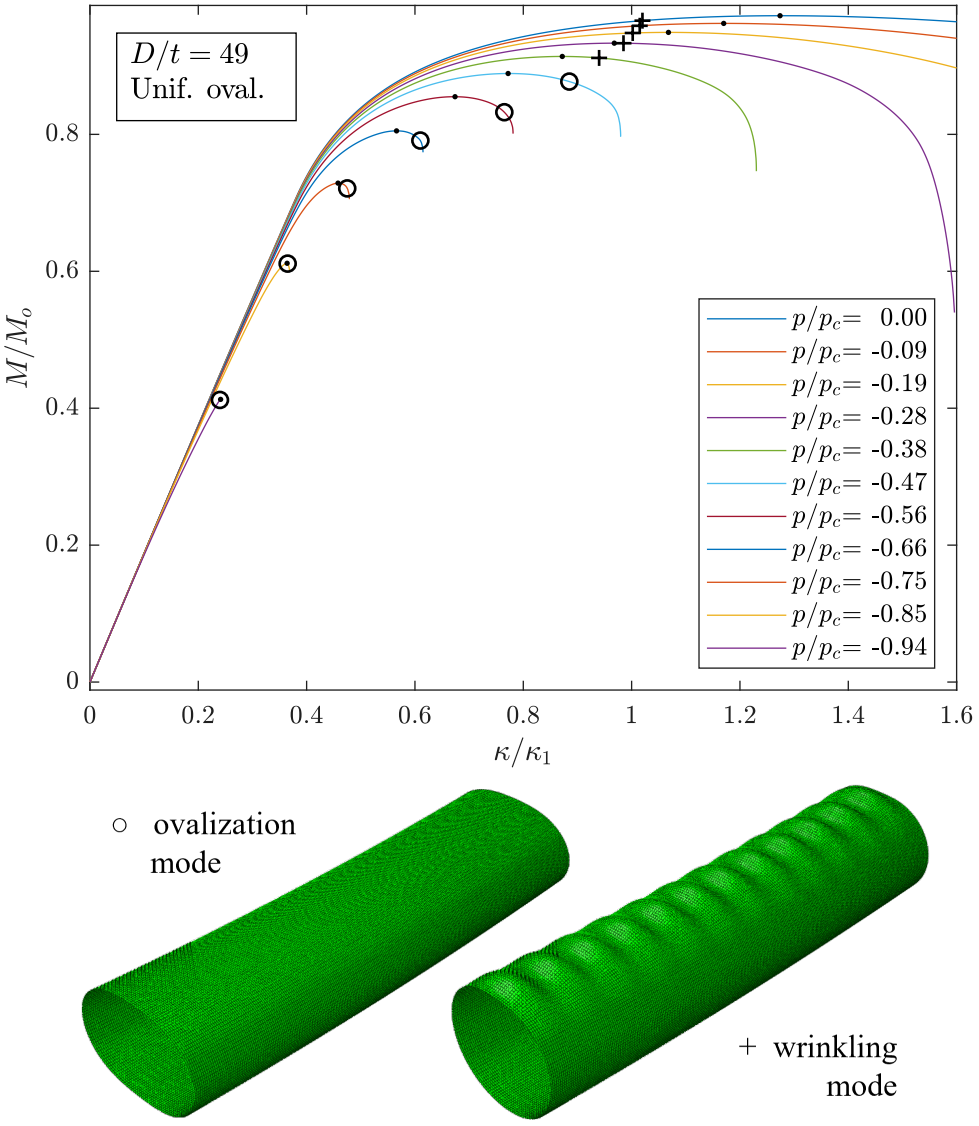

Figure 7.8: (a) Moment-curvature response of cylinder under external pressure (b) bifurcation modes

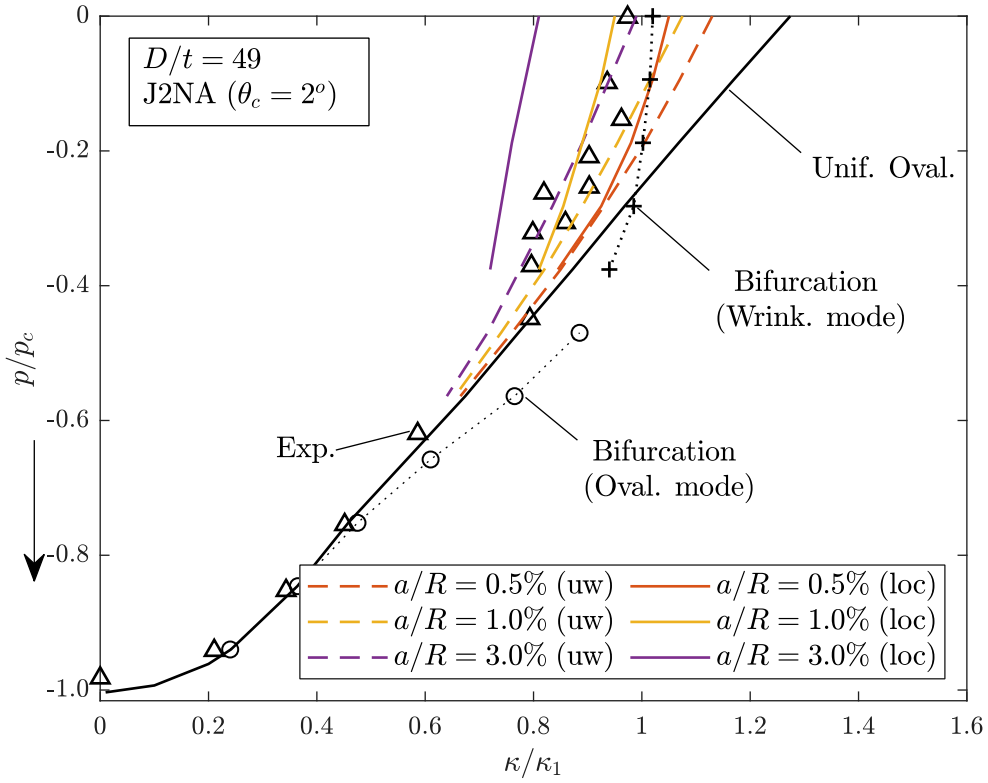

Figure 7.9: Limit curvature versus external pressure

7.2 Elastic versus elastic-plastic wavelength in pressurized bending

Figure 7.4 shows that internal pressure tends to increase the wrinkling wavelength for inelastic cylinders under bending. In the literature the opposite effect has been reported for elastic cylinders: wavelengths decrease for increasing internal pressure (Houliara & Karamanos, 2006). This mismatch in the cylinder's behaviour is addressed below, employing LBH.

The wavelength λ_{HW} of the pressurized cylinder under bending is normalized with the $\lambda_{c.el} = \pi\sqrt{Rt}[12(1-\nu^2)]^{1/4}$ which is the wrinkling wavelength of the cylinder under uniform compression, assuming elastic material behaviour. Employing the LBH, the wavelength under bending is equal to the wavelength of the 'equivalent' compressed cylinder $\lambda_{c.el|EQ}$, calculated from (7.5). So, the normalized wavelength s is expressed as:

$$s = \frac{\lambda_{HW}}{\lambda_{c.el}} = \frac{\lambda_{c.ep|EQ}}{\lambda_{c.el}} \tag{7.7}$$

For elastic shells, the equivalent compressed cylinder is also elastic $\lambda_{c.el|EQ}$, and it is calculated using (7.2), so the normalized wavelength simplifies to:

$$s_{el} = \frac{\lambda_{c.el|EQ}}{\lambda_{c.el}} = \sqrt{\frac{R_{eq}}{R}} = \hat{r} \tag{7.8}$$

This expression is used for obtaining the wavelength of elastic cylinders under bending, and it clearly shows that s_{el} increases for higher values of R_{eq} at bifurcation. In Figure 7.1, bending is shown to induce ovalization in the cross section of inelastic cylinders, while internal pressure tends to counteract it, leading to lower local hoop radius R_{eq} at bifurcation. The same effect was shown in elastic cylinders, so eq. (7.8) indicates that for elastic cylinders under bending, internal pressure tends to lower wrinkling wavelength.

For inelastic cylinders, the normalized wavelength does not simplify in the same way. Instead, it is expressed as:

$$s = \frac{\lambda_{c.ep|EQ}}{\lambda_{c.el|EQ}} \frac{\lambda_{c.el|EQ}}{\lambda_{c.el}} = \hat{l}\left(p, R_{eq}/t\right) \sqrt{\frac{R_{eq}}{R}} = \hat{l} \cdot \hat{r} \tag{7.9}$$

where $\lambda_{c.el|EQ}$ is the half wavelength of the equivalent compressed cylinder, assuming elastic behaviour -eq. (7.2)-. The value of s is the product of two terms: (i) $\hat{r}$ accounting for the change of local hoop radius at bifurcation compared to the initial configuration, and (ii) the additional factor $\hat{l}(p, R_{eq}/t)$ which accounts for the inelastic material behaviour including the effect of the hoop stress level.

Lower ovalization (and a lower value of R_{eq}) is found at buckling of pressurized shells under bending, so the term $\hat{r}$ reduces, which tends to reduce wavelength. From the LBH calculations in Figure 7.3 for pure bending ($p/p_0 = 0.00$) and pressure $p/p_0 = 0.40$, term $\hat{r}$ takes values 1.060 and 1.015, respectively. However, for inelastic cylinders the factor $\hat{l}$ increases significantly with pressure, which is demonstrated in Figure 7.10. Factor $\hat{l}$ is relatively constant for small changes in D/t but increases from 1.008 in pure bending to 1.292 for $p/p_0 = 0.40$. As a result, despite the higher ovality at bifurcation under pure bending, the normalized wavelength is $s = 1.07$, which is 15% smaller than in the pressurized case where $s = 1.30$. It follows that the inelastic material behaviour and biaxial stress state have a more pronounced influence on the wavelength. Figure 7.11 demonstrates the increasing trend of the wrinkling wavelength of compressed inelastic cylinders with various D/t ratios with respect to internal pressure.

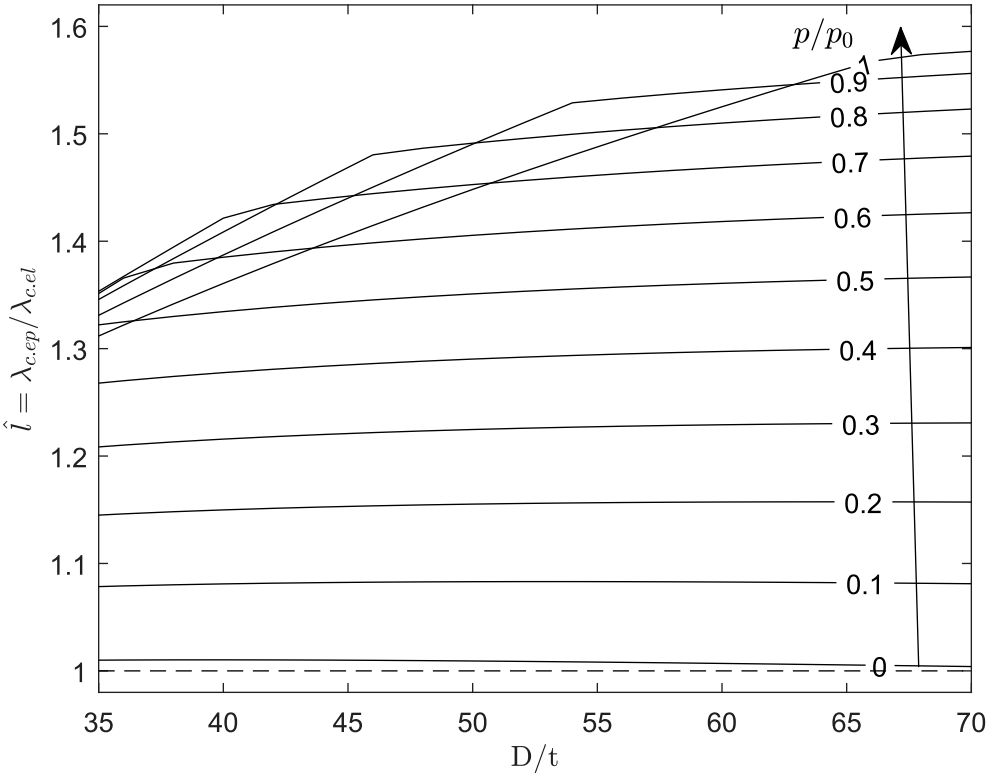

Figure 7.10: Factor $\hat{l}$ for compressed cylinders with respect to D/t ratio for various levels of internal pressure

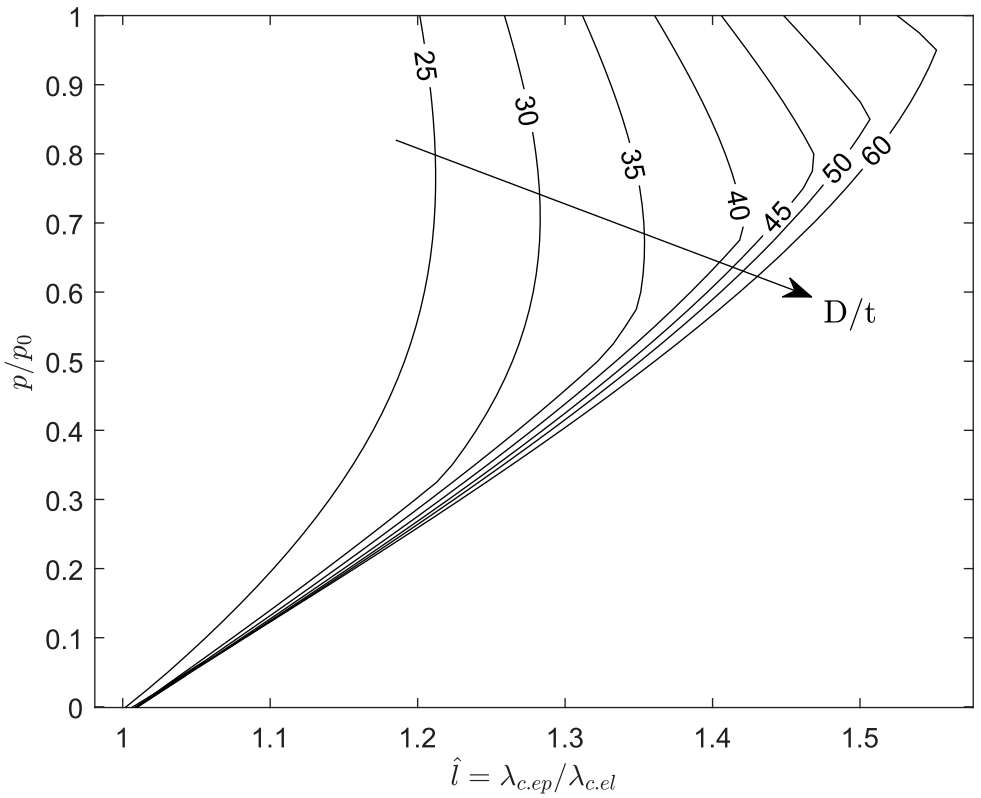

Figure 7.11: Factor $\hat{l}$ versus with internal pressure for axially compressed cylinders of various D/t values.

In summary, the perceived mismatch in the wavelength behaviour in elastic and elastoplastic cylinders bent under pressure is explained by the consideration of ‘equivalent’ compressed cylinders. The wavelength increases with ovality, so internal pressure tends to reduce it. Oppositely, buckling into the inelastic range under biaxial loading tends to increase wavelength. The influence of ovality is less pronounced than the influence of plasticity, so the latter governs the increasing trend of the wavelength with respect to internal pressure in bending of inelastic cylinders, while the former in elastic ones.

8 CONCLUSIONS

This doctoral work develops a new perspective in traditional instability problems of thick-walled metal shells, where standard numerical simulation approaches do not always produce reliable buckling predictions and rely on overly high geometric and other imperfections.

A fundamental objective of this work is the development of a special-purpose constitutive model for simulating the structural behaviour of thick-walled metal cylinders under compressive loads and, in particular, accounting for their structural instability and post-buckling response. The model assumes a Von Mises yield surface and a non-associative flow rule, dependent on the direction of the strain rates, which mimics the effect of a yield surface vertex. Fully elastic unloading is implemented for strain rates directed tangent to or inwards the yield surface. In this model, any discontinuity in the plastic strain production is eliminated for strain rate directions near the yield surface tangent, by adopting a strain-direction-dependent non-associative hardening parameter $\bar{h}$, which moderates the production of plastic strain. Upon proper definition of $\bar{h}$, the model's formulation can represent several pseudo-corner models proposed elsewhere, which account for different material stiffness.

A two-branch flow rule is developed in the present plasticity model. For small deviations from proportional loading, it employs the rate form of the J_2 deformation theory to inherit its effectiveness in predicting bifurcation. For larger deviations from proportional

loading, the plastic flow mimics the effect of a corner in the yield surface, constraining the plastic strain increment to be directed within this ‘vertex’. The non-associative hardening parameter $\bar{h}$ determines the model’s pseudo-corner effect and enables a smooth transition to elastic unloading.

A robust integration algorithm is developed for implementing the constitutive model using a backward-Euler scheme for three-dimensional (solid) elements, together with an enhanced version suitable for shell element analysis. In both cases, the consistent algorithmic moduli are derived. This implementation scheme maintains the main features of the standard J_2 flow theory (J2FT), and it can be efficiently introduced in a finite element code. Key modifications incorporate the non-associative behaviour and offer a versatile framework for implementing various other pseudo-corner plasticity models in an implicit numerical environment, while meticulously accounting for the non-standard material behaviour.

The model is programmed and introduced in the commercial finite-element software Abaqus as a material user subroutine (UMAT) for shell element analyses. Several benchmark problems of inelastic shell buckling are simulated, demonstrating the capabilities of the model. The structural behaviour of thick-walled cylindrical shells is considered under various monotonic compressive loads, which are characteristic for tubular structures and pipelines. The most important advantage of this model is that the analyses use a single constitutive law for both tracing the equilibrium path and estimating instability, using of the capabilities of the software. The bifurcation estimates from the present model agree with experimental data in a range of loading conditions. The results demonstrate that the present methodology can accurately and efficiently predict buckling and post-buckling into the inelastic range. Numerical analyses investigate further aspects of the structural response of tubulars in the inelastic range, factors that influence their post-buckling performance, and comparisons are made with results obtained using the J2FT.

Starting with uniform compression, buckling estimates compare well with available experimental data and analytical solutions. They are juxtaposed with the high load and, more markedly, large deformation estimates obtained from the J2FT and the low estimates obtained from the pseudo-corner model by Simo (1987). The analyses go beyond buckling, investigating the post-buckling response of compressed cylinders. The growth of wrinkles, the localization of deformation and structural failure are addressed, accounting for the influence of geometric imperfection. In spite of the trivial pre-buckling

equilibrium path under uniform compression, significant non-proportional loading is shown to follow tube-wall wrinkling, and the influence of non-associative modelling is clarified. Finite element modelling allows for accurately tracing the structural response of compressed thick-walled cylinders well into the post-buckling regime.

The problem of pure bending is addressed next, characterized by a non-trivial pre-buckling path, involving biaxial, non-proportional loading, which occurs prior to bifurcation. Numerical analyses successfully estimate inelastic instability and trace the structural behaviour of cylinders, their ovalization, wrinkling and post-wrinkling. Cylinders with various D/t values are considered, examining the influence of constitutive modelling and imperfection. The structural behaviours obtained with this model are in good agreement with experimental data for a range of thick-walled tubulars, showing their deformation capacity and ability to sustain load beyond yielding and bifurcation instability, depending on their D/t value.

Followingly, bending under uniform pressure conditions is considered as a problem with inherently non-proportional loading, where the two loads are applied in sequence (first pressure, then bending). Low values of internal pressure have a stiffening effect, reducing ovalization and delaying ultimate load formation in cylinders. For increasing values of pressure, wrinkling is found to grow stably for an increased range of deformation and the imperfection amplitude has greater influence in the ultimate load capacity of the section. Localization of deformation instigates the collapse of the cylinders and, depending on the pressure level, it can alter the failure mode of the section compared to pure bending. Simulations of experimental data show the capability of the developed numerical tools to describe accurately the structural behaviour, instability and post-buckling response of pressurized cylinders subjected to bending.

In the final part of this thesis, a simplified method is considered for estimating buckling of thick-walled cylindrical shells under various loading conditions. It is used primarily to predict the buckling load and deformation of cylinders, and it explains the increase in wrinkling wavelength of inelastic cylinders, when they are subjected to bending in the presence of internal pressure. This is the opposite to the effect of internal pressure in elastic tubes, an issue pinpointed in experimental observations.

Overall, the results in the present research work demonstrate that the developed numerical approach can be used as an effective tool for performing calculations in shell instability problems. It can accurately reproduce the structural behaviour of inelastic shells under

compressive loads, predicting structural instabilities and tracing the post-buckling response. The model can be employed towards the assessment of the structural behaviour of tubular members and may be integrated as a tool in pipeline engineering design and in analysis of shell structures.

Novelty

A key contribution of the present research is the development of a constitutive law that can be efficiently incorporated into finite element tools, allowing for reliably simulating the structural behaviour and instabilities of shells subjected to compressive loads into the inelastic range. Numerical tools are developed and successfully tested on cylinders under various loading conditions, proving the capability for both (a) accurately predicting bifurcation and (b) consistently tracing the post-buckling equilibrium path of shells, using a single constitutive law, when traditional approaches employ a distinct material model for each function.

Analyses show the applicability of the developed model in big-scale finite element simulations of thick-walled cylinders subjected to a range of compressive loads, not limited to problems with trivial prebuckling paths and simple loading histories, e.g. uniform compression. Simulations provide reliable buckling estimates for cylinders under bending and pressure, which are characterized by non-trivial equilibrium paths and non-proportional loading prior to bifurcation.

Comparisons with available experimental data and analytic predictions demonstrate the effectiveness of the present approach, allowing for monitoring the structural performance of thick-walled cylinders, predicting their ultimate load and deformation capacity. Numerical investigations offer insight in the evolution of local buckling and verify the ability of thick-walled members to sustain loading into the inelastic range before structural failure, in analyses considering ‘vertex-type’ effects. They indicate that accounting for the development of small yield surface corners (i.e. $\theta_c = 2^o$) in metal materials suffices to describe the structural behaviour of metal shells and alleviates the sensitivity to geometric imperfection that standard plasticity exhibits.

Recommendations for future research

An important extension for this work could include experimental studies on the behaviour of structural metals, subjected to non-proportional strain paths, to examine the material stiffness. These can provide useful insight towards the calibration of the constitutive

model, offer the means to refine the definitions of the material hardening $\bar{h}$ and to directly determine parameter θ_c, which is expected to take small values, as the present work indicates.

Several fundamental problems of tube buckling have been addressed in the context of the present research. Further investigations can be undertaken for tubulars subjected to compressive and pressure loads, particularly for high-strength steel members, whose design under present guidelines may be quite conservative. To address problems of instability under reverse or cyclic plastic loading, the model can be extended to adopt kinematic hardening, along with the non-associative flow rule. In pipeline engineering, the reeling installation method offers a classical example, where tubes are bent and straightened before deployment in the seawater and must be designed against local buckling. The introduction of Hill's yield criterion would further allow for the consideration of yield anisotropy, and its influence in the structural performance of tubes.

Besides tubulars, problems in buckling of spherical shells and plates could be addressed, starting with the classical problem of torsional buckling of cruciform columns, which still attracts research attention. The applicability of the developed approach in metal forming simulation could be considered, as in the relevant literature interest has been directed in accounting for non-associative material effects, with positive indications.

9 References

Ades, C. S. (1957). Bending strength of tubing in the inelastic range. Journal of Aeronautical Sciences, 2, 605–610.

Axelrad, E. L. (1965). Refinement of buckling-load analysis for tube flexure by way of considering precritical deformation. Izvestiya Akademii Nauk SSSR, Otdelenie Tekhnicheskikh Nauk, Mekhanika i Mashinostroenie, 4, 133–139.

Bardi, F. C. (2006). Plastic Buckling and Collapse of Circular Cylinders Under Axial Compression (The University of Texas at Austin). Retrieved from http://legacy.lib.utexas.edu/etd/d/2006/bardif49583/bardif49583.pdf

Bardi, F. C., & Kyriakides, S. (2006). Plastic buckling of circular tubes under axial compression-part I: Experiments. International Journal of Mechanical Sciences, 48(8), 830–841. https://doi.org/10.1016/j.ijmecsci.2006.03.005

Bardi, F. C., Kyriakides, S., & Yun, H. D. (2006). Plastic buckling of circular tubes under axial compression-part II: Analysis. International Journal of Mechanical Sciences, 48(8), 842–854. https://doi.org/10.1016/j.ijmecsci.2006.03.002

Batdorf S. B.; Budiansky, B. (1949). A mathematical theory of plasticity based on the concept of slip. Retrieved from https://ntrs.nasa.gov/archive/nasa/casi.ntrs.nasa.gov/19930082547.pdf

Batdorf, S. B. (1949). Theories of Plastic Buckling. Journal of the Aeronautical Sciences, 16(7), 405–408. https://doi.org/10.2514/8.11821

Batterman, S. C. (1965). Plastic buckling of axially compressed circular cylindrical shells. AIAA Journal, 3(2), 316–325. https://doi.org/10.2514/3.2848

Blachut, J., Galletly, G. D., & James, S. (1996). On the Plastic Buckling Paradox for Cylindrical Shells. Proceedings of the Institution of Mechanical Engineers, Part C: Journal of Mechanical Engineering Science, 210(5), 477–488. https://doi.org/10.1243/PIME_PROC_1996_210_221_02

Brazier, L. G. (1927). On the Flexure of Thin Cylindrical Shells and Other “Thin” Sections. Proceedings of the Royal Society A: Mathematical, Physical and Engineering Sciences, 116(773), 104–114. https://doi.org/10.1098/rspa.1927.0125

Brush, D., & Almroth, B. (1975). Buckling of Bars, Plates, and Shells. New York: McGraw-Hill.

Budiansky, B. (1959). A reassessment of deformation theories for plasticity. Journal of Applied Mechanics, 26, 259–264.

Bushnell, D. (1974). Bifurcation buckling of shells of revolution including large deflections, plasticity and creep. International Journal of Solids and Structures, 10(11), 1287–1305. https://doi.org/10.1016/0020-7683(74)90073-0

Bushnell, D. (1982). Plastic Buckling. In S. Y. Zamrik & D. Dietrich (Eds.), Pressure Vessels and Piping: Design Technology - 1982 A decade of Progress (pp. 47–117). American Society of Mechanical Engineers.

Chakrabarty, J. (2006). Theory of Plasticity (3rd ed.). https://doi.org/10.1016/C2009-0-05774-2

Christoffersen, J., & Hutchinson, J. W. (1979). A class of phenomenological corner theories of plasticity. Journal of the Mechanics and Physics of Solids, 27(5–6), 465–487. https://doi.org/10.1016/0022-5096(79)90026-7

Corona, E., & Kyriakides, S. (1987). An Unusual Mode of Collapse of Tubes Under Combined Bending and Pressure. Journal of Pressure Vessel Technology, 109(3), 302. https://doi.org/10.1115/1.3264868

Corona, E., Lee, L. H., & Kyriakides, S. (2006). Yield anisotropy effects on buckling of circular tubes under bending. International Journal of Solids and Structures, 43(22–23), 7099–7118. https://doi.org/10.1016/j.ijsolstr.2006.03.005

de Souza Neto, E. A., Peri, D., & Owen, D. R. J. (2008). Computational Methods for Plasticity: Theory and Applications. John Wiley & Sons. https://doi.org/10.1002/9780470694626

Elchalakani, M., Zhao, X. L., & Grzebieta, R. (2002). Bending tests to determine slenderness limits for cold-formed circular hollow sections. Journal of Constructional Steel Research, 58(11), 1407–1430. https://doi.org/10.1016/S0143-974X(01)00106-7

Fabian, O. (1977). Collapse of cylindrical, elastic tubes under combined bending, pressure and axial loads. International Journal of Solids and Structures, 13(12), 1257–1270. https://doi.org/10.1016/0020-7683(77)90099-3

Fabian, O. (1981). Elastic-plastic collapse of long tubes under combined bending and pressure load. Ocean Engineering, 8(3), 295–330. https://doi.org/10.1016/0029-8018(81)90027-5

Fatemi, A., & Kenny, S. (2017). Parameters affecting the local buckling response of high strength linepipe. Journal of Offshore Mechanics and Arctic Engineering, 139(3), 1–15. https://doi.org/10.1115/1.4035995

Gellin, S. (1979). Effect of an axisymmetric imperfection on the plastic buckling of an axially compressed cylindrical shell. Journal of Applied Mechanics, Transactions ASME, 46(1), 125–131. https://doi.org/10.1115/1.3424483

Gellin, S. (1980). The plastic buckling of long cylindrical shells under pure bending. International Journal of Solids and Structures, 16, 397–407. https://doi.org/10.1016/0020-7683(80)90038-4

Gerard, G., & Becker, H. (1957). Handbook of Structural Stability – Part III – Buckling of Curved Plates and Shells. National advisory committee for aeronautics.

Giezen, J. J. (1988). Plastic buckling of cylinders under biaxial loading. California Institute of Technology.

Gotoh, M. (1985). A Simple Plastic Constitutive Equation with Vertex Effect. Engineering Fracture Mechanics, 21(4), 673–684. https://doi.org/0013-7644/85

Goya, M., & Ito, K. (1991). An expression of elastic-plastic constitutive law incorporating vertex formation and kinematic hardening. Trans. ASME: J. Appl. Mech., 58(September 1991), 617–622. https://doi.org/10.1115/1.2897240

Guarracino, F., & Simonelli, M. G. (2018). Numerical Evaluation of Plastic Buckling of Short Cylinders under Combined Loading. International Journal of Structural Stability and Dynamics, 18(6), 1–21. https://doi.org/10.1142/S0219455418500815

Hecker, S. S. (1972). Experimental investigation of corners in the yield surface. Acta Mechanica, 13(1–2), 69–86. https://doi.org/10.1007/BF01179659

Hencky, H. (1924). Zur Theorie plastischer Deformationen und der hierdurch im Material hervorgerufenen Nachspannungen. Journal of Applied Mathematics and Mechanics, 4, 323–334. https://doi.org/10.1002/zamm.19240040405

Houliara, S., & Karamanos, S. A. (2006). Buckling and post-buckling of long pressurized elastic thin-walled tubes under in-plane bending. International Journal of Non-Linear Mechanics, 41(4), 491–511. https://doi.org/10.1016/j.ijnonlinmec.2005.11.002

Houliara, S. (2008). Computational techniques in structural stability o of thin-walled cylindrical shells. University of Thessaly.

Hughes, T. J. R., & Shakib, F. (1986). Pseudo-corner theory: A simple enhancement of J_2 flow theory for applications involving non-proportional loading. Engineering Computations, 3(2), 116–120. https://doi.org/https://doi.org/10.1108/eb023649 Permanent

Hutchinson, J. W. (1974). Plastic Buckling. Advances in Applied Mechanics, Vol. 14, pp. 67–144. https://doi.org/10.1016/S0065-2156(08)70031-0

Hutchinson, J. W., & Budiansky, B. (1976). Analytical and Numerical Study of the Effects of Initial Imperfections on the Inelastic Buckling of a Cruciform Column. In B. Budiansky (Ed.), Buckling of Structures (pp. 98–105). Berlin, Heidelberg: Springer Berlin Heidelberg.

Ju, G. T., & Kyriakides, S. (1991). Bifurcation Buckling Versus Limit Load Instabilities of Elastic-Plastic Tubes Under Bending and External Pressure. Journal of Offshore Mechanics and Arctic Engineering, 113(1), 43. https://doi.org/10.1115/1.2919895

Ju, G. T., & Kyriakides, S. (1992a). Bifurcation and localization instabilities in cylindrical shells under bending—II. Predictions. International Journal of Solids and Structures, 29(9), 1143–1171. https://doi.org/10.1016/0020-7683(92)90140-O

Karamanos, S. A. (2002). Bending instabilities of elastic tubes. International Journal of Solids and Structures, 39(8), 2059–2085. https://doi.org/10.1016/S0020-7683(02)00085-9

Karamanos, S. A., & Tassoulas, J. L. (1991). Stability of inelastic tubes under external pressure and bending. Journal of Engineering Mechanics, 117(12), 2845–2861. https://doi.org/10.1061/(ASCE)0733-9399(1991)117:12(2845)

Karamanos, S. A., & Tassoulas, J. L. (1996). Tubular members. II: Local buckling and experimental verification. Journal of Engineering Mechanics, 122(1), 72–78.

Kaya, E. S., Uckan, E., O'Rourke, M. J., Karamanos, S. A., Akbas, B., Cakir, F., & Cheng, Y. (2017). Failure analysis of a welded steel pipe at Kullar fault crossing. Engineering Failure Analysis, 71, 43–62. https://doi.org/10.1016/j.engfailanal.2016.10.004

Koiter, W. T. (1963) Effect of Axisymmetric Imperfections on the Buckling of Cylindrical Shells Under Axial Compression, Proceedings, Kan. Ned. Ak. Wet., Vol. 66, Series B, pp. 265-279.

Kuroda, M. (2004). A phenomenological plasticity model accounting for hydrostatic stress-sensitivity and vertex-type of effect. Mechanics of Materials, 36(3), 285–297. https://doi.org/10.1016/S0167-6636(03)00023-1

Kuroda, M. (2015). A higher-order strain gradient plasticity theory with a corner-like effect. International Journal of Solids and Structures, 58, 62–72. https://doi.org/10.1016/j.ijsolstr.2014.12.019

Kuroda, M., & Tvergaard, V. (1999). Use of abrupt strain path change for determining subsequent yield surface: illustrations of basic idea. Acta Materialia, 47(14), 3879–3890. https://doi.org/10.1016/S1359-6454(99)00213-X

Kuroda, M., & Tvergaard, V. (2001a). A phenomenological plasticity model with non-normality effects representing observations in crystal plasticity. Journal of the Mechanics and Physics of Solids, 49(6), 1239–1263. https://doi.org/10.1016/S0022-5096(00)00080-6

Kuroda, M., & Tvergaard, V. (2001b). Shear band development predicted by a non-normality theory of plasticity and comparison to crystal plasticity predictions. International Journal of Solids and Structures, 38(50–51), 8945–8960. https://doi.org/10.1016/S0020-7683(01)00166-4

Kuwabara, T. (2007). Advances in experiments on metal sheets and tubes in support of constitutive modeling and forming simulations. International Journal of Plasticity, 23(3), 385–419. https://doi.org/10.1016/j.ijplas.2006.06.003

Kuwabara, T., Kuroda, M., Tvergaard, V., & Nomura, K. (2000). Use of abrupt strain path change for determining subsequent yield surface: experimental study with metal sheets. Acta Materialia, 48, 2071–2079. https://doi.org/10.1016/S1359-6454(00)00048-3

Kyriakides, S., & Corona, E. (2007). Mechanics of Offshore Pipelines: Volume 1 Buckling and Collapse (1st ed., p. 448). 1st ed., p. 448. https://doi.org/10.1128/JCM.03067-14

Kyriakides, S., & Ju, G. T. (1992). Bifurcation and localization instabilities in cylindrical shells under bending—I. Experiments. International Journal of Solids and Structures, 29(9), 1117–1142. https://doi.org/10.1016/0020-7683(92)90139-K

Kyriakides, S., & Shaw, P. K. (1982). Response and stability of elastoplastic circular pipes under combined bending and external pressure. International Journal of Solids and Structures, 18(11), 957–973. https://doi.org/10.1016/0020-7683(82)90086-5

Kyriakides, S., Bardi, F. C., & Paquette, J. A. (2005). Wrinkling of circular tubes under axial compression: Effect of anisotropy. Journal of Applied Mechanics, Transactions ASME, 72(2), 301–305. https://doi.org/10.1115/1.1839590

Lee, L. H. N. (1962). Inelastic Buckling of Initially Imperfect Cylindrical Shells Subject to Axial Compression. Journal of the Aerospace Sciences, 29(1), 87–95. https://doi.org/10.2514/8.9306

Limam, A., Lee, L. H., Corona, E., & Kyriakides, S. (2010). Inelastic wrinkling and collapse of tubes under combined bending and internal pressure. International Journal of Mechanical Sciences, 52(5), 637–647. https://doi.org/10.1016/j.ijmecsci.2009.06.008

Meng, X., Gardner, L., Sadowski, A. J., & Rotter, J. M. (2020). Elasto-plastic behaviour and design of semi-compact circular hollow sections. Thin-Walled Structures, 148(October 2019), 106486. https://doi.org/10.1016/j.tws.2019.106486

Needleman, A., & Tvergaard, V. (1982). Aspects of Plastic Postbuckling Behavior. In Mechanics of Solids (pp. 453–498). https://doi.org/10.1016/B978-0-08-025443-

2.50020-3

Ore, E., & Durban, D. (1992). Elastoplastic buckling of axially compressed circular cylindrical shells. International Journal of Mechanical Sciences, 34(9), 727–742. https://doi.org/10.1016/0020-7403(92)90005-2

Pappa, P., & Karamanos, S. A. (2016). Non-associative J_2 plasticity model for finite element buckling analysis of shells in the inelastic range. Computer Methods in Applied Mechanics and Engineering, 300, 689–715. https://doi.org/10.1016/j.cma.2015.11.031

Paquette, J. A., & Kyriakides, S. (2006). Plastic buckling of tubes under axial compression and internal pressure. International Journal of Mechanical Sciences, 48(8), 855–867. https://doi.org/10.1016/j.ijmecsci.2006.03.003

Peek, R. (2000). An incrementally continuous deformation theory of plasticity with unloading. International Journal of Solids and Structures, 37(36), 5009–5032. https://doi.org/10.1016/S0020-7683(99)00294-2

Peek, R., & Hilberink, A. (2013). Axisymmetric wrinkling of snug-fit lined pipe. International Journal of Solids and Structures, 50(7–8), 1067–1077. https://doi.org/10.1016/j.ijsolstr.2012.11.023

Reddy, B. D. (1979). An experimental study of the plastic buckling of circular cylinders in pure bending. International Journal of Solids and Structures, 15(9), 669–683. https://doi.org/10.1016/0020-7683(79)90066-0

Reissner, E. (1959). On Finite Bending of Pressurized Tubes. Trans. ASME J. Appf. Mech. 81, 386-392

Rønning, L., Hopperstad, O. S., & Larsen, P. K. (2010). Numerical study of the effects of constitutive models on plastic buckling of plate elements. European Journal of Mechanics - A/Solids, 29(4), 508–522. https://doi.org/10.1016/j.euromechsol.2010.02.001

Sadowski, A. J., & Rotter, J. M. (2013). Solid or shell finite elements to model thick cylindrical tubes and shells under global bending. International Journal of Mechanical Sciences, 74, 143–153. https://doi.org/10.1016/j.ijmecsci.2013.05.008

Sanders, J. L. (1954). Plastic stress-strain relations based on linear loading functions. 2nd U.S. National Congress of Applied Mechanics, 455–460.

Schurig, M. (2006). The Vertex Effect in Polycrystalline Materials, PhD Thesis (Otto-von-Guericke-Universität Magdeburg). Retrieved from http://diglib.uni-magdeburg.de/Dissertationen/2006/micschurig.htm

Seide, P., & Weingarten, V. I. (1961). On the buckling of circular cylindrical shells under pure bending. ASME Journal of Applied Mechanics, 28(1), 112–116.

Shamass, R., Alfano, G., & Guarracino, F. (2014). A numerical investigation into the plastic buckling paradox for circular cylindrical shells under axial compression. Engineering Structures, 75, 429–447. https://doi.org/10.1016/j.engstruct.2014.05.050

Shaw, P. K., & Kyriakides, S. (1985). Inelastic analysis of thin-walled under cyclic bending tubes. International Journal of Solids and Structures, 21(11), 1073–1100.

Simo, J. C. (1987). A J_2-flow theory exhibiting a corner-like effect and suitable for large-scale computation. Computer Methods in Applied Mechanics and Engineering, 62(2), 169–194. https://doi.org/10.1016/0045-7825(87)90022-3

Simo, J. C., & Taylor, R. L. (1985). Consistent tangent operators for rate-independent elastoplasticity. Computer Methods in Applied Mechanics and Engineering, 48(1), 101–118. https://doi.org/10.1016/0045-7825(85)90070-2

Simo, J. C., & Taylor, R. L. (1986). A Return Mapping Algorithm For Plane Stress Elastoplasticity. International Journal for Numerical Methods in Engineering, 22(July 1985), 649–670. https://doi.org/10.1002/nme.1620220310

Sobel, L. H., & Newman, S. Z. (1979). Plastic Buckling of Cylindrical Shells Under Axial Compression. American Society of Mechanical Engineers (Paper), 102(79-PVP-99), 40–44.

Stephens, W. B., Starnes, J. H., Almroth, B. O., Polo, L., & Alto, P. (1975). Collapse of Long Cylindrical Shells under Combined Bending and Pressure Loads. AIAA Journal, 13(1), 20–25. https://doi.org/10.2514/3.49624

Tabeshpour, M. R., Erfani, M. H., & Sayyaadi, H. (2019). Challenges in calculation of critical buckling load of tubular members of jacket platforms in finite element modeling. Journal of Marine Science and Technology (Japan), (0123456789). https://doi.org/10.1007/s00773-019-00686-5

Takla, M. (2018). Bifurcation of elastic–plastic thick-walled cylindrical structures. International Journal of Mechanical Sciences, 141(March), 303–315.

https://doi.org/10.1016/j.ijmecsci.2018.04.001

Tuğcu, P. (1991). Plate buckling in the plastic range. International Journal of Mechanical Sciences, 33(1), 1–11. https://doi.org/10.1016/0020-7403(91)90023-V

Tvergaard, V. (1983a). On the transition from a diamond mode to an axisymmetric mode of collapse in cylindrical shells. International Journal of Solids and Structures, 19(10), 845–856. https://doi.org/10.1016/0020-7683(83)90041-0

Tvergaard, V. (1983b). Plastic buckling of axially compressed circular cylindrical shells. Thin-Walled Structures, 1(2), 139–163. https://doi.org/10.1016/0263-8231(83)90018-6

Tvergaard, V., & Needleman, A. (1980). On the localization of buckling patterns. Journal of Applied Mechanics, Transactions ASME, 47(3), 613–619. https://doi.org/10.1115/1.3153742

Tvergaard, V., & Needleman, A. (2000). Buckling localization in a cylindrical panel under axial compression. International Journal of Solids and Structures, 37(46), 6825–6842. https://doi.org/10.1016/S0020-7683(99)00316-9

Vasilikis, D. (2012). Structural behavior and stability of cylindrical steel shells with lateral confinement. University of Thessaly.

Wang, C. M., Xiang, Y., & Chakrabarty, J. (2001). Elastic / plastic buckling of thick plates. International Journal of Solids and Structures, 38, 8617–8640. https://doi.org/10.1016/S0020-7683(01)00144-5

Wang, J., Sadowski, A. J., & Rotter, J. M. (2018). Influence of ovalisation on the plastic collapse of thick cylindrical tubes under uniform bending. International Journal of Pressure Vessels and Piping, 168(February), 94–99. https://doi.org/10.1016/j.ijpvp.2018.05.004

Yoshida, K. (2017). A plastic flow rule representing corner effects predicted by rate-independent crystal plasticity. International Journal of Solids and Structures, 120(May 2017), 1339–1351. https://doi.org/10.1016/j.ijsolstr.2017.05.004

Yoshida, K., & Tsuchimoto, T. (2018). Plastic flow of thin-walled tubes under nonlinear tension-torsion loading paths and an improved pseudo-corner model. International Journal of Plasticity, 104(January), 214–229. https://doi.org/10.1016/j.ijplas.2018.02.013

10 APPENDICES

APPENDIX 1: DETAILS FOR THE NUMERICAL IMPLEMENTATION OF J2NA

According to eq.(3.35), the deviatoric stress tensor at the converged state is expressed as:

$$\begin{aligned}\mathbf{s}_{n+1}\left(\Delta\varepsilon_q,\zeta^*,\Delta\mathbf{e}\right) &= \sqrt{2/3}\,k_{n+1}\,\mathbf{n}_{n+1}\\ &= \sqrt{2/3}\,k_{n+1}\,[\cos(\zeta^e-\zeta^*)\,\mathbf{n}_n+\sin(\zeta^e-\zeta^*)\,\mathbf{m}_n]\\ &= \sqrt{2/3}\,k_{n+1}\left(\Delta\varepsilon_q\right)\cdot\\ &\quad[\cos(\zeta^e(\Delta\mathbf{e})-\zeta^*)\,\mathbf{n}_n+\sin(\zeta^e(\Delta\mathbf{e})-\zeta^*)\,\mathbf{m}_n(\Delta\mathbf{e})]\end{aligned} \tag{10.1}$$

From equation (10.1), the following derivatives are obtained, which are used in the calculation of linearized moduli:

$$\mathbf{s}_{n+1,\Delta\varepsilon_q} = \sqrt{2/3}\,H_{n+1}\mathbf{n}_{n+1} \tag{10.2}$$

$$\mathbf{s}_{n+1,\zeta^*} = -\sqrt{2/3}\,k_{n+1}\mathbf{m}_{n+1} \tag{10.3}$$

$$\mathbf{s}_{n+1,\Delta\mathbf{e}} = \sqrt{2/3}\,k_{n+1}\left[\mathbf{m}_{n+1}\otimes\frac{\partial\zeta^e}{\partial\Delta\mathbf{e}}+\sin(\zeta^e-\zeta^*)\frac{\partial\mathbf{m}_n}{\partial\Delta\mathbf{e}}\right] \tag{10.4}$$

where

$$\zeta^e_{,\Delta\mathbf{e}} = \frac{2G}{\|\mathbf{s}^e\|}[-\sin\zeta^e\,\mathbf{n}_n+\cos\zeta^e\,\mathbf{m}_n] \tag{10.5}$$

$$\frac{\partial\mathbf{m}_n}{\partial\Delta\mathbf{e}} = \frac{1}{\|\Delta\mathbf{e}\|\sin\theta_n}[\mathbf{I}^{dev}-\mathbf{n}_n\otimes\mathbf{n}_n-\mathbf{m}_n\otimes\mathbf{m}_n] \tag{10.6}$$

Equations (10.5) and (10.6) are obtained by differentiating the definitions in equations (3.18) and (3.12) respectively. The ratio $\sin\zeta/\sin\theta_n$ which appears in (10.4), may demand care under proportional loading as both angles approach zero. In such cases the ratio may be substituted by the value $\left(2G\sqrt{3/2}\,\|\Delta\mathbf{e}\|-3G\Delta\varepsilon_q\right)/k_{n+1}$, obtained at the limit $\theta_n\to 0$. Additionally, since $\theta^e = \theta_n-\zeta^e$, the following expressions can be derived:

$$\begin{aligned}\theta^e_{,\Delta\mathbf{e}} = \frac{1}{\|\Delta\mathbf{e}\|}&[-\sin\theta_n\,\mathbf{n}_n+\cos\theta_n\,\mathbf{m}_n]\\ &-\frac{2G}{\|\mathbf{s}^e\|}[-\sin\zeta^e\,\mathbf{n}_n+\cos\zeta^e\,\mathbf{m}_n]\end{aligned} \tag{10.7}$$

Expressions (10.1)-(10.7) are applicable for the integration algorithm and its linearization, irrespective of the definition of $\bar{h}$, and refer to both three-dimensional and shell elements.

First branch of the model ($\theta^p \leq \theta_c$)

For the first branch of the model, the algorithm reduces to the system of equations (10.8) and (10.9), which is solved numerically, employing a local Newton scheme.

$$F_1(\Delta\varepsilon_q, \zeta^*, \Delta\mathbf{e}) = F_{p1} = 1 + \tan^2\zeta^* - \left[\frac{q^e}{k_{n+1} + 3G\Delta\varepsilon_q}\right]^2 = 0 \tag{10.8}$$

$$F_2(\Delta\varepsilon_q, \zeta^*, \Delta\mathbf{e}) = \tan\zeta^* - \frac{\tan\theta^e}{c-1} = 0 \tag{10.9}$$

where

$$c = \frac{\|\mathbf{s}^e\|}{2G\|\Delta\mathbf{e}\|\cos\theta^e}\left[1 + \frac{h_{n+1}}{3G}\right] = \frac{\mathbf{s}^e \cdot \mathbf{s}^e}{2G\Delta\mathbf{e}\cdot\mathbf{s}^e}\left[1 + \frac{h_{n+1}}{3G}\right] \tag{10.10}$$

The derivatives, used in the Newton scheme are:

$$F_{p1,\Delta\varepsilon_q} = 2\left[\frac{q^e}{k_{n+1} + 3G\Delta\varepsilon_q}\right]^2 \frac{H_{n+1} + 3G}{k_{n+1} + 3G\Delta\varepsilon_q} \tag{10.11}$$

$$F_{p1,\zeta^*} = 2\tan\zeta^*\left(1 + \tan^2\zeta^*\right) \tag{10.12}$$

$$F_{p1,\Delta\mathbf{e}} = -2\frac{3G\,\mathbf{s}^e}{\left[k_{n+1} + 3G\Delta\varepsilon_q\right]^2} \tag{10.13}$$

$$F_{2,\Delta\varepsilon_q} = \frac{\tan\theta^e}{(c-1)^2}\,\frac{\|\mathbf{s}^e\|}{2G\|\Delta\mathbf{e}\|\cos\theta^e}\,\frac{\partial h_{n+1}/\partial\Delta\varepsilon_q}{3G} \tag{10.14}$$

$$F_{2,\zeta^*} = 1 + \tan^2\zeta^* \tag{10.15}$$

$$F_{2,\Delta\mathbf{e}} = -\frac{1 + \tan^2\theta^e}{c-1}\theta^e_{,\Delta\mathbf{e}} + \frac{\tan\theta^e}{(c-1)^2}\,\frac{1}{\|\Delta\mathbf{e}\|\cos\theta^e}\left[2\frac{\mathbf{s}^e}{\|\mathbf{s}^e\|} - \frac{\|\mathbf{s}^e\|}{\|\Delta\mathbf{e}\|\cos\theta^e}\left[\frac{\mathbf{s}^e}{2G} + \Delta\mathbf{e}\right]\right]\left[1 + \frac{h_{n+1}}{3G}\right] \tag{10.16}$$

Those derivatives are also employed in the linearization of the model.

Remark: Following a relevant discussion in paragraph 3.3, equation (10.9) offers an explicit expression for ζ^*, which can be used to eliminate ζ^* from (10.8), leading to:

$$\bar{F}_{p1}\left(\Delta\varepsilon_q, \Delta\mathbf{e}\right) = F_{p1}\left(\Delta\varepsilon_q, \zeta^*\left(\Delta\varepsilon_q, \Delta\mathbf{e}\right), \Delta\mathbf{e}\right) = 1 + \left[\frac{\sin\theta^e}{\frac{\|\mathbf{s}^e\|}{2G\|\Delta\mathbf{e}\|}\left[1 + \frac{h_{n+1}}{3G}\right] - \cos\theta^e}\right]^2 - \left[\frac{q^e}{k_{n+1} + 3G\Delta\varepsilon_q}\right]^2 \tag{10.17}$$

For the three-dimensional formulation, equation (10.17) can be solved for $\Delta\varepsilon_q$ which is next substituted into (10.9) to provide ζ^*. Therefore, single variable equations need to be solved to define each of the unknowns. The derivatives used in this alternative expression of the problem and the subsequent linearization are:

$$\bar{F}_{p1,\Delta\varepsilon_q} = F_{p1,\Delta\varepsilon_q} + F_{p1,\zeta^*}\zeta^*_{,\Delta\varepsilon_q} = F_{p1,\Delta\varepsilon_q} + F_{p1,\zeta^*}\left(-\frac{F_{p2,\Delta\varepsilon_q}}{F_{p2,\zeta^*}}\right) \tag{10.18}$$

$$\bar{F}_{p1,\zeta^*} = 0 \tag{10.19}$$

$$\bar{F}_{p1,\Delta\mathbf{e}} = F_{p1,\Delta\mathbf{e}} + F_{p1,\zeta^*}\zeta^*_{,\Delta\mathbf{e}} = F_{p1,\Delta\mathbf{e}} + F_{p1,\zeta^*}\left(-\frac{F_{p2,\Delta\mathbf{e}}}{F_{p2,\zeta^*}}\right) \tag{10.20}$$

Remark: Either version: $F_1 = F_{p1}$ or $F_1 = \bar{F}_{p1}$ can be used in solving for $\Delta\varepsilon_q$, ζ^* and either may be used in the subsequent linearization of the model, leading to identical results.

Second branch of the model ($\theta^p = \theta_c$)

For the second branch of the present model, equations (10.21) and (10.22) are solved numerically.

$$F_1 = F_{p2}(\Delta\varepsilon_q, \Delta\mathbf{e}) = \left[\Delta\varepsilon_q + \frac{k_{n+1}}{3G}\right]^2 + \left[\Delta\varepsilon_q \tan\theta_c\right]^2 - \left(\frac{q^e}{3G}\right)^2 = 0 \tag{10.21}$$

$$F_2 = \sin\zeta^* - \frac{3G\Delta\varepsilon_q \tan\theta_c}{q^e} = 0 \tag{10.22}$$

Using only (10.21), the equivalent plastic strain increment $\Delta\varepsilon_q$ can be obtained directly. Subsequently, (10.22) may then be solved to find ζ^*. The derivatives necessary for the solution of the two equations, also used in the consistent linearization, are:

$$F_{p2,\Delta\varepsilon_q} = 2\left[\Delta\varepsilon_q + \frac{k_{n+1}}{3G}\right]\left[1 + \frac{H_{n+1}}{3G}\right] + 2\Delta\varepsilon_q \tan^2\theta_c \tag{10.23}$$

$$F_{p2,\zeta^*} = 0 \tag{10.24}$$

$$F_{p2,\Delta\mathbf{e}} = -6G\,\mathbf{s}^e/(3G)^2 \tag{10.25}$$

and

$$F_{2,\Delta\varepsilon_q} = -\frac{3G\tan\theta_c}{q^e} \tag{10.26}$$

$$F_{2,\zeta^*} = \cos\zeta^* \tag{10.27}$$

$$F_{2,\Delta\mathbf{e}} = -\frac{3G\Delta\varepsilon_q \tan\theta_c}{q^e}\frac{3G\boldsymbol{s}^e}{(q^e)^2} \tag{10.28}$$

Explicit definition of $\bar{h}(\Delta\varepsilon_q, \theta)$

A similar methodology can be applied in the case where a function $\bar{h}(\Delta\varepsilon_q, \theta)$ is defined explicitly. Adopting such an approach, the model by Pappa & Karamanos (2016) could be integrated and linearized, with $\bar{h}$ defined as reported Table 2.2. The system of equations (3.31) and (3.32) can be solved in terms of $\left(\Delta\varepsilon_q, \zeta^*\right)$ with $\theta = \theta^e + \zeta^*$, and it can be written as follows:

$$F_{p\bar{h}}\left(\Delta\varepsilon_q, \zeta^*, \Delta\mathbf{e}\right) = q^e\cos\zeta^* - \left[k_{n+1} + 3G\Delta\varepsilon_q\right] = 0 \tag{10.29}$$

$$L_{p\bar{h}}\left(\Delta\varepsilon_q, \zeta^*, \Delta\mathbf{e}\right) = q^e\sin\zeta^* - \sqrt{2/3}\frac{3G\|\Delta\mathbf{e}\|\sin(\theta^e+\zeta^*)}{1+\bar{h}_{n+1}/3G} = 0 \tag{10.30}$$

with

$$\bar{h}_{n+1} = \bar{h}_{n+1}\left(\Delta\varepsilon_q, \theta = \theta^e + \zeta^*\right) \tag{10.31}$$

The derivatives used in the integration and the linearized moduli of the model are:

$$F_{p\bar{h},\Delta\varepsilon_q} = -[H_{n+1} + 3G] \tag{10.32}$$

$$F_{p\bar{h},\zeta^*} = -q^e\sin\zeta^* \tag{10.33}$$

$$F_{p\bar{h},\Delta\mathbf{e}} = \frac{3G\mathbf{s}^e}{q^e}\cos\zeta^* \tag{10.34}$$

and

$$L_{p\bar{h},\Delta\varepsilon_q} = +\sqrt{2/3}\frac{3G\|\Delta\mathbf{e}\|\sin(\theta^e+\zeta^*)}{\left[1+\bar{h}_{n+1}/3G\right]^2}\frac{\bar{h}_{n+1,\Delta\varepsilon_q}}{3G} \tag{10.35}$$

$$L_{p\bar{h},\zeta^*} = q^e\cos\zeta^* - \left[\sqrt{2/3}\frac{3G\|\Delta\mathbf{e}\|\cos(\theta^e+\zeta^*)}{1+\bar{h}_{n+1}/3G} - \sqrt{2/3}\frac{3G\|\Delta\mathbf{e}\|\sin(\theta^e+\zeta^*)}{\left[1+\bar{h}_{n+1}/3G\right]^2}\frac{\bar{h}_{n+1,\theta}}{3G}\right] \tag{10.36}$$

$$
\begin{aligned}
L_{p\bar{h},\Delta\mathbf{e}} = \frac{3G\mathbf{s}^e}{q^e}\sin\zeta^* \\
&- \left[\sqrt{2/3}\frac{3G\sin(\theta^e+\zeta^*)}{1+\bar{h}_{n+1}/3G}\right. \\
&\left. - \sqrt{2/3}\frac{3G\|\Delta\mathbf{e}\|\sin(\theta^e+\zeta^*)}{\left[1+\bar{h}_{n+1}/3G\right]^2}\frac{\bar{h}_{n+1,\|\Delta\mathbf{e}\|}}{3G}\right]\frac{\Delta\mathbf{e}}{\|\Delta\mathbf{e}\|} \\
&- \left[\sqrt{2/3}\frac{3G\|\Delta\mathbf{e}\|\cos(\theta^e+\zeta^*)}{1+\bar{h}_{n+1}/3G}\right. \\
&\left. - \sqrt{2/3}\frac{3G\|\Delta\mathbf{e}\|\sin(\theta^e+\zeta^*)}{\left[1+\bar{h}_{n+1}/3G\right]^2}\frac{\bar{h}_{n+1,\theta}}{3G}\right]\theta^e_{,\Delta\mathbf{e}}
\end{aligned}
\tag{10.37}
$$

Enhancement for shell element implementation

For shell element, the extra unknown strain increment component $\Delta\varepsilon_{33}$ needs to be calculated using the additional condition (3.52), to define the plastic corrector. The latter can be rewritten in the form of equation (10.38) below:

$$F_{shell}\big(\Delta\varepsilon_q,\zeta^*,\Delta\boldsymbol{\varepsilon}(\Delta\varepsilon_{33})\big) = \mathbf{a}\cdot\mathbf{s}_{n+1} - p_{n+1} = 0 \tag{10.38}$$

and its derivatives used to solve the 3x3 system are:

$$F_{shell,\Delta\varepsilon_q} = \mathbf{a}\cdot\mathbf{s}_{n+1,\Delta\varepsilon_q} \tag{10.39}$$

$$F_{shell,\zeta^*} = \mathbf{a}\cdot\mathbf{s}_{n+1,\zeta^*} \tag{10.40}$$

$$F_{shell,\Delta\varepsilon_{33}} = \mathbf{a}\cdot\mathbf{s}_{n+1,\Delta\mathbf{e}} - K \tag{10.41}$$

For the two branches of the J2NA model, F_2 can be easily rewritten as an explicit expression of angle $\zeta^*\big(\Delta\varepsilon_q,\Delta\mathbf{e}(\Delta\varepsilon_{33})\big)$. This allows for the system to reduce to a single equation of a scalar unknown $\Delta\varepsilon_q$, for three dimensional elements. Similarly, for shell element implementation, the explicit expression for ζ^* allows for the solution of a simpler system of two unknowns $\big(\Delta\varepsilon_q,\Delta\varepsilon_{33}\big)$, expressed as follows:

$$\hat{F}_1\big(\Delta\varepsilon_q,\Delta\varepsilon_{33}\big) = F_1\big(\Delta\varepsilon_q,\zeta^*\big(\Delta\varepsilon_q,\Delta\varepsilon_{33}\big),\Delta\varepsilon_{33}\big) = 0 \tag{10.42}$$

$$\hat{F}_{shell}\big(\Delta\varepsilon_q,\Delta\varepsilon_{33}\big) = F_{shell}\big(\Delta\varepsilon_q,\zeta^*\big(\Delta\varepsilon_q,\Delta\varepsilon_{33}\big),\Delta\varepsilon_{33}\big) = 0 \tag{10.43}$$

To solve the system of equations (10.42) and (10.43), a local Newton scheme is used; assuming from some trial values $\big(\Delta\varepsilon_q,\Delta\varepsilon_{33}\big)$, functions $\hat{F}_1$, $\hat{F}_{shell}$ and their derivatives

are calculated. A correction to these trial values $\left(\delta(\Delta\varepsilon_q), \delta(\Delta\varepsilon_{33})\right)$ is obtained as:

$$\begin{bmatrix} A_{11} & A_{12} \\ A_{21} & A_{22} \end{bmatrix} \cdot \begin{bmatrix} \delta(\Delta\varepsilon_q) \\ \delta(\Delta\varepsilon_{33}) \end{bmatrix} = \begin{bmatrix} b_1 \\ b_2 \end{bmatrix} \tag{10.44}$$

or

$$\begin{bmatrix} \delta(\Delta\varepsilon_q) \\ \delta(\Delta\varepsilon_{33}) \end{bmatrix} = \frac{1}{A_{11}A_{22} - A_{12}A_{21}} \begin{bmatrix} A_{22} & -A_{12} \\ -A_{21} & A_{11} \end{bmatrix} \cdot \begin{bmatrix} b_1 \\ b_2 \end{bmatrix} \tag{10.45}$$

In the above equations, A_{ij} and b_i are obtained by the following expressions:

$$A_{11} = \frac{\partial \hat{F}_1}{\partial \Delta\varepsilon_q} = F_{1,\Delta\varepsilon_q} + F_{1,\zeta^*}\zeta^*_{,\Delta\varepsilon_q} \tag{10.46}$$

$$A_{12} = \frac{\partial \hat{F}_1}{\partial \Delta\varepsilon_{33}} = \mathbf{a} \cdot \left[F_{1,\Delta\mathbf{e}} + F_{1,\zeta^*}\zeta^*_{,\Delta\mathbf{e}}\right] \tag{10.47}$$

‘ $$A_{21} = \frac{\partial \hat{F}_{shell}}{\partial \Delta\varepsilon_q} = \mathbf{a} \cdot \left[\mathbf{s}_{n+1,\Delta\varepsilon_q} + \mathbf{s}_{n+1,\zeta^*}\zeta^*_{,\Delta\varepsilon_q}\right] \tag{10.48}$$

$$A_{22} = \frac{\partial \hat{F}_{shell}}{\partial \Delta\varepsilon_{33}} = \mathbf{a} \cdot \left[\mathbf{a} \cdot \mathbf{s}_{n+1,\Delta\mathbf{e}} + \mathbf{a} \cdot \mathbf{s}_{n+1,\zeta^*}\zeta^*_{,\Delta\mathbf{e}}\right] - K \tag{10.49}$$

and

$$b_1 = -\hat{F}_1\left(\Delta\varepsilon_q, \Delta\varepsilon_{33}\right) = -F_1\left(\Delta\varepsilon_q, \zeta^*\left(\Delta\varepsilon_q, \Delta\varepsilon_{33}\right), \Delta\varepsilon_{33}\right) \tag{10.50}$$

$$b_2 = -\hat{F}_{shell}\left(\Delta\varepsilon_q, \Delta\varepsilon_{33}\right) = -F_{shell}\left(\Delta\varepsilon_q, \zeta^*\left(\Delta\varepsilon_q, \Delta\varepsilon_{33}\right), \Delta\varepsilon_{33}\right) \tag{10.51}$$

The derivatives $\zeta^*_{,\Delta\varepsilon_q}$, $\zeta^*_{,\Delta\mathbf{e}}$ can be calculated by differentiating $\zeta^*\left(\Delta\varepsilon_q, \Delta\mathbf{e}(\Delta\varepsilon_{33})\right)$, or equivalently, directly from F_2:

$$\zeta^*_{,\Delta\varepsilon_q} = -F_{2,\Delta\varepsilon_q}/F_{2,\zeta^*} \tag{10.52}$$

$$\zeta^*_{,\Delta\mathbf{e}} = -F_{2,\Delta\boldsymbol{e}}/F_{2,\zeta^*} \tag{10.53}$$

Derivatives $\mathbf{s}_{n+1,\Delta\varepsilon_q}, \mathbf{s}_{n+1,\zeta^*}, \mathbf{s}_{n+1,\Delta\mathbf{e}}, F_{1,\Delta\varepsilon_q}$, F_{1,ζ^*} , $F_{1,\Delta\mathbf{e}}$, F_{1,ζ^*} , $F_{2,\Delta\varepsilon_q}$, F_{2,ζ^*} , $F_{2,\Delta\boldsymbol{e}}$ have been presented earlier in this Appendix, and are summed up in Table 10.1.

The trial values of $\Delta\varepsilon_q$ and $\Delta\varepsilon_{33}$ are updated as follows

$$\begin{aligned} \Delta\varepsilon_q &\leftarrow \Delta\varepsilon_q + \delta\left(\Delta\varepsilon_q\right) \\ \Delta\varepsilon_{33} &\leftarrow \Delta\varepsilon_{33} + \delta(\Delta\varepsilon_{33}) \end{aligned} \tag{10.54}$$

and the iterative process continues until both b_1, b_2 vanish, as indicated in Table 10.1.

Table 10.1: Newton scheme for solving the system of $\hat{F}_1$ and $\hat{F}_{shell}$ for the two branches of the model for shell elements

	$\mathbf{n}_n = \mathbf{s}_n/\|\mathbf{s}_n\|, \quad k_n = k(\varepsilon_{q\|n})$	
	$\Delta\varepsilon_q = 0, \quad \delta(\Delta\varepsilon_q) = 0\,, \hat{F}_1 = \infty$	
	$\Delta\varepsilon_{33} = 0, \ \delta(\Delta\varepsilon_{33}) = 0, \hat{F}_{shell} = \infty$	
WHILE $\max\{\|\hat{F}_1\|, \|\hat{F}_{shell}\|\} > TOL$		
	$\Delta\varepsilon_q = \Delta\varepsilon_q + \delta(\Delta\varepsilon_q), \quad \Delta\varepsilon_{33} = \Delta\varepsilon_{33} + \delta(\Delta\varepsilon_{33})$	
	$\Delta\boldsymbol{\varepsilon} = \Delta\bar{\boldsymbol{\varepsilon}} + \Delta\varepsilon_{33}\mathbf{a}$	
	$\boldsymbol{\sigma}^e = \boldsymbol{\sigma}_n + \mathbf{D}\Delta\boldsymbol{\varepsilon}$, $\mathbf{s}^e = \mathbf{I}^{dev}\boldsymbol{\sigma}^e = \mathbf{s}_n + 2G\Delta\mathbf{e}$	
	$p^e = -1/3\,(\mathbf{I}\cdot\boldsymbol{\sigma}^e)\,, \quad q^e = \sqrt{3/2}\,\|\mathbf{s}^e\|$	
	$\cos\theta_n = \dfrac{\mathbf{s}_n\cdot\Delta\mathbf{e}}{\|\mathbf{s}_n\|\|\Delta\mathbf{e}\|}, \quad \mathbf{m}_n = \dfrac{[\mathbf{I}^{dev} - \mathbf{n}_n\otimes\mathbf{n}_n]\,\Delta\mathbf{e}}{\|[\mathbf{I}^{dev} - \mathbf{n}_n\otimes\mathbf{n}_n]\,\Delta\mathbf{e}\,\|}$	
	$\cos\zeta^e = \dfrac{\mathbf{s}_n\cdot\mathbf{s}^e}{\|\mathbf{s}_n\|\|\mathbf{s}^e\|}\,, \quad \cos\theta^e = \dfrac{\Delta\mathbf{e}\cdot\mathbf{s}^e}{\|\Delta\mathbf{e}\|\|\mathbf{s}^e\|}$	
	$\zeta^e_{,\Delta\mathbf{e}}$ (10.5), $\theta^e_{,\Delta\mathbf{e}}$ (10.7), $\mathbf{m}_{n,\Delta\mathbf{e}}$ (10.6)	
	1st branch	2nd branch
ζ^*	$\tan\zeta^* = \dfrac{\sin\theta^e}{\dfrac{\|\mathbf{s}^e\|}{2G\|\Delta\mathbf{e}\|}\left[1+\dfrac{h_{n+1}}{3G}\right] - \cos\theta^e}$	$\sin\zeta^* = \dfrac{3G\Delta\varepsilon_q\,\tan\theta_c}{q^e}$
	$\theta = \theta^e + \zeta^*, \zeta = \zeta^e - \zeta^*$	
	$\mathbf{n}_{n+1} = \cos\zeta\,\mathbf{n}_n + \sin\zeta\,\mathbf{m}_n$	
	$\mathbf{m}_{n+1} = -\sin\zeta\,\mathbf{n}_n + \cos\zeta\,\mathbf{m}_n$	
	$\mathbf{s}_{n+1} = \sqrt{2/3}\,k_{n+1}\,\mathbf{n}_{n+1}$(10.1)	
	$\mathbf{s}_{n+1,\Delta\varepsilon_q}$(10.2), $\mathbf{s}_{n+1,\zeta^*}$ (10.3), $\mathbf{s}_{n+1,\Delta\mathbf{e}}$(10.4)	
	1st branch	2nd branch
F_1 & F_2	(10.8) & (10.9)	(10.21) & (10.22)
$F_{1,\Delta\varepsilon_q}$ & $F_{2,\Delta\varepsilon_q}$	(10.11) & (10.14)	(10.23) & (10.26)
F_{1,ζ^*} & F_{2,ζ^*}	(10.12) & (10.15)	(10.24) & (10.27)
$F_{1,\Delta\mathbf{e}}$ & $F_{2,\Delta\mathbf{e}}$	(10.13) & (10.16)	(10.25) & (10.28)
	$\hat{F}_1 = F_1(\Delta\varepsilon_q, \zeta^*, \Delta\varepsilon_{33})$	
	$\hat{F}_{shell} = F_{shell}(\Delta\varepsilon_q, \zeta^*, \Delta\varepsilon_{33})$(10.38)	
	Calculate $A_{11}, A_{12}, A_{21}, A_{22}$ and the corrections $\delta(\Delta\varepsilon_q), \delta(\Delta\varepsilon_{33})$	
	$A_{11} = F_{1,\Delta\varepsilon_q} + F_{1,\zeta^*}\zeta^*_{,\Delta\varepsilon_q}$	
	$A_{12} = \mathbf{a}\cdot\left[F_{1,\Delta\mathbf{e}} + F_{1,\zeta^*}\zeta^*_{,\Delta\mathbf{e}}\right]$	
	$A_{21} = \mathbf{a}\cdot\left[\mathbf{s}_{n+1,\Delta\varepsilon_q} + \mathbf{s}_{n+1,\zeta^*}\zeta^*_{,\Delta\varepsilon_q}\right]$,	
	$A_{22} = \mathbf{a}\cdot\left[\mathbf{a}\cdot\mathbf{s}_{n+1,\Delta\mathbf{e}} + \mathbf{a}\cdot\mathbf{s}_{n+1,\zeta^*}\zeta^*_{,\Delta\mathbf{e}}\right] - K$	
	where $\zeta^*_{,\Delta\varepsilon_q} = -F_{2,\Delta\varepsilon_q}/F_{2,\zeta^*}$, $\zeta^*_{,\Delta\mathbf{e}} = -F_{2,\Delta\mathbf{e}}/F_{2,\zeta^*}$	
	$\begin{bmatrix}\delta(\Delta\varepsilon_q)\\ \delta(\Delta\varepsilon_{33})\end{bmatrix} = \dfrac{1}{A_{11}A_{22} - A_{12}A_{21}}\begin{bmatrix}A_{22} & -A_{12}\\ -A_{21} & A_{11}\end{bmatrix}\cdot\begin{bmatrix}-\hat{F}_1\\ -\hat{F}_{shell}\end{bmatrix}$	
END		

Remark: For 3D elements, only $\hat{F}_1(\Delta\varepsilon_q) = F_1(\Delta\varepsilon_q, \zeta^*) = 0$ needs to be solved. The correction to $\Delta\varepsilon_q$ using a Newton scheme is ontained as $\delta(\Delta\varepsilon_q) = -\hat{F}_1/\hat{F}_{1,\Delta\varepsilon_q}$.(10.46)

APPENDIX 2: DETAILS ON OTHER MODELS IN THE LITERATURE

In this appendix, some additional details are provided about the formulation properties and implementation of material models in the literature. Namely, the limitations of the model by Hughes & Shakib (1986) are indicated and implementation schemes are developed for the J2DT, and the original model by Simo (1987).

Limitation in the model by Hughes & Shakib (1986)

Hughes & Shakib (1987) developed an associative "pseudo-corner" model, incorporating increased plastic flow for non-proportional loading paths. It employs a modified hardening modulus $\bar{H}$ explicitly dependent on the strain rate direction (angle θ), defined as:

$$\bar{H} = 3G\left(\left(1+\frac{H}{3G}\right)\frac{\cos\theta}{\cos\psi}-1\right) \tag{10.55}$$

with

$$\psi(\theta) = \max\left\{0, \quad \pi/2\frac{\theta-\theta_c}{\pi/2-\theta_c}\right\} \tag{10.56}$$

and θ_c was suggested as a material parameter to be calibrated form experimental data. However, from Drucker's requirements, plastic work must be positive ($\dot{\mathbf{s}} \cdot \dot{\mathbf{e}}^{\boldsymbol{p}} \geq 0$), which creates a restriction for θ_c:

$$\dot{\mathbf{s}} \cdot \dot{\mathbf{e}}^p \geq 0 \quad \leftrightarrow \quad 2G(\dot{\mathbf{e}} - \dot{\mathbf{e}}^p) \cdot \dot{\mathbf{e}}^p \geq 0 \leftrightarrow \cos\theta \geq \frac{\|\dot{\mathbf{e}}^p\|}{\|\dot{\mathbf{e}}\|} = \frac{w^*(\theta, \varepsilon_q)}{1+H/3G} \tag{10.57}$$

which under the definition (10.56) demands $\theta_c \leq (\pi/2)/(1+3G/H) = \theta_{c\,max}$. This is restrictive for materials with low hardening $\theta_{c\,max} \approx 0$, and the model allows for very limited increases in the plastic flow compared to the J2FT. Yet, different definitions $\psi(\theta)$ may provide further applicability in materials with low hardening. Simo (1987), also noted that under non-proportional loading, this plastic flow may be accompanied by a reduction of the initial radius of the Von Mises yield surface, making it a softening model.

Implementation of J_2 Deformation Theory

As discussed in paragraph 2.4 the J2DT is a total strain theory, postulating there is a one-to-one relation between total strain and stress, so no integration is needed for implementation in an FE environment. However, in an incremental analysis, a stress update algorithm is used to calculate the size of plastic strain after an imposed strain increment $\Delta\boldsymbol{\varepsilon}$. Isolating volumetric and deviatoric parts of the strain and accounting for additive decomposition, it can be easily seen that:

$$\boldsymbol{\varepsilon}_{n+1} = \boldsymbol{\varepsilon}_n + \Delta\boldsymbol{\varepsilon} \tag{10.58}$$

$$\mathbf{e}^e_{n+1} + \mathbf{e}^p_{n+1} + tr(\boldsymbol{\varepsilon}_{n+1})/3\,\mathbf{I} = \mathbf{e}^e_n + \mathbf{e}^p_n + \Delta\mathbf{e} + tr(\boldsymbol{\varepsilon}_n + \Delta\boldsymbol{\varepsilon})/3\,\mathbf{I} \tag{10.59}$$

From the postulate that total plastic strain and stress are codirectional it is:

$$\mathbf{e}^e_n = \mathbf{s}_n/2G = \sqrt{2/3}\,q_n/2G\,\mathbf{n}_n\,, \qquad \mathbf{e}^p_n = \sqrt{3/2}\,\varepsilon_{q|n}\mathbf{n}_n \tag{10.60}$$

$$\mathbf{e}^e_{n+1} = \mathbf{s}_{n+1}/2G = \sqrt{2/3}\,q_{n+1}/2G\,\mathbf{n}_{n+1}\,, \qquad \mathbf{e}^p_{n+1} = \sqrt{3/2}\,\varepsilon_{q|n+1}\mathbf{n}_{n+1} \tag{10.61}$$

So that the deviatoric part of (10.59) takes the form:

$$\sqrt{3/2}\left[\frac{q_{n+1}}{3G} + \varepsilon_{q|n+1}\right]\mathbf{n}_{n+1} = \sqrt{3/2}\left[\frac{q_n}{3G} + \varepsilon_{q|n}\right]\mathbf{n}_n + \Delta\mathbf{e} \tag{10.62}$$

This defines the direction of the final deviatoric stress tensor

$$\mathbf{n}_{n+1} = \frac{\sqrt{2/3}\,\Delta\mathbf{e} + \left[q_n/3G + \varepsilon_{q|n}\right]\mathbf{n}_n}{\left\|\sqrt{2/3}\,\Delta\mathbf{e} + \left[q_n/3G + \varepsilon_{q|n}\right]\mathbf{n}_n\right\|} \tag{10.63}$$

and its amplitude is calculated by solving:

$$\left\|\sqrt{2/3}\,\Delta\mathbf{e} + \left[q_n/3G + \varepsilon_{q|n}\right]\mathbf{n}_n\right\| = q_{n+1}/3G + \varepsilon_{q|n+1} \tag{10.64}$$

It is advantageous to square (10.64) and further using the consistency condition $q_{n+1} = k_{n+1} = k(\varepsilon_{q|n+1})$, equation (10.65) is obtained which is solved in terms of $\varepsilon_{q|n+1}$ to identify the size of the plastic part of the strain, to be used together with eq.(10.63) to find what is the new stress state.

$$\begin{aligned} F_{DT}(\Delta\varepsilon_q) = {} & \left[\frac{k_{n+1}}{3G} + \varepsilon_{q|n+1}\right]^2 - \left[\sqrt{2/3}\,\|\Delta\mathbf{e}\|\right]^2 - \left[\frac{q_n}{3G} + \varepsilon_{q|n}\right]^2 \\ & - 2\left(\sqrt{2/3}\right)\left(\frac{q_n}{3G} + \varepsilon_{q|n}\right)\mathbf{n}_n \cdot \Delta\mathbf{e} = 0 \end{aligned} \tag{10.65}$$

And the derivative

$$F_{DT,\varepsilon_q} = 2\left[\frac{k_{n+1}}{3G} + \varepsilon_{q|n+1}\right]\left(\frac{H_{n+1}}{3G} + 1\right) \tag{10.66}$$

A schematic representation of this implementation scheme is provided in Figure 10.1 juxtaposed to the backward Euler integration for J2FT.

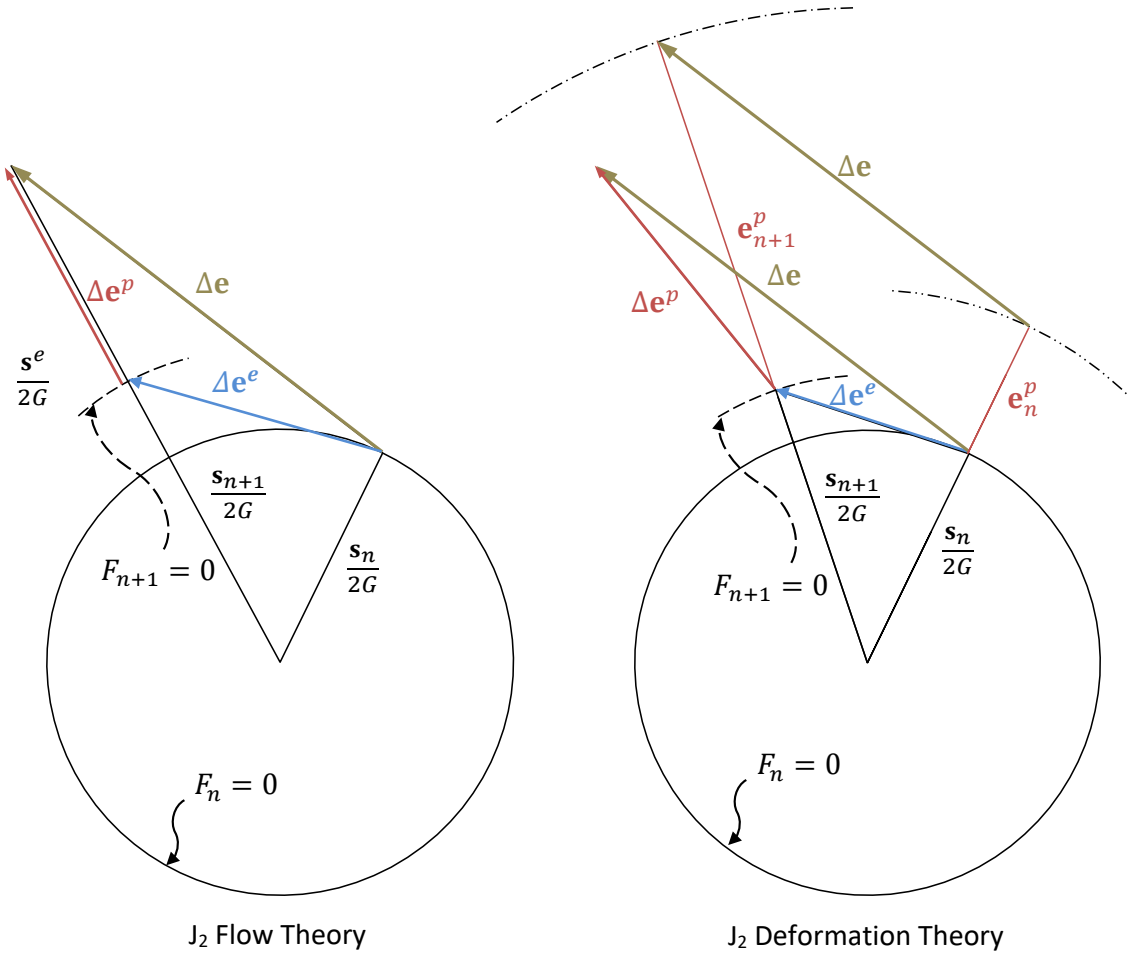

Figure 10.1: Stress update algorithm for the J2FT and J2DT.

The algorithmic moduli are obtained as described in paragraph 4, and their form is identical to the rate form and the tangent continuum rigidity

$$\begin{aligned}\mathbf{D}^{cc}_{ep} = 3K\mathbf{I}^{vol} &+ \frac{2G}{1+3G/h_{n+1}}[\mathbf{I}^{dev} - \mathbf{n}_{n+1}\otimes\mathbf{n}_{n+1}] \\ &+ \frac{2G}{1+3G/H_{n+1}}[\mathbf{n}_{n+1}\otimes\mathbf{n}_{n+1}]\end{aligned} \tag{10.67}$$

Implementation of the model by Simo (1987)

The key properties of model by Simo (1987) were presented in paragraph 2.6. Below, a backward Euler integration scheme is presented, accounting for nonlinear isotropic

hardening. This model can be directly addressed via the developed framework for J2NA, for any definition of the explicitly chosen function $\hat{\delta}(\theta, \Delta\varepsilon_q)$. The plastic strain increment is expressed as:

$$\Delta\mathbf{e}^p = \sqrt{3/2}\,\Delta\varepsilon_q\,\mathbf{n}_{n+1} + \frac{1}{1+\bar{h}_{SM}/3G}\left[\mathbf{I}^{dev} - \mathbf{n}_{n+1}\otimes\mathbf{n}_{n+1}\right]\Delta\mathbf{e} \tag{10.68}$$

where $\bar{h}_{SM}$ is calculated by the demand $\tan\theta^p = \hat{\delta}(\theta = \theta^e + \zeta^*, \Delta\varepsilon_q)$, and the internal variables are obtained by solving the system of:

$$F_1 = F_{\hat{\delta}}(\Delta\varepsilon_q, \zeta^*) = \left[\Delta\varepsilon_q + \frac{k_{n+1}}{3G}\right]^2 - \left(\frac{q^e}{3G}\right)^2 + \Delta\varepsilon_q^2\,\hat{\delta}^2 = 0 \tag{10.69}$$

$$F_2 = F_{\hat{\delta}0}(\Delta\varepsilon_q, \zeta^*) = 3G\Delta\varepsilon_q\hat{\delta} - q^e\sin\zeta^* = 0 \tag{10.70}$$

and

$$F_{\hat{\delta},\Delta\varepsilon_q} = 2\left[\Delta\varepsilon_q + \frac{k_{n+1}}{3G}\right]\left[1 + \frac{H_{n+1}}{3G}\right] + 2\Delta\varepsilon_q\hat{\delta}^2 + 2\Delta\varepsilon_q^2\hat{\delta}\hat{\delta}_{,\Delta\varepsilon_q} \tag{10.71}$$

$$F_{\hat{\delta},\zeta^*} = 2\Delta\varepsilon_q^2\hat{\delta}\hat{\delta}_{,\theta} \tag{10.72}$$

$$F_{\hat{\delta},\Delta\mathbf{e}} = -6G\mathbf{s}^{\mathrm{e}} + 2\Delta\varepsilon_q^2\hat{\delta}\hat{\delta}_{,\theta}\theta^e_{,\Delta\mathbf{e}} \tag{10.73}$$

$$F_{\hat{\delta}0,\Delta\varepsilon_q} = 3G\,\hat{\delta} + 3G\Delta\varepsilon_q\hat{\delta}_{,\Delta\varepsilon_q} \tag{10.74}$$

$$F_{\hat{\delta}0,\zeta^*} = 3G\Delta\varepsilon_q\hat{\delta}_{,\theta} - q^e\cos\zeta^* \tag{10.75}$$

$$F_{\hat{\delta}0,\Delta\mathbf{e}} = -3G\frac{\mathbf{s}^e}{q^e}\sin\zeta^* + 3G\Delta\varepsilon_q\hat{\delta}_{,\theta}\theta^e_{,\Delta\mathbf{e}} \tag{10.76}$$

The derivatives $\hat{\delta}_{,\theta}$ and $\hat{\delta}_{,\Delta\varepsilon_q}$ are known. Furthermore, due to the geometric meaning of the specific $\hat{\delta} = \tan[\max(\theta, \theta_c)]$ in eq.(2.35), further simplification of this scheme is achieved, eliminating ζ^* from (10.69). For the first branch of the model the procedure is given below, while for the second branch the result is identical to the second branch of the model presented in in paragraph 3.1.2 and Appendix 1. A geometric representation of the return mapping scheme for the two branches of this model is offered in Figure 10.2

In the first branch, the straining angle is $\theta \le \theta_c$ and $\hat{\delta} = \tan\theta = \tan\theta^p$, so the plastic strain increment forms an angle $\theta^{\,p} = \theta$. The sine law offers a simple way for expressing angle θ from further calculations:

$$\tan^2\theta = \frac{(q^e \sin\theta^e)^2}{q_{n+1}^2 - (q^e \sin\theta^e)^2} \tag{10.77}$$

Which inserted to (10.69) and accounting for consistency, leaves only the plastic strain increment $\Delta\varepsilon_q$ as an unknown. The system of equations (10.78), (10.79) must then be solved.

$$F_{SM1}(\Delta\varepsilon_q) = \left[\Delta\varepsilon_q + \frac{k_{n+1}}{3G}\right]^2 - \left(\frac{q^e}{3G}\right)^2 + \Delta\varepsilon_q^2 \frac{(q^e \sin\theta^e)^2}{k_{n+1}^2 - (q^e \sin\theta^e)^2} = 0 \tag{10.78}$$

$$F_{SM2}(\Delta\varepsilon_q, \zeta^*) = \tan^2(\theta^e + \zeta^*) - \frac{(q^e \sin\theta^e)^2}{q_{n+1}^2 - (q^e \sin\theta^e)^2} = 0 \tag{10.79}$$

With the derivatives

$$\begin{aligned} F_{SM1,\Delta\varepsilon_q} = {} & 2\left[\Delta\varepsilon_q + \frac{k_{n+1}}{3G}\right]\left[1 + \frac{H_{n+1}}{3G}\right] + 2\Delta\varepsilon_q \frac{(q^e \sin\theta^e)^2}{k_{n+1}^2 - (q^e \sin\theta^e)^2} \\ & - \Delta\varepsilon_q^2 \frac{(q^e \sin\theta^e)^2}{[k_{n+1}^2 - (q^e \sin\theta^e)^2]^2}[2k_{n+1}H_{n+1}] \end{aligned} \tag{10.80}$$

$$F_{SM1,\zeta^*} = 0 \tag{10.81}$$

$$\begin{aligned} F_{SM1,\Delta\mathbf{e}} = {} & +\Delta\varepsilon_q^2 \frac{k_{n+1}^2 (q^e \sin\theta^e)^2}{[k_{n+1}^2 - (q^e \sin\theta^e)^2]^2} 2q^e \sin\theta^e \left(6G\mathbf{s}^e \sin\theta^e \right. \\ & \left. + q^e \cos\theta^e\, \theta^e_{,\Delta\mathbf{e}}\right) - 2\frac{\mathbf{s}^e}{3G} \end{aligned} \tag{10.82}$$

$$F_{SM2,\Delta\varepsilon_q} = +\frac{(q^e \sin\theta^e)^2}{[k_{n+1}^2 - (q^e \sin\theta^e)^2]^2}[2k_{n+1}H_{n+1}] \tag{10.83}$$

$$F_{SM1,\zeta^*} = 2\tan(\theta^e + \zeta^*)\,[1 + \tan^2(\theta^e + \zeta^*)] \tag{10.84}$$

$$\begin{aligned} F_{SM1,\Delta\mathbf{e}} = {} & 2\tan(\theta^e + \zeta^*)\,[1 + \tan^2(\theta^e + \zeta^*)]\theta^e_{,\Delta\mathbf{e}} \\ & - \frac{2k_{n+1}^2 q^e \sin\theta^e}{[k_{n+1}^2 - (q^e \sin\theta^e)^2]^2}\left[6G\mathbf{s}^e \sin\theta^e + q^e \cos\theta^e\, \theta^e_{,\Delta\mathbf{e}}\right] \end{aligned} \tag{10.85}$$

The algorithmic material moduli are obtained as in the Appendix 1 using the above data.

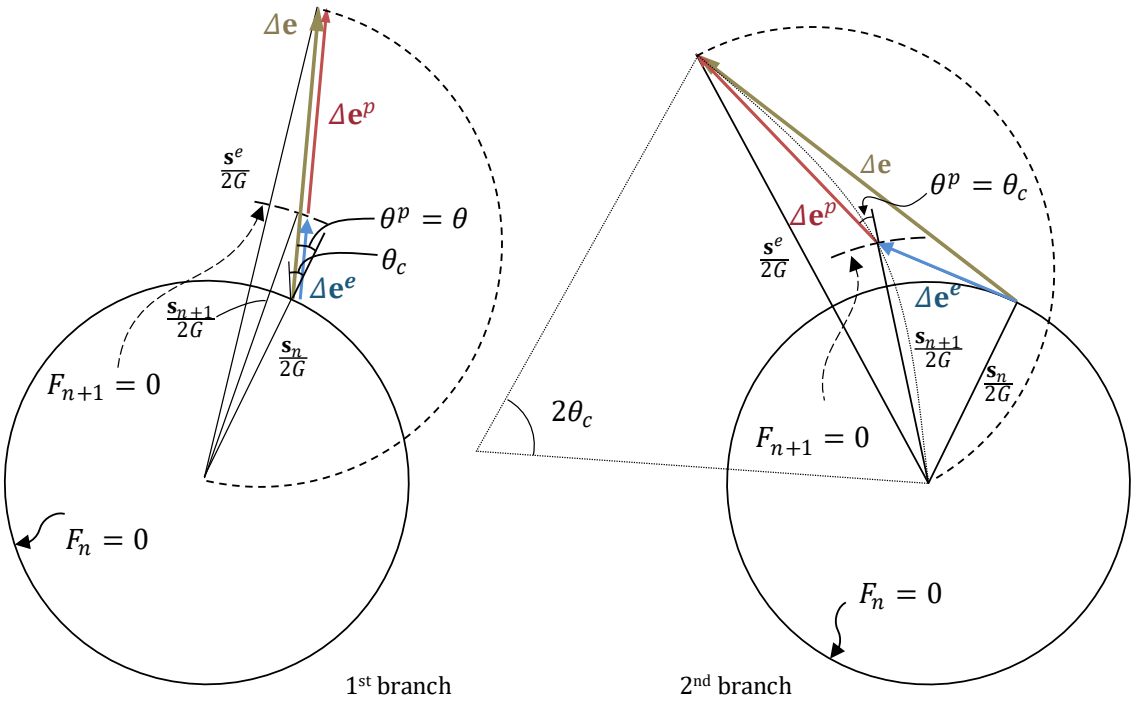

Figure 10.2: Geometric interpretation of the return mapping of the model by Simo (1987):(a) in the corner branch ($\theta \leq \theta_c$) and (b) in the critical angle branch ($\theta > \theta_c$), for a given stress state and strain increment

APPENDIX 3: BUCKLING STRESS OF AXIALLY COMPRESSED SHELLS IN THE PRESENCE OF PRESSURE

In this Appendix, the principle of virtual work is employed to obtain the analytical expressions for the bifurcation stress of elastic-plastic cylindrical shells under compressive loads. Buckling under axial compression and pressure loads is addresses first, which leads to an axisymmetric wrinkling mode, uniform along the cylinder. Followingly, bifurcation into an ovalization mode is examined for inelastic cylinders under external pressure and axial load.

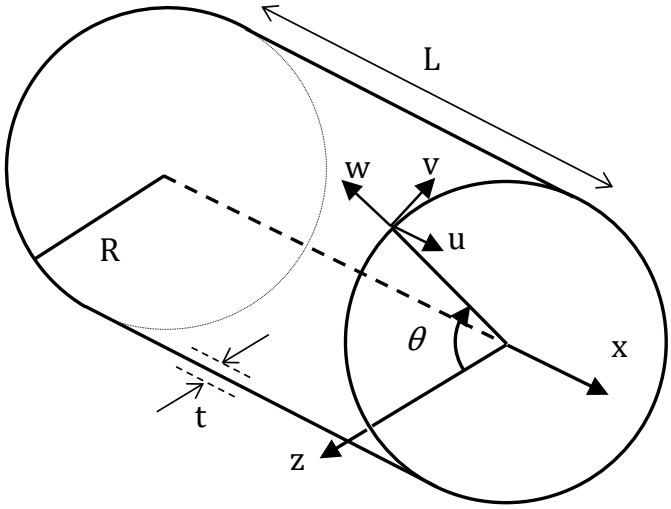

Figure 10.3: Cylindrical shell and displacement field in cylindrical coordinates

Kinematics

Considering a circular cylindrical shell of mean radius R and wall thickness t, described in a cylindrical coordinate system (x, θ, z), with the corresponding displacements (u, v, w) and employing the Donnell kinematic relations, the membrane and bending components of the strains are expressed as:

$$\varepsilon_{xx} = u_{,x} + \frac{w_{,x}^2}{2} \tag{10.86}$$

$$\varepsilon_{\theta\theta} = \frac{v_{,\theta} + w}{R} + \frac{1}{2}\left(\frac{w_{,\theta} - v}{R}\right)^2 \tag{10.87}$$

$$\varepsilon_{x\theta} = \frac{1}{2}\left(\frac{u_{,\theta}}{R} + v_{,x}\right) + \frac{1}{2} w_{,x} \frac{(w_{,\theta} - v)}{R} \tag{10.88}$$

$$\kappa_{xx} = -w_{,xx} \tag{10.89}$$

$$\kappa_{\theta\theta} = -\frac{1}{R^2}(w_{,\theta\theta} - v_{,\theta}) \tag{10.90}$$

$$\kappa_{x\theta} = -\frac{1}{2R}[w_{,x\theta} + (w_{,x\theta} - v_{,x})] \tag{10.91}$$

The strain at all points across the shell thickness is calculated as:

$$\bar{\varepsilon}_{\alpha b} = \varepsilon_{\alpha\beta} + z\,\kappa_{\alpha\beta} \tag{10.92}$$

and the stresses are connected to the strains though the instantaneous constitutive relations of the material model under consideration, is expressed as:

$$\dot{\bar{\sigma}}_{\alpha b} = D_{\alpha\beta\gamma\delta}\dot{\bar{\varepsilon}}_{\gamma\delta} \tag{10.93}$$

where $D_{\alpha\beta\gamma\delta}$ are the instantaneous material moduli (material tangent tensor -eq. (2.51)) accounting for $\sigma_{zz} = 0$ (condensed material moduli – eq. (3.58)). The force and moment intensities are:

$$N_{\alpha\beta} = \int_{-t/2}^{t/2} \bar{\sigma}_{\alpha b}\, dz \tag{10.94}$$

$$M_{\alpha\beta} = \int_{-t/2}^{t/2} \bar{\sigma}_{\alpha b} z\, dz \tag{10.95}$$

Bifurcation stress and wavelength of pressurized cylindrical shells under compression

A thick-walled cylindrical shell of mean diameter D_o, radius $R = D_o/2$, thickness t, and cross-section area A is loaded with internal fluid pressure p and subjected to an axial compressive force F, as shown in Figure 10.4. Gellin (1979) showed that the first bifurcation mode of shells under compression takes place in an axisymmetric, periodic mode. A similar instability mode is encountered in cases of cylinders under internal pressure (Paquette & Kyriakides, 2006). The shell experiences instability at a compressive axial stress $\sigma_{c.ep}$, whence it transitions to an axisymmetric, uniformly wrinkled buckling mode, periodic along its length, with a wavelength equal to $2\lambda_c$, indicated in Figure 10.4.

Axis-symmetry implies that displacement $v = 0$ and $u_{,\theta} = w_{,\theta} = 0$, so the shell kinematics reduce to the following:

$$\varepsilon_{xx} = u_{,x} + w_{,x}^2/2 \tag{10.96}$$

$$\varepsilon_{\theta\theta} = w/R \tag{10.97}$$

$$\varepsilon_{x\theta} = 0 \tag{10.98}$$

$$\kappa_{xx} = -w_{,xx} \tag{10.99}$$

$$\kappa_{\theta\theta} = 0 \tag{10.100}$$

$$\kappa_{x\theta} = 0 \tag{10.101}$$

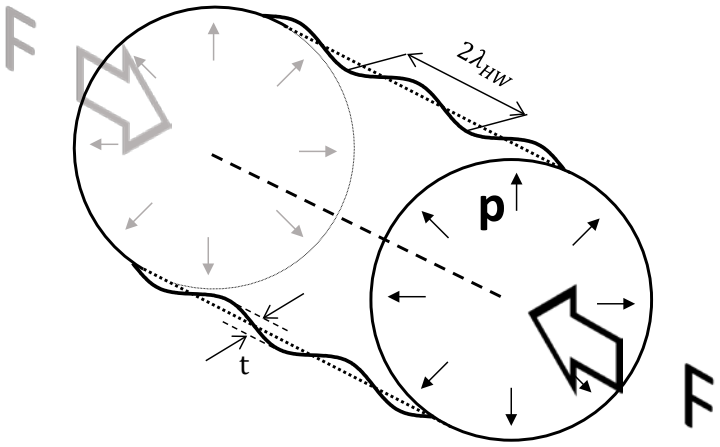

Figure 10.4: Bifurcation into a periodic axisymmetric wrinkled shape of pressurized cylindrical shells under axial compression

The principle of virtual work (PVW) for shells under conservative external forces is expressed as:

$$\delta\Pi = \delta U_m + \delta U_b + \delta\Omega = 0 \tag{10.102}$$

where U_m is the membrane strain energy of the shell, U_b the bending strain energy, and Ω is the potential energy of the external conservative loads, equal to the negative of the work done by the loads as the structure is deformed.

For compressed pressurized cylinders, in the prebuckling configuration deformation is longitudinally uniform, while it remains periodic axisymmetric when buckling onsets. So, it is sufficient to address a single halfwave of the shell to identify instability, and the virtual work terms reduce to:

$$\delta U_m = \int_S \{N_{\alpha\beta}\delta\varepsilon_{\alpha\beta}\}\, dS = \int_S \{N_{xx}\delta\varepsilon_{xx} + N_{\theta\theta}\delta\varepsilon_{\theta\theta}\}\, dS \tag{10.103}$$

$$\delta U_b = \int_S \{M_{\alpha\beta}\delta\kappa_{\alpha\beta}\}\, dA = \int_S \{M_{xx}\delta\kappa_{xx}\}\, dS \tag{10.104}$$

$$\delta\Omega = \int_S -p_{int}\delta\left\{w + \frac{1}{2R}(v^2 + vw_{,\theta} - v_{,\theta}\, w + w^2)\right\} dS \tag{10.105}$$

$$= -p_{int}R\int_0^{\lambda}\int_0^{2\pi}\delta\left\{w+\frac{1}{2R}(w^2)\right\}dxd\theta$$

where S is the surface of the one halfwave long cylinder segment. To identify the onset of buckling, an arbitrary small perturbation of the displacement field is assumed:

$$u = u_0 + u_1 \tag{10.106}$$

$$v = 0 \tag{10.107}$$

$$w = w_0 + w_1 \tag{10.108}$$

So, the membrane strains and curvatures are:

$$\varepsilon_{xx} = \varepsilon_{xx0} + \varepsilon_{xx1} + \varepsilon_{xx2} = \quad u_{0,x} \quad + u_{1,x} \quad + w_{1,x}^2/2 \tag{10.109}$$

$$\varepsilon_{\theta\theta} = \varepsilon_{\theta\theta0} + \varepsilon_{\theta\theta1} \qquad = w_0/R \quad + w_1/R \tag{10.110}$$

$$\kappa_{xx} = \kappa_{xx0} + \kappa_{xx1} \qquad = \quad 0 \quad - w_{1,xx} \tag{10.111}$$

$$\kappa_{\theta\theta} = 0 \tag{10.112}$$

In the above, the notation by (Bardi, 2006) is used, where the additional indices 0,1,2 refer to the order of different terms of strain and curvature components. The force and moment intensities, accounting for the prebuckling equilibrium, are expressed as:

$$N_{xx} = N_{xx0} + N_{xx1} \qquad = \ -\sigma t \quad + t[D_{11}\varepsilon_{xx1} + D_{12}\varepsilon_{\theta\theta1}] \tag{10.113}$$

$$N_{\theta\theta} = N_{\theta\theta0} + N_{\theta\theta1} \qquad = p_{int}R \quad + t[D_{12}\varepsilon_{xx1} + D_{22}\varepsilon_{\theta\theta1}] \tag{10.114}$$

$$M_{xx} = M_{xx0} + M_{xx1} \qquad = \quad 0 \quad + t^3/12\,[D_{11}\kappa_{xx1}] \tag{10.115}$$

$$M_{\theta\theta} = 0 \tag{10.116}$$

where $D_{11} = D_{xxxx}$, $D_{12} = D_{xx\theta\theta}$, $D_{22} = D_{\theta\theta\theta\theta}$.

Substituting (10.103)-(10.116) to (10.102) the PVW takes the form:

$$\begin{aligned}\int_0^{\lambda}\{\ & (N_{xx0}\delta\varepsilon_{xx1} + N_{\theta\theta0}\delta\varepsilon_{\theta\theta1} + M_{xx0}\delta\kappa_{xx1} - p_{int}\delta w)\\ &+(N_{xx1}\delta\varepsilon_{xx1} + N_{xx0}\delta\varepsilon_{xx2} + N_{\theta\theta1}\delta\varepsilon_{\theta\theta1} + M_{xx1}\delta\kappa_{xx1} - p_{int}\,w\delta w/R)\\ &+(N_{xx1}\delta\varepsilon_{xx2})\quad\}\,2\pi R dx = 0\end{aligned} \tag{10.117}$$

Keeping only the second order terms, the stability equation is obtained:

$$\delta^2\Pi = \int_0^{\lambda} \{ \; N_{xx1}\delta\varepsilon_{xx1} + N_{xx0}\delta\varepsilon_{xx2} \; + N_{\theta\theta1}\delta\varepsilon_{\theta\theta1} + M_{xx1}\delta\kappa_{xx1} \\ -p_{int}\, w\delta w/R \quad \} 2\pi R dx = 0 \tag{10.118}$$

The buckling mode is assumed to be axisymmetric, periodic expressed as:

$$\bar{w} = a\cos px \tag{10.119}$$

$$\bar{u} = b\sin px \tag{10.120}$$

with $p = \pi/\lambda$, and the stability equation (10.118) becomes

$$\delta^2\Pi = \int_0^{\lambda} \{N_{xx0}\delta\varepsilon_{xx2,ab} + N_{xx1,a}\delta\varepsilon_{xx1,b} \; + N_{\theta\theta1,a}\delta\varepsilon_{\theta\theta1,b} \\ + M_{xx1,a}\delta\kappa_{xx1,b} - p_{int}/R \; w_{1,\alpha}\, w_{1,\beta}\}\delta q_a \delta q_b \, 2\pi R dx \\ = H_{ab}\delta q_a \delta q_b = 0 \tag{10.121}$$

where $(\cdot)_{,a} = \partial(\cdot)/\partial q_a$ and $q = [a \quad b]^T$, hence

$$\delta\varepsilon_{xx1,1} \; = 0, \qquad \delta\varepsilon_{xx1,2} \; = p\cos px \tag{10.122}$$

$$\delta\,\varepsilon_{xx2,11} = p^2\sin^2 px\,, \qquad \delta\varepsilon_{xx2,11} = \delta\varepsilon_{xx2,12} = \delta\varepsilon_{xx2,21} = 0 \tag{10.123}$$

$$\delta\varepsilon_{\theta\theta1,1} \; = \cos px/R\,, \qquad \delta\varepsilon_{\theta\theta1,2} \; = 0 \tag{10.124}$$

$$\delta\kappa_{xx1,1} \; = -p^2\cos px\,, \qquad \delta\kappa_{xx1,2} \; = 0 \tag{10.125}$$

And the integration identities:

$$\int_0^{\lambda=\pi/p} \cos^2 px\, dx = \int_0^{\lambda=\pi/p} \sin^2 px\, dx = \frac{\pi}{2p} \tag{10.126}$$

Using (10.119)-(10.126), the components $H_{\alpha\beta}$ of tensor $\mathbf{H}$, defined in (10.121), are expressed as:

$$\mathbf{H} = \frac{\pi^2 t}{\bar{\lambda}}\begin{bmatrix} -\bar{\lambda}^2\sigma + (D_{22} - p_{int}/\tau) + \bar{\lambda}^4\dfrac{\tau^2}{12}D_{11} & \bar{\lambda}D_{12} \\ \bar{\lambda}D_{12} & \bar{\lambda}^2 D_{11} \end{bmatrix} \tag{10.127}$$

where $\tau = t/R$, and $\bar{\lambda} = pR = \pi R/\lambda$. The determinant of $\mathbf{H}$ should vanish at bifurcation:

$$\det(\mathbf{H}) = H_{11}H_{22} - H_{12}H_{21} = 0 \tag{10.128}$$

$$= (\pi^2 t)^2 D_{11} \bar{\lambda}^2 \left[-\sigma + \frac{D_{22} - D_{12}^2/D_{11} - p_{int}/\tau}{\bar{\lambda}^2} + \bar{\lambda}^2 \frac{\tau^2}{12} D_{11} \right] = 0$$

or

$$\sigma = D_{11} \left[\frac{1}{\bar{\lambda}^2} \frac{det\, D - D_{11}\, p_{int}/\tau}{D_{11}^2} + \bar{\lambda}^2 \frac{\tau^2}{12} \right] \tag{10.129}$$

where $det\, D = D_{11}D_{22} - D_{12}D_{12}$. Minimizing σ in terms of $\bar{\lambda}$, the critical halfwave $\lambda_{c.ep}$ and the bifurcation stress $\sigma_{c.ep}$ are obtained

$$\lambda_{c.ep} = \pi \left[\frac{D_{11}^2}{12(det\, D - p_{int} D_{11} R/t)} \right]^{1/4} (Rt)^{1/2} \tag{10.130}$$

and

$$\sigma_{c.ep} = \left[\frac{det\, D - D_{11} p_{int}\, R/t}{3} \right]^{1/2} \left(\frac{t}{R} \right) \tag{10.131}$$

For any given shell R/t and pressure p_{int}, accounting for the stress-controlled loading, the bifurcation stress $\sigma_{c.ep}$ is obtained by solving (10.132) in terms of σ_x and the applied axial load F/A using (10.133):

$$abs(\sigma_x) - \sigma_{c.ep}(\sigma_x, p_{int}, R/t) = 0 \tag{10.132}$$

$$F/A = \sigma_{c.ep} + \frac{p_{int} R/t}{2} \tag{10.133}$$

As σ_x appears in both terms of (10.132), a local iterative scheme for nonlinear equations is employed to solve it. An exception is the case of bifurcation occurring in the elastic range of the material, where σ_x is eliminated from the material moduli in the second term, hence the solution is found in a straightforward manner.

Equation (10.132) may, equivalently, be used to identify the $R/t(\sigma_x, p_{int})$ of the shell that is pressurized with p_{int} and does not bifurcate before the axial stress reaches σ_x. Or it may be used to obtain the pressure $p_{int}(\sigma_x, R/t)$ that must be applied in advance of axial compression, so that a shell of a given R/t does not bifurcate before the axial stress reaches σ_x. Additionally, the dependence of eq. (10.132) on the R/t ratio and not on the radius R itself, indicates that all long shells of a given material and R/t, bifurcate at the same stress $\sigma_{c.ep}$ independent of their scale. As soon as eq. (10.132) is solved, eq. (10.130) is used to obtain the wrinkling halfwave.

Buckling formulas for shells under uniform compression equivalent to (10.130), (10.131) have been presented in several publications e.g. (Batterman, 1965; Reddy, 1979; Tvergaard, 1983). The analysis by (Bardi & Kyriakides, 2006) provided the formulas in (4.1), (4.2) for $\sigma_{c.ep}$, $\lambda_{c.ep}$which are identical to (10.130), (10.131) for the case of no pressure $(p_{int} = 0)$. Formulas (4.1), (4.2) were further suggested by (Paquette & Kyriakides, 2006) for compressed cylinders under internal pressure. The above proof demonstrates that an additional term $(-D_{11}p_{int}R/t)$ arises from the potential of the internal pressure, which should not be neglected a priori. However, this term is found to be generally small, and the two sets of formulas produce very similar predictions.

The components of $D_{\alpha\beta}$ may be equivalently obtained from the respective components of the flexibility moduli $C_{\alpha\beta}$, which are readily available, which allows circumventing the complexity of performing static condensation of the material rigidity tensor.

$$\begin{bmatrix} D_{11} & D_{12} \\ D_{12} & D_{22} \end{bmatrix} = \frac{1}{\det C}\begin{bmatrix} C_{11} & -C_{12} \\ -C_{12} & C_{22} \end{bmatrix} \tag{10.134}$$

where $\det C = C_{11}C_{22} - C_{12}^2$. An explicit expression for the flexibility tensor C for the axisymmetric problem is given in eq.(10.135), which is applicable for several isotropic material models in plane stress conditions, upon appropriate definition of the parameters $\bar{h}$ offered in Table 2.2.

$$C = \frac{1}{E_T}\begin{bmatrix} 1 - \bar{\eta}\frac{3}{4}\frac{{\sigma_{\theta\theta}}^2}{q_e^2} & -\nu_T + \bar{\eta}\frac{3}{4}\frac{\sigma_{xx}\sigma_{\theta\theta}}{q_e^2} \\ -\nu_T + \bar{\eta}\frac{3}{4}\frac{\sigma_{xx}\sigma_{\theta\theta}}{q_e^2} & 1 - \bar{\eta}\frac{3}{4}\frac{{\sigma_{xx}}^2}{q_e^2} \end{bmatrix} \tag{10.135}$$

where

$$\bar{\eta} = 1 - \frac{E_T}{\bar{E}_S} = \frac{1 - H/\bar{h}}{1 + H/E} \tag{10.136}$$

$$\nu_T = \frac{1}{2} - \frac{E_T}{E}\left(\frac{1}{2} - \nu\right) \tag{10.137}$$

In the above, $E, E_T, \bar{E}_S$ are the elasticity (Young), tangent and modified secant material moduli -see eq. (10.138)- , ν is the Poisson ratio, H is the material hardening modulus and $q_e^2 = \sigma_{xx}^2 + \sigma_{\theta\theta}^2 - \sigma_{xx}\sigma_{\theta\theta}$ is the Von Mises stress. Note that $3\sigma_{xx}^2/4q_e^2 \leq 1$ and:

$$\frac{1}{E_T} = \frac{1}{H} + \frac{1}{E}, \qquad \frac{1}{\bar{E}_S} = \frac{1}{\bar{h}} + \frac{1}{E} \tag{10.138}$$

Finally, the bifurcation stress $\sigma_{c.ep}$ and half wavelength $\lambda_{c.ep}$ for the pressurized shell under compression may be written as:

$$\lambda_{c.ep} = \pi \left[\frac{C_{22}^2}{12 \det C \,(1 - C_{22}\sigma_{\theta\theta})}\right]^{1/4} (Rt)^{1/2} = \pi R \left[\frac{\mathrm{C}_{22}}{2(1 - C_{22}\sigma_{\theta\theta})}\sigma_{c.ep}\right]^{1/2} \tag{10.139}$$

and

$$\sigma_{c.ep} = \left[\frac{1 - C_{22}\sigma_{\theta\theta}}{3 \det C}\right]^{1/2} \left(\frac{t}{R}\right) \tag{10.140}$$

It is noted that in the absence of pressure and using J2DT to model inelastic behaviour ($\bar{E}_S = E_S$), these formulas reduce to the ones obtained by (Gellin, 1979) for axially compressed cylinders:

$$\sigma_{c.ep|0} = \frac{E_T}{\sqrt{1 - \nu_d^2}}\frac{t}{R}, \quad \nu_d^2 = \nu_T^2 + \frac{3}{4}\bar{\eta} \tag{10.141}$$

and

$$\lambda_{c.ep|0} = \frac{\pi\sqrt{Rt}}{\sqrt[4]{12(1 - \nu_d^2)}}\sqrt{\frac{1}{4}\left(1 + \frac{3E_T}{E_S}\right)} \tag{10.142}$$

Bifurcation into the elastic range

For elastic shells or when bifurcation takes place while the material is loaded into the elastic range, the calculation of the elastic bifurcation stress in (10.140) and the elastic wavelength from (10.139) simplifies to:

$$\sigma_{c.el} = \left[\frac{E}{\sqrt{1 - \nu^2}}\frac{t}{R}\right]\sqrt{1 - p_{int}R/(Et)} = \sigma_{c.el|0}\sqrt{1 - \bar{p}} \tag{10.143}$$

$$\lambda_{c.el} = \left[\frac{\pi}{\sqrt[4]{12(1 - \nu^2)}}\sqrt{Rt}\right]\frac{1}{\sqrt[4]{1 - p_{int}R/(Et)}} = \lambda_{c.el|0}\frac{1}{\sqrt[4]{1 - \bar{p}}} \tag{10.144}$$

These formulas reduce to the well know expressions for the buckling stress $\sigma_{c.el|0}$ and halfwave length $\lambda_{c.el|0}$ of the non-pressurized shell under compression ($\bar{p} = 0$). Further considering that $\bar{p} = p_{int}R/(Et) = \sigma_\theta/E \ll 1$ the above may be written as:

$$\frac{\sigma_{c.el}}{\sigma_{c.el|0}} = \sqrt{1 - \bar{p}} \approx 1 - \bar{p}/2 \tag{10.145}$$

$$\frac{\lambda_{c.el}}{\lambda_{c.el|0}} = \frac{1}{\sqrt[4]{1-\bar{p}}} \approx 1 + \bar{p}/4 \tag{10.146}$$

It is seen that pressurization tends to increase the wrinkling wavelength of the shell, while it reduces the axial stress at buckling. The external axial compression leading to buckling is $F_{c.el} = [\sigma_{c.el} + p_{int}R/2t]A$ (accounting for the axial tension induced by pressurization through cap forces). Normalizing by the buckling force under pure compression ($p = 0$) $A\sigma_{c.el|0}$, it is expressed as:

$$\begin{aligned}\frac{F_{c.el}/A}{\sigma_{c.el|0}} &= \sqrt{1-\bar{p}} + \frac{\bar{p}\sqrt{1-\nu^2}}{2t/R} \approx 1 - \bar{p}/2 + \frac{\bar{p}\sqrt{1-\nu^2}}{2t/R} \\ &\approx 1 + \bar{p}/2\left(\frac{\sqrt{1-\nu^2}}{t/R} - 1\right) \approx 1 + \frac{\bar{p}}{2t/R} \approx 1 + \frac{p_{int}/2E}{(t/R)^2}\end{aligned} \tag{10.147}$$

This shows that by applying internal pressure a shell can sustain greater axial loads before buckling occurs than the case of pure compression, as expected. This effect is more pronounced in the thin-walled shells, with large R/t values. It is noted that for metal shells, $\bar{p} = \sigma_\theta/E \ll \sigma_o/E \approx 0.5\%$, so any influence in $\sigma_{c.el}$, $\lambda_{c.el}$ due to pressure is limited.

Bifurcation under external pressure

Using the PVW, the bifurcation pressure is calculated for a tube subjected to external fluid pressure p_{ext} and axial load F, leading to an axially uniform ovalization buckling mode. The second order terms of the PVW reduce to:

$$\begin{aligned}\delta^2\Pi = \int_S \{&N_{xx}\delta\varepsilon_{xx} + N_{\theta\theta}\delta\varepsilon_{\theta\theta} + M_{\theta\theta}\delta\kappa_{\theta\theta} \\ &-(-p_{ext})\delta^2\left\{w + \frac{1}{2R}(v^2 + vw_{,\theta} - v_{,\theta}\,w + w^2)\right\}\Big\}\,dS = 0\end{aligned} \tag{10.148}$$

To identify the onset of buckling, an arbitrary small perturbation of the displacement field is assumed:

$$u = u_0 \tag{10.149}$$

$$v = v_0 + v_1 = 0 + b\sin n\theta \tag{10.150}$$

$$w = w_0 + w_1 = w_0 + a\cos n\theta \tag{10.151}$$

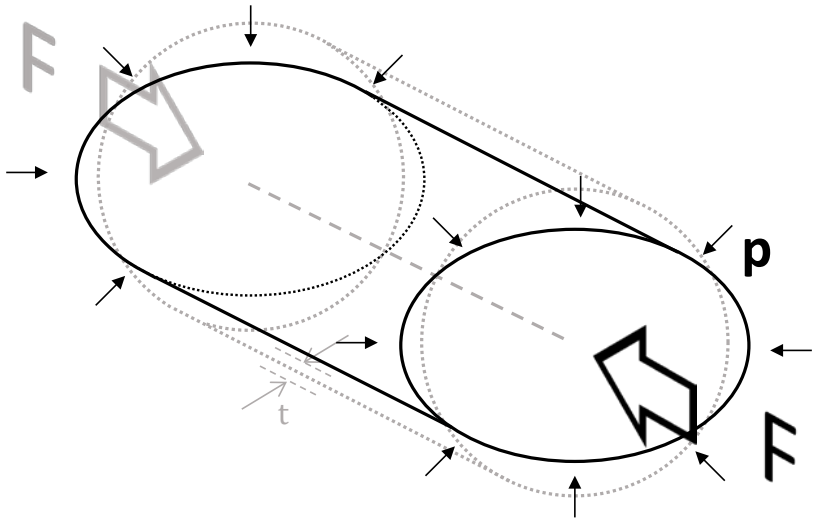

Figure 10.5: Bifurcation into an axially uniform ovalization buckling mode of cylindrical shells under external pressure and axial compression.

The membrane strains and curvatures are:

$$\varepsilon_{xx} = \varepsilon_{xx0} = u_{0,x} \tag{10.152}$$

$$\begin{aligned}\varepsilon_{\theta\theta} &= \varepsilon_{\theta\theta0} + \varepsilon_{\theta\theta1} + \varepsilon_{\theta\theta2} \\ &= \frac{w_0}{R} + \frac{(bn+a)}{R}\cos n\theta + \frac{(b-an)^2}{2R^2}\sin^2 n\theta\end{aligned} \tag{10.153}$$

$$\kappa_{xx} = 0 \tag{10.154}$$

$$\kappa_{\theta\theta} = \kappa_{\theta\theta0} + \kappa_{\theta\theta1} = 0 + n\frac{(b+an)}{R^2}\cos n\theta \tag{10.155}$$

The force and moment intensities are given by:

$$N_{xx} = N_{xx0} + N_{xx1} = -\sigma t + tD_{12}(bn+a)/R\cos n\theta \tag{10.156}$$

$$N_{\theta\theta} = N_{\theta\theta0} + N_{\theta\theta1} = -p_{ext}R + tD_{22}(bn+a)/R\cos n\theta \tag{10.157}$$

$$M_{xx} = M_{xx0} + M_{xx1} = 0 + t^3/12\, D_{12}n(b+an)/R^2\cos n\theta \tag{10.158}$$

$$M_{\theta\theta} = M_{\theta\theta0} + M_{\theta\theta1} = 0 + t^3/12\, D_{22}n(b+an)/R^2\cos n\theta \tag{10.159}$$

The PVW takes the form:

$$\begin{aligned}\delta^2\Pi = 2\pi RL\int_0^{2\pi}\{&N_{\theta\theta0}\delta\varepsilon_{\theta\theta2,ab} + N_{\theta\theta1,a}\delta\varepsilon_{\theta\theta1,b} + N_{xx1,a}\delta\varepsilon_{xx1,b} \\ &+M_{\theta\theta1,a}\delta\kappa_{\theta\theta1,b} + \frac{p_{ext}}{2R}\delta(v^2 + vw_{,\theta} - v_{,\theta}\,w + w^2)_{,ab}\}\, d\theta\delta q_a\delta q_b \\ &= H_{ab}\delta q_\alpha\delta q_\beta = 0\end{aligned} \tag{10.160}$$

Accounting for (10.149)-(10.159) and the identities:

$$\int_0^{2\pi} \cos^2 n\theta \, d\theta = \int_0^{2\pi} \sin^2 n\theta \, d\theta = \pi \tag{10.161}$$

the tensor **H** takes the form:

$$\mathbf{H} = \pi\lambda_c \tau D_{22} \begin{bmatrix} -\frac{p_{ext}}{\tau D_{22}}(n^2-1) + 1 + \frac{\tau^2}{12}n^4 & n\left(1+\frac{\tau^2}{12}n^2\right) \\ n\left(1+\frac{\tau^2}{12}n^2\right) & n^2\left(1+\frac{\tau^2}{12}\right) \end{bmatrix} \tag{10.162}$$

where $\tau = t/R$. The shell becomes unstable when $\det \mathbf{H} = H_{11}H_{22} - H_{12}H_{21} = 0$ which solved in terms of p_{ext} reduces to

$$p_{ext} = \frac{(n^2-1)D_{22}}{(1+\tau^2/12)}\frac{\tau^3}{12} \tag{10.163}$$

For $n = 1$, the bucking mode represents solid body translation of the tube, which is postulated to be constrained, so the critical (minimum) buckling pressure p_c is obtained for $n = 2$, in which case $b \approx -a/2$ and the eigenmode represents uniform ovalization at:

$$p_c = \frac{D_{22}}{4[1+(1/12)(t/R)^2]}\left(\frac{t}{R}\right)^3 \tag{10.164}$$

Or equivalently using (10.134)

$$p_c = \frac{C_{11}/\det C}{4[1+(1/12)(t/R)^2]}\left(\frac{t}{R}\right)^3 \tag{10.165}$$

The critical axial stress for cylindrical shells under a specified external pressure p_c can be obtained by solving iteratively eq. (10.165) in terms of σ_x, which appears in the material flexibility moduli in C. For linear elastic thin-walled cylinders it reduces to the well know expression:

$$p_{c.el} = \frac{E}{4(1-\nu^2)}\left(\frac{t}{R}\right)^3 \tag{10.166}$$

The analysis by (Ju & Kyriakides, 1992) resulted in a formula almost identical to (10.164) for p_c, with the sole difference of an additional term Δ in the denominator, which takes the form $[1+(1/12\Delta)(t/R)^2]$. The term $\Delta = 1 - D_{12}^2/D_{11}D_{22}$ originates from the demand for ($N_{xx1} = 0$), meaning no change in the axial stress may occur at any point of the cross section. However, this demand implies that axial strain is non-zero ($\varepsilon_{xx1} =$

$-D_{12}/D_{11}\,\varepsilon_{\theta\theta 1}$) and it does not conform with the assumed buckling mode in (10.149)-(10.151) that is the basis of both the present analysis and the one by (Ju & Kyriakides, 1992). It is assumed that the intended demand was for no change in the overall axial force in the cross section, expressed as:

$$\delta F_1 = \int_0^{2\pi} N_{xx1}\, R d\theta = 0 \tag{10.167}$$

This more reasonable demand is satisfied by identity, considering the definition of N_{xx1} in (10.156) and the assumed buckling mode.

The obtained bifurcation formula (10.164) refers to any axial loading conditions (hydrostatic stress, zero axial stress, zero axial strain) adopting the relevant stress values when calculating the stiffness component D_{22}. It is noted that in all cases, the term Δ is close to unity and it is multiplied by a small quantity small value $(1/12)(t/R)^2$ so it has very limited influence in the calculated critical values by (Ju & Kyriakides, 1992), which are practically identical to the ones obtained by (10.164).